Non-Linear Response and Instabilities of a Two-Degree-of-Freedom Airfoil Oscillating in Dynamic Stall

Gerasimos Fragiskatos

Department of Mechanical Engineering

McGill University

Montréal, Canada

March, 1999

Thesis submitted to the Faculty of Graduate Studies and Research in partial fulfillment of the requirements for the degree of Master of Engineering

0-612-50606-1

ABSTRACT

The system under study is that of a two-dimensional, two-degree-of-freedom airfoil (NACA 0012) in a steady subsonic airstream with external forcing. This airfoil is flexibly mounted in both degrees-of-freedom, and thus, describes an aeroelastic system. Non-linearities arising from the aerodynamics are responsible for the phenomenon of dynamic stall when the airfoil oscillates past the static-stall angle of attack. These non-linearities also cause the system to produce non-linear classes of motion, the most important of which is chaotic motion. Aeroelastic instabilities are also present in the system. This thesis explores the instabilities present in this system as well as its non-linear behaviour.

A semi-empirical numerical model revolving around the concept of an indicial response is used to model the non-linear aerodynamics in both degrees-of-freedom. The structural components of the system are modeled using simple linear elements such as translational and torsional springs. Structural damping is ignored. Simple force and moment balancing equations allow for the derivation of the pertinent aeroelastic equations, which are then solved using numerical techniques.

Self-excited oscillations, examples of aeroelastic instability, were found in the one-degree-of -freedom system for oscillations about the static-stall angle. Binary flutter, another form of aeroelastic instability, was found in the two-degree-of-freedom system. Every class of non-linear motion (equilibrium, periodic, quasi-periodic and chaotic) was discovered in the non-linear analysis, and several routes to chaos were discovered. These routes included the quasi-periodic route, period-doubling route and intermittency route. Some of the routes discovered compared well with classical examples.

SOMMAIRE

Le système à l'étude est celui d'une aile bidimensionnelle (NACA 0012), de deux degrés de liberté, dans un écoulement subsonique stationnaire, soumis à des oscillations forcées. Cette aile est montée avec flexibilité dans les deux degrés de liberté, et ainsi, décrit un système aéroélastique. Les non-linéarités résultant de l'aérodynamique sont responsables du phénomène de décrochage dynamique quand l'aile oscillante dépasse l'angle d'attaque du décrochage stationnaire. Ces non-linéarités font également produire des réponses de classes non-linéaires, le plus important étant la réponse chaotique. Les instabilités aéroélastiques sont également présentes dans le système. Cette thèse explore les instabilités dans ce système aussi bien que sa portée non-linéaire.

Un modèle numérique, semi-empirique utilisant le concept d'une réponse indicielle est employé pour modéliser l'aérodynamique non-linéaire dans les deux degrés de liberté. Les composantes structurelles du système sont modélisées en utilisant des éléments linéaires tels que les ressorts de translation et de rotation. L'amortissement dû à la structure est ignoré. Les équations d' équilibrage permettent la dérivation d' équations aéroélastiques convenables, qui sont alors résolues en utilisant des techniques numériques.

Les auto-oscillations, exemples d'instabilité aéroélastique, ont été trouvées dans le système d'un degré de liberté pour des oscillations autour de l'angle du décrochage stationnaire. Le flottement, une autre forme d'instabilité aéroélastique, a été trouvé dans le système de deux degrés de liberté. Toutes les classes de réponse non-linéaire (équilibre, périodique, quasi-périodique et chaotique) ont été découvertes dans l'analyse non-linéaire et plusieures routes au chaos ont été découvertes. Certaines de ces routes étaient comparables aux exemples classiques.

ACKNOWLEDGEMENTS

The author would like to express his gratitude to Professor S.J. Price for his guidance and patience throughout the entire process of creating this thesis. The author would also like to express his gratitude to his family, Nikolaos, Panagiota, Cathy and Doxy for their undying support.

CONTENTS

NOMENCLATURE

a	Speed of Sound
a_h	Non-Dimensional Distance from Mid-Chord to Elastic Axis
[C]	Damping Matrix
$C(k)$	Theodorsen's Function = $F(k)+iG(k)$
C_l	Lift Force Coefficient
$C_{l\alpha}$	Lift Curve Slope
C_m	Moment Coefficient
C_n	Normal Force Coefficient
c	Chord Length
D	Energy Dissipation
[E]	Stiffness Matrix
[F]	External Forcing Matrix
F,f	Generalized Functions
f	Non-Dimensional Distance from Leading Edge of Airfoil to the Separation Point
h	Heave or Plunge
i	Complex Variable $=\sqrt{-1}$
k	Non-Dimensional or Reduced Frequency
k_a	Pitch Structural Stiffness
k_h	Plunge Structural Stiffness
L	Lift Force
M	Mach Number
M	Moment

[M]	Mass Matrix
N	Normal Force
n	Integer Counter
P	Power Input
Po	Non-Dimensional Plunge Forcing
p	Pressure or Laplace Operation
[Q]	Aerodynamic Matrix
Qo	Non-Dimensional Pitch Forcing
q	Non-Dimensional Pitch-Rate
R1	Residual of Plunge D.O.F. Aeroelastic Equation
R2	Residual of Pitch D.O.F. Aeroelastic Equation
r_a	Non-Dimensional Radius of Gyration about Elastic Axis
s	Non-Dimensional Time
T	Kinetic Energy
t	Time
U^*	Non-Dimensional Free-Stream Flow Velocity
U_∞	Free-Stream Velocity
u,v,w	Velocity Vector Components
V	Potential Energy
$\bar{V}$	Velocity Vector
$w_{3/4c}$	Induced Velocity in the Z-Direction at the 3/4 Chord
x,y,z	Cartesian Coordinates
x_a	Non-Dimensional Distance from Elastic Axis to Center of Gravity

α	Pitch
α_{mean}	Pitch with Zero Structural Moment
β	Prandtl-Glauert Correction Factor
Γ	Circulation
ς	Damping Ratio
μ	Airfoil Air-Mass Ratio
ξ	Non-Dimensional Heave
ρ	Density
Φ	Velocity Potential Function
Φ'	Perturbation Velocity Potential
$\phi(s)$	Wagner's Function or other Indicial Admittance Function
$\psi(s)$	Kussner's Function
ω	Frequency
ϖ	Ratio of Natural frequencies (Pitch/Plunge)
$\mathbf{1}$	Step Input
$\dot{}$	Differentiation with Respect to Time
$'$	Differentiation with Respect to Non-Dimensional Time

<u>Subscripts</u>

a	Airfoil
c	Circulatory
f	Trailing Edge Separation

h	Heave or Plunge
m	Moment
n	Normal Force
q	Pitch-Rate Input
r	Response
v	Vortex
α	Pitch Input
∞	Free-Stream

Superscripts

c	Circulatory
f	Trailing Edge Separation
I	Impulsive
V	Vortex
$\_$	Mean
'	Transformed

Chapter 1

Introduction

1.1 Introduction to Aeroelasticity

Aeroelasticity refers to the static and dynamic response of flexible structures, which interact with aerodynamic forces. When an airstream interacts with a flexible surface, the aerodynamic forces dramatically change the dynamic behaviour of that surface. If structures remained rigid when exposed to an airstream, aeroelastic analysis would not be necessary. Many aeroelastic phenomena are undesirable; some may even lead to the catastrophic failure of the structure involved. Accurate predictions of aeroelastic instabilities are therefore necessary.

There are many types of aeroelastic systems. From very large structures, such as bridges or buildings, to all kinds of cylindrical structures, such as oil pipelines, smokestacks and nuclear reactor cooling rods. The systems that will be the focus of this thesis are those which involve lifting surfaces, such as airplane wings, helicopter rotors and turbines. More specifically, the aeroelastic response of a two-dimensional, two-degree-of-freedom airfoil (NACA 0012) in a steady subsonic airstream, and with external forcing will be studied.

Aeroelastic instabilities are of primary importance, due to the possibility of structural failure. There are two general categories of instabilities: static and dynamic. Static aeroelasticity refers to the study of aeroelastic systems, while ignoring the effects of inertia. This category therefore cannot include any types of oscillations, and only includes airfoil motion at zero frequency. Instabilities arising under these conditions are known as static instabilities. An example of this is known as divergence. This occurs when aerodynamic effects create negative stiffness in the pitch direction. If the structural stiffness is insufficient, the total effective stiffness of the airfoil may be zero, causing the airfoil to be unstable and the pitch to diverge. Early monoplanes needed to overcome this problem.

Dynamic aeroelasticity includes interaction between all of the aeroelastic effects: aerodynamic, structural, and inertial. Instabilities arising under these conditions are known as dynamic instabilities. A major problem of aeroelastic systems is flutter. This is an example of a dynamic instability. Flutter is a special case of a self-excited oscillation, in which the airfoil absorbs energy from the airstream in such a way that that the added energy overpowers the natural damping of the structure and causes the amplitude of the oscillations to diverge. This extraction of energy may come from negative damping supplied by the nature of the aerodynamics. This scenario allows for one-degree-of-freedom flutter. Another scenario involves the coupling of two degrees of freedom, and is called binary flutter. For the airfoil under study this situation occurs when the plunge motion acts to add energy in unison with the pitch. This happens at a particular phase difference between the two types of motion. For this situation to cause flutter, this phase difference must persist. This happens when the frequencies of these two types of motion are close to one another; it is known as "frequency coalescence", and is necessary for binary flutter to occur. Certain combinations of system parameters, the most important of which being airflow velocity, may cause the airfoil to experience instabilities. Linear analysis allows for instability boundaries to be found. These boundaries are crucial so as to avoid instabilities that may lead to divergent oscillations. Linear analysis of aeroelastic systems is often sufficient. There are cases, however, where non-linearities in the system may no longer be ignored. Such is the case in helicopter rotors, high performance aircraft and turbomachinery.

There are potentially many sources of non-linearities in aeroelastic systems. The most commonly encountered ones, however, are those arising from the structural or aerodynamic elements of the system. The system under study in this thesis assumes no structural non-linearities. This assumption is not made for the aerodynamics. Airfoils with structural non-linearities have been studied by many: (Hauenstein, Zara, Eversman and Qumei, 1992; Lee and Tron, 1989; Price and Alighanbari, 1995). Airfoils with aerodynamic non-linearities have also been studied by many: (Lee and LeBlanc, 1986; Tang and Dowell, 1992; Price and Keleris, 1995).

The aeroelastic model adopted in this thesis comes from the work of Lee and LeBlanc (1986). Because of the complexity of the non-linear behaviour of the aerodynamics, a purely theoretical analysis is impossible. Numerical methods are therefore a necessity. Lee and LeBlanc suggest the use of Houbolt's numerical scheme (Houbolt, 1950) in their work. This choice was therefore also adopted in this thesis. This thesis does not, however, adopt the aerodynamic analysis used by Lee and LeBlanc (1986). Lee and LeBlanc based their aerodynamic model on the work of Bielawa et al. (1983). They used that particular aerodynamic model to study the unsteady, non-linear aerodynamic loads for the one-degree-of-freedom airfoil, and used linear superposition to add plunge into the system. In this thesis an attempt is made to model the non-linearities in both degrees of freedom. The treatment of the aerodynamics comes from the works of Leishman and Beddoes (1986), for the one-degree-of-freedom airfoil, and Leishman and Tyler (1992) for the two-degree-of-freedom airfoil.

1.2 Introduction to Dynamic Stall

One source of non-linearities in the aerodynamics is due to separation of the flow over the airfoil at large angles of attack. When separation occurs, the airfoil loses its lift and is said to stall. For a steady airfoil (constant angle of attack) this is referred to as static stall, and the angle at which this occurs at is known as the static stall angle. For large unsteadiness in the airfoil, the stalling process is delayed to larger values of pitch, and there is also hysteresis in the reattachment of the flow over the airfoil when the pitch comes back below the static stall angle. This is a simplified explanation for a complex series of events that occurs in this dynamic situation, and is referred to, appropriately, as dynamic stall. Large excursions in lift and pitching moment also occur during dynamic stall. These effects are caused mainly by vortex flow over the airfoil.

Although the non-linear differential equations, which describe the flow over the airfoil, may be solved numerically, this would require enormous computational power. A semi-empirical model for dynamic stall is therefore necessary. Many different semi-empirical models for dynamic stall exist: (Bielawa et al., 1983; Leishman and Beddoes, 1986; Tran and Petot, 1981). The one adopted in this thesis is the model of Leishman and Beddoes, as mentioned before. Their model involves the indicial response of the airfoil (i.e.: response of the airfoil to a step input). This formulation is very versatile because, by simple superposition, the response of the airfoil to **arbitrary** forcing may be found. Also, according to Leishman and Tyler (1992), the plunge degree-of-freedom may be added easily, with only minor modifications to the model to account for non-linear plunge effects.

The aeroelastic model described above allows for the creation of a computer program, which will output the approximate non-linear response of the airfoil to a given input. The next step is to interpret this response. Non-linear dynamics is a relatively new science and revolves around the mathematical concept of chaos. The possible existence of chaos in the system described in this thesis is a major focus.

1.3 Introduction to Non-Linear Dynamics and Chaos

Chaos is a relatively new concept in mathematics, although scientists such as Henri Poincaré (1854-1912) have postulated its existence in earlier centuries. It took the breakthrough of digital computing, which allowed the solutions to many non-linear problems to be found, to shed light on this phenomenon. Chaos is a misnomer, traditionally used to describe complete disorder; this is not the case in the mathematical definition. Simply put, a chaotic response is a response whose long-term behaviour can not be predicted because of its extreme sensitivity to initial conditions. A small error in the measurement of the input means a large error in the output, thus destroying the chance of predictability. Chaos has been observed in many physical systems including turbulence in fluid mechanics, various chemical reactions, weather systems, the bouncing of billiard balls etc… (Moon, 1987). The amazing thing about chaotic solutions is that they arise from deterministic systems, for which there are no unpredictable or random inputs.

In linear systems, solutions are easily defined; non-linear systems, however, display a more complex behaviour. The state of dynamical motion is called an attractor. This name has been adopted because, under the influence of dissipation, dynamical systems are attracted to these states after the transient motion has decayed. Non-linear systems can display the same type of motion as linear systems, but they may also display motion peculiar only to non-linear systems. The general categories of attractors are as follows: 1) equilibrium 2), periodic motion, called a limit cycle 3), quasiperiodic motion, and 4) chaotic motion, sometimes called a strange attractor. Attractors are best identified in the phase plane, where state variables are plotted against each other (i.e.: pitch rate versus pitch, plunge rate versus plunge). Equilibrium points show up as a single point in the phase plane, limit cycles show up as closed loops, quasi-periodic motion shows up as an open loop, and chaotic motion fills up a portion of the phase plane. Chaotic motion has very distinct characteristics. Some of these characteristics are: 1) sensitivity to initial conditions, measured with Lyapunov exponents; 2) strange attractors in the phase plane of the system, measured by Poincaré maps; 3) fractal geometry in the phase plane, measured by Poincaré maps and fractal dimension; 4) broad band character in frequency spectrum of the output, measured by the fast Fourier transform.

Using various tools, some of which already have been mentioned briefly, the nature of the motion may be identified. The motion may also be compared to classical examples of chaos, to examine for similarities, and hence, possibly have a better understanding of the origin of the chaos. Also, through the use of bifurcation plots, the routes to the various states of motion, as a system parameter is altered, may be analyzed.

Figure 1.1, shows a summary of all the classes of motion that a non-linear system can produce.

The aeroelastic model being used in this thesis is derived from fundamental differential equations yet because it is semi-empirical in nature many of the tools used to analyze non-linear motion can not be used here. This is because, often, the tools used to analyze non-linear response take advantage of the differential equation. Therefore the tools used in this thesis are restricted to ones that do not require the differential equation as a reference.

1.3.1 Useful Tools

Time History

The time history of the response of the airfoil is a useful plot. Its usefulness lies in the fact that one may visualize the motion of the airfoil from this plot and relate it to physical reality. Other plots tend to be more abstract. From this plot one sees the way that the airfoil enters and exits stall, and may compare it to other examples with different system parameters (i.e.: stiffness, initial conditions etc…). This type of plot gives a lot of qualitative information about the response. From the time history one may identify the following qualities of the response: 1) the response may be identified as being of high or low frequency; 2) the response may be identified as being periodic; 3) if the response is period two or greater, one may see the relative amplitudes of the constituent periodic responses; 4) if the response is chaotic this plot will seem to be random, although it may also be quasi-periodic or in its transient state; 5) if the response is not always chaotic, one may examine the region between chaos and regular motion and see how they interact. To get the most information from this plot the following rule will be followed. The plot should be examined after many cycles, so that there is no transient motion.

Fast Fourier Transform (FFT)

The fast Fourier transform is a technique which can further help to distinguish between periodic, quasiperiodic and chaotic motion. The frequency spectrum plot produced using this technique reveals the constituent frequencies that can be used to reproduce the response using the superposition of periodic solutions. It also reveals the relative amplitude of these constituents. Non-chaotic solutions are equilibrium points, periodic solutions or quasi-periodic solutions. They are characterized by pronounced peaks, without a broad-band character, and are distinguished in the following way. An equilibrium point has no constituent frequencies, a periodic solution has a finite number of frequencies, depending on the number of periods, and these frequencies are whole number multiples of each other, a quasi-periodic solution has the same general character as a periodic solution except for the fact that the constituent frequencies are not whole number multiples of each other; they are incommensurate. Chaotic solutions, on the other hand, have a broad-band character made up of infinitely many frequencies, they appear to have random noise surrounding the main frequencies.

The accuracy of the FFT is important. It is therefore necessary to define an error. The error of the FFT is simply the resolution of the FFT plot, which may be found as follows. The airfoil response is sampled at a rate of $f_s = 1/\Delta t$. This is the maximum frequency possible for the response. The resolution of the FFT is therefore the sample rate divided by the total number of points or iterations that are sampled: $\Delta f_r = f_s / \#iter. = (1/\Delta t)/(\#iter.)$ Converting to rads/sec yields: $\Delta\omega_r = (2\pi/\Delta t)/(\#iter)$.. In the program used in this thesis the time step size is defined by the number of iteration that the program runs per cycle of the pitch forcing function: $\Delta t = (2\pi/\omega_{forcing})/(\#iter./\,cycle\ of\ pitch\ forcing)$. Combining expressions and simplifying gives the following FFT error definition:

$$FFT\ Error = \Delta\omega_r = \omega_{forcing}/(\#\ of\ pitch\ forcing\ cycles\ sampled)$$
$$or\ converting\ to\ non\text{-}dimensional\ parameters$$
$$FFT\ Error = \Delta k_r = k_{forcing}/(\#\ of\ pitch\ forcing\ cycles\ sampled)$$

Note, subscript s refers to sampling, and subscript r refers to resolution.

Phase Plane Plots

The phase plane plots are the plots that are first examined for the topological behaviour of the response of the airfoil. By plotting the velocity versus the displacement (angular or translational), one may examine the non-linear response of an airfoil in terms of the geometry of the attractor in phase-space. These plots offer information similar to the time history plots, but in a more condensed form. Periodic solutions form closed loops, equilibrium points show up as a single dot, chaotic solutions fill up a region in this space, are open loops and form "strange" attractors. These plots are used as a further indication of chaos, which may not be obvious from looking at the time history.

The trajectory of the system in phase space is called a flow. In dissipative systems these flows are attracted to a geometrical shape called an attractor. The region surrounding the attractor, which defines the set of initial conditions whose steady state lies within the attractor is called the basin of attraction. One of the characteristics of an attractor is the contraction of areas associated with the attraction of the initial conditions to their final state. For example, in a periodic response, areas containing a set of initial conditions contract into a single curve called the limit cycle. This means that there is a loss of information concerning initial conditions. Strange attractors, which are the hallmarks of chaos, have certain additional characteristics. The most important being sensitivity to initial conditions. This means that flows starting very close to each other will diverge quickly from each other. This may seem contradictory to the idea of attraction but it is not, the paths may diverge but they will still dwell within the same attractor, meaning that the maximum distance between neighboring trajectories will be the maximum length of the attractor. Another characteristic of a strange attractor is that its dimension is fractal, which will be discussed later.

Poincaré Maps

Poincaré mapping is a technique which samples the phase-space stroboscopocaly at intervals of $T = 2\pi / \omega_f$, where the denominator is the frequency of the forcing function or another characteristic frequency. It is a condensed form of the phase-plane, which allows more cycles to be examined, while extracting only the useful information from them. The Poincaré map can be used as another tool to distinguish between the various types of motion, and can also provide some additional information. Periodic solutions appear as single dots on the Poincaré map, the number of dots represents the number of periods. Quasi-periodic solutions appear as closed loops because the sampling frequency is not a whole number multiple of the constituent frequencies. Chaotic solutions appear as elaborate designs in this map and often have fractal geometry. This is where the greatest contribution lies: this map can be used to identify chaos, it is like a chaotic fingerprint. This is a profound finding, although chaotic solutions cannot be predicted because of the extreme sensitivity to initial conditions, similarities may be found in chaos. This means that even though non-linear systems are modeled using various degrees of accuracy, depending on which programming scheme is used, the chaotic solutions should display similar forms on the Poincaré maps. This justifies the whole premise of using approximations to model non-linear systems.

Return Maps

Poincaré maps are two-dimensional maps, return maps are one-dimensional. There are two types of return maps that are of interest: the first and second return maps. In return mapping the information contained in a Poincaré map is condensed by removing the rate terms. This is accomplished by plotting the pitch term versus either the pitch term immediately preceding or that preceding it by two samples on the Poincaré map. The usefulness of these maps lies in their comparison to famous maps that are known to exhibit particular behaviour. These maps include the Hénon map and the Logistic map.

Lyapunov Exponents and Fractal Dimension

Lyapunov exponents and fractal dimension are used as ways to quantify chaos. A positive Lyapunov exponent implies a chaotic solution, and fractal dimension in the phase-space implies the existence of a strange attractor, which is the elaborate structure underlying chaos.

The Lyapunov exponent measures the sensitivity of the system to changes in initial conditions. It measures the degree of separation between solutions, starting at points near each other. If we imagine a small sphere in phase-space of diameter d_o, which represents a collection of all possible initial conditions, then as the system evolves this sphere deforms into an irregular ellipse with maximum diameter d. The Lyapunov exponent measures the deformation through the following equation.

$$d = d_o 2^{\lambda(t-t_o)}$$

where λ is the Lyapunov exponent.

To find the true exponent one must do this calculation over different regions of the phase space and average the Lyapunov exponent. This task is beyond the scope of this thesis; however, a plot showing the divergence between solutions, with initial conditions separated by a minute amount, can demonstrate a sensitivity to initial conditions and will be done for certain examples as an indication of chaos. In fact, this plot can be used as a rough estimate of the Lyapunov exponent.

All attractors leave gaps in the phase space; fractal dimension is a measure of the space that a response occupies in the phase-space. More specifically it measures the extent to which an orbit fills up a subspace in the phase-plane. Strange attractors have a non-integer fractal dimension, and strange attractors almost always indicate chaos. This measurement is also beyond the scope of this thesis. Rather, as a further indication of chaos, fractal geometry will be looked for in the chaotic attractors. Fractal geometry simply implies complex patterns at many magnification levels, often having self-similar structure.

Bifurcation Plot

Bifurcation plots are very important plots; they allow one to examine the way a system's steady state response changes as a system parameter is varied. They also allow the route that a system takes from one type of motion to another to be identified, and more importantly, the way a system goes into and out of chaos. A bifurcation is a sudden change in behaviour in the response of a system. Bifurcations are characterized by the changing of a response from equilibrium to a periodic, or quasi-periodic, or chaotic vibration (in any order), and they may also be characterized by a change in period of the response (i.e.: period 1,2,3...).

1.3.2 Identification of Routes to Chaos

The identification of routes to chaos requires the use of the bifurcation plot. It is in this plot that the transition from one type of motion to another can be observed. Unfortunately bifurcation diagrams cannot distinguish between quasi-periodic and chaotic vibrations; it is therefore necessary to cross-reference this plot with the other plots mentioned before to make that determination.

There are many ways that the response of a system may become chaotic; the only way to classify the route is to compare it to a well established one. Three general categories of routes shall be examined; it is important to note however that the route taken by the system under study may be a combination, and may not be as clearly defined as the classical examples. They do however serve as a handy framework.

Period-Doubling

In the period doubling scenario, the system starts off as a periodic response and then, as a system parameter is varied, the response undergoes a bifurcation whereby the period of the periodic response doubles. As the system parameter is further varied the response experiences another period doubling, and this behaviour continues until the solution becomes chaotic. This route has been discovered in a difference equation of the following form:

$$x_{n+1} = 4\lambda x_n(1 - x_n)$$

When the parameter, λ, is varied, period doublings occur, and the values at which they occur follow this scaling rule:

$$\frac{\lambda_n - \lambda_{n-1}}{\lambda_{n+1} - \lambda_n} \rightarrow 4.6692016 \text{ (Feigenbaum number)}$$

Note, in the cases that are going to be studied it will be impossible to verify this rule because there will be an insufficient number of bifurcations, and the route to chaos will not be governed exclusively by period-doubling.

Quasi-Periodic Route

This route to chaos comes about when there is a transition from a quasi-periodic motion to a chaotic motion. It is characterized by the breakup of a closed loop on the Poincaré map. This breakup can be in the form of folding, development of wrinkles, or unraveling. There are more specific theories on the transition between quasi-periodic and chaotic motion, but because of the difficulty involved in identifying them they will not be used as comparison tools. Some examples include the Ruelle-Takens Scenario, torus breakdown and torus doubling (Nayfeh and Balachandran, 1995). Therefore, quasi-periodic routes will be identified as such, when a quasi-periodic motion turns into a chaotic motion by distortion of the torus structure (closed loop on the Poincaré map).

Intermittency Route

The intermittency route to chaos describes a situation where regular periodic motion is interrupted by bursts of chaotic motion. This situation becomes more prominent as a system parameter is varied; meaning that the period of chaotic motion becomes longer and longer until the motion is completely chaotic.

There are three types of intermittency, appropriately named type I, type II and type III. The distinction between these three types of intermittency depends on definitions of Floquet theory, which describes the stability of limit cycles. Other important tools used to identify intermittency are the return maps. Comparison of the first and second return maps with classical examples can be used to give an educated guess as to whether the motion is of type I or III intermittency (type II is very uncommon). To be more certain of the choice would require the use of the governing differential equation, on which Floquet theory depends.

1.4 Thesis Objectives and Summary

The main objective of this thesis is to identify and classify as many different types of motion that the aeroelastic system under study can produce in a broad range of system parameters. Another objective is to determine the route from which the motion changes from one type to another (i.e.: periodic, quasi-periodic, chaotic) as a system parameter is varied. The focus, of course, being chaotic motion, and the route thereto. Comparisons with classical cases will be used as much as possible, and physical explanations will be used to explain some of the phenomena whenever possible. A secondary objective of this thesis is to explore aeroelastic instabilities, whenever they are encountered, to see how these instabilities are manifested in the non-linear system. Comparisons to instabilities found in the linearized system may be used to further this objective. The first part of the thesis will deal with the design and testing of the aeroelastic model, while the latter part will deal with the interpretation of the results obtained from the model.

The second chapter presents a very detailed derivation of the aerodynamic model. This is necessary because the aerodynamic model is pieced together from several different papers written by Leishman and/or Beddoes. These papers include misprints, and do not explain every detail of the Leishman and Beddoes model. It is therefore necessary to derive each portion of the model from first principles using aerodynamic theory, so as to justify the modifications and extrapolations that were made. This chapter also discusses in detail the numerical methods that were used in the aerodynamic model.

This facilitates the integration of the aerodynamic portion of the model into the overall aeroelastic model, which was based on the work of Lee and LeBlanc. The third chapter tests the aerodynamic model. This is done by comparing its results to experimental data for airfoils subject to well-defined inputs (i.e.: harmonic or ramp) obtained from the relevant papers and by comparing qualitative trends to aerodynamic theory.

The fourth chapter deals with the derivation of the final aeroelastic model. Once again it is derived in detail to assure that it is correct. This chapter is basically a reiteration of Lee and LeBlanc's work, with the main difference being that a different aerodynamic model is used. Special attention is therefore paid to the integration of the Leishman and Beddoes dynamic stall model into the numerical framework of Lee and LeBlanc's work. The fifth chapter tests the overall aeroelastic model. This is done by defining numerical error terms and their respective tolerances, and assuring that the model falls within these tolerances.

The sixth chapter focuses on the one-degree-of-freedom system. It begins with a description of the system, and the simplifications that were made in order to obtain a one-degree-of -freedom system. The non-linear analysis techniques, discussed in section 1.3, are then used to analyze four different cases, which were defined by bifurcation plots. Many different types of motion are identified, including chaos. Several different routes to chaos are also identified. Aeroelastic instability is explored in the form of negative damping supplied from the aerodynamics when oscillating around the stall angle. This allows for a self-excited oscillation, which was discovered in one of the cases.

The seventh chapter explores the two-degree of freedom system. Once again the chapter starts with a description of the system and the simplifications that were made.

Binary flutter is shown to exist in the non-linear system. A linear flutter boundary is derived, and is shown to correspond well with that of the non-linear system. One case is studied, which is defined by a bifurcation plot. The presence of chaos is found near the flutter boundary, and the significance of this is discussed.

The final chapter summarizes the main conclusions that were made throughout the thesis. It also suggests some ways of improving the model, and discusses some of the other capabilities that were built into the model but not explored. It is therefore meant as an evaluation on how well the thesis accomplished its objectives, and perhaps to suggest avenues for future research for those readers who are so inclined.

Classes of Motion in Nonlinear Deterministic Systems

Regular Motion—Predictable: Periodic oscillations, quasiperiodic motion; not sensitive to changes in parameters or initial conditions

Regular Motion—Unpredictable: Multiple regular attractors (e.g., more than one periodic motion possible); long-time motion sensitive to initial conditions

Transient Chaos: Motions that look chaotic and appear to have characteristics of a strange attractor (as evidenced by Poincaré maps) but that eventually settle into a regular motion

Intermittent Chaos: Periods of regular motion with transient bursts of chaotic motion; duration of regular motion interval unpredictable

Limited or Narrow-Band Chaos: Chaotic motions whose phase space orbits remain close to some periodic or regular motion orbit; spectra often show narrow or limited broadening of certain frequency spikes

Large-Scale or Broad-Band Chaos—Weak: Dynamics can be described by orbits in a low-dimensional phase space $3 \leq n < 7$ (1–3 modes in mechanical systems) and usually one can measure fractal dimensions < 7; chaotic orbits traverse a broad region of phase space; spectra show broad range of frequencies especially below the driving frequency (if one is present)

Large-Scale Chaos—Strong: Dynamics must be described in a high-dimensional phase space; large number of essential degrees of freedom present; difficult to measure reliable fractal dimension; dynamical theories currently unavailable

Figure 1.1: Classes of Motion in Non-Linear Deterministic Systems; Reproduced from Moon (1987).

Chapter 2

The Aerodynamic Model for Dynamic Stall

2.1 Introduction

The motion of an airfoil in pitch and heave is explored in and out of dynamic stall. This investigation is then expanded to include an aeroelastic analysis of the airfoil. An indicial formulation is used for the attached flow regime. This method is implemented because it lends itself to arbitrary forcing, which is usually found in aeroelastic analyses. Vortex lift, a phenomenon in dynamic stall, is represented empirically. The corresponding vortex induced moment is modeled by allowing the center of pressure to displace itself during dynamic stall. The problem at hand is highly non-linear, mainly due to the moving separation point which travels from the trailing edge to the leading edge as the airfoil proceeds from lower to higher angles of attack. The separation point travel is modeled independently from the other phenomena and can be considered as an additional degree of freedom. Adjustments are made to the linear attached flow solution to account for the non-linearities. The onset of leading edge separation introduces the airfoil into the dynamic stall region. This leading edge separation is abrupt, unlike the trailing edge separation, which is progressive. A criterion is used to introduce leading edge separation based on the attainment of a critical leading edge pressure.

The model used to study the dynamic stall of a NACA 0012 airfoil was presented by Leishman and Beddoes (1986). The objective of this model was to synthesize unsteady aerodynamic data, so as to be able to predict the resulting unsteady loading. Although the model is approximate and semi-empirical in nature, it represents the key physical events of dynamic stall. To understand the features of the model one must first understand the main events of the dynamic stall process.

Dynamic stall is not a single event. It is a complex series of events whereby an airfoil experiencing unsteady motion stalls at an angle of attack greater than the static stall angle. The result of this excursion past the static stall angle also results in excursions from the static lift and pitching moment quantities as well as, in the case of oscillating airfoils, hysteresis in the reattachment process. The physical events of dynamic stall can be seen in Figure 2.1. The main events are as follows: 1) the static stall angle is exceeded; 2) flow reversal within the boundary layer causes the formation of a vortex at the leading edge of the airfoil; 3) the vortex detaches from the leading edge and convects downstream over the airfoil, meanwhile moment stall occurs whereby the pitching moment diverges towards a relatively large negative value; 4) the vortex reaches the trailing edge, signaling the beginning of lift stall as well as the maximum negative moment; 5) the flow becomes fully separated; 6) the boundary layer reattaches, initially at the leading edge of the airfoil and then progressing to the rear. The main features of the analytical model directly correlate to these events. The model is separated into sub-systems and describes, in an open loop sense, a simplified model of the dynamic stall process of an airfoil. The non-linear parts of the model are arranged in an open-loop chain, where the output from one sub-system of the model feeds into the next sub-system. The systems, their significance with respect to the dynamic stall events, and the resulting equations are discussed next.

2.2 Derivation of the Semi-Empirical Aerodynamic Model

2.2.1 Objective

The purpose of this section is: 1) to derive the analytical portion of the aerodynamic model, showing all the key features of its derivation; 2) to list all of the pertinent assumptions; 3) to justify the empirical portion of the model; and 4) to comment on the approach being used with respect to the main objectives of this thesis. These objectives being to maximize the accuracy of the unsteady aerodynamic loads whilst minimizing the use of computer resources, and to create a model which is physically representative of the phenomenon of dynamic stall.

2.2.2 Preliminaries

The most exact derivation for the flow around a three-dimensional body executing unsteady motion without any restrictions, taking into account all of the features of the flow (including separation) was discovered independently by M. Navier and G. Stokes.

The resulting set of partial differential equations is known as the Navier-Stokes equations. These equations are highly non-linear, and can only be solved using numerical techniques, which require a large amount of computer resources. Strategic assumptions can be made, however, to simplify the analysis. The approach that will be used here is adopted from a paper written by Leishman and Beddoes which was presented at the 42nd annual forum of the American Helicopter Society (Leishman and Beddoes, 1986). The approach used by Leishman and Beddoes splits the problem into sections: 1) the main section of the problem involves the attached flow solution, which is linear; 2) the second section involves the extension of the model to the non-linear regime, by taking into account trailing edge separation; 3) the third section determines a criterion for leading edge separation; and 4) the final section incorporates the effects of vortex flow and the dynamic stall event. All four sections are linked and form an open loop chain. In this manner the problem has been dissected into manageable parts of physical significance. The strategy used may be summarized as follows. Make enough assumptions to simplify the problem and then, through the use of empirical tools, account for these assumptions.

2.3 Attached Flow, Linear Regime Solution

The first step of the strategy requires making assumptions in order to obtain a linearized solution. Linearized solutions offer many advantages. One such advantage is the use of a transfer function, which allows the explicit solution to a well-described input to be found. If an arbitrary input is used, which is the case for aeroelastic responses, a solution may also be found by the linear superposition of idealized inputs, which are used to approximate the arbitrary input. The most convenient input for such an approximation is that of a step (or ramp) change of input. This class of input produces what is known as the indicial response. The derivation of the **indicial response** is the main objective of this section.

2.3.1 Fundamental Equations and Boundary Conditions

To fully appreciate the techniques employed to linearize such a highly non-linear problem, one must start from the beggining. In the case of a fluid flowing over a body one must first derive the equation(s) governing the dynamics of the surrounding fluid. The first set of assumptions that are made to simplify the model are as follows: **1) the flow is inviscid; 2) the fluid is a frictionless perfect gas; 3) the thermodynamic processes are isentropic; 4) all processes are reversible.**

When the flow is still attached over the airfoil, viscous effects are localized within a thin boundary layer, and therefore, for the most part the flow may be considered inviscid. The effects of the boundary layer which are non-linear may then be studied separately and subsequently added into the model. The other assumptions also degrade within the boundary layer.

When studying the flow of a perfect gas, the state of the flow may be described completely by specifying the pressure, density, temperature and all three components of velocity in mutually orthogonal directions as a function of position in three-dimensional space. There are therefore six variables that need to be solved for. The first equation, called the continuity equation, is found by applying the condition of conservation of mass through a control volume. Three more equations may be derived by realizing that the change of momentum of a flow in a given direction with respect to time is given by the change of pressure of that fluid in that direction in addition to external forces. These equations are a result of the conservation of momentum. Two more equations are needed to solve for all six variables. These last two equations come from the perfect gas law and the isentropic relation. These six equations which may be found in any fluids textbook create a determinate set of equations for which the state of the fluid flow may be found. To do so, however, one must integrate the non-linear partial differential equations, which is impossible except by numerical methods. Simplifications need to be made to achieve a linearized solution.

An excellent way to simplify the problem is to reduce the number of unknowns. This may be done through the definition of potential functions for velocity or acceleration (related to pressure). The potential function for velocity reduces the number of unknowns by two through the relationship

$$\vec{V} = \nabla\Phi \tag{2-1}$$

The existence of the velocity potential for the flow, however, requires that **5) the flow is irrotational**, implying that the fluid particles have zero angular momentum. This is **not** an assumption however; it may be proven through the use of Kelvin's Theorem:

$$\frac{D\Gamma}{Dt} = \oint_c \frac{dp}{\rho} \tag{2-2}$$

where D( )/Dt is the substantial derivative, i.e.: the time rate of change of a quantity for an individual fluid element and not for a control volume which is denoted by d( )/dt.

The quantity Γ is known as the circulation and is related to the curl of the velocity vector as follows:

$$\Gamma = \oint_c \vec{V} \cdot d\vec{s} \tag{2-3}$$

Equation (2-2) turns out to be equal to zero because of the perfect gas assumption. This implies that the rate of change of circulation with time is zero. Since the circulation is initially zero in the problem under study, this implies that the circulation is always zero around a closed curve of the same particles. This proves the irrotational nature of the flow and allows for the use of a velocity potential function.

The velocity potential allows the problem at hand to be simplified greatly, yet the fluid pressure is of more importance in the determination of the lift and moment coefficients, hence, an expression relating pressure to the velocity potential is required. Using the momentum equation and the velocity potential such a relationship can be found, and is known as Bernoulli's Equation:

$$\nabla\left[\frac{\partial\Phi}{\partial t} + \frac{\vec{V}\cdot\vec{V}}{2} + \int\frac{dp}{\rho}\right] = 0 \tag{2-4}$$

After some manipulation a single differential equation may be obtained related only to the velocity potential

$$\nabla^2\Phi - 1/a^2\left[\frac{\partial^2\Phi}{\partial t^2} + \frac{\partial(\vec{V}\cdot\vec{V})}{\partial t} + \vec{V}\cdot\nabla\cdot(\vec{V}\cdot\vec{V}/2)\right] = 0 \tag{2-5}$$

where a= $\sqrt{\frac{dp}{d\rho}}$ is the speed of sound and $\vec{V} = \nabla\Phi$.

Finally, we have a single differential equation describing the flow. However, this equation is often too difficult to solve. We must therefore simplify our approach once again. This leads to our next significant assumption. The sixth assumption is: **6) the assumption of small disturbances.** This means that the variables over the disturbed region (the region near the airfoil) have only a small difference compared to the free-stream value, or all variables are equal to their free-stream value plus a small perturbation. This allows us to linearize the differential equation given in (2-5) using a perturbation velocity potential (Φ'):

$$\Phi = \Phi' + U_\infty \cdot x \tag{2-6}$$

Using the small disturbances assumption, and also assuming: **7) the speed of sound remains constant over the disturbed region** the final differential equation is obtained

$$\nabla^2\Phi' - 1/a_\infty^2\left[\frac{\partial^2\Phi'}{\partial t^2} + 2U_\infty\frac{\partial^2\Phi'}{\partial x\partial t} + U_\infty{}^2\frac{\partial^2\Phi'}{\partial x^2}\right] = 0 \tag{2-7}$$

It is worth noting that assuming the speed of sound to be constant is not correct for high Mach numbers. However, only subsonic flow is examined in this thesis. The next assumption is therefore: **8) the flow is subsonic**. This assumption also validates the isentropic assumption, since only weak shock waves may develop over the airfoil. Another fact, which is worth noting, is that the small perturbation assumption is no longer correct at a stagnation point. These regions however do not occupy a significant percentage of the chord length of an airfoil, which means that the linearized equation still holds for the most part when examining the flow over an airfoil.

We now have a usable linearized differential equation for the velocity potential, which may be used in conjunction with Bernoulli's equation to determine the lift and moment coefficients. (For a more in depth derivation see Bisplinghoff, Ashley and Halfman (1955).

Boundary Conditions

Now that we have a usable equation for the surrounding fluid flow, we must fully define our problem; this is done through the boundary conditions. The problem we wish to examine is that of the flow around an airfoil which is both pitching and plunging. In particular, we wish to determine the lift and moment coefficients. Boundary conditions must be found and then simplified so that the problem remains linear.

The boundary condition of a body submerged in a fluid is that the normal velocity of the fluid with respect to the body surface be equal to the normal velocity of the body. A function of the form $f(x,y,z,t)=0$ may be used to define the surface of a body. Note that it is not only a function of spatial variables but of time as well, which incorporates the motion of the body as well as its shape. The boundary condition reads as follows in mathematical terms:

$$\frac{Df}{Dt} = \frac{\partial f}{\partial t} + u\frac{\partial f}{\partial x} + v\frac{\partial f}{\partial y} + w\frac{\partial f}{\partial z} = 0 \tag{2-8}$$

where u,v,w are the components of $\vec{V} = u\vec{i} + v\vec{j} + w\vec{k}$;

In simpler terms we see that the rate of change of the surface function $f=0$ with respect to time does not change when following a fluid element, meaning that the element is continually in contact with the surface and therefore has no perpendicular component of velocity relative to the airfoil.

Equation (2-8) may now be applied to the problem at a hand. **The problem is that of a thin camberless airfoil (NACA 0012) pitching and plunging in an airflow with a fluid velocity of U_∞ in the x-direction. Once the velocity potential is found, the pressure field may be found, thus allowing the moment and lift coefficients to be determined.**

The surface of a wing may be defined by a function $F_{u/l}(x,y,z,t)=z-f_{u/l}(x,y,t)=0$ (u and l denoting the upper and lower surfaces, respectively). Plugging this function into equation (2-8) we get

$$\frac{\partial \Phi'}{\partial z} = w = \frac{\partial f_{u/l}}{\partial t} + u\frac{\partial f_{u/l}}{\partial x} + v\frac{\partial f_{u/l}}{\partial y} \text{ for } z=z_{u/l} \qquad (2\text{-}9)$$

Another assumption which needs to be made in order to obtain linear boundary conditions is: **9) the airfoil is thin.** Using this assumption, along with the fact the $u<<U_\infty$, the boundary condition may be changed so that it is defined at $z=0$ since $z_{u/l}\approx 0_{+/-}$. This can be done using a Taylor series expansion about $z=0$, and ignoring terms higher than first order. The linear and homogeneous boundary conditions are thus obtained:

$$w = \frac{\partial f_{u/l}}{\partial t} + U_\infty \frac{\partial f_{u/l}}{\partial x} \text{ for } z=0_{+/-} \qquad (2\text{-}10)$$

where +/- denotes approaching zero from the positive or negative side, respectively.

Finally, the last assumption is that: **10) we have a two-dimensional airfoil which is camberless and symmetric.** In this case the function defining the surface of the airfoil is due exclusively to its motion and angle of attack. If the airfoil did have camber this could easily be superimposed. The boundary condition may then easily be introduced in terms of quantities such as pitch, pitch rate and plunge rate. This is done as per Figure 2.2 using the small perturbation assumption in a manner consistent with the previous equations. The equation of the surface of the airfoil is then

$$z_a(x,t)=-h(t)-\alpha(t)[x-(c \times a)/2] \quad \text{for} \quad -c/2 \leq x \leq c/2 \qquad (2\text{-}11)$$

where a is the non-dimensional distance from the mid-chord to where h is measured.

Hence, equation (2-10) gives:

$$w_a(x,t)=-\dot{h}(t)-\dot{\alpha}(t)[x-(c \times a)/2]-U_\infty\alpha(t) \quad \text{for} \quad -c/2 \leq x \leq c/2 \qquad (2\text{-}12)$$

where the subscript a indicates on the airfoil and the other quantities are as defined in Figure 2.2.

Equation (2-12) expresses the boundary condition on the airfoil surface and therefore represents the input to be used to solve the problem. The boundary condition is not merely a mathematical tool, it also has a physical meaning, w_a is the normal perturbation velocity of the airfoil. In equation (2-12) we see that there are two types of terms, those that are a function of time only, and those which also vary along the chord of the airfoil.

Boundary Conditions due to Angle of Attack or Plunge Rate

In equation (2-12) we see that the terms which contain either plunge rate or angle of attack are functions of time only. In other words at any given time they are constant along the chord. In the context of linear boundary conditions, these two terms may be used interchangeably by introducing an equivalent angle of attack of $\dot{h}/U_\infty$ for the plunge motion. The geometrical interpretation of this can be seen in Figure 2.3. In physical terms, a change of angle of attack or plunge rate causes the airfoil to have a constant normal velocity across the chord. Since the free-stream flow has no normal component of velocity, a normal perturbation velocity at the airfoil surface must be induced which is equal to the normal velocity of the surface, such that the flow remains tangential to the surface. A sketch of the normal perturbation velocity, with respect to distance along the airfoil, can be seen in Figure 2.3.

Boundary Condition due to Pitch Rate

When there is a change in angle of attack it implies a pitch rate term. (This term is absent from pure plunging motion.) Pitch rate differs from the previous type of boundary condition because its effect varies along the chord. The best way to describe the perturbation velocity due to pitch rate is through a diagram, as in Figure 2.4. In equation (2-12) we see, however, that the pitch rate term itself also has a component which does not vary along the chord. This is caused by the choice of axes. This term may also be transformed into an equivalent angle of attack term. This will later be shown to be useful in simplifying the results.

Along with the boundary conditions given above, there is also another condition that needs to be addressed. When the above equations are solved for a potential flow many solutions are possible, yet only one of them is correct. The Kutta condition must then be implemented to get this solution. The Kutta condition in its simplest form states that the flow must leave the trailing edge of an airfoil smoothly.

This concludes all of the necessary components required to obtain a linear solution for the attached flow case.

Solving the Unsteady Partial Differential Equation

The mathematical problem may be summarized as follows

Partial Differential Equation:

$$\nabla^2\Phi' - 1/a_\infty^2\left[\frac{\partial^2\Phi'}{\partial t^2} + 2U_\infty\frac{\partial^2\Phi'}{\partial x\partial t} + U_\infty{}^2\frac{\partial^2\Phi'}{\partial x^2}\right] = 0 \qquad (2\text{-}13)$$

Boundary Conditions:

$$\frac{\partial\Phi'}{\partial z} = w_a(x,t) = -\dot{h}(t) - \dot{\alpha}(t)[x-(c\times a)/2] - U_\infty\alpha(t) \text{ for } -c/2 \le x \le c/2 \qquad (2\text{-}14)$$

and the Kutta condition.

A usable linearized differential equation with the accompanying linearized boundary conditions have been obtained. Once this has been done there are many different methods which may be used to solve this problem. If, for example, an arbitrary motion is imposed on the airfoil many different avenues may be taken to solve this problem. The first approach would be to solve the differential equation directly using the boundary conditions imposed by this motion. This approach however can be very tedious, if not impossible, and does not take advantage of the tools that may be used in linear analyses. A second approach involves obtaining solutions to this problem due to a harmonically oscillating input, and then through the use of Fourier or Laplace transforms to construct the appropriate solution. A third avenue, which is of greatest interest to this investigation, is to determine the solution to a step change in input, i.e. an indicial response, then by using linear superposition in the form of Duhamel's integral to determine the solution. The arbitrary input may be considered as the sum of many step inputs, and therefore, due to the linear relation, the output to the corresponding arbitrary input may be found by summing the step input responses (indicial responses). The advantages of the last two approaches are obvious. First, there is no need to redefine the problem every time a new input is introduced. Second, a basic architecture can be created which may be manipulated by simple mathematical tools to produce the final result. One must emphasize that, since this is a linear analysis, the particular choice of method lies in convenience only, since, theoretically, all the above procedures will produce equivalent results provided that the appropriate boundary conditions are satisfied. The indicial response is the approach of choice in this investigation; however, the other methods are used to cross-reference the results, and are therefore also of great importance, as will be seen in the following sections.

2.3.2 Solution to Incompressible Flow

A famous solution (Theodorsen, 1935) to the unsteady problem involves making a further assumption about the flow, this being that the flow is incompressible. Theodorsen solved this problem for a harmonically oscillating airfoil. The solutions obtained for the incompressible case, are very attractive due to their simplicity. There is no such closed-form solution for the compressible case. The approach adopted in this thesis is to include the effects of compressibility semi-empirically. It is therefore very important to examine the incompressible version of the problem.

The derivation of the solution for the incompressible case, for either a harmonically oscillating airfoil or for an airfoil experiencing a step change in input, is tedious. It would serve no purpose in deriving it in its entirety. Therefore only the key features of Theodorsen's solution will be discussed. For the entire derivation many sources may be consulted: (Bisplinghoff, Ashley and Halfman, 1955; Theodorsen, 1935; Thwaits, 1961). It is important to note that the solutions to the step change and harmonically oscillating input are equivalent, in as much as one may be derived from the other through the use of mathematical tools such as the reciprocal relation (Lomax, 1952 and 1968; Mazelsky and Drishler, 1952), or through transfer functions in the Laplace domain (Beddoes, 1983). The harmonically oscillating airfoil will be discussed first, because it is less abstract and more physically realistic than an airfoil experiencing a step change in input.

Harmonic Response

When the flow is incompressible equation (2-13) reduces to the Laplace equation:

$$\nabla^2\Phi' = 0 \tag{2-15}$$

In physical terms, in an incompressible fluid the speed of sound is infinite. This means that every particle in the field "knows" what every other particle is doing and reacts instantaneously. This fact also makes the rest of the terms of equation (2-13) vanish. For an oscillating airfoil the boundary conditions may be found by using equation (2-14) and replacing α (t) and h(t) by harmonic functions, and finding their derivatives accordingly. With the aid of Kutta's hypothesis a solution may be found. The exact linear solution for a two-dimensional, harmonically oscillating airfoil in inviscid incompressible flow is:

<u>Input Motion</u>

$$h = \bar{h}e^{iwt} \ \& \ \alpha = \bar{\alpha}e^{iwt}$$

<u>Output Loads</u>

$$L = 2\pi\rho U_\infty (c/2)C(k)[\dot{h} + U_\infty\alpha + (c/2)(1/2 - a)\dot{\alpha}] + \pi\rho c^2/4[\ddot{h} + U_\infty\dot{\alpha} - (c/2)a\ddot{\alpha}]$$

$$M = 2\pi\rho U_\infty (c^2/4)(a + 1/2)C(k)[\dot{h} + U_\infty\alpha + (c/2)(1/2 - a)\dot{\alpha}] +$$
$$\pi\rho c^2/4[(c/2)a\ddot{h} - U_\infty(c/2)(1/2 - a)\dot{\alpha} - (c^2/4)(1/8 + a^2)\ddot{\alpha}]$$

(2-16)

where $k = \dfrac{wc}{2U_\infty}$ is the reduced frequency and L and M are the lift and moment.

The first important feature of Theodorsen's solution is that it has been split into two parts. One part is circulatory in nature, and the other part is impulsive or non-circulatory. The first part of the solution is the circulatory part, it is recognizable by the function C(k) which is made up of Bessel functions and is called Theodorsen's function C(k)=F(k)+iG(k) (Bisplinghoff, Ashley and Halfman, 1955). These functions introduce a phase lag in time between the input and the output, which is introduced by the unsteady nature of the movement of the airfoil. As the airfoil is oscillating, the circulation around the airfoil is changing. If Kelvin's circulation theory is to hold, counter vortices must be shed into the wake, so that the total circulation is zero. Each counter-vortex has an effect on the airfoil's lift and moment quantities, and their influence diminishes as they convect downstream. If the airfoil is brought to rest these counter-vortices (or starting vortex) are convected far downstream, and after a time will have no effect on the flow around the airfoil. Ignoring these vortices in unsteady motion is part of the **quasi-steady assumption**. Theodorsen's solution does not ignore them, it does assume, however, that they all lie on the same plane. This leads to our next assumption: **11) the planar wake assumption**. Therefore, the function C(k) is a measure of the circulatory lag, if it were equal to unity the solution would be the quasi-steady solution.

The next part of the solution is impulsive or non-circulatory in nature and stems from the fact that the airfoil is displacing fluid when it is oscillating. In incompressible flow any change in the field can be accounted for instantaneously, and therefore, there is no time lag between the input motion and the output quantities. It can therefore be regarded as an added mass or moment of inertia, and is sometimes referred to as a virtual or apparent mass term, it also accounts for the damping associated with the displacement of air.

Other interesting facts appear from further examination of Theodorsen's solution: 1) the plunge motion may be used interchangeably with the angle of attack term, which means that the only thing that distinguishes pitch and plunge is a pitch rate term; 2) **only the induced velocity about the 3/4 chord point need be specified to determine the circulatory lift and moment contributions** $w_{3/4c}=[\dot{h}+U_\infty\alpha+(c/2)(1/2-a)\dot{\alpha}]$; 3) the circulatory lift acts at the quarter chord, meaning that if the moment is taken about the quarter chord there will be no circulatory contribution in the moment term; 4) the impulsive lift acts at the 3/4 chord. All these facts are important, and will be utilized to simplify the final results.

Indicial Response

The next step is to find the response to a step change in motion, which can then be used in conjunction with Duhamel's superposition integral to determine the desired solution to an arbitrary input. Two such solutions are of importance to this thesis. These are the solution to a step change in motion (Wagner's solution), as well as the solution for entry of the airfoil into a sharp edged gust (Kussner's solution); see Bisplinghoff, Ashley and Halfman (1955). Once again the solutions have two parts, the impulsive part and the circulatory part. In incompressible flow the impulsive term reacts immediately to changes in motion. In the case of a step change in motion (pitch or plunge), during the first instant of time, the rates of change of pitch and plunge are infinite; any time later they are zero. This implies that the impulsive term must do the same according to equation (2-16), resulting in a singularity at t=0. Using Piston theory (Thwaits, 1961) one can determine the impulsive terms at t=0, which would include a Kronecker delta, but in the end they are of no importance and are therefore ignored. They will be discussed in the subsequent compressible regime section. The circulatory term, however, may be expressed as follows.

Input Motion

$w_{3/4c}\mathbf{1}$

Output Loads

$$L = \pi\rho U_{\infty}^{2}\left[\frac{w_{3/4c}}{U_{\infty}}\right]\phi(s)\mathbf{1}$$

$$M = 0$$

(2-17)

where $\phi(s)$ is Wagner's function , $s=2U_{\infty}t/c$ (non-dimensional time) and $w_{3/4c}\mathbf{1}$ (**1**: step input) is a step change of induced velocity at the 3/4 chord.

Wagner's function can be expressed in terms of Theodorsen's function in the following way, using the reciprocal relation

$$\phi(s) = \frac{2}{\pi}\int_{0}^{\infty}\frac{F(k)}{k}\sin(ks)dk = 1 + \frac{2}{\pi}\int_{0}^{\infty}\frac{G(k)}{k}\cos(ks)dk \qquad (2\text{-}18)$$

Wagner's function is not expressible in terms of well-known functions, however an approximation, in terms of exponential functions, is:

$$\phi(s) = 1\text{-}0.165\exp(\text{-}0.0455s)\text{-}0.335\exp(\text{-}0.3s) \qquad (2\text{-}19)$$

Kussner's function $\psi(s)$replaces Wagner's function when the input is a sharp edged gust (see Figure 2.5).

$$\psi(s) = 1\text{-}0.5\exp(-0.13s)\text{-}0.5\exp(-s) \qquad (2\text{-}20)$$

For a more in depth treatment of exponential approximations refer to Peterson and Crawley (1988).

2.3.3 Empirical Extension to Compressible Regime

Ideally, a general closed form solution is desired for the compressible regime. Unfortunately, the incompressible solution can only be used for low Mach numbers (i.e.: M<0.3), and there is no such closed form solution in the compressible regime that works for any Mach number and for all modes of input. Solutions have been found for various Mach numbers (Mazelsky and Drischler, 1952), yet there is no easy correction factor that can be added (as is the case for steady flow) to convert from the incompressible to the compressible regime. The strategy taken by Leishman & Beddoes (1986) is to do just that, however. In other words they add a Prandtl-Glauert type correction factor into the solution empirically.

In the same spirit as for the incompressible solution, Leishman and Beddoes (1986) separate the problem into two parts. One part involves circulation and the other does not. Besides the new correction factor for compressibility, added to generalize the solution, there are a few more differences in the approach that is taken compared with the approach taken to solve the incompressible case. In the incompressible regime there is a singularity at t=0 when a step change in motion is made. This singularity is caused by the impulsive term. Compressible flow cushions this singularity. This is due to the fact that since the speed of sound is now finite, there is an added lag in the response to any input. The circulatory solution also has this new lag. This new lag term is the essence of the new correction factor. Piston theory allows for a solution for the impulsive lift at t=0. Another major difference is that it is no longer sufficient to simply specify the downwash velocity at the 3/4 chord. The modes of motion must be separated. Two modes are involved in the solution: 1) angle of attack and equivalent angle of attack, and 2) pitch rate term. This means that instead of having one Wagner function there must be two.

Many references give solutions for the indicial response for the compressible case (Mazelsky and Drischler, 1952; Lomax, 1968). They have even separated the contributions from circulation and non-circulatory terms (Reissner, 1951; Mazelsky, 1952). In this investigation two different approaches are used simultaneously to find the indicial response. One approach is used to find the initial loading, which is impulsive in nature, and another is used to find the circulatory loading, which starts from zero and then tends towards the steady state value.

Approach #1: Circulatory Loading

Lomax (1968) has shown that the circulatory loading is proportional to the loading caused by the penetration of a sharp edged gust. For the incompressible case this is given by Kussner, equation (2-20). The solution to the compressible case is given by Beddoes (1980), and is shown in Figure 2.6 for several Mach numbers. The steady state solution is the same as the incompressible case scaled by the Prandtl-Glauert correction factor $1/\sqrt{1-M^2}$. It is shown by Beddoes (1980) that by scaling time by $(1-M^2)$ the compressible solution collapses almost perfectly to a single solution (see Figure 2.6):

$$\psi_c(s) = 1/\sqrt{1-M^2}\,(1-0.5\exp(-0.13s')-0.5\exp(-s')) \qquad (2\text{-}21)$$

where $s'=s(1-M^2)$.

The lift curve slope $2\pi/\sqrt{1-M^2}$ for the compressible case is replaced by the value $C_{l\alpha}(M)$ which is a function of Mach number and is found experimentally for greater accuracy. Therefore the compressible version of the solution to a sharp edged gust is:

<u>Incompressible</u> | <u>Compressible</u>

$$C_l=2\pi\left[\frac{w}{U_\infty}\right]\psi(s) \qquad C_l= C_{l\alpha}(M)\left[\frac{w}{U_\infty}\right]\psi_c(s)$$

(2-22)

It is shown in Figure 2.6 that the approximate compressible solution matches the theoretical ones quite nicely, which justifies the simplification. Similarly, it can be shown that a modified version of equation (2-22) can be used to match the circulatory component for a step change in angle of attack for compressible flow, i.e. a compressible Wagner function:

$$\phi_\alpha^c(s,M) = 1.0-0.3\exp(-0.14(1-M^2)s)-0.7\exp(-0.53(1-M^2)s) \qquad (2\text{-}23)$$

where subscript α denotes a step change in angle of attack, and superscript c denotes circulatory contribution. The constants were determined by Beddoes through a combination of experiments, theoretical analysis and CFD models.

Equation (2-23) is only one of the admittance functions, which are necessary to determine the entire circulatory loading. Other similar functions must be found for a step-change in pitch-rate and for the moment terms. For a complete explanation refer to (Bisplinghoff, Ashley and Halfman, 1955). This is unlike the incompressible case where only one admittance function (Wagner's Function) was necessary.

The choice of axes is very important in compressible flow, as was also the case for incompressible flow. With a strategic choice of axes, the number of admittance functions necessary may be reduced. Once again by choosing the moment axis about the quarter chord there is no circulatory contribution in the moment term. Also, if the pitch axis is taken about the 3/4 chord the circulatory term resulting from pitch rate is incorporated in the angle of attack and equivalent term. With this choice of axis the only other circulatory term is the moment due to the pitch rate. The indicial function for this is equal to:

$$\phi_{qm}^{c}(s,M)=1.0-\exp(-0.5(1-M^{2})s) \tag{2-24}$$

where subscripts m and q denote moment and a step change in pitch rate, respectively, while superscript c denotes circulatory contribution.

Therefore the circulatory contributions for compressible flow are:

$$C_{n\alpha}^{c}(\mathrm{s,M})=\mathrm{C_{l\alpha}(M)}\phi_{\alpha}^{c}(\mathrm{s,M})(\alpha_{3/4c}+\frac{\dot{h}}{U_{\infty}}) \tag{2-25}$$

$$C_{mq}^{c}(\mathrm{s,M})=-(\mathrm{C_{l\alpha}(M)}/16)\phi_{qm}^{c}(s,M)(\mathrm{q}) \tag{2-26}$$

where n and m denote normal force and moment coefficient and q=$\dot{\alpha}\, c/U_{\infty}$. Note that normal force and normal force coefficient shall be used interchangeably with lift and lift coefficient. They are considered equal for small angles. The transition has been made here because normal forces are used in the aeroelastic analysis found in Chapter 4.

If the pitch axis is not at the 3/4 chord, $\alpha_{3/4c}$ also includes a pitch rate term according to the following relationship:

$$\alpha_{3/4c} = \alpha_{off-axis} + q(1/2 - a) \tag{2-27}$$

where a is defined in Figure 2.2 and off-axis refers to an arbitrary chord position. This transformation is analogous to the transformation seen in Figure 2.4. The only difference here is that the ¾ chord point is the position of relevance and not the mid-chord.

We see that using this strategy, there is no increased complexity in the solution compared with the incompressible case, except for the fact that there are two admittance functions replacing the one Wagner function in the incompressible case.

Approach #2: Impulsive Loading

The initial loading due to a step change in motion can be shown to be entirely non-circulatory. Piston theory can be used to determine the initial value. Purely impulsive loading occurs when the air is not flowing, i.e.: U_∞=0. Using equation (2-13) with U_∞=0, and also assuming that for the first instant in time all the elements of the airfoil act as small pistons moving in the z-direction only, we get the acoustic differential equation:

$$\frac{\partial^2 \Phi'}{\partial z^2} = 1/a_\infty^2 \frac{\partial^2 \Phi'}{\partial t^2}$$

with the following boundary condition

$$\frac{\partial \Phi'}{\partial z} = w(t = 0, x) \quad for\ z = 0, t > 0\ (ie: step\ change) \tag{2-28}$$

Without further explanation this equation, in conjunction with the linearized version of Bernoulli's equation (equation (2-4)), gives the following relationship, refer to Appendix 1-C for a complete derivation):

$$\Delta C_p(x, t = 0) = \frac{p_{lower} - p_{upper}}{\frac{1}{2}\rho U_\infty^2} = -\frac{4}{M}\frac{w_a(x)}{U_\infty} \tag{2-29}$$

where $w_a(x)$ is the downwash along the chord. For each mode of input as shown in Figures 2.3 and 2.4, the following values of $w_a(x)$ are obtained. For a step change of angle of attack the downwash is

$$w_a(x) = -(\alpha_{3/4c} U_\infty + \dot{h}). \tag{2-30}$$

For a step change of pitch rate at the 3/4 chord the downwash is

$$w_a(x) = qU_\infty(3/4 - x/c\ ). \tag{2-31}$$

Substitution of (2-30) and (2-31) into (2-29), and integration along the chord using the expressions

$$C_n(t = 0) = \frac{1}{c}\int_0^c \Delta C_p(x, t = 0)dx \tag{2-32}$$

$$C_{m@1/4c}(t = 0) = \frac{1}{c^2}\int_0^c \Delta C_p(x, t = 0)(x - 1/4c)dx \tag{2-33}$$

gives the following expression for the impulsive loading:

$$C_{n\alpha}^{I}(t = 0) = \frac{4}{M}(\alpha_{3/4c} + \dot{h}/U_\infty) \tag{2-34}$$

$$C^{l}_{m\alpha @1/4c}(t=0) = -\frac{1}{M}(\alpha_{3/4c} + \dot{h}/U_{\infty}) \tag{2-35}$$

$$C^{l}_{nq}(t=0) = \frac{-1}{M}(q) \tag{2-36}$$

$$C^{l}_{mq @1/4c}(t=0) = \frac{-1}{12M}(q) \tag{2-37}$$

It is known from the solutions offered by various references (Mazelsky, 1952; Beddoes, 1980; Leishman and Beddoes, 1986) that the initial impulsive loading decays to zero in an exponential manner. The only thing that need be addressed now is how many exponential functions need be used, and what are their time constants. Fortunately there is an explicit solution for the indicial response for the first few semi-chords of airfoil travel. It was presented by Lomax (1952) whereby an analogy was made between the three-dimensional steady-state problem and the two-dimensional unsteady problem. In its simplest form it involved considering the time variable as a third spatial variable. The indicial response was evaluated explicitly from $0 \le s \le \frac{2M}{M+1}$. The explicit solutions now allow us to evaluate the time constants for the impulsive loading by realizing the following:

$$\frac{dC_{total}}{ds} = \frac{dC_{circulatory}}{ds} + \frac{dC_{impulsive}}{ds} \text{ (at t=0)} \tag{2-38}$$

For the most part one exponential function was used for the impulsive part. Refer to Appendix 1-A for the derivation of the time constants. Finally we are able to write the total linear indicial response for an airfoil:

Angle of Attack and Equivalent

$$C_{n\alpha}(s,M) = [\frac{4}{M}\phi_\alpha^I(s,M) + C_{l\alpha}(M)\phi_\alpha^C(s,M)](\alpha_{3/4c} + \dot{h}/U_\infty) \qquad (2\text{-}39)$$

$$C_{m\alpha@1/4c}(s,M) = [-\frac{1}{M}\phi_{\alpha m}^I(s,M)](\alpha_{3/4c} + \dot{h}/U_\infty) \qquad (2\text{-}40)$$

Pitch Rate at the 3/4 chord

$$C_{nq}(s,M) = [\frac{-1}{M}\phi_q^I(s,M)](q) \qquad (2\text{-}41)$$

$$C_{mq@1/4c}(t=0) = [\frac{-1}{12M}\phi_{qm}^I(s,M) - (\mathrm{C_{l\alpha}(M)}/16)\phi_{qm}^{c}(s,M)](q) \qquad (2\text{-}42)$$

2.3.4 Numerical Procedure

After a usable indicial response has been formulated, it must be used in conjunction with Duhamel's integral to find a solution to an arbitrary input. A finite difference approximation to Duhamel's integral can be used to determine the cumulative effect from an arbitrary time history of input. To be able to determine the accuracy of the numerical approximation it must be cross-referenced with both experimental and theoretical results. Since it is physically impossible to create an idealized step input, it is more advantages to examine harmonic oscillations. There must be a way, however, to relate any errors back to the indicial response. The easiest way to do this is by determining the transfer function.

The Transfer Function

If we take the circulatory coefficient of lift for a step change of angle of attack, and transform it to the Laplace domain we get:

<u>Input</u>

Step change of angle of attack $\alpha_{eff}(p)=1/p$;

<u>Output</u>

Time Domain : $C_{nc}(t)=C_{l\alpha}(M)[1-A_1\exp(-\frac{t}{T_1})-A_2\exp(-\frac{t}{T_2})]\alpha_{eff}1$

Laplace Domain: $$C_{nc}(p)=C_{l\alpha}(M)[\frac{1}{p}-\frac{A_1T_1}{1+T_1p}-\frac{A_2T_2}{1+T_2p}] \qquad (2\text{-}43)$$

where p=Laplace variable, $A_1=0.3$, $A_2=0.7$, $T_1=c/(2*0.14*(1-M^2)*U_\infty)$

$T_2= c/(2*0.53*(1-M^2)*U_\infty)$ and the time domain output comes from equations (2-24) and (2-25).

From (2-43) the transfer function may be easily found by realizing that $(1-A_1-A_2)=0$ and dividing (2-43) by 1/p to give:

$$\frac{C^c{}_{n\alpha}(p)}{\alpha_{eff}(p)}=C_{l\alpha}(M)[\frac{A_1}{1+T_1p}+\frac{A_2}{1+T_2p}] \qquad (2\text{-}44)$$

Now we need only replace $\alpha_{eff}(p)$ by the desired input and then transform back from the Laplace domain to the time domain to determine the response. Some of the other transfer functions are:

$$\frac{C^I{}_{n\alpha}(p)}{\alpha(p)}=\frac{4}{M}[\frac{T_Ip}{1+T_Ip}] \qquad (2\text{-}45)$$

where T_I is given in Appendix 1-A, and

$$\frac{C'_{nq}(p)}{q(p)} = \frac{-1}{M}\left[\frac{T_q p}{1+T_q p}\right] \tag{2-46}$$

where $T_q = T_I$.

If, for example, the response to a harmonic input is desired where α (t)=sin(wt) , w being the frequency of the oscillation, one would simply replace $\alpha(p)$ by $\frac{1}{w}[\frac{1}{1+p^2/w^2}]$, or for the response to a ramp input α (t)=k_at, one would use $\alpha(p)=\frac{k_a}{p^2}$. In this manner mistakes found in one type of input can be used to improve the solution to another type of input. Hence, we see one of the great advantages of linear solutions. In fact it is through this method that Beddoes determined the time constants for the circulatory lift functions. Using a more rigorous program (LTRAN 2) and experiments using both oscillatory and ramp inputs Beddoes was able to determine accurate coefficients for the circulatory functions see Beddoes (1982).

Derivation of Numerical Algorithm For Attached Flow

Now that the techniques of verification have been established, the derivation of the numerical algorithm can be better understood. The purpose of the algorithm is to determine the response to an arbitrary input. This arbitrary input can be reconstructed as the sum of step inputs applied at equal time intervals; therefore, the response will be equal to the sum of the step responses. This concept is explained in Appendix (1-B), where it is shown how a single exponential function of the indicial output may be used to derive the numerical algorithm for an arbitrary input. Since all of the functions used are approximated by exponential functions this is critical. Therefore in a similar fashion to that presented in Appendix (1-B) the numerical solution due to a step change in motion is:

Time Domain Indicial Response:

$$C^{C}{}_{n\alpha}\ (t) = C_{l\alpha}(M)[1 - A_1 \exp(-\frac{s}{T_1}) - A_2 \exp(-\frac{s}{T_2})]\alpha$$

Corresponding Numerical Algorithm:

$$C^{C}_{n\alpha}(n) = C_{l\alpha}(M)[\alpha(n) - X(n) - Y(n)]$$

$$X(n) = X(n-1)\exp(-\Delta s / T_1) + A_1(\alpha(n) - \alpha(n-1))$$

$$Y(n) = Y(n-1)\exp(-\Delta s / T_2) + A_2(\alpha(n) - \alpha(n-1))$$

(2-47)

where n denotes the sample under examination (i.e.: t=0 $\Rightarrow$ n=0 , t=Δt $\Rightarrow$n=1 , t=2Δt $\Rightarrow$n=2 etc). Note, X(n) and Y(n) are deficiency functions, and are a measure of the circulatory lag and the compressibility lag introduced in the correction factor. If X(n)=Y(n)=0 equation (2-47) would give the quasi-steady solution.

$$C^{I}_{n\alpha}(n) = \frac{4}{M} I(n)$$

$$I(n) = I(n-1)\exp(-\Delta s / T_I) + (\alpha(n) - \alpha(n-1)) \qquad (2\text{-}48)$$

$$C^{I}_{nq}(n) = \frac{-1}{M} Q(n)$$

$$Q(n) = Q(n-1)\exp(-\Delta s / T_q) + (\alpha(n) - \alpha(n-1)) \qquad (2\text{-}49)$$

Note, I(n) and Q(n) are also deficiency functions which arise from the fact that the flow is compressible.

The solutions given by equations (2-47) - (2-49) serve as a starting point. After being used to approximate the solution to a harmonic input, and being compared to the explicit solution for a harmonic input, several problems in accuracy arose which required that the solution be modified. It was found that a ramp algorithm gave better results for the impulsive loading. The derivation of the ramp algorithm is very similar to that of the step function, therefore, only the solution shall be given (Beddoes, 1982):

$$C^{I}_{n\alpha}(n) = \frac{4T_I}{M}(D\alpha(n) - DI(n))$$

$$DI(n) = DI(n-1)\exp(-\Delta s / T_I) + (D\alpha(n) - D\alpha(n-1)) \qquad \text{(2-50)}$$

where $D\alpha(n) = (\alpha(n) - \alpha(n-1)) / \Delta t$ & T_I=c/a;

$$C^{I}_{nq}(n) = \frac{-T_q}{M}(Dq(n) - DQ(n))$$

$$DQ(n) = DQ(n-1)\exp(-\Delta s / T_q) + (Dq(n) - Dq(n-1)) \qquad \text{(2-51)}$$

where $Dq(n) = (q(n) - q(n-1)) / \Delta t$.

One last modification was made to improve the accuracy of the solution. Using the step or ramp response at the beginning of each sample (or interval) was inaccurate; it introduced an unnecessary phase lag. To help eliminate this phase lag a half-step lead was incorporated in the forcing functions. This means that the forcing function starts half an interval before the beginning of the sample. This half-step lead is incorporated into the deficiency functions in the following manner:

<u>Deficiency without half-step lead</u>

$$DEFFICIENCY(n) = DEFFICIENCY(n-1)\exp(-\Delta s / T) + (INPUT(n) - INPUT(n-1))$$

<u>Deficiency with half-step lead</u>

$$DEFFICIENCY(n) = DEFFICIENCY(n-1)\exp(-\Delta s/T) + (INPUT(n) - INPUT(n-1))\exp(-\Delta s/2T) \tag{2-52}$$

Simply put, the output has been allowed to decay by half a time step at each interval, hence, the addition of the exponential function with half a time step lead.

In the end, a "hybrid" algorithm is used, incorporating the best features of each numerical method. The moment terms are found in an analogous fashion. Therefore, the numerical algorithm used to solve for the attached linear flow is

$$C^C_{n\alpha}(n) = C_{l\alpha}(M)[\alpha(n) - X(n) - Y(n)]$$

$$C^I_{n\alpha}(n) = \frac{4T_I}{M}(D\alpha(n) - DI(n))$$

$$C^I_{nq}(n) = \frac{-T_q}{M}(Dq(n) - DQ(n))$$

$$C^I_{m\alpha}(n) = -C^I_{n\alpha}\ /\ 4$$

$$C^I_{mq}(n) = -C^I_{nq}(n)/4 - (T_q^2/3M)(Dq(n) - DQM(n)) \tag{2-53}$$

where:

$$X(n) = X(n-1)\exp(-\Delta s/T_1) + A_1(\alpha(n) - \alpha(n-1))\exp(-\Delta s/2T_1)$$

$$Y(n) = Y(n-1)\exp(-\Delta s/T_2) + A_2(\alpha(n) - \alpha(n-1))\exp(-\Delta s/2T_2)$$

$$DI(n) = DI(n-1)\exp(-\Delta s/T_I) + (D\alpha(n) - D\alpha(n-1))\exp(-\Delta s/2T_I)$$

$$D\alpha(n) = (\alpha(n) - \alpha(n-1))/\Delta t$$

$$DQ(n) = DQ(n-1)\exp(-\Delta s/T_q) + (Dq(n) - Dq(n-1))\exp(-\Delta s/2T_q)$$

$$DQM(n) = DQM(n-1)\exp(-\Delta s/T_q^2) + (Dq(n) - Dq(n-1))\exp(-\Delta s/2T_q^2)$$

$$Dq(n) = (q(n) - q(n-1))/\Delta t$$

Note, the numerical model does not include a circulatory contribution in the moment term for pitch-rate (i.e.: equation (2-26)). It was ignored by Leishman & Beddoes (1986).

2.4 Semi-Empirical Extension to the Non-Linear Regime

Now that a solution has been found for when the flow is attached, it is necessary to account for non-linearities, which are introduced by viscous flow within the boundary layer as well as vortex flow when the airfoil enters dynamic stall. Viscous effects become more prominent as the flow over the airfoil separates. The first order of business is to determine the mode of separation. One mode of separation is progressive trailing edge separation, which starts from the trailing edge, and as the angle of attack increases, travels towards the leading edge. This has an adverse effect on the circulation around the airfoil. Although trailing-edge separation is important in both static and dynamic conditions, it has been shown that it is suppressed under moderate pitch-rates (Carr, 1977). This suppression is caused by the time lags in both the pressure response and the boundary layer response relative to the static case. Another type of stall is leading edge stall, which starts abruptly at the leading edge and is severe. It is caused by an adverse pressure gradient near the leading edge, which is strong enough to cause flow reversal. At low Mach numbers, unless the airfoil has a sharp leading edge, separation will be dominated by trailing edge separation. However, at higher Mach numbers, supercritical flow develops over the top of the airfoil, near the leading edge, causing the creation of a shock wave, which creates the right pressure conditions for separation. Therefore, the dominant mode of separation is leading edge or shock-induced separation at relatively low pitch-rates and Mach numbers larger than 0.3. This form of separation is much more abrupt and has different effects than that of trailing edge separation. Although the primary source of separation is at the leading edge, it has been shown that some trailing edge separation is also present. It is therefore necessary to consider both modes.

2.4.1 Leading Edge Separation

As previously mentioned, leading edge separation is abrupt. It is therefore necessary to define a criterion to signal leading edge separation. During this event there are two possible scenarios. At lower Mach numbers it is sufficient to specify a critical pressure and pressure gradient to identify the onset of leading edge stall. At higher Mach numbers the process of separation is more complex, a region of supersonic flow develops over the airfoil which is terminated by a shock wave. As the angle of incidence is increased this shock wave strengthens and moves towards the trailing edge. At some point the pressure gradient right after the shock wave becomes positive and causes separation that reattaches further downstream forming a bubble. As the severity of separation increases there is a point at which the motion of the shock reverses and heads back towards the leading edge. There are only minor deviations in the manner in which the lift and moment change with respect to angle of attack until the point when the shock wave reverses its motion. In the case of higher Mach numbers it is therefore necessary to determine a criterion for shock reversal. Fortunately, in the steady case a simple criterion may be used for both leading edge and shock induced separation. A critical normal force coefficient C_{nl} may be defined as a criterion for the above-mentioned events, this is possible because the pressure distribution directly correlates to the normal force on the airfoil. The separation boundary for a NACA 0012 airfoil can be seen in Figure 2.7.

Now that a criterion has been established it must be expanded to include the unsteady nature of the problem. Fortunately there is an easy way to do this. At low Mach numbers it can be shown from a harmonic response that there is a phase lag between the unsteady value of the leading edge pressure and the steady value. This phase lag is linear with respect to frequency. For the indicial response this behaviour may be represented by adding a first-order time lag to the normal force coefficient. This means that for the unsteady case, although the normal force coefficient has surpassed the critical value the accompanying pressure at the leading edge has not. There is a time lag between the pressure and normal force response. Introducing a modified normal force coefficient, which represents the equivalent steady pressure response, represents this. It is defined as follows:

$$\frac{C_n'(p)}{C_n(p)} = \frac{1}{1+T_p p} \Rightarrow C_n'(n) = C_n(n) - DP(n) \tag{2-54}$$

where $DP(n) = DP(n-1)\exp(-\Delta s / T_p) + (C_n(n) - C_n(n-1))\exp(-\Delta s / 2T_p)$ is the pressure deficiency function, and T_p is the pressure response time constant.

Although for higher Mach numbers the lag is no longer linear it may still be represented by a first order term. Therefore, when the modified unsteady normal force coefficient surpasses the critical (steady) value, leading edge separation or shock induced separation occurs. This point defines the transition between the linear attached flow behaviour and the non-linear separated flow behaviour. It also initiates the process of **dynamic stall** (Beddoes, 1982).

2.4.2 Trailing Edge Separation

Although the primary source of separation is either at the leading edge or at the shock wave, trailing edge separation is also present. To determine the non-linear effects of separation the theory of Kirchhoff is used (Thwaits, 1961). According to Kirchhoff the static normal force coefficient is given by

$$C_n = 2\pi \left(\frac{1+\sqrt{f}}{2}\right)^2 \alpha \tag{2-55}$$

where f is the separation point x/c (see Figure 2.8).

An empirical relation is used for the variation of f as a function of α

$$\begin{aligned} f &= \{1 - 0.3\exp((\alpha - \alpha_1)/S_1)\} \quad \text{if}\ \alpha \le \alpha_1 \\ f &= \{0.04 - 0.66\exp((\alpha - \alpha_1)/S_2)\} \quad \text{if}\ \alpha > \alpha_1 \end{aligned} \tag{2-56}$$

where α_1 is the static stall angle.

A value of f=0.7 has been established by Leishman and Beddoes (1986) as the critical point dividing light dynamic stall and deep dynamic stall, therefore the first relation describes separation in the light dynamic stall regime (f<0.7), while the second relation describes the deep stall regime (f>0.7). The effects of leading edge separation are small in the light stall region, and therefore, trailing edge separation dominates and the travel of f is gradual towards the leading edge. In deep stall, however, leading edge separation plays a role in accelerating the travel of the separation point towards the leading edge, and the travel is more abrupt. Trailing edge separation is, of course, also caused by an adverse pressure gradient sufficient to cause flow reversal within the boundary layer. In the unsteady case it is therefore affected by the pressure lag, described by equation (2-54). A modification therefore needs to be made to equation (2-55) to account for this. Other effects which are discussed by Ericsson and Reding (1988), cause a further lag in the boundary layer response. These effects are very complicated, yet they may be incorporated in the same manner as the pressure lag. Using the modified normal force coefficient for the pressure response, equation (2-54), an effective angle of attack can be used for the analogous static case. This angle is defined as

$$\alpha_f(n) = \frac{C'_n(n)}{C_{l\alpha}(M)} \qquad \text{(2-57)}$$

where $C_{l\alpha}(M)$ is the compressible lift curve slope. Using this angle of attack and substituting it into equation (2-51) the modified separation point is obtained to account for the leading edge pressure lag and is denoted by f'. The next step is to add a lag term to the boundary layer response, this is done analogously to the pressure response. The unsteady separation point is found thus:

$$f'' = f' - DF(n) \qquad \text{(2-58)}$$

where $DF(n) = DF(n-1)\exp(-\Delta s / T_f) + (f'(n) - f'(n-1))\exp(-\Delta s / 2T_f)$.

Now that the separation point has been found, it is used to modify the linear solution to account for trailing edge separation non-linearities. As mentioned before, trailing edge separation only affects the circulatory term, therefore the new circulatory normal force is

$$C^f_{nc}(n) = ((1 + \sqrt{f''(n)})/2)^2\, C_{nc}(n) \qquad \text{(2-59)}$$

In the linear response there is no circulatory contribution in the moment term. This is because the center of pressure of the circulatory normal force is at the quarter chord. For the non-linear case, however, there exists a modified non-linear center of pressure, which is found empirically and is:

$$COP(n) = k_o + k_1(1 - f'') + k_2 \sin(\pi (f''(n))^2) \qquad \text{(2-60)}$$

where COP(n) is the non-dimensional distance of the center of pressure away from the quarter chord. This term accounts for the non-linear effects on the center of pressure of the circulatory normal force. Each constant serves in the curve fitting to better match the unsteady response. The constant k_o is a mean offset of the center of pressure from the static value, the k_1 term is the main contributor to the non-linear offset and shows that the offset increases linearly with increasing separation, finally the k_2 term causes the moment curve to have the correct curvature when it goes into stall (f=0.7). Therefore, the new non-linear contribution to the moment term is

$$C_{mc}^{f}(n) = COP(n) \cdot C_{nc}^{f}(n) \tag{2-61}$$

2.4.3 Vortex Flow and Dynamic Stall

The onset of leading edge separation starts the process of dynamic stall. The first non-linear effect is seen with the progressive trailing edge separation, which acts simultaneously with leading edge separation. Another non-linear effect that accompanies the dynamic stall process is the creation of a leading edge vortex, which subsequently is convected toward the trailing edge. The vortex is created from the discontinuous change in circulation of the airfoil when the abrupt leading edge stall occurs. The loss of circulation, due to leading edge stall, is counteracted by the creation of this vortex, this means that the linear region is extended. It is the rate of change of circulation, which is important in the creation of this vortex. This means that vorticity is continually shed from the trailing edge separation point throughout the airfoil's travel, yet because this change is gradual these vortices have little effect. Along the same lines the lower the unsteadiness, the lower the rate of change of circulation near the leading edge, and the weaker the vortex is, which means that for the static case this effect is absent.

The dominant vortex created near the leading edge is called the dynamic stall vortex. This vortex has many effects on the aerodynamic behaviour of the airfoil. Modeling this phenomenon must be consistent with physical reality, and the following points must be incorporated in the model: 1) the shedding process commences when leading edge stall occurs, and the vortex convects downstream at an almost constant speed irregardless of airfoil motion; 2) the strength of the vortex must revert to zero when the motion reverts to steady motion; 3) if stall continues for a sufficiently long time, secondary vortices are created and shed. Staying consistent with the model being used, the increment of buildup of circulatory lift due to the vortex may be related to the loss of circulation due to trailing edge separation. This means that the separation is nullified in the presence of this vortex, thus, extending the linear region. This increment is defined as

$$CV\ (n) = C_{nc}(n) - C_{nc}^{f}(n) = \{1 - [(1 + \sqrt{f''(n)})^2 / 4]\}\, C_{nc}(n) \qquad (2\text{-}62)$$

At the same time that the circulatory increments help to build up the vortex, they also decay. This means that for small pitch-rates the vortex lift decays faster than it builds up, thus reverting to the steady case and making trailing edge separation the dominant mode of separation. These two facts are consistent with physical reality. Therefore the total vortex lift is

$$CNV(n) = CNV(n-1)\exp(-\Delta s / T_v) + (CV(n) - CV(n-1))\exp(-\Delta s / 2T_v) \qquad (2\text{-}63)$$

When leading edge separation commences the vortex is shed downstream. The vortex lift continues to build-up according to equation (2-58). The center of pressure of the vortex lift starts to deviate from the quarter chord position, causing an abrupt and large nose down pitching moment. The center of pressure and associated moment are

$$CPV(n) = 0.2(1-\cos(\pi\tau_v / Tvl))$$
$$C_m^V(n) = CPV(n)\cdot CNV(n) \tag{2-64}$$

The largest deviation in the center of pressure of the vortex lift is when the vortex reaches the trailing edge. When the vortex detaches from the leading edge a vortex time variable τ_v is initialized as zero, when the vortex reaches the trailing edge $\tau_v = T_{vl}$. At this point the build up of vortex lift is terminated and the center of pressure reverts back to the quarter chord position.

Vortex lift is the main culprit in the delay of reattachment on the airfoil, in conjunction with the time lags due to unsteadiness. The reason for the added hysterisis due to vortex travel is its relative independence of airfoil motion. This means that although the airfoil has passed the angle for reattachment the vortex still affects the airloads. Leishman and Beddoes use the critical normal force coefficient C_{nl} to terminate the effects of the vortex and to start the reattachment. To summarize, only when $C_n > C_{nl}$, does the vortex travel have an effect.

As for secondary vortices the following time constant is used to replace T_{vl} when the first vortex has traveled past the airfoil

$$Ts=(1-f'')/0.2 \tag{2-65}$$

In other words, the secondary vortices are shed after the previous vortex is shed into the wake for a time period of Ts (Leishman and Beddoes, 1986).

2.5 Modifications to the Model

2.5.1 Addition of Plunge Degree of Freedom

Thus far plunge has been used interchangeably with angle of attack. Its effects have been accounted for simply by adding an equivalent angle of attack of $\dot{h}/U_\infty$. As far as linear analysis is concerned this method of accounting for plunge is correct. The question now is how to account for the non-linear effects of plunge. The entire formulation of the aerodynamic model has been based on the work of Leishman and Beddoes (1986), it would be beyond the scope of this thesis to formulate a new empirical model to account for plunge. This is especially true without more information on the experiments used by the Leishman and Beddoes from which their work is based. Fortunately Leishman and Tyler (1992) explored this very same avenue. Their conclusions are as follows; 1) **There are no major physical differences between a pitching or plunging airfoil, either in attached flow or dynamic stall;** 2) The unsteady airfoil behaviour in attached flow can be well predicted using linear theory. The main differences that exist in the unsteady airloads are a result of a pitch-rate "induced camber" effect, which contributes significantly to the unsteady lift , pitching moment and aerodynamic damping during pitching motion. This contribution is absent during plunge forcing. 3) The effects of unsteadiness contribute to determining the leading edge pressure distribution on the airfoil, and the effects of this must properly be accounted for in the modeling. These "inviscid" effects have been found to be the primary influence in determining the onset point of stall. 4) For "equivalent forcing" conditions any differences in the unsteady airloads between pitching and plunging motions arise because the critical conditions for leading edge separation are met at different equivalent angles of attack. Generally, for equivalent forcing, airfoils undergoing pitch oscillations will exhibit stall onset before airfoils undergoing plunge forcing. 5) The duration of vortex shedding during dynamic stall was found to take place at approximately the same rate during either pitch or plunge motion. This has been modeled using a common non-dimensional time constant. 6) Airfoils undergoing plunge into dynamic stall generally exhibited a loss of aerodynamic damping at a lower mean angle of attack than for the equivalent pitching case (Leishman and Tyler, 1992). Thus, although a pitching airfoil will stall at a lower "equivalent" angle of attack, the increased damping due to pitch-rate means that conditions for stall flutter will be met at higher mean angles of attack.

Leishman refers to the same empirical model as the one used in this thesis. The only difference suggested was a change in the pressure lag time constant T_p to account for the differences in angle of attack (including plunge) and pitch-rate. Unfortunately new experimentation was used to calculate these constants and to change them would mean that some accuracy would be lost in the purely pitch motion. It was therefore decided not to change the constants, especially when one realizes that underestimating the time constants is as dangerous as overestimating them. Fortunately there were no changes to the main structure of the program, meaning that to increase the accuracy one need only determine new time constants from new experiments. It was therefore concluded that the model previously described, has already sufficiently accounted for plunge by separating its effects with its lack of a pitch-rate term.

2.5.2 Modification of Time Constants

According to Leishman and Beddoes (1986), there are two reasons why the time constants needed to be modified. The first reason is the physical coupling between the elements of the model, and the second involved an underestimation in the hysterisis of the reattachment process.

The separation of the various sub-systems completely ignores the physical coupling of these elements. The way Leishman and Beddoes corrected for this was to modify two of the time constants. These were the trailing edge separation time constant T_f, and the vortex shedding time constant T_v. The following modifications were made: 1) the rate of movement toward the leading edge of the trailing edge separation point is accelerated during vortex presence, under this scenario T_f is halved; 2) if the direction of pitching motion changes during vortex travel the separation point moves more quickly towards the leading edge and the vortex diffuses faster, under this scenario both T_f and T_v are halved; 3) when the vortex reaches the trailing edge it diffuses into the wake faster than it does on the airfoil, T_v is halved.

Another phenomenon which is not sufficiently well modeled is the hysteresis in the reattachment process. The hysteresis loops were found to be too small when compared against experiments. The addition of an empirically derived dynamic offset angle added to the trailing edge separation point sub-system, as modeled by equations (2-56), during the reattachment process was sufficient and modeled the reattachment process nicely. This offset was added as an additional angle of attack:

$$\delta\alpha_1 = (f''(n-1))^{0.25}\Delta\alpha_1 \textit{ (where } \Delta\alpha_1 \textit{ is Mach number dependant)} \qquad (2\text{-}66)$$

2.5.3 Errors Discovered in Referenced Papers

Errors were discovered in the paper used to derive this model (Leishman and Beddoes, 1986). The first error was that the circulatory term in the moment expression due to pitch-rate was ignored, nonetheless the impulsive loading used was comprised of two exponential functions and accurately portrays the behaviour for the reduced frequency range of interest, (this fault is discussed in Leishman (1988)). The other errors that were found were in the table of constants (Leishman and Beddoes, 1986); it seems that the constants S_1 and S_2 should be reversed with respect to the constants used to define the separation point. Justification for this was found in two ways, first, in an earlier paper by Beddoes (1982) a similar table of constants is presented, which more closely resembles the reverse situation. Also the output from the program, especially the output to a ramp input, suggests the constants to be reversed. Another constant which seems to be in error is the k2 constant at Mach 0.7. This was discovered because it seems anomalous, compared to the trend among the other Mach numbers, and also the output supports a different value. It was changed from 0.15 to 0.05, which is supported by the output, the trend among the Mach numbers, and also suggests a simple typographical error. The following flow-chart represents a summary of the numerical algorithm with all of the corrections, accompanied by Table 2.1 which provides the numerical values for all the constants used in the dynamic stall model.

2.6 Flow-Chart Summarizing the Dynamic Stall Process

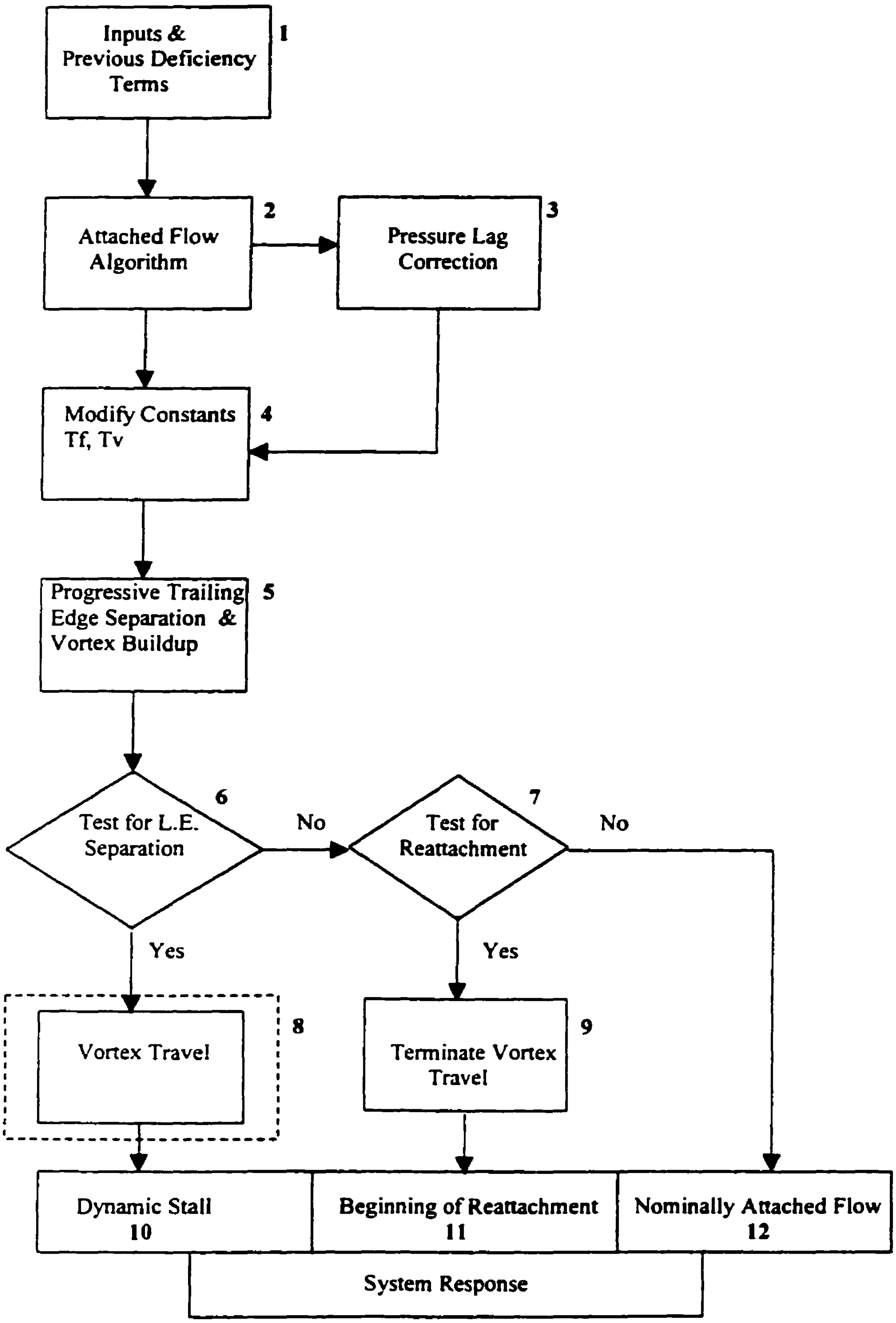

Vortex Travel Sub-System (#8) from Previous Page in More Detail

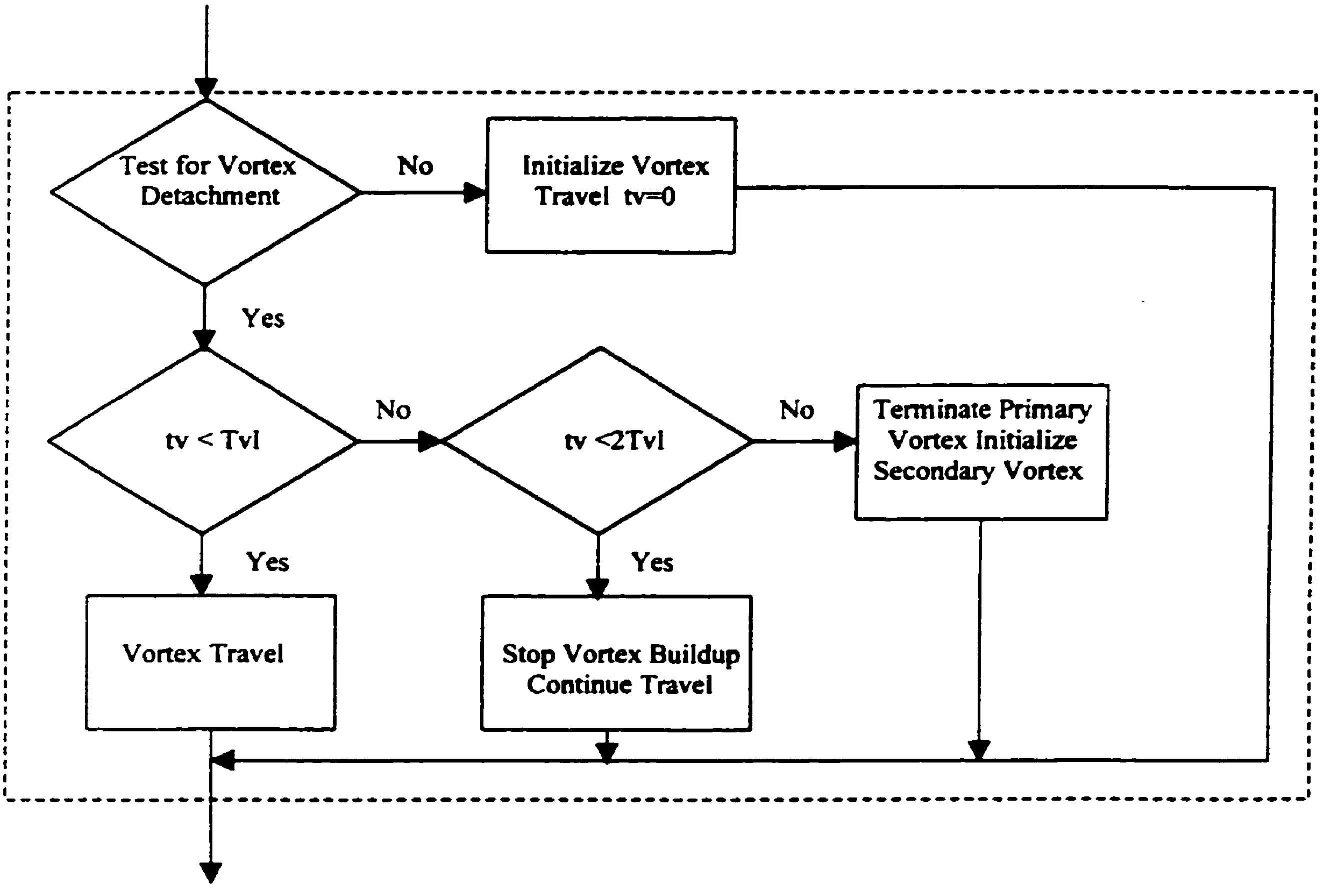

1: Inputs: $\alpha(n), \dot{\alpha}(n), \dot{h}(n)$, Deficiencies(n - 1)

2: Attached Flow Algorithm: equation (2-53)

3: Pressure Lag Correction: equation (2-54)

4: Modification of Time Constants: (See Section 2.5.2)

5: Progressive Trailing Edge Separation: (2-59,2-61), Vortex Buildup: (2-63)

6: Test for Leading Edge Separation: $C_n^{'}(n) > C_{nl}$ (2-54)

7: Test for Reattachment: $\dot{\alpha} < 0, C_n^{'}(n) < C_{nl}$ (2-54)

8: Vortex Travel: (2-63, 2-64)

9: Terminate Vortex Travel: (2-64)=0

10: Dynamic Stall: $C_n = C_{nc}^f + C_{n\alpha}^I + C_{nq}^I + C_n^V, C_m = C_{mc}^f(n) + C_{m\alpha}^I + C_{mq}^I + C_m^V$

11: Beginning of Reattachment: $C_n^V = C_m^V = 0$

12: Nominally Attached Flow: $C_n \approx C_{nc} + C_{n\alpha}^I + C_{nq}^I, C_m \approx C_{m\alpha}^I + C_{mq}^I$ (Trailing edge separation is small in this region, it is still incorporated in the algorithm hence the approximately equal signs)

Table of Mach Number Dependant Constants

Mach #	0.3	0.4	0.5	0.6	0.7	0.8
Cla	0.108	0.113	0.117	0.127	0.154	0.215
α_I	15.25	12.5	10.5	8.5	5.6	0.7
$\Delta\alpha_I$	2.1	2	1.45	1	0.8	0.1
S1	3	3.25	3.5	4	4.5	0.7
S2	2.3	1.6	1.2	0.7	0.5	0.18
K0	0.0025	0.006	0.02	0.038	0.03	-0.01
K1	-0.135	-0.135	-0.125	-0.12	-0.09	0.02
K2	0.04	0.05	0.04	0.04	0.05	-0.01
Cnl	1.45	1.2	1.05	0.68	0.68	0.18
Tp	1.7	1.8	2	3	3	4.3
Tf	3	2.5	2.2	2	2	2
Tv	6	6	6	6	6	4
Tvl	7	9	9	9	9	9

Table 2.1

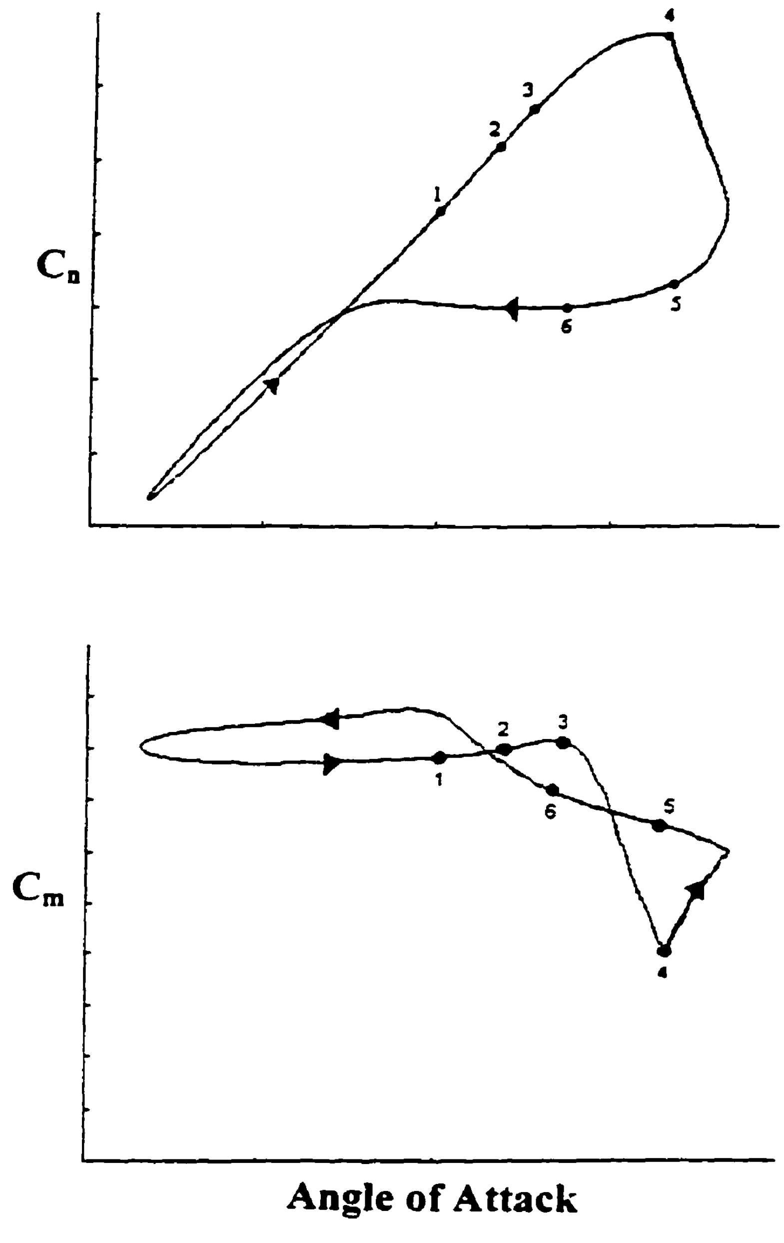

1) The static stall angle is exceeded.

2) Flow reversals in the boundary layer causes the formation of a vortex at the leading edge.

3) Vortex detaches from the leading edge and convects downstream, moment stall occurs.

4) Vortex reaches trailing edge, lift stall and maximum negative moment occur.

5) Flow becomes fully separated.

6) Boundary layer reattaches from front to rear.

Figure 2.1: Schematic Showing the Main Events of Dynamic Stall. Reproduced from Leishman and Beddoes (1989).

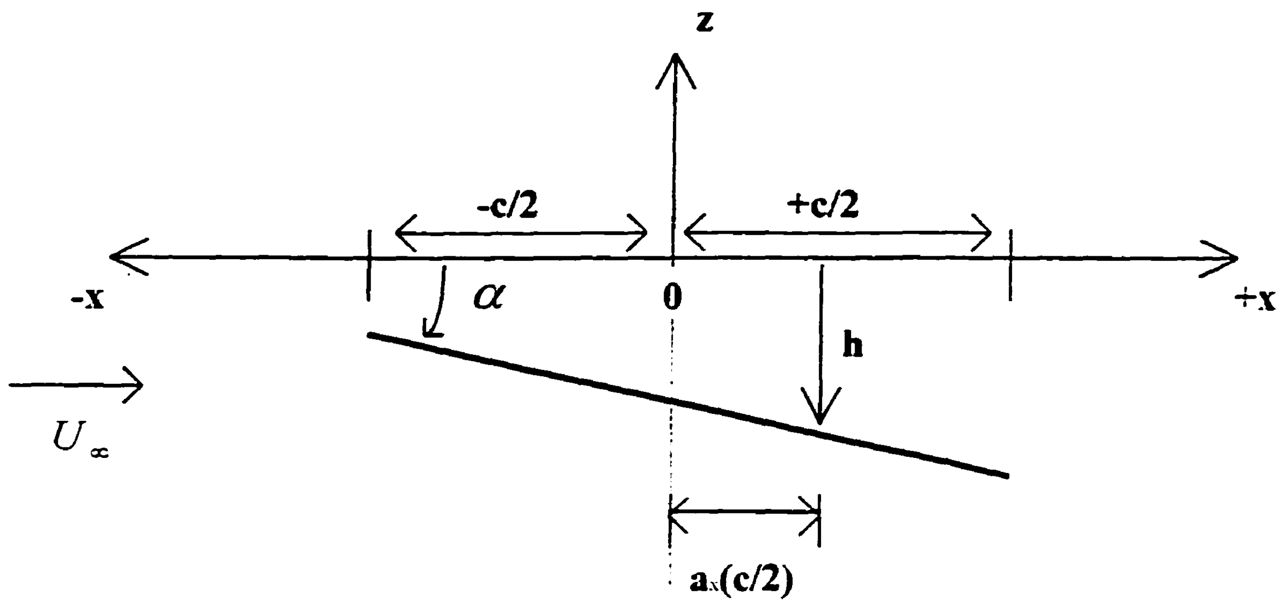

Equation of Airfoil

$$Z_a(x,t) = -h(t) - \alpha(t)[x - a(\frac{c}{2})] \text{ for} -c/2 \le x \le c/2$$

Figure 2.2: Schematic Showing Location of Airfoil Surface.

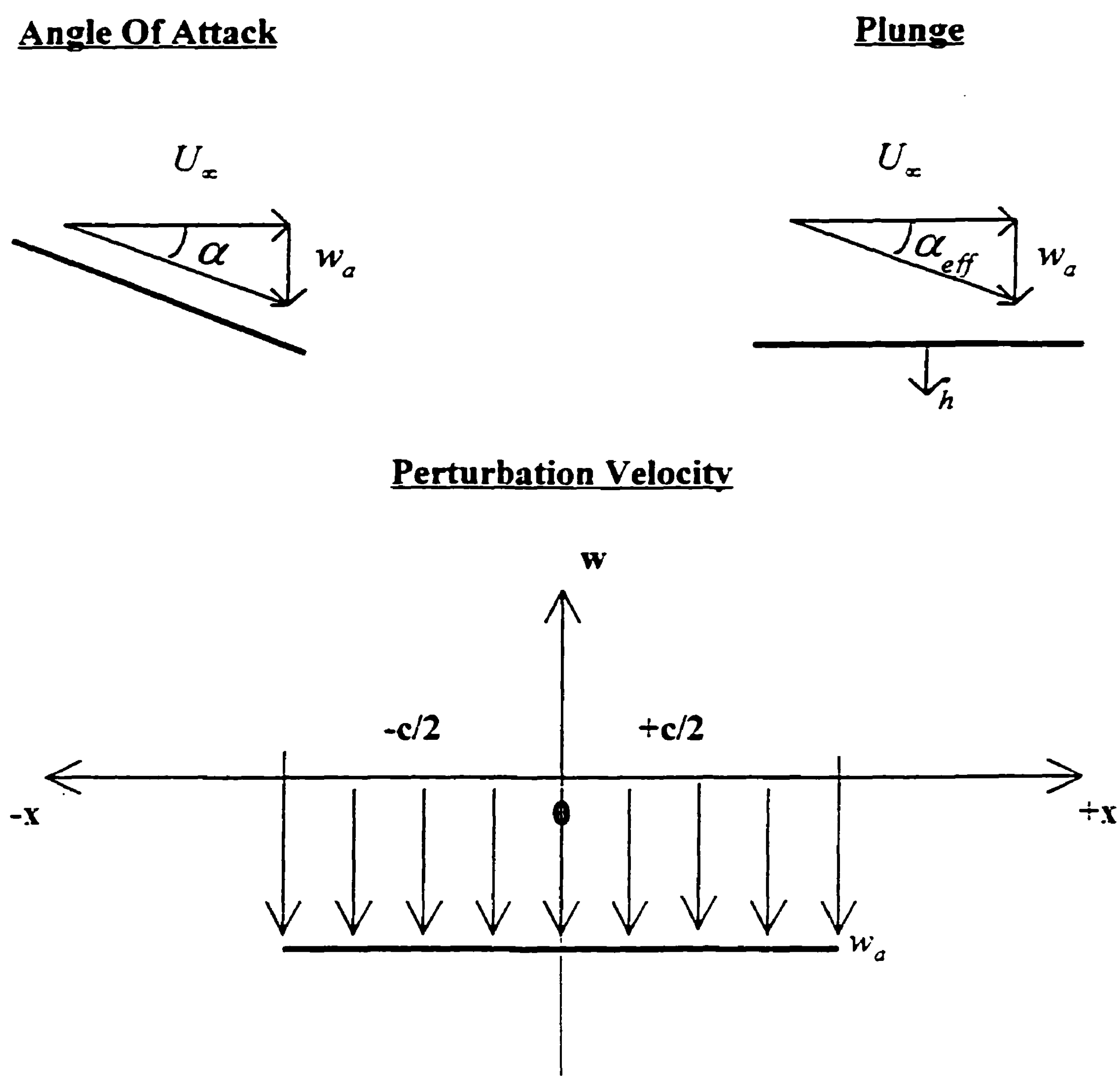

$$\text{Pitch:}\, w_a = -U_\infty \alpha \;\;\text{or}\;\; \text{Plunge:}\, w_a = -\dot{h}$$

Figure 2.3: Schematic Showing Equivalence Between Pitch and Plunge-Rate.

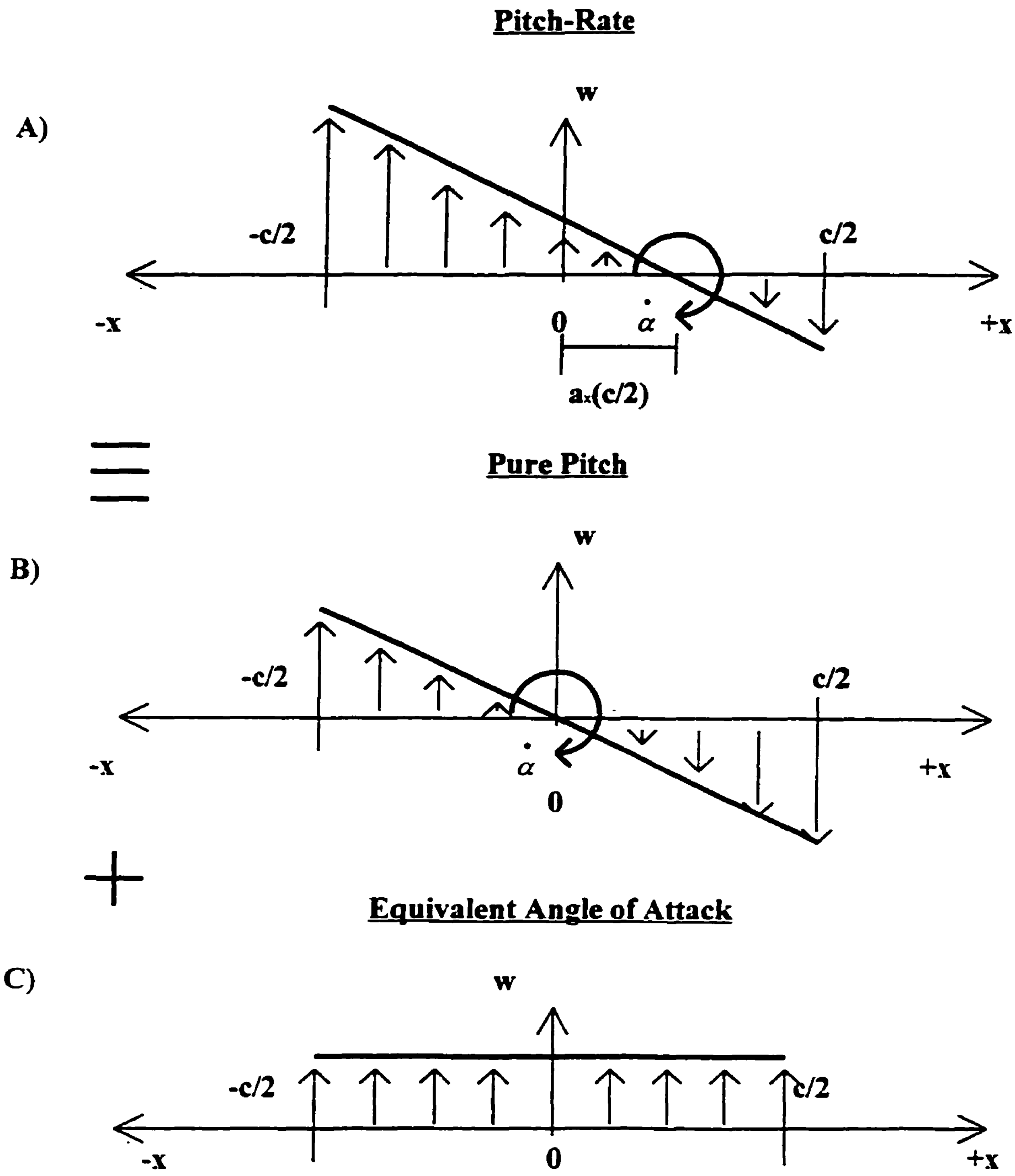

Figure 2.4 : Schematic Showing Equivalence Between Pitch-Rate and Pitch Plus Equivalent Angle of Attack. a) $w_a = -\dot{\alpha}[x - a(\frac{c}{2})]$**, b)** $w_a = -\dot{\alpha}\, x$**, c)** $w_a = a(\frac{c}{2})$**.**

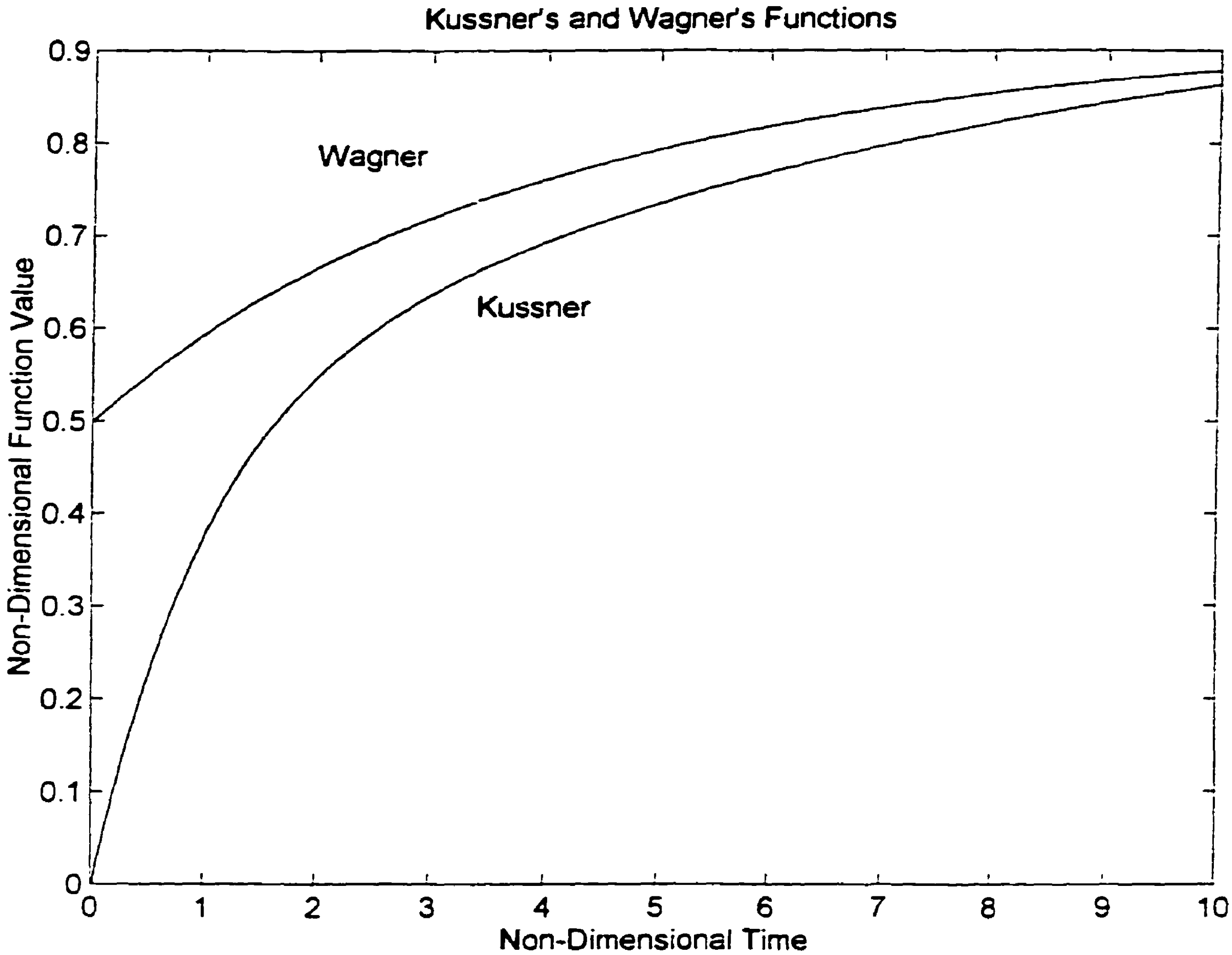

Figure 2.5: Kussner's and Wagner's Functions.

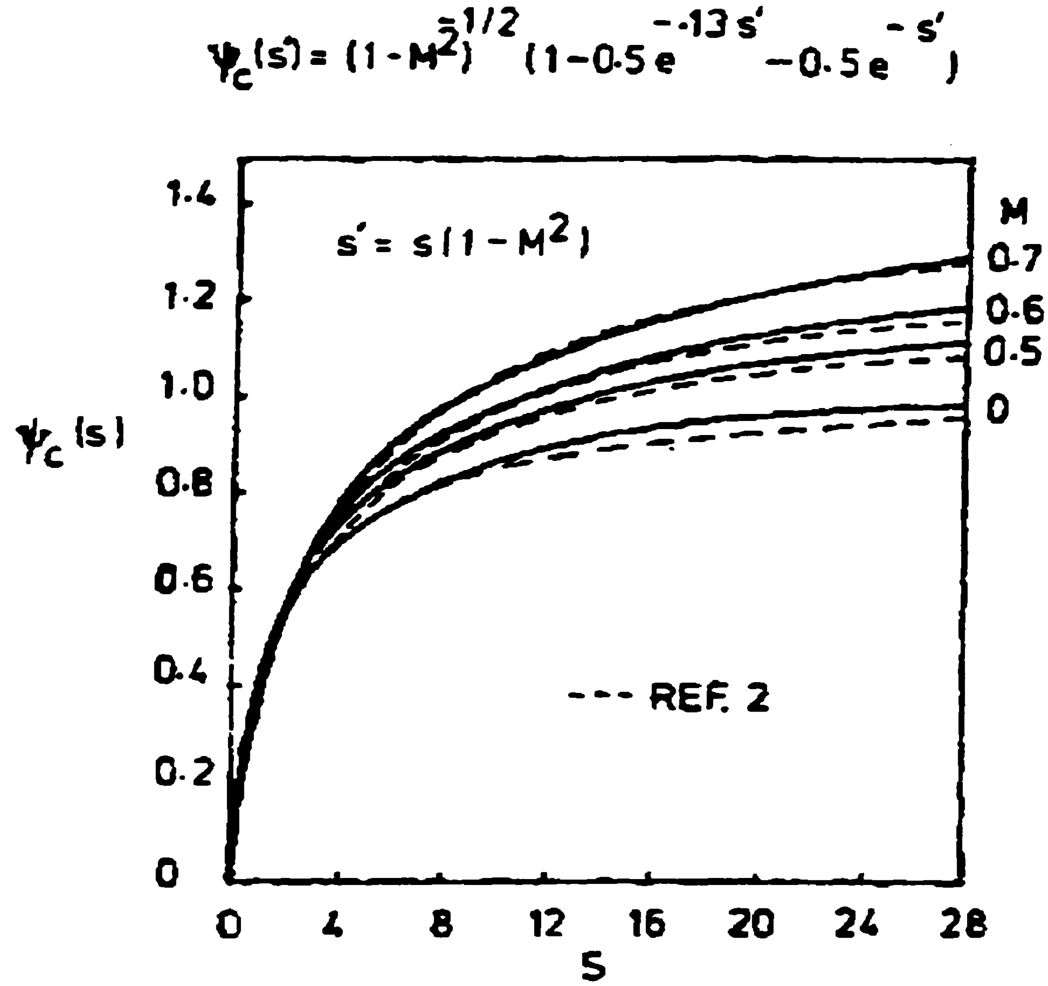

Figure 2.6: Comparison Between Kussner's Function and Beddoes' Semi-Empirical Approximation (Dotted Line) for Various Mach Numbers. Reproduced from Beddoes (1980).

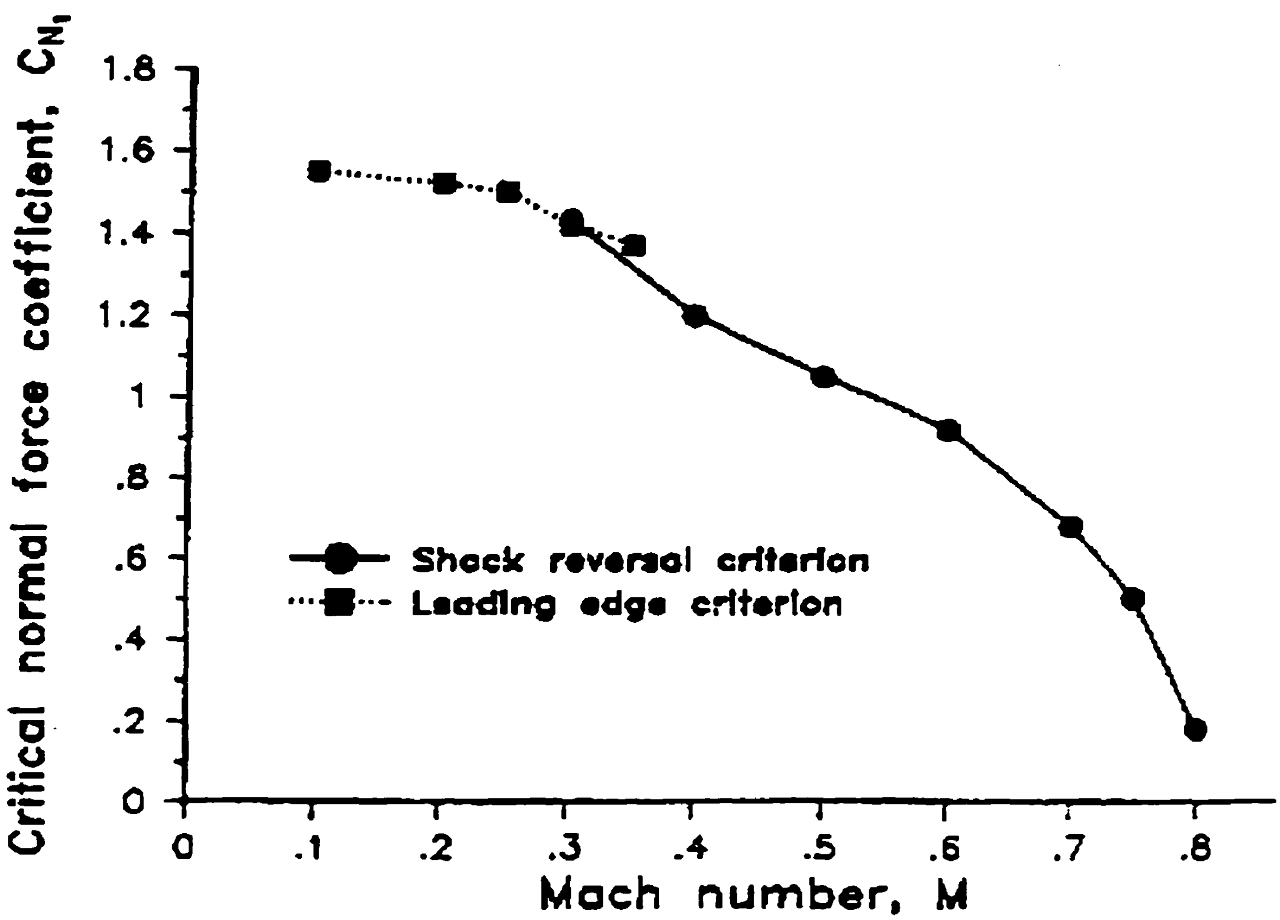

Figure 2.7: Critical Normal Force Separation Onset Boundary. Reproduced from Leishman and Beddoes (1989).

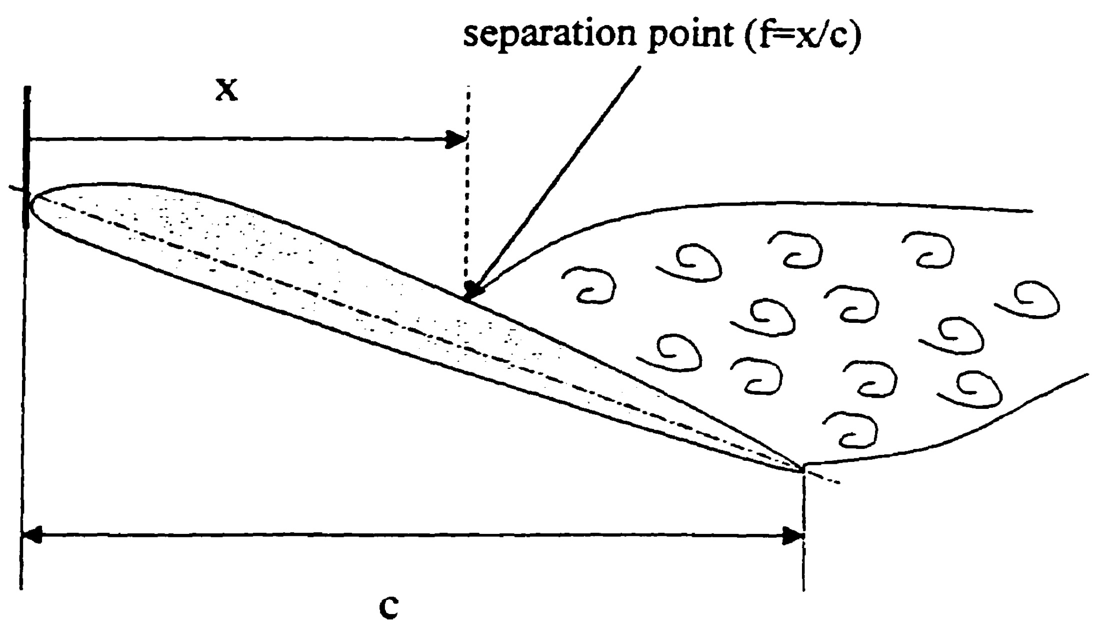

Figure 2.8: Trailing Edge Separation Point.

Chapter 3

Justification of the Aerodynamic Model

3.1 Introduction

To justify the aerodynamic model two approaches will be used. The first approach involves comparing the model to the physical situation, and the second approach involves comparing the output of the program with data from Leishman and Beddoes (1986). The first approach verifies the qualitative trends, while the second approach verifies the model against quantitative data acquired by Leishman and Beddoes (1986).

3.2 Comparison with Physical Reality

The physics associated with dynamic stall was explored in the previous chapter. In its essence it involves the dynamic overshoot in lift and angle of attack of the stalling process. There are two categories of overshoot. The first involves a shift in the time domain, which translates to a shift in the pitch angle at which stall occurs. This shift can be modeled using quasi-steady aerodynamics. The second category is transient in nature and involves the non-linear modeling. This category is responsible for the overshoot in lift.

Time-Lags

The first time lag is the circulatory lag and is introduced by the unsteady nature of the movement of the airfoil. As the airfoil oscillates, the circulation around the airfoil changes. If Kelvin's circulation theory is to hold, counter vortices must be shed into the wake so that the total circulation is equal to zero. Each counter vortex has a negative effect on the airfoil normal force and moment quantities. Their influence diminishes as they travel further and further into the wake. If the airfoil stops its unsteady motion, and reverts to a steady configuration, these counter-vortices, after a period of time, will have no effect. In Figure 3.1(a) we see the circulatory contribution, due to pitch, to the normal force coefficient, which is obtained from the term described by equation (2-25) and described numerically by equation (2-47). This is the response to a harmonic oscillation of the airfoil about the quarter chord described by the following equation: $\alpha_{1/4c} = 10^{o}\sin(ks)$ (the quarter chord is chosen in accordance with Leishman and Beddoes (1986)). As the frequency is increased, two effects are apparent, the amplitude of the normal force response is decreased and there is a shift to the right as compared to the steady pitch case. As the frequency increases to a very large value, the circulatory normal force becomes very small; this is consistent with aerodynamic theory, which indicates that the large quantity of shed counter-vortices will have a negative effect on the airfoil lift. As the frequency goes to a very small value, the circulatory normal force matches the steady pitch case, which makes sense because steady implies zero frequency. Therefore, the behaviour in Figure 3.1 is in accordance to aerodynamic theory.

To get the total circulatory normal force coefficient, the circulatory contribution due to pitch-rate must be included. If the axis were at the 3/4 chord, the pitch-rate contribution would be zero as discussed in Chapter 2. Figure 3.1(b) shows the circulatory contribution to the normal force coefficient caused by the pitch-rate. This term is derived from adding the equivalent angle of attack due to pitch-rate, as per equation (2-27). For oscillations about the quarter chord this pitch-rate equivalent angle is q/2. This figure demonstrates that the pitch-rate contribution exhibits a time lead with respect to the steady pitch case, which has no pitch-rate contribution. Is this to say that the larger the pitch-rate the greater the time lead on the total circulatory normal force coefficient? The answer is no, in fact the opposite is true. Although the pitch and pitch-rate contributions to the circulatory normal force coefficient are treated separately in the analysis, they are linked. A larger pitch-rate is the consequence of a larger unsteadiness (higher value of k) in the pitch oscillation, which implies a larger lag with respect to the steady case in the pitch contribution. The pitch-rate contribution comes exclusively from the choice of axis. If the pitch axis were taken at the 3/4 chord, the pitch-rate contribution would not exist, in fact if the axis were moved further to the rear the pitch-rate contribution would even serve to increase the total circulatory time lag. Therefore the pitch-rate term simply implies that the net circulatory time lag varies depending on the choice of axis. Three conclusions may be drawn from the circulatory subsystem. The first is that the higher the frequency of oscillation the larger the time lag is in the normal force response with respect to the steady pitch case and therefore the greater the delay in time until stall. The second is that increasing the frequency diminishes the effect of circulation on the normal force and the third is that moving the axis of oscillation towards the rear will increase the total circulatory time lag in the normal force response. Carr (1987) discusses all of these facts in greater detail.

A second category of time lags exists in the model. Not only does the unsteady lift response lag behind the steady case, so do the pressure and boundary layer responses relative to the unsteady normal force response. These time lags do not shift the normal force coefficient curve; they do however extend the linear region of normal force response and delay the transient effects, which depend on the pressure distribution and boundary layer response. This delay increases with increasing frequency. This lag combines many physical effects into one usable time lag; these effects include: boundary layer effects, accelerated flow effects, the moving wall effect etc. (Ericsson and Reding, 1988). It is for these reasons that time constant modifications were required in the aerodynamic model depending on the specific situation. The physical justification for the choice of constants was given in Chapter 2.

Another time lag comes from the compressibility of the flow. At a given Mach number it simply creates a general empirically derived time lag of $1\text{-}M^2$. This makes physical sense, as the speed of sound is finite, implying that disturbances at one location in the flow take time to affect the entire flow.

Another contributor to normal force coefficient is the impulsive loading. This loading is less significant than the circulatory loading in the frequency range of interest, yet it must be included. In Figure 3.2(a) we see the impulsive loading due to the pitch contribution, which is described by equation (2-50). As the frequency of oscillation is increased, the amplitude of the normal force coefficient response increases. Figure 3.2(b) presents the impulsive contribution due to pitch-rate (described by equation (2-51)). The pitch-rate term, once again, is due to the choice of axis. In this case, if the mid-chord is used this contribution would disappear. The effect of increasing the frequency for the pitch-rate contribution is to increase the amplitude. Therefore, the only conclusion for the impulsive loading is that as frequency increases the impulsive loading becomes greater. The converse is that as the frequency decreases the effect of the impulsive loading becomes less. This is also consistent with aerodynamic theory since for the steady case there is no impulsive loading.

Transient Effects

The transient effects include the vortex flow and the trailing edge separation point. Their formulation was discussed thoroughly in the previous chapter. These effects are complex and depend largely on the exact input, and are therefore better verified against experimental data through a large range of variables. The only trend that may be verified is that their effects become more pronounced as the frequency (unsteadiness) increases. This means that in any given situation as the frequency is increased the lift overshoot should also increase, and the hysteresis loops should also become larger. These effects are shown in Figure 3.3, which uses the following harmonic input: ($\alpha_{1/4c} = 10^{o} + 8^{o}\sin(ks)$). In the steady case there is no hysteresis and the normal force at stall is at its lowest level. As the frequency is increased the amount of hysteresis increases and the lift overshoot also increases, thus justifying the general trend.

In conclusion, the aerodynamic model displays trends in accordance to aerodynamic theory as the frequency of oscillation is changed. It is therefore qualitatively correct. Note that only the normal force curves were verified. The moment curves are directly related to the normal force curves and involve only the addition of empirically derived center of pressure formulae. They are therefore better verified against experimental data.

3.3 Comparison with Experimental Results

No experiments were undertaken to prove the validity of the model. The only experimental data available was the data presented by Leishman and Beddoes (1986), when comparing their own model. Therefore the best way to justify the model used in this thesis is to compare it to all of the plots generated by Leishman and Beddoes in their paper. Figures 3.4 to 3.8 presents a comparison between the model used in this thesis and the results obtained from the model used by Leishman and Beddoes, which is in turn compared to experimental data for a large range of inputs. The two sets of plots are almost identical, thus justifying the model. The only discrepancy that was found was corrected by the addition of a third harmonic, which was said to be present in the experimental apparatus used by Leishman and Beddoes. This third harmonic was incorporated in the model for all the results shown in Figures 3.4 to3.8 and was given an amplitude of 0.5 deg.

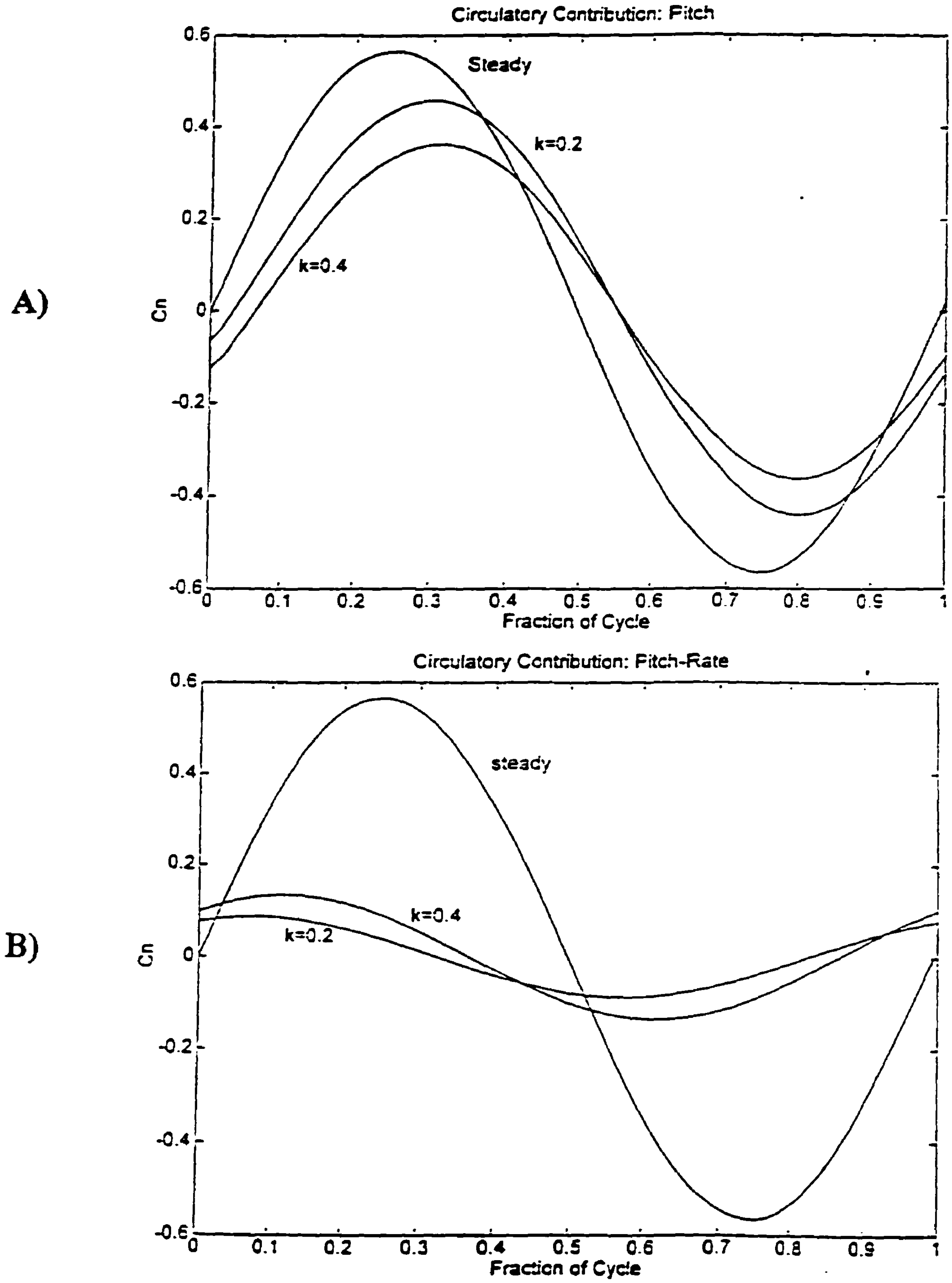

Figure 3.1: Circulatory Normal Force Response to a Harmonic Input; $\alpha_{1/4c} = 10^o \sin(ks)$, M=0.4: a) Pitch Contribution: k=0, k=0.2, k=0.4 b) Pitch-Rate Contribution: k=0.2,k=0.4.

A)

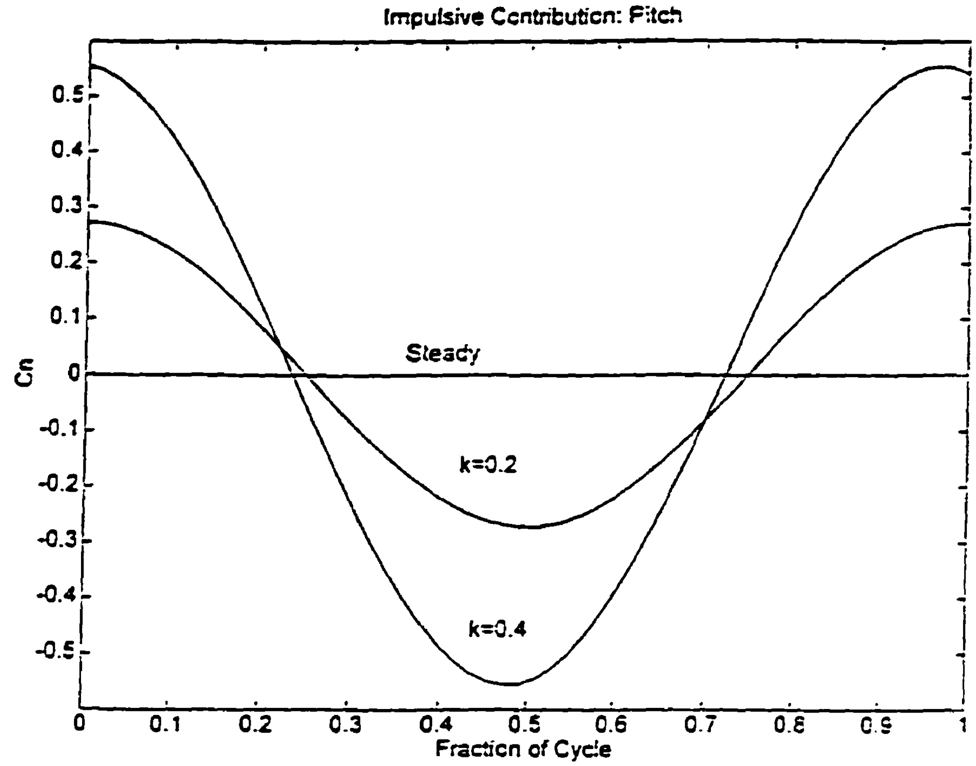

B)

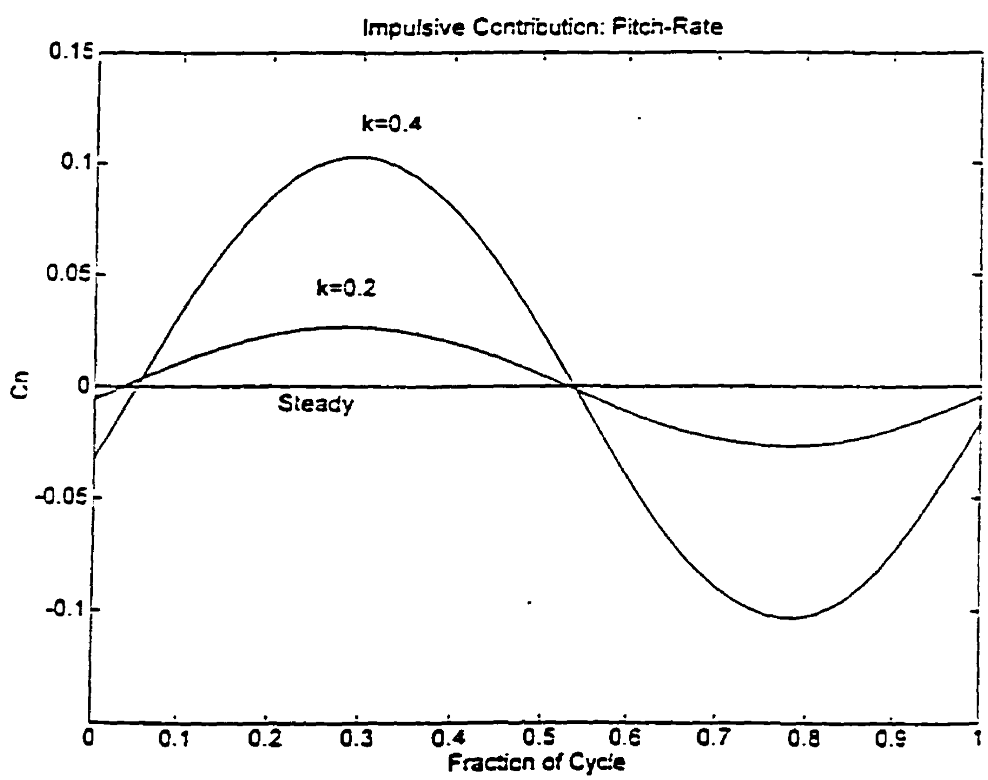

Figure 3.2: Impulsive Normal Force Response to a Harmonic Input; $\alpha_{1/4c} = 10^o \sin(ks)$, M=0.4: a) Pitch Contribution: k=0, k=0.2, k=0.4 b) Pitch-Rate Contribution: k=0.2,k=0.4.

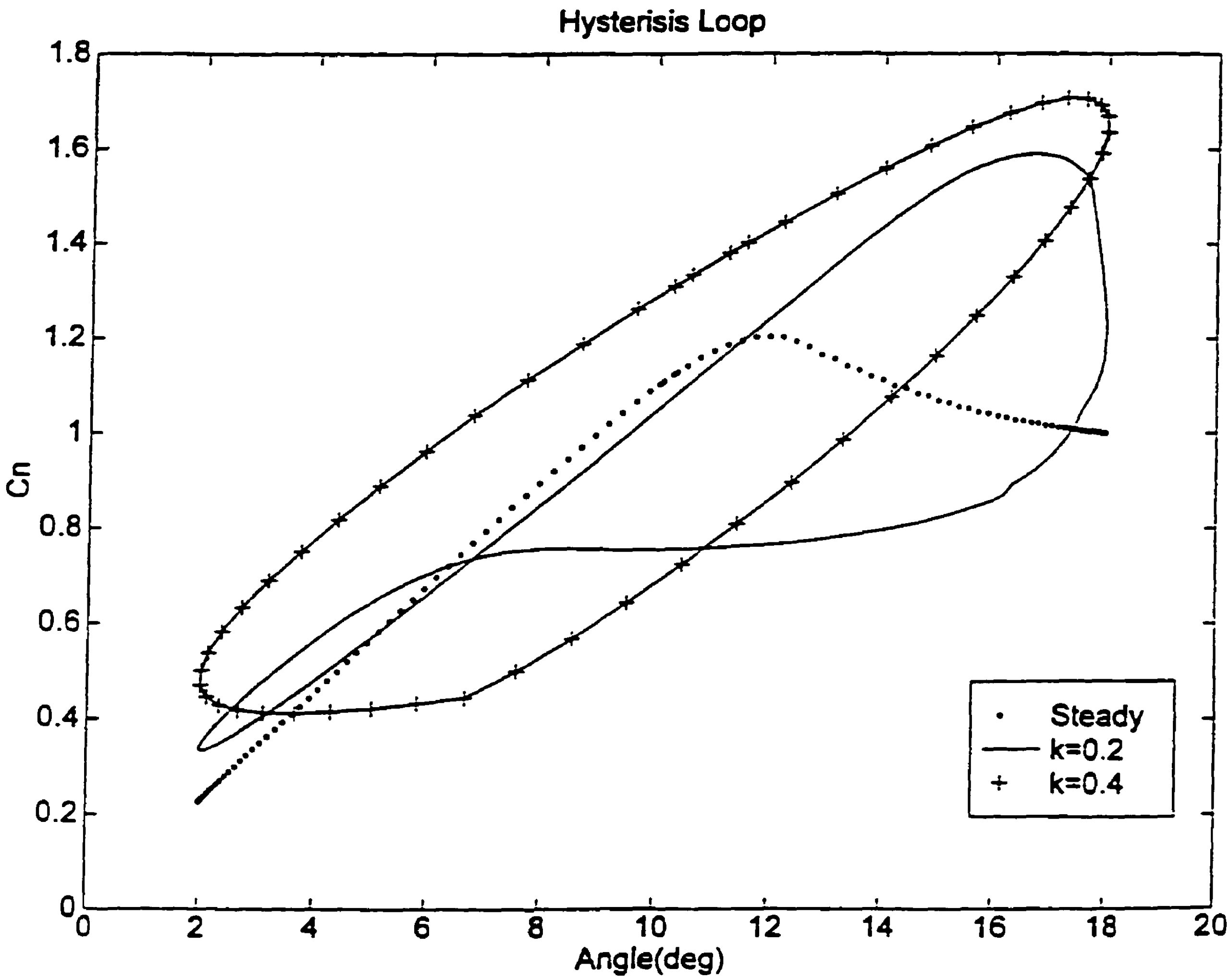

Figure 3.3: Normal Force Coefficient vs Angle of Attack (Hysterisis Loops); $\alpha_{1/4c} = 10^o + 8^o \sin(ks)$, M=0.4, k=0, k=0.2, k=0.4.

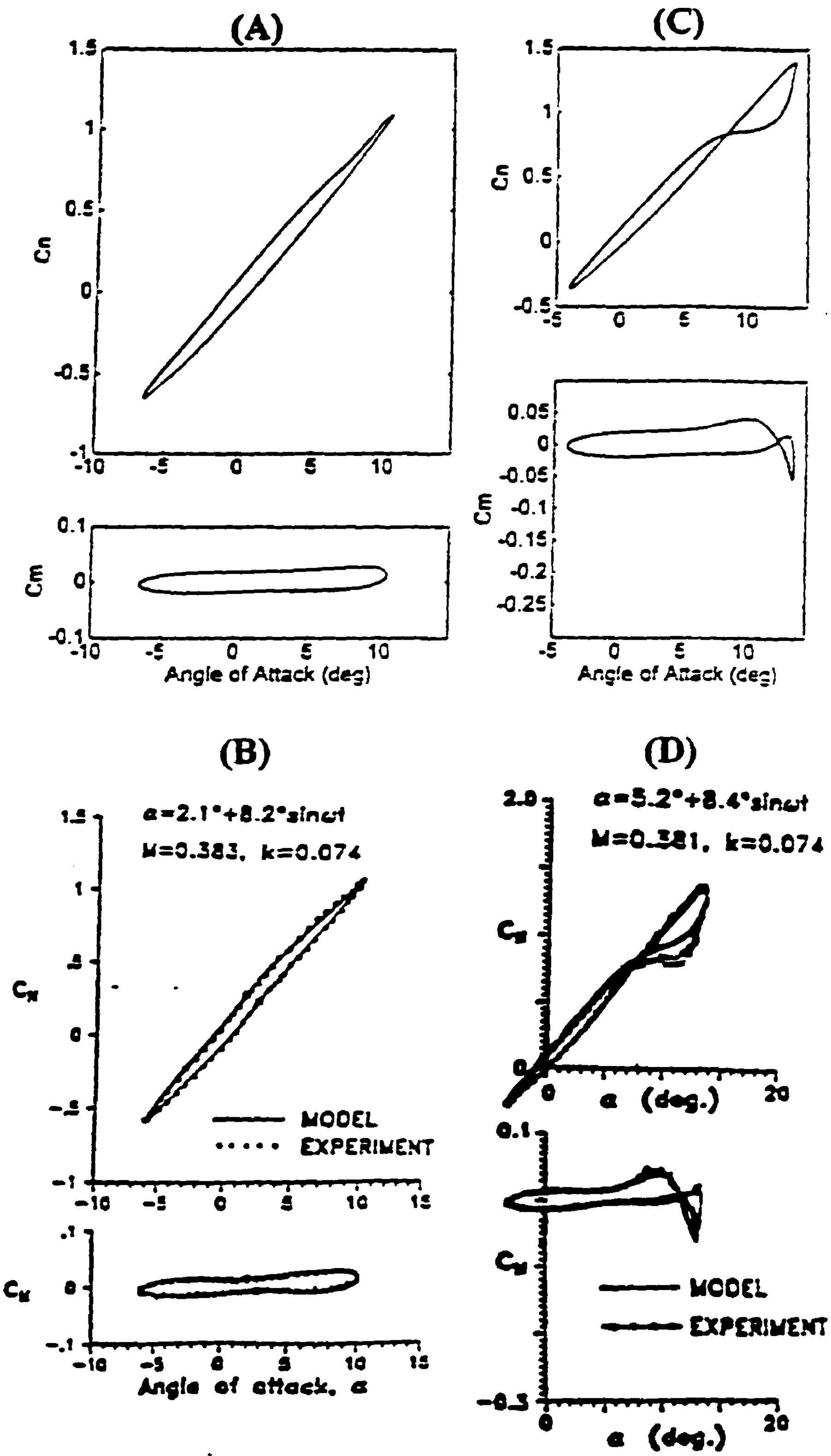

Figure 3.4: Comparison of Model with Results Obtained by Leishman and Beddoes (1989); $\alpha_{1/4c} = 2.1^o + 8.2^o \sin(0.074s)$, M=0.4: **a) Model b) Results,** $\alpha_{1/4c} = 5.2^o + 8.4^o \sin(0.074s)$, M=0.4: **c) Model d) Results.**

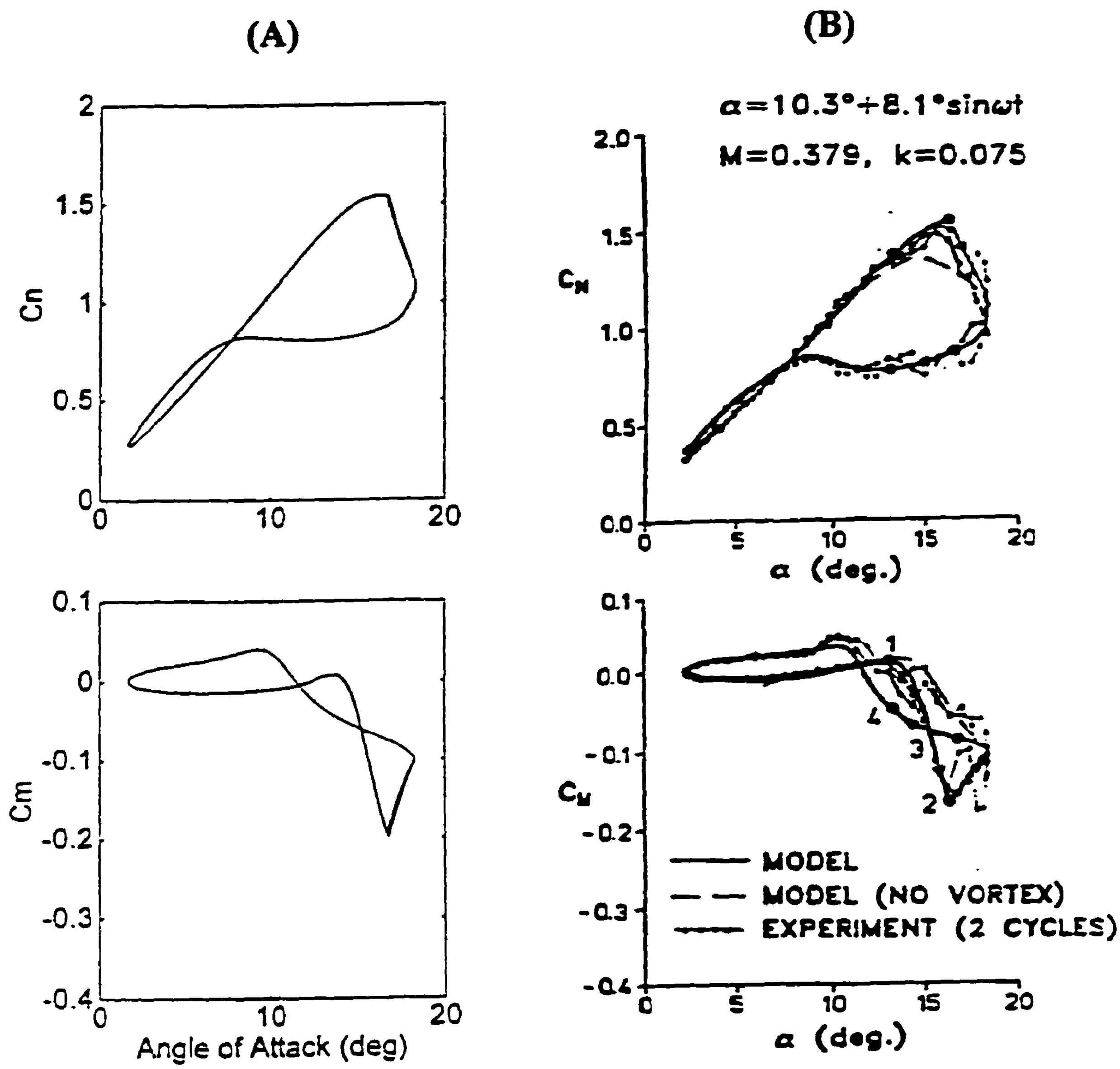

Figure 3.5: Comparison of Model with Results Obtained by Leishman and Beddoes (1989); $\alpha_{1/4c} = 10.3^o + 8.1^o \sin(0.075s)$, M**=0.4: a) Model b) Results.**

A)

B)

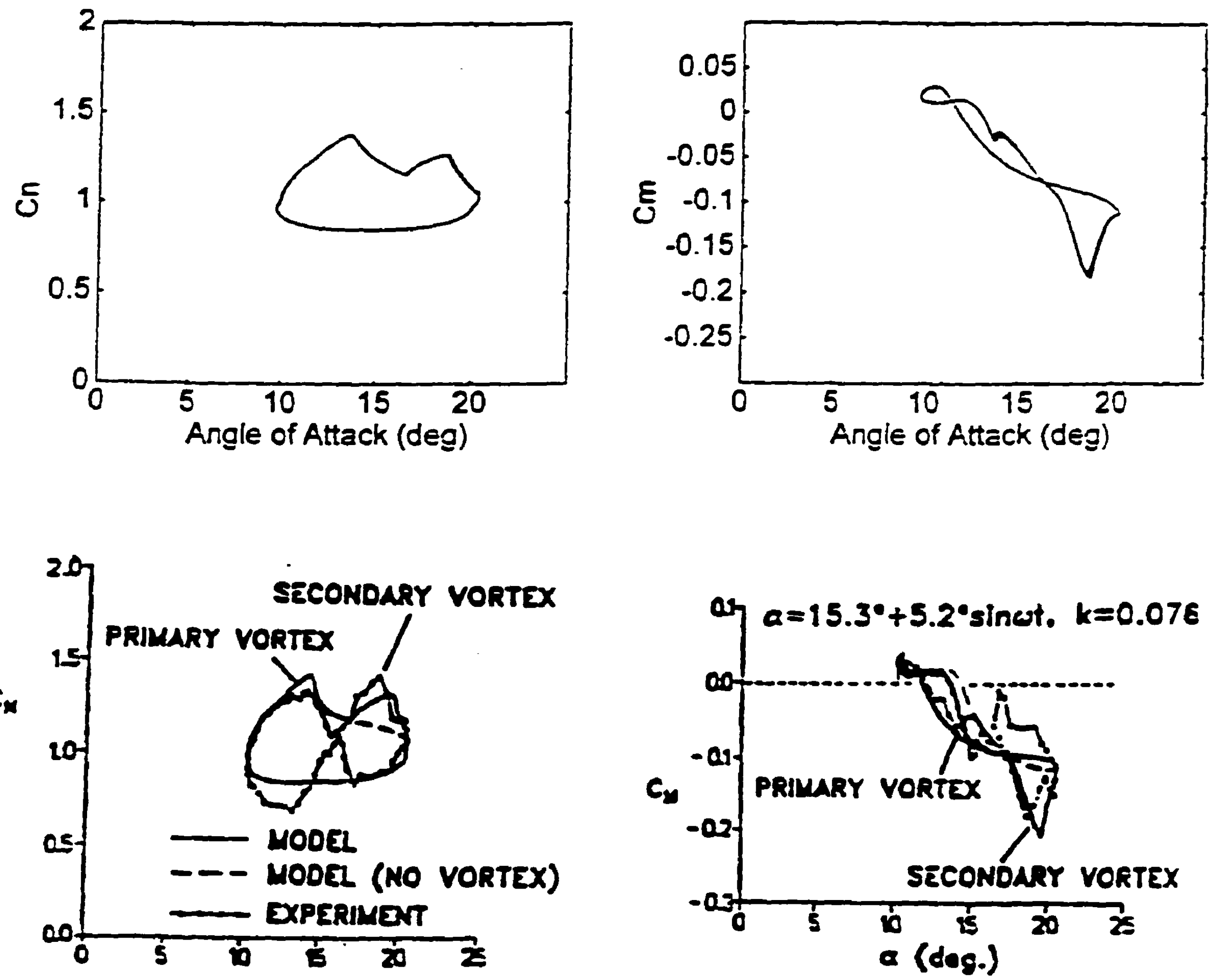

Figure 3.6: Comparison of Model with Results Obtained by Leishman and Beddoes (1989); $\alpha_{1/4c} = 15.3^o + 5.2^o \sin(0.076s)$, M=0.4: a) Model b) Results.

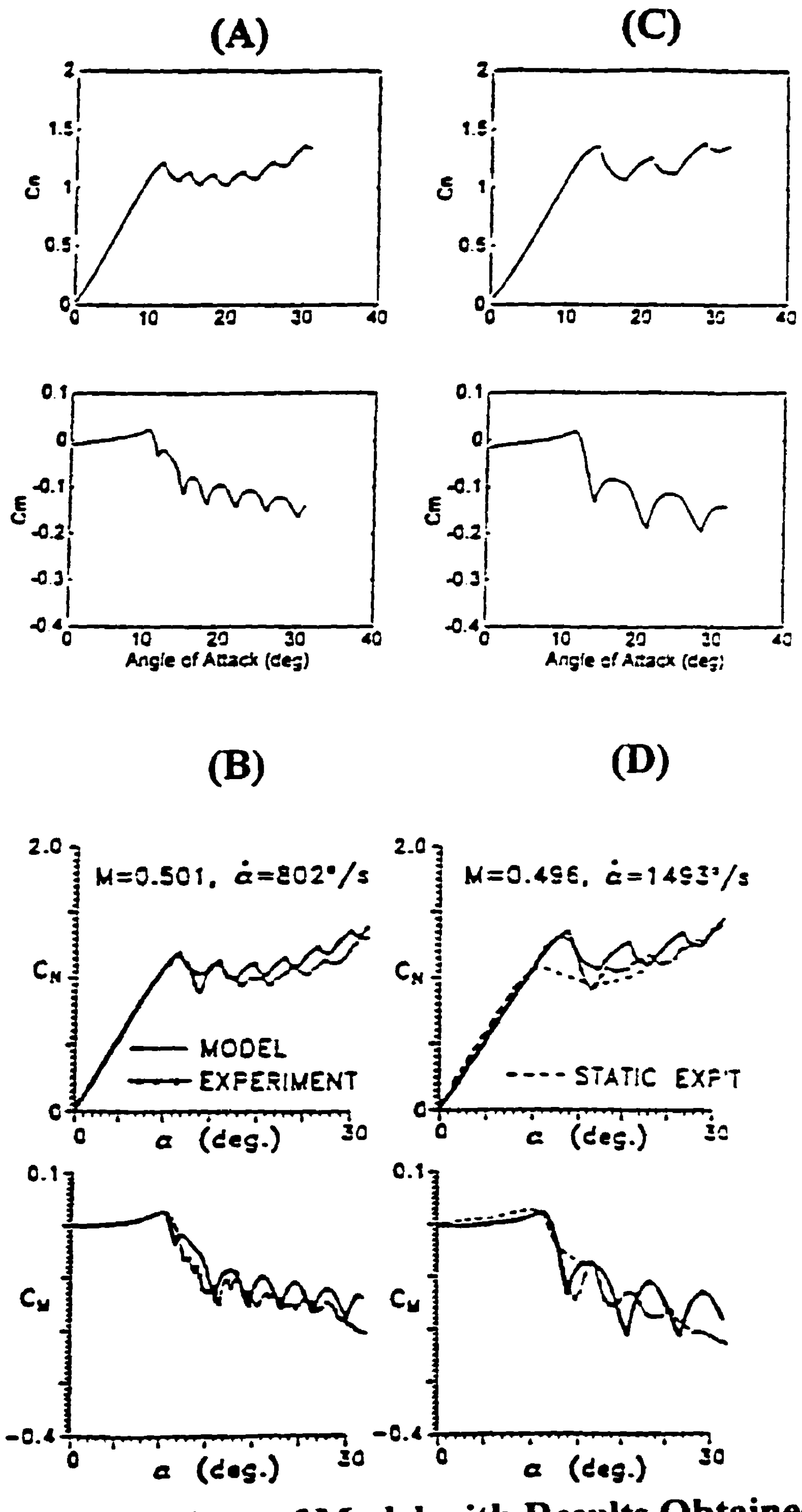

Figure 3.7: Comparison of Model with Results Obtained by Leishman and Beddoes (1989) for a Ramp Input; $\dot{\alpha} = 802^o/s$, M=0.5: a) Model b) Results; $\dot{\alpha} = 1493^o/s$, M=0.5: c) Model d) Results;

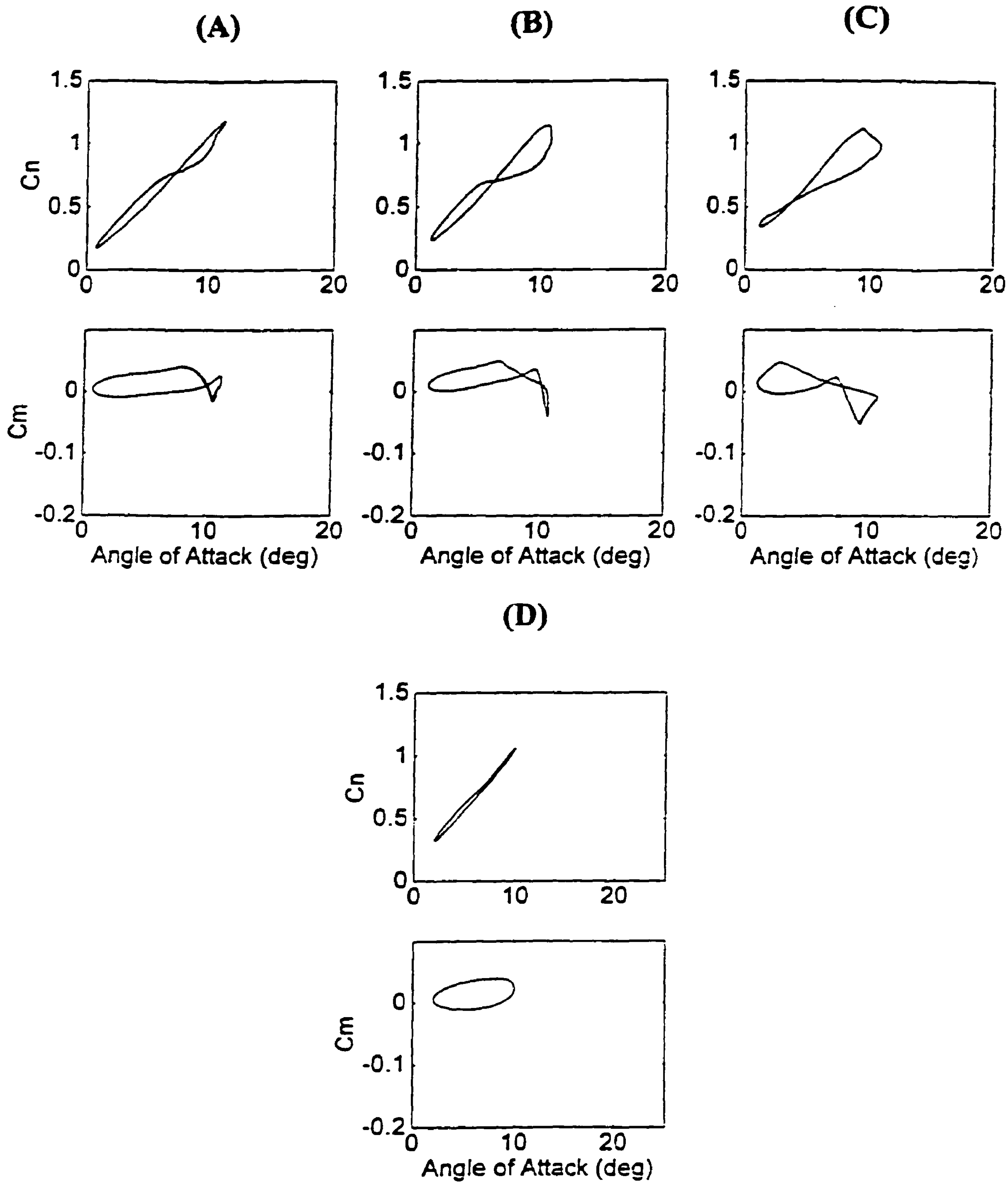

Figure 3.8: Comparison of Model with Results Obtained by Leishman and Beddoes (1989) for Various harmonic Inputs and Mach Numbers; a),b),c),d): Model, e),f),g),h): Results.

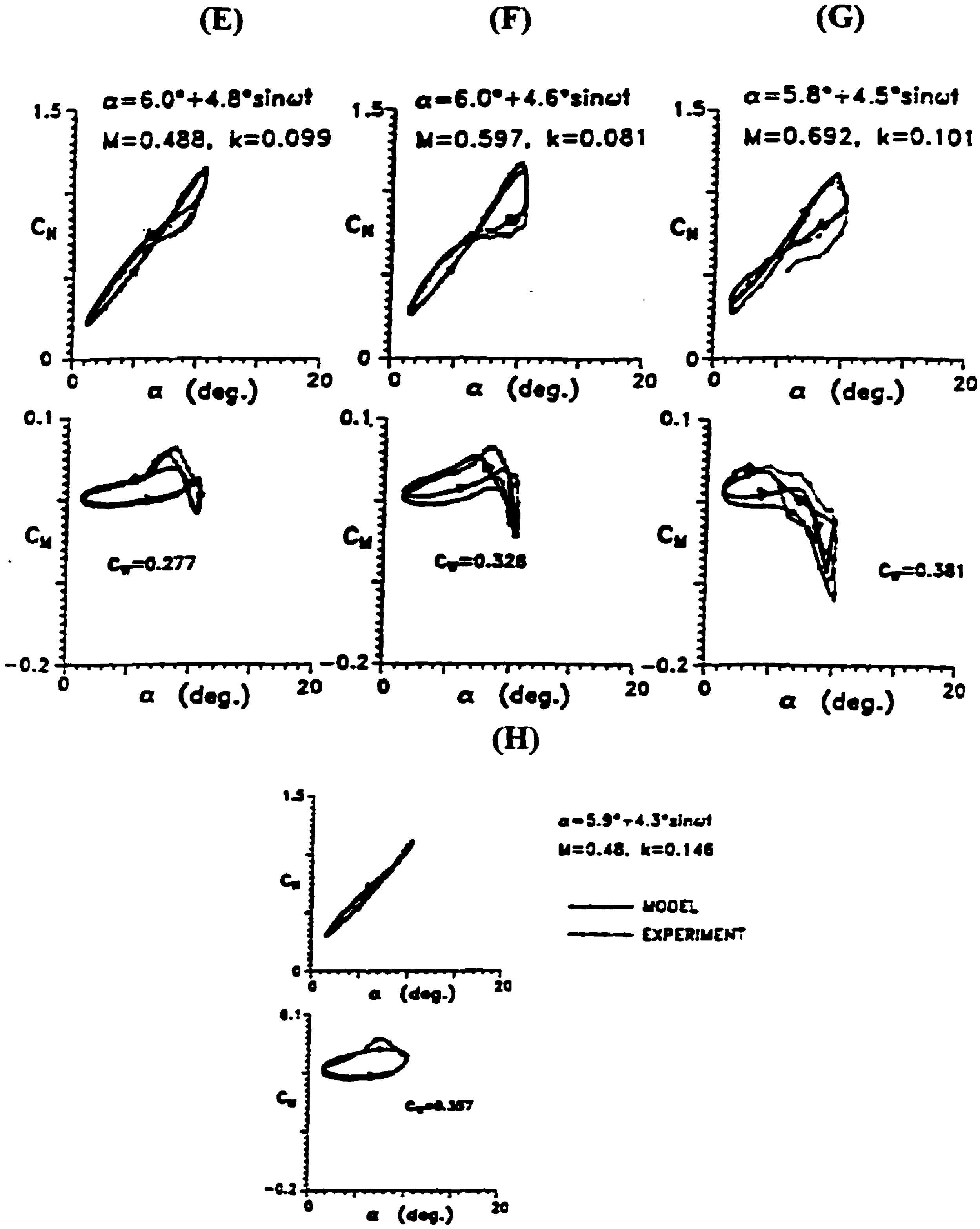
(E)
(F)
(G)
α=6.0°+4.8°sinωt
M=0.488, k=0.099
α=6.0°+4.6°sinωt
M=0.597, k=0.081
α=5.8°+4.5°sinωt
M=0.692, k=0.101
C_N
C_M
α (deg.)
C_W=0.277
C_W=0.328
C_W=0.381
(H)
α=5.9°+4.3°sinωt
M=0.48, k=0.146
MODEL
EXPERIMENT

Chapter 4

The Aeroelastic Model

4.1 Introduction

The aerodynamic model is used to determine the moment coefficient and normal force coefficient of an airfoil at a specific point in time. These values may then be added to the aeroelastic model as forcing terms. The non-linearities in the aeroelastic response, provided that the airfoil does not have any structural non-linearities, reside in the aerodynamic part. Using Figure 4.1 as a guide, one can use the Lagrangian method to determine the resulting differential equations. Once this has been done, a finite difference scheme may be used to solve the equations numerically. The procedure used is identical to that given by Lee and LeBlanc (1986).

4.2 Derivation of Aeroelastic Equations

The following are the energy terms to be used in conjunction with the Lagrangian equation to determine the aeroelastic differential equations:

$$T = \frac{1}{2} m \dot{h}^2 + \frac{1}{2} I \dot{\alpha}^2 + m x_a \left(\frac{c}{2}\right) \dot{h} \dot{\alpha} \qquad \text{(Kinetic Energy, 4-1)}$$

$$V = \frac{1}{2} k_\alpha \alpha^2 + \frac{1}{2} k_h h^2 \qquad \text{(Potential Energy, 4-2)}$$

$$D = \frac{1}{2} C_h \dot{h}^2 + \frac{1}{2} C_\alpha \dot{\alpha}^2 \qquad \text{(Energy Dissipation, 4-3)}$$

$$P=(-N(t)+P(t))\dot{h}+[M(t)+N(t)(\frac{1}{2}c)(\frac{1}{2}+a_h)+Q(t)]\dot{\alpha}$$

(Power Input, 4-4)

(Refer to the Nomenclature for the definition of variables.)

Using the Lagrangian equation

$$\frac{\partial}{\partial t}(\frac{\partial T}{\partial \dot{x}})+\frac{\partial V}{\partial x}=\frac{\partial P}{\partial \dot{x}}-\frac{\partial D}{\partial \dot{x}} \tag{4-5}$$

where x is the generalized coordinate (h or α) yields the following coupled aeroelastic differential equations

$$m\ddot{h}+mx_a(\frac{c}{2})\ddot{\alpha}+C_h\dot{h}+k_h h=-N(t)+P(t) \tag{4-6}$$

$$I\ddot{\alpha}+mx_a(\frac{c}{2})\ddot{h}+C_\alpha\dot{\alpha}+k_\alpha\alpha = M(t)+N(t)(\frac{1}{2}c)(\frac{1}{2}+a_h)+Q(t) \tag{4-7}$$

The uncoupled natural frequencies and damping ratios are thus defined:

Heave:

$$\varsigma_h=\frac{C_h}{2\sqrt{k_h m}} \tag{4-8}$$

$$\omega_h^{\,2}=\frac{k_h}{m} \tag{4-9}$$

Pitch:

$$\varsigma_\alpha=\frac{C_\alpha}{2\sqrt{k_\alpha I}} \tag{4-10}$$

$$\omega_\alpha^{\,2}=\frac{k_\alpha}{I} \tag{4-11}$$

Non-Dimensionalisation

To simplify the problem the following non-dimensional groups were formed:

heave: $$\xi = \frac{h}{(c/2)} \tag{4-12}$$

where the denominator is a semichord length

mass: $$\mu = \frac{m}{\pi\rho(c/2)^2} \tag{4-13}$$

where the denominator is the mass of the air that occupies the space the airfoil can rotate in, i.e. the mass of air in a cylinder of unit thickness with the radius equal to a semi-chord

time: $$s = \frac{U_\infty t}{(c/2)} \tag{4-14}$$

where the reference time is the time it takes the airfoil to travel one semi-chord

normal force: $$C_n = \frac{N}{(\frac{1}{2}\rho U_\infty{}^2)c} \tag{4-15}$$

moment: $$C_m = \frac{M}{(\frac{1}{2}\rho U_\infty{}^2)c^2} \tag{4-16}$$

where the denominators are the dynamic pressure of the free stream multiplied by a reference length or area.

Using the above non-dimensional quantities the aeroelastic equations can be reduced to non-dimensional form as follows,

$$\xi'' + x_\alpha \alpha'' + 2\varsigma_h \frac{\varpi}{U^*}\xi' + \frac{\varpi^2}{U^{*2}}\xi = -\frac{1}{\pi\mu}Cn(s) + P_o(s) \tag{4-17}$$

$$x_\alpha \xi'' + r_a{}^2 \alpha'' + r_\alpha{}^2 2\varsigma_\alpha \frac{\alpha'}{U^*} + \frac{r_\alpha{}^2}{U^{*2}}\alpha = \frac{2}{\pi\mu}(Cm(s) + (\frac{1}{4} + \frac{a_h}{2})Cn(s)) + r_\alpha{}^2 Q_o(s) \tag{4-18}$$

where $\varpi = \frac{\omega_h}{\omega_\alpha}$, $U^* = \frac{U_\infty}{(c/2)\omega_\alpha}$, $P_o(s) = P(s)\frac{c}{2mU_\infty{}^2}$, $Q_o(s) = \frac{Q(s)}{mU_\infty{}^2}\frac{1}{r_\alpha{}^2}$ and ' denotes differentiation with respect to non-dimensional time.

4.3 Numerical Procedure

4.3.1 Houbolt's Finite Difference Scheme

Once the differential equations have been found, it is necessary to devise a numerical scheme to solve the problem. Houbolt's finite difference scheme (Houbolt, 1950) is used in this analysis and is written as follows:

$$\alpha''(s) = \frac{1}{\Delta s^2}(2\alpha(s) - 5\alpha(s-\Delta s) + 4\alpha(s-2\Delta s) - \alpha(s-3\Delta s)) \qquad \text{(4-19)}$$

$$\alpha'(s) = \frac{1}{6\Delta s}(11\alpha(s) - 18\alpha(s-\Delta s) + 9\alpha(s-2\Delta s) - 2\alpha(s-3\Delta s)) \qquad \text{(4-20)}$$

(The same formula applies to heave.)

If the above two formulas, (4-19) and (4-20), are plugged into the aeroelastic equations, (4-17) and (4-18), then once the values of pitch and heave are known for the previous three time steps the only unknowns are the current values of heave and pitch. Since there are two equations, these two quantities may be solved for. The following form is used to ultimately solve the aeroelastic problem:

$$A\xi(s) + B\alpha(s) = C \qquad \text{(4-21)}$$

$$D\xi(s) + E\alpha(s) = F \qquad \text{(4-22)}$$

(4-21) comes from (4-17), while (4-22) comes from (4-18). The coefficients of (4-21) and (4-22) are known quantities and depend on previous values of pitch and heave, as well as the forcing terms and aerodynamic terms, which are also known. For a full definition of these coefficients see Lee and LeBlanc (1986).

4.3.2 Starting Scheme

The scheme that is being used requires the values of heave and pitch at three time steps, before the current one, to solve the equations. This means that a starting procedure must be implemented to acquire solutions to two more time steps consecutive to the initial conditions, which are already known quantities. Using the differential equations, (4-17) and (4-18), at s=0 the values of pitch and heave acceleration ($\alpha''(0)$ and $h''(0)$) may be solved for provided the initial conditions are known: $C_n(0)$, $Po(0)$, $C_m(0)$, $Qo(0)$, $\alpha(0),\alpha'(0),\xi(0),\xi'(0)$, (see Lee and LeBlanc (1986) for solution). Once this has been done the values for the quantities of pitch and heave for times $+\Delta s$ and $-\Delta s$ can be found using a Taylor series expansion:

$$\alpha(-\Delta s) = \alpha(0) - \Delta s\alpha'(0) + \frac{\Delta s^2}{2}\alpha''(0) \qquad (4\text{-}23)$$

$$\alpha(+\Delta s) = \alpha(0) + \Delta s\alpha'(0) + \frac{\Delta s^2}{2}\alpha''(0) \qquad (4\text{-}24)$$

(The same can be used for heave.)

Therefore, equations (4-23) and (4-24), in conjunction with the initial conditions allows for the solution of heave and pitch at times, $-\Delta s, 0, +\Delta s$. This means that the solution may now be found for $+2\Delta s$, using the numerical scheme described before. This means that the Taylor series expansion is used to find the solution for the first time step after and before the initial conditions (s=0). This is more desirable than using the Taylor series expansion to determine the solutions for two time steps before the initial condition (i.e.: $-\Delta s, -2\Delta s$). This is because the error in the Taylor approximation is compounded when it is used on consecutive time steps.

4.3.3 Interaction Between Aerodynamic and Structural Components

The largest difficulty in creating the aeroelastic model is the interface between the aerodynamic portion, which was modelled from Leishman and Beddoes' (1986) work, and the aeroelastic portion derived from the work of Lee and LeBlanc (1986), who used another aerodynamic model (Bielawa et al., 1983).

The first problem is the conversion of units of the variables. The following conversions were made so that the two portions are consistent.

Model	Aerodynamic	Aeroelastic	Conversion
Pitch-rate	$q = \dot{\alpha} c / U_\infty$	$\alpha' = \dot{\alpha} c / (2U_\infty)$	$q = 2\alpha'$
Heave equivalent angle	$\alpha_{heq} = \dot{h} / U_\infty$	$\xi' = \dot{h} / U_\infty$	$\alpha_{heq} = \xi'$

(4-25)

Another conversion problem arises in the choice of axis. The aerodynamic model has been created to find the moment about the quarter chord, while the aeroelastic model needs the moment about the elastic axis. A change of axis has been discussed in the aerodynamic section. In the context of the new variables the change of axis contribution may be added as an additional angle of attack:

$$\alpha_{axis} = \frac{1}{2}\left(\frac{1}{2} - a_h\right) q = \left(\frac{1}{2} - a_h\right) \alpha' \tag{4-26}$$

where a_h is the non-dimensional distance from the mid-chord to the elastic axis.

Yet another problem arises from the choice of zero deflection angle. In the aeroelastic model all angles and the heave deflection are measured from where the springs are undeflected. Although the vertical location (heave) is arbitrary and makes no difference to the aerodynamics, the zero deflection or mean angle of attack needs to be added to the aerodynamics as an additional angle of attack.

A fourth problem comes from the starting procedure. The starting procedure used in the aeroelastic model does not apply to the aerodynamic model. The aerodynamics depend on the time history of the airfoil. Since it is impossible to know the time history before the program is run, it is assumed that the airfoil is steady for all time before $-\Delta s$. Static theory is then used to determine all of the aerodynamic quantities (including separation) at $-\Delta s$, thus creating an assumed time history, which is the easiest to handle.

The final problem that needs to be tackled is the fact that the aerodynamic forcing, which is an input to the system, depends on the current values of the output. A unique numerical scheme needs to be implemented to solve this problem. The numerical technique used is the predictor-corrector scheme, which is described in the following section.

4.3.4 The Predictor-Corrector Scheme

The predictor-corrector scheme works in the following way. It starts by assuming the aerodynamic input, i.e. the normal force and moment coefficients, to be equal to their values at the previous time-step. They are then used in conjunction with the aeroelastic algorithm to calculate the output (i.e. pitch, pitch-rate, heave and heave rate), these are the predictor values. This new output is then used to calculate the aerodynamic input, which is reintroduced into the algorithm to find a new output, these values are known as the corrector values. Once this is done, the corrector values are compared to the predictor values, if they are within a specified tolerance the scheme stops and keeps the corrector values for that particular time-step. The tolerance used in this thesis was set at 0.0001% difference between the predictor and corrector value relative to the predictor.

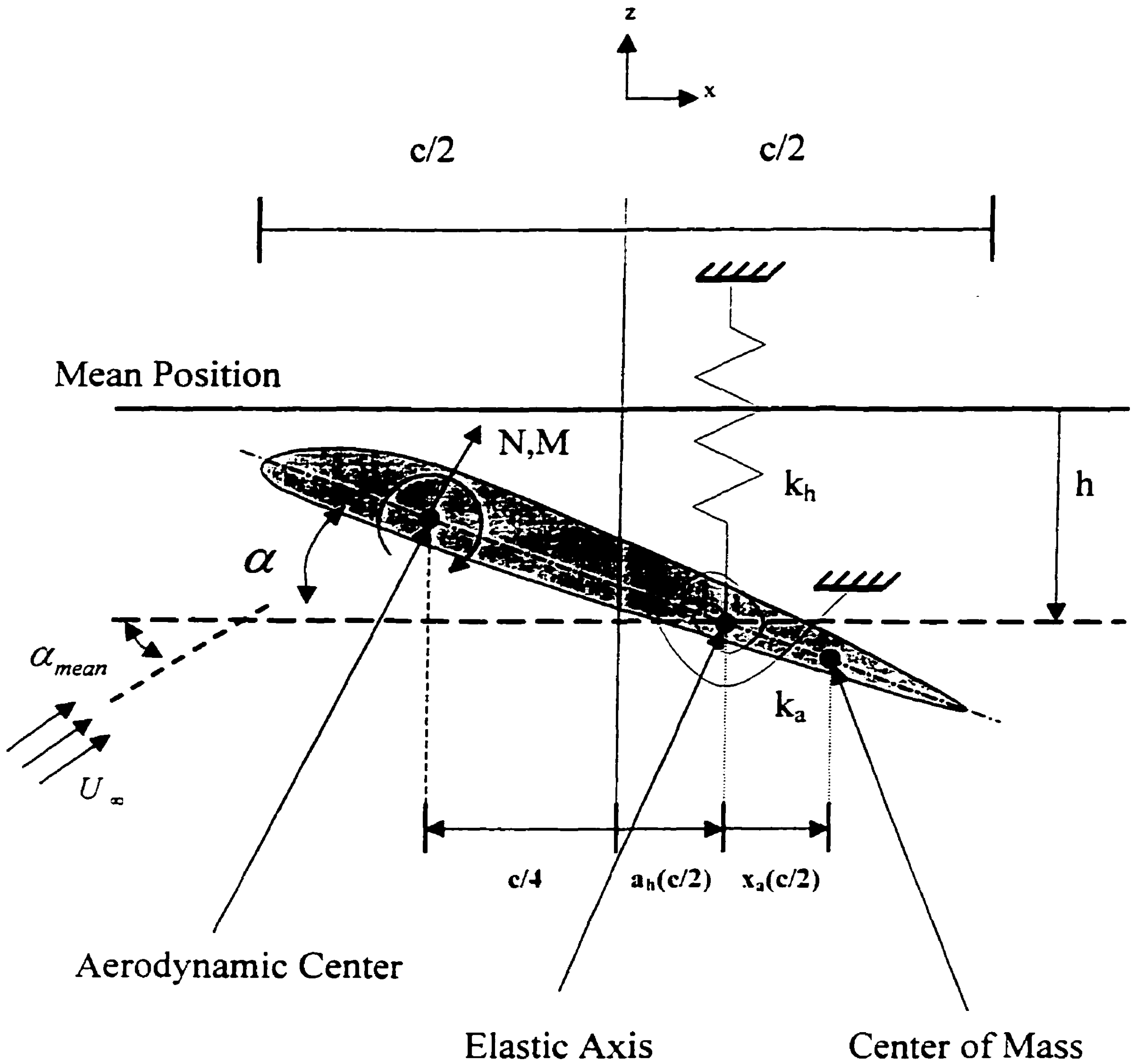

Figure 4.1: The 2-DOF Airfoil.

Chapter 5

Justification of the Aeroelastic Model

5.1 Residuals of the Aeroelastic Equations

The aeroelastic model is a combination of Leishman and Beddoes' (1986) aerodynamic work and Lee and LeBlanc's (1986) aeroelastic work, and is unique to this thesis. There is therefore no data against which to verify the results, unlike the aerodynamic model, which had data. A different approach must be used to accomplish this task. Knowing that the aerodynamic portion of the model is correct, as proven in Chapter 3, the only thing that may be erroneous with the model is the newly added aeroelastic portion. This newly added portion consists of the aeroelastic equations, (4-18) and (4-19), which are solved numerically according to the procedures presented in Chapter 4. The following equations may be used as a measure of the numerical error in the aeroelastic equations:

$$R1 = P(s)\frac{c}{2mU_\infty^{\;2}} - \frac{1}{\pi\mu}Cn(s) - \xi'' - x_\alpha\alpha'' - 2\varsigma_h\frac{\varpi}{U*}\xi' - \frac{\varpi^2}{U*^2}\xi \qquad (5\text{-}1)$$

$$R2 = \frac{2}{\pi\mu}(Cm(s) + (\frac{1}{4} + \frac{a_h}{2})Cn(s)) + \frac{Q(s)}{mU_\infty^{\;2}} - x_\alpha\xi'' - r_\alpha^{\;2}\alpha'' - r_\alpha^{\;2}2\varsigma_\alpha\frac{\alpha'}{U*} - \frac{r_\alpha^{\;2}}{U*^2}\alpha \qquad (5\text{-}2)$$

where velocities and accelerations are calculated according to Houbolt's finite difference scheme, equations (4-19) and (4-20). Equations (5-1) and (5-2) are simply the right-hand side of the aeroelastic equations, (4-17) and (4-18), minus the left-hand side, and may be referred to as the residuals or remainders of these equations. Theoretically these residuals should be equal to zero. The fact that they are not equal to zero is due to the predictor-corrector scheme. In other words the response (pitch and plunge) of the airfoil depends on the effect of the aerodynamic loads on the aeroelastic system, but the aerodynamic loads depend on the response of the airfoil. Bearing this in mind, a choice has to be made as to where the numerical error should lie. If the aeroelastic equations are to have no error then there must be error in the aerodynamic loads. The values of pitch and plunge, which are the corrector values found from solving the aeroelastic equations are obviously not the ones used to calculate the aerodynamic loads. The predictor values were used to calculate the aerodynamic loads. In this case the above residual formulae would be exactly zero and another error must be defined for the aerodynamic loads, which does not correspond to the corrector values for the response of the airfoil. If on the other hand the aerodynamic loads are recalculated, with the corrector values found from the aeroelastic equations then, as they are a part of the aeroelastic equations, they will cause a slight error or residual in these equations. Since it is easier to calculate the error in the aeroelastic equations, and since the non-linear component arises from the aerodynamic loads, it is wiser to recalculate the aerodynamic loads so that they match the corrector response.

The residuals were calculated for the following case: Pitch: M=0.4, $\alpha_{mean}=10^0$, Qo=0.0007, k=0.04, $U^*=21$; Plunge: $\varpi=9$, while all other inputs are zero. This case was chosen because the airfoil response seemed to be chaotic, and thus it represented a very severe test for the numerical solution. Figure 5.1 shows the residual for the two equations calculated for a period of 20 cycles of the pitch forcing. As can be seen they are of the order of 10^{-8} or less. When it is realized that the other terms in equations (5-1) and (5-2), which are in fact the terms in the aeroelastic differential equations, are of the order of 10^{-4} or greater, it indicates that the residuals are sufficiently small. In Figures 5.2 and 5.3 it can be seen that the residuals, which appear to be straight lines, are essentially zero compared to the rest of the terms of equations (5-1) and (5-2), which are the oscillations.

5.2 Predictor-Corrector Error

The residual calculations showed that the aeroelastic equations are solved accurately. This does not, however, prove the convergence of the predictor-corrector scheme. In other words, showing that the predictor and corrector values are solved accurately, since they are solutions to the aeroelastic equations, does not show that they have converged. An error analysis must now be done to verify the convergence of the predictor-corrector scheme. The difference between this error and the one discussed in the previous section is that the bounds of this error are pre-defined. Ultimately, sufficiently small residuals in the aeroelastic equations allow the accurate calculation of the predictor-corrector error, which is a measure of the convergence of the numerical scheme.

As mentioned in section 5.1, the aerodynamic loads are recalculated after a solution to the aeroelastic equations has been found. This means that the predictor values (defined in section 4.3.4) are the ones that are kept as a final solution. The corrector values, which are the values obtained when the aeroelastic equations are solved with the new aerodynamic loads, can now be used to verify the convergence of the predictor-corrector scheme. The error in this scheme may be defined as follows:

$$\text{Predictor - Corrector Error} = \frac{\text{Predictor Value - Corrector Value}}{\text{Predictor Value}} \qquad (5\text{-}3)$$

(or P.C.E. for short)

The tolerance for the predictor-corrector scheme was set to P.C.E.=1×10^{-6}, which gave an accuracy of at least five significant digits (for the justification of this value, see section 5.3). The P.C.E. for both plunge and pitch variables are shown as a function of time in Figure 5.4 for the same case as that used in the previous figures. As can be seen, the error is indeed within the assigned tolerance, which means that the predictor-corrector scheme converged for all time steps for the example given.

5.2.1 Non-Convergence due to Feed-Back Loops

There are cases when the scheme is not capable of converging. This occurs in the form of a feed-back loop. This means that the predictor values of pitch and plunge produce corrector values that reproduce the predictor values, and the cycle continues. This phenomenon can be seen in Figure 5.5. There are several ways to counteract this problem. One way is to implement a relaxation scheme. This, however, is too complex because there are upwards of thirty variables, which depend on their time-histories in the program (for example, all the deficiency terms). Only approaches that can be dynamically implemented shall be considered. Another, easier way, is to perturb the predictor values when a feed-back loop has been identified, causing the scheme to pursue a different route to the solution which will not cause a feed-back loop. This has a good success rate, but it does not always work. In those cases when this does not work the program is restarted with a finer time-step, and the program then almost always converges.

It may seem improbable that a feed-back loop should occur, as there are so many inputs into the program (i.e.: pitch, plunge and their respective velocities and accelerations and the aerodynamic loads) which must all coincide to produce this phenomenon. Under further inspection, however, one realizes that all of these values at a given time step depend **only** on the pitch and plunge values at that time step, the time histories from which the rest of the inputs are calculated are already set. This, coupled with the large amount of iterations required makes these loops a problem, but one which is solved using the procedure discussed above.

5.3 Time-Step Size and P.C.E. Tolerance

Two factors affect the accuracy of the final solution: 1) the size of the time-step used, and 2) the tolerance for the predictor-corrector error (or P.C.E.). Both a smaller time-step size and smaller P.C.E. tolerance will increase the accuracy of the final solution. They will also increase the number of iterations required, which will use up computer time and also increase the chances of feed-back loops which requires even more computer time to rectify. A balance must therefore be struck between accuracy and computer resources.

Setting the number of iterations per cycle of forcing controls the size of the time-step. The greater this value, the finer the time-step. This value is used instead of setting the time-step directly because, more often than not, the airfoil's response frequency is in the region of the forcing frequency, and the time-step should be adjusted according to this. In Figure 5.6, a convergence analysis is done on the predictor-corrector scheme. More specifically, the mean number of iterations before the scheme converges (the average is taken over 5 cycles of the program) is plotted against the size of the time-step. Globally the number of iterations until convergence decreases as a finer time step is used (locally it is more erratic). This justifies using a finer time-step to rectify feed-back loops because faster convergence rates implies less chance of encountering these loops. It is also clear that the convergence rate of the scheme increases rapidly up to approximately 256 iter./cycle and then begins to plateau, meaning that the number of iterations per cycle should be at least in the hundreds to most effectively avoid feed-back loops. According to Lee and LeBlanc (1986) a value of 128 iterations per cycle is acceptable; a value of 256 iterations per cycle has been adopted in this thesis.

The second factor, which affects the accuracy of the solution, is the tolerance set for the P.C.E. Of the two parameters, the size of the time step is more important than the tolerance of the P.C.E. This is seen clearly in Figures 5.7 and 5.8, which are the phase plots for the case under study. We see that in this case doubling the iterations/cycle (starting from the suggested value by Lee and LeBlanc) significantly alters the output (Figure 5.7), whereas altering the tolerance for the P.C.E. has significantly less of an influence (Figure 5.8). The values, which best seem to balance computer resources and accuracy are those of 256 iteration per cycle of forcing and $1x10^{-6}$ for the predictor-corrector error.

A)

B)

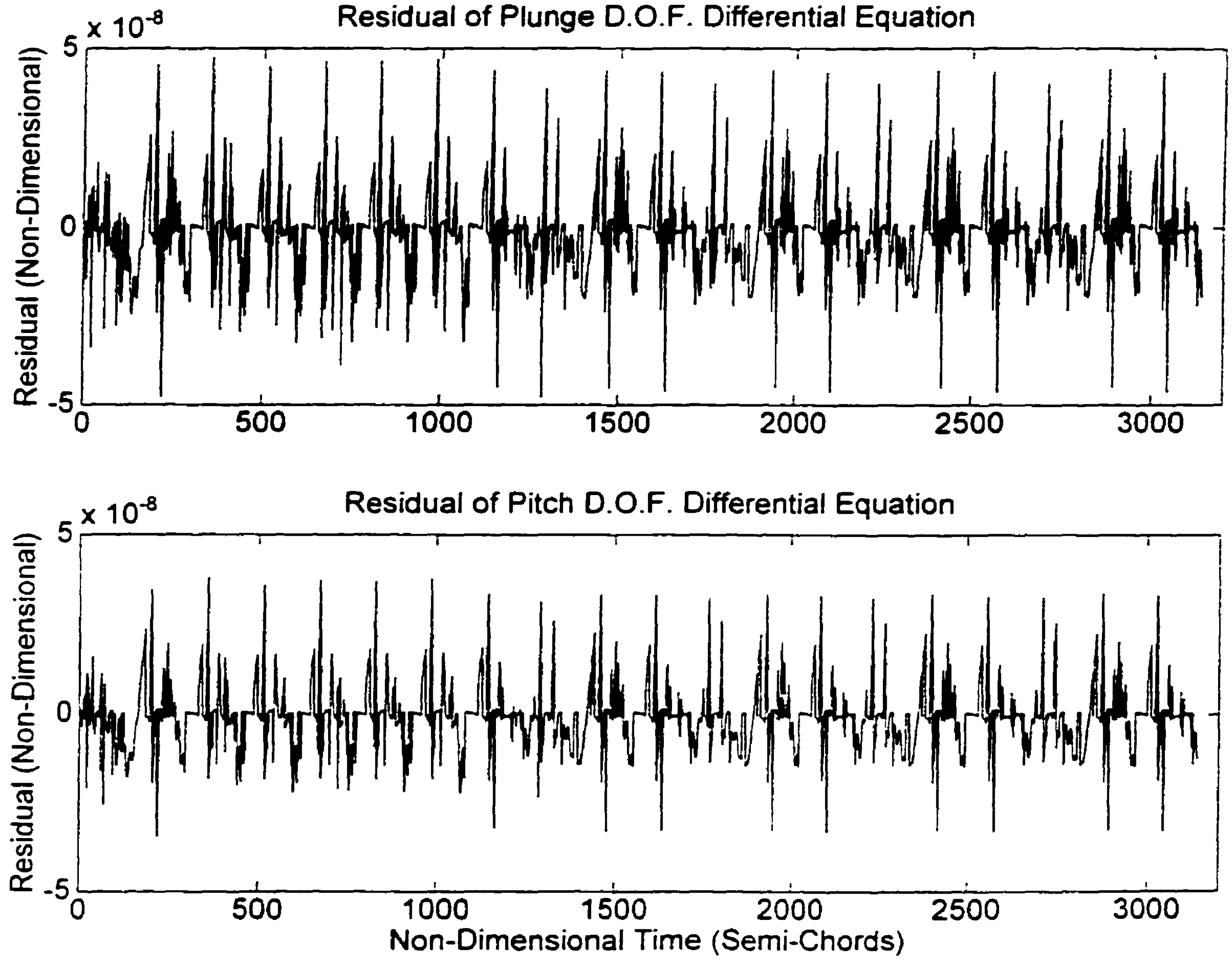

Figure 5.1: Residuals of the Aeroelastic Differential Equations; a) Plunge D.O.F. (Equation 5-1) b) Pitch D.O.F. (Equation 5-2): $\alpha_{mean} = 10$ deg, k=0.04, U*=21, Qo=7x10^{-4}, $\varpi = 9$, M=0.4.

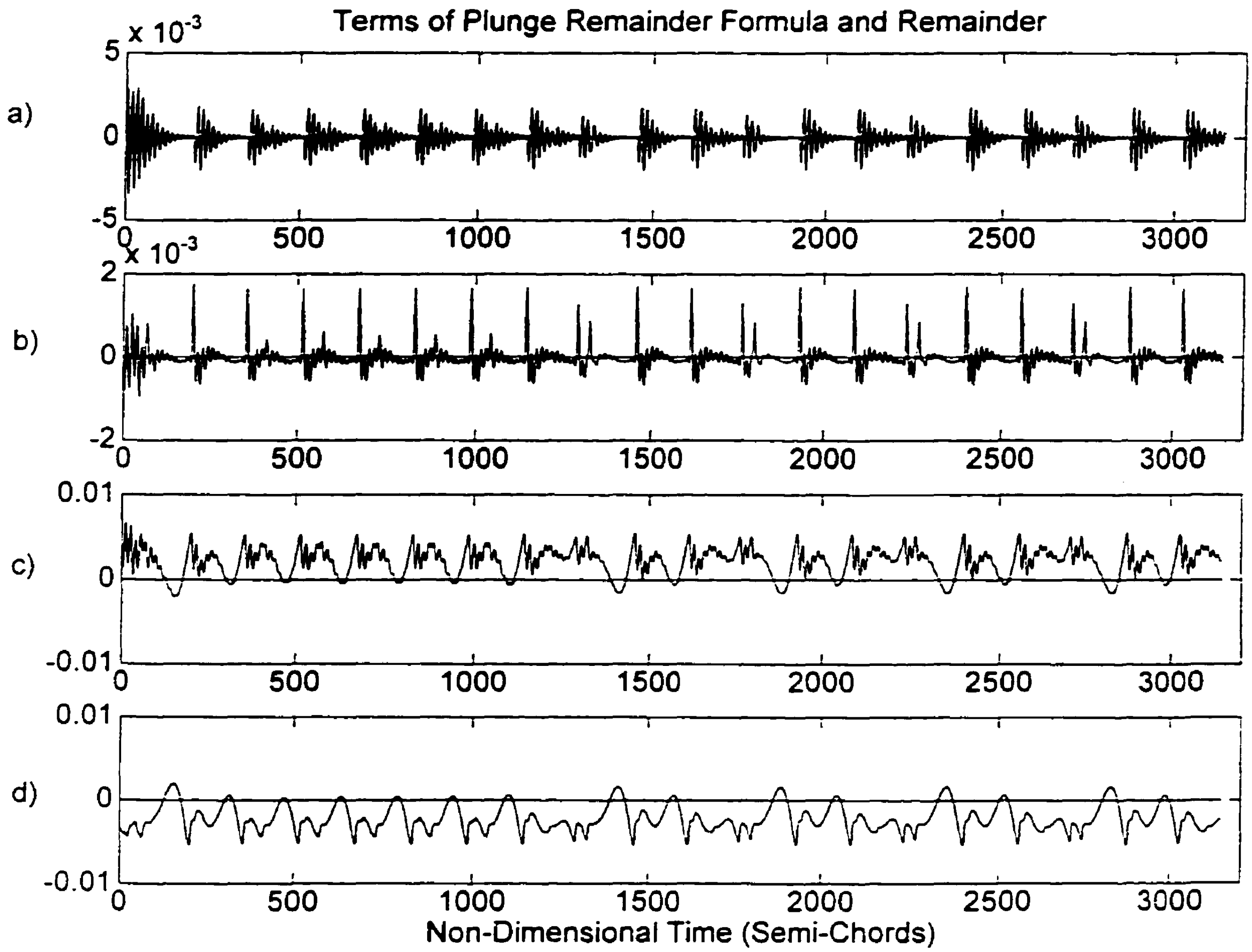

Figure 5.2: Comparison of Terms of the Plunge Aeroelastic Differential Equation (Equation 4-17) with the Plunge D.O.F. Residual (Equation 5-1); a)ξ'' b) $x_a\alpha''$ c) $(\varpi^2/U^{*2})\xi$ d) $(1/\pi\mu)Cn$: $\alpha_{mean}=10$ deg, k=0.04, U^*=21, Qo=7x10^{-4}, $\varpi=9$, M=0.4.

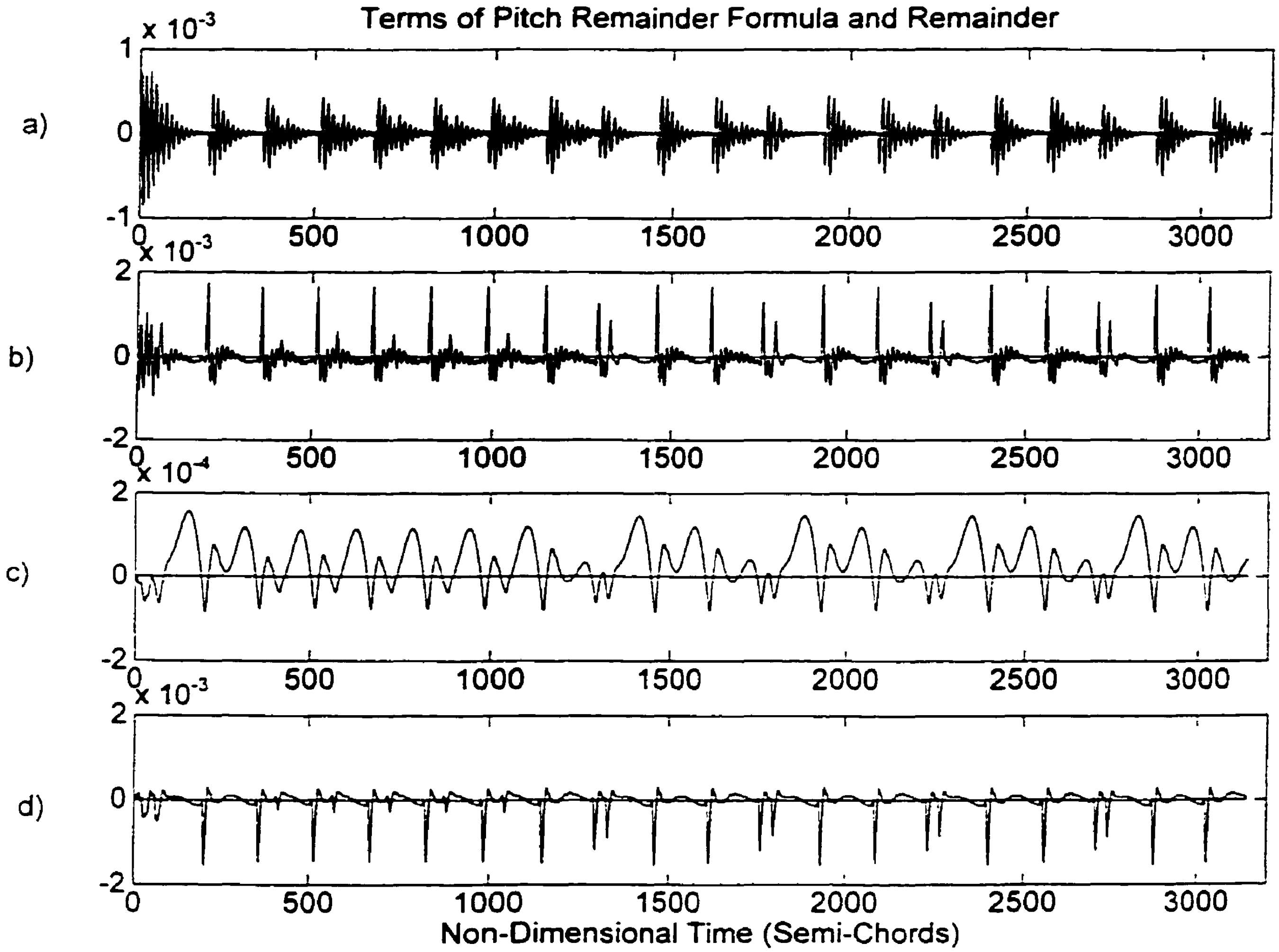

Figure 5.3: Comparison of Terms of the Pitch Aeroelastic Differential Equation (Equation 4-18) with the Pitch D.O.F. Residual (Equation 5-2); a)$x_\alpha \xi''$ b) $r_\alpha^2 \alpha''$ c) $(r_\alpha^2 / U^{*2})\xi$ d) $(2/\pi\mu)Cm$: $\alpha_{mean} = 10$ deg, k=0.04, U^*=21, Qo=7x10^{-4}, $\varpi = 9$, M=0.4.

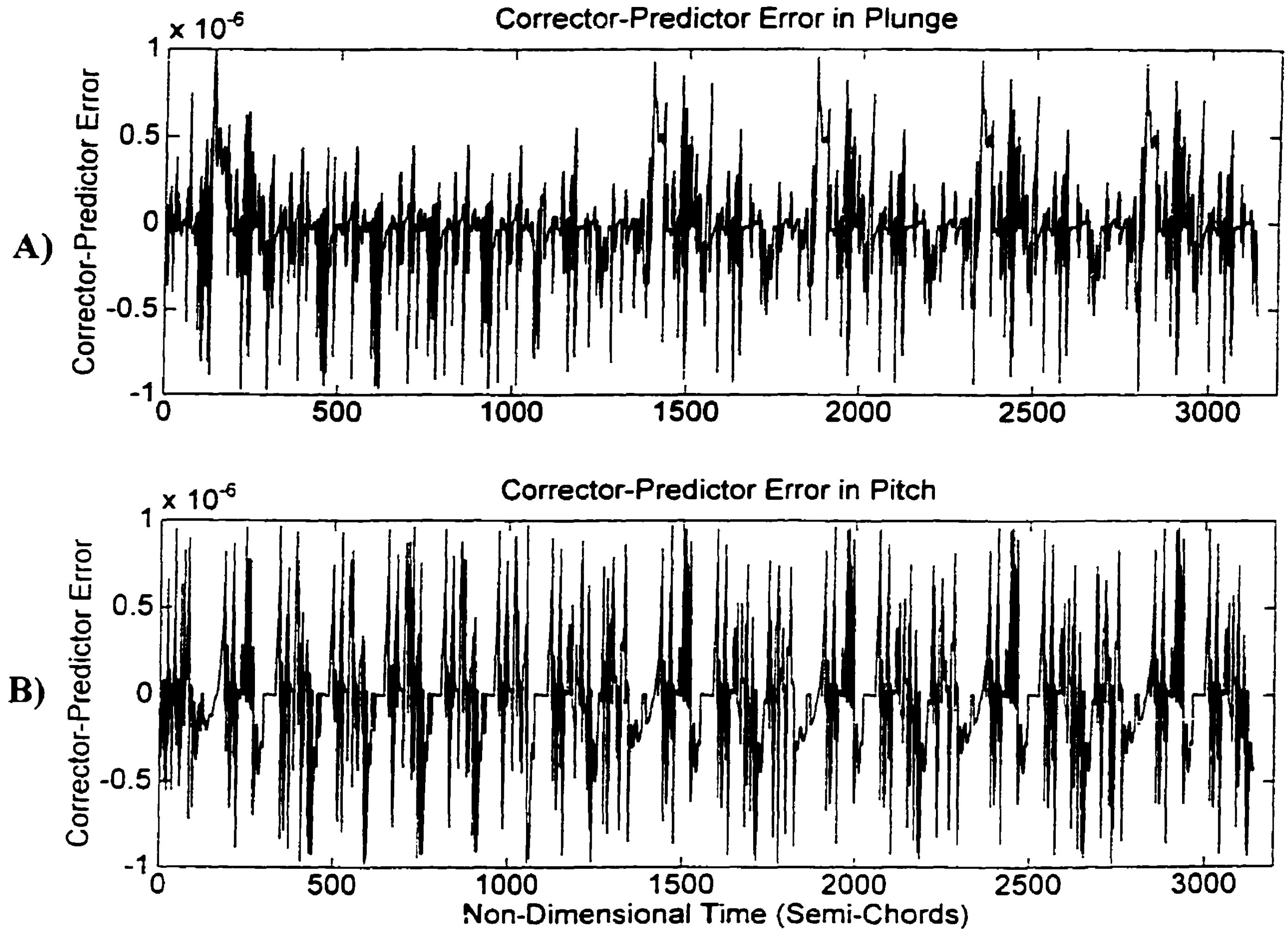

Figure 5.4: Predictor-Corrector Error; a) Plunge D.O.F. b) Pitch D.O.F.: $\alpha_{mean} = 10$ deg, k=0.04, U^*=21, Qo=7x10^{-4}, $\varpi = 9$, M=0.4.

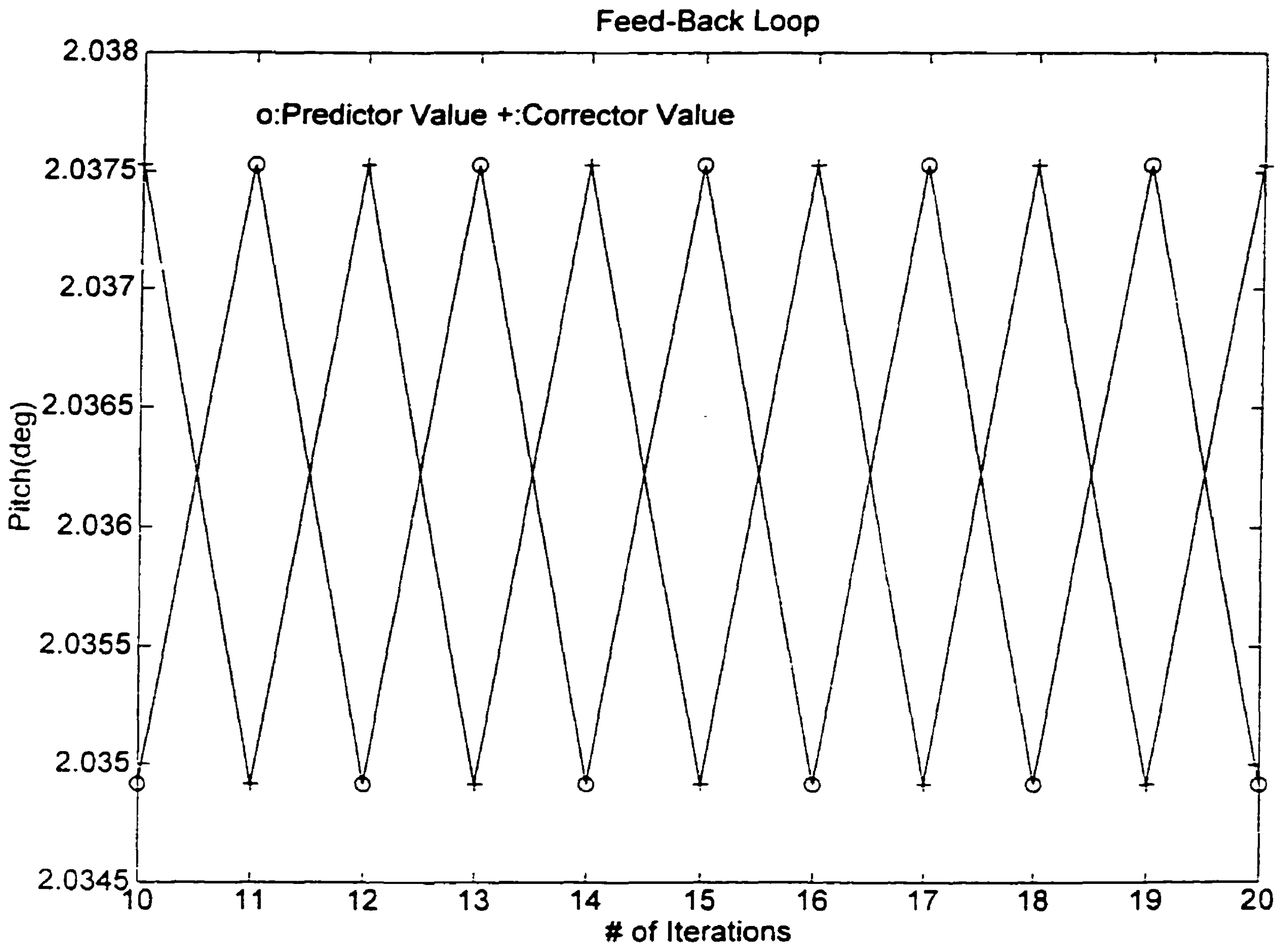

Figure 5.5: Feed-Back Loop in Pitch Response; $\alpha_{mean} = 10$ **deg,** k**=0.04,** U^***=21,** Qo**=7x10**$^{-4}$**,** $\varpi = 9$**,** M**=0.4.**

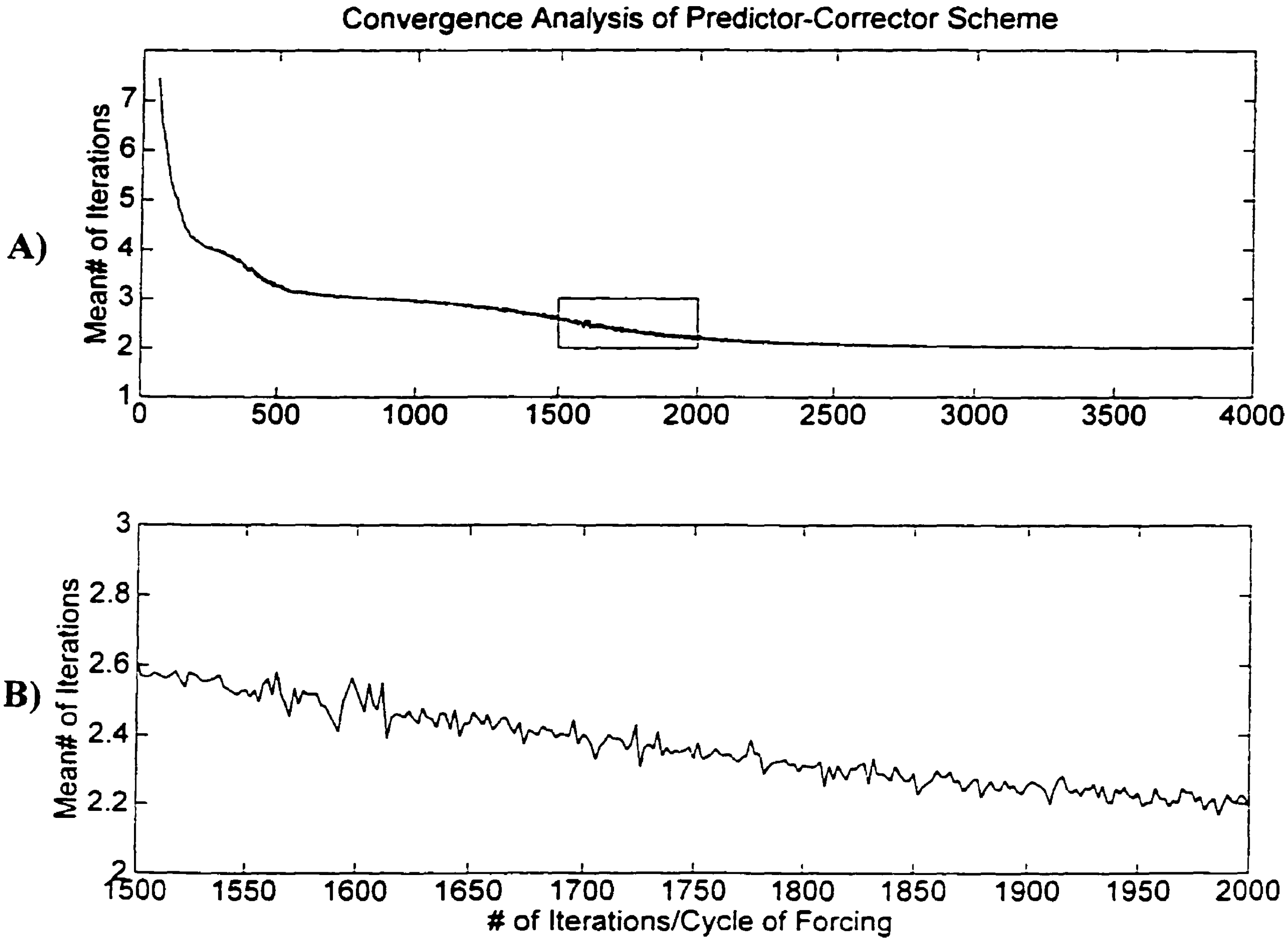

Figure 5.6: Convergence Analysis of Predictor-Corrector Scheme; a) Mean Number of Iterations until Predictor-Corrector Scheme Convergence vs Time-Step Size b) Close-Up: $\alpha_{mean} = 10$ deg, k=0.04, U^*=21, Qo=7x10^{-4}, $\varpi = 9$, M=0.4.

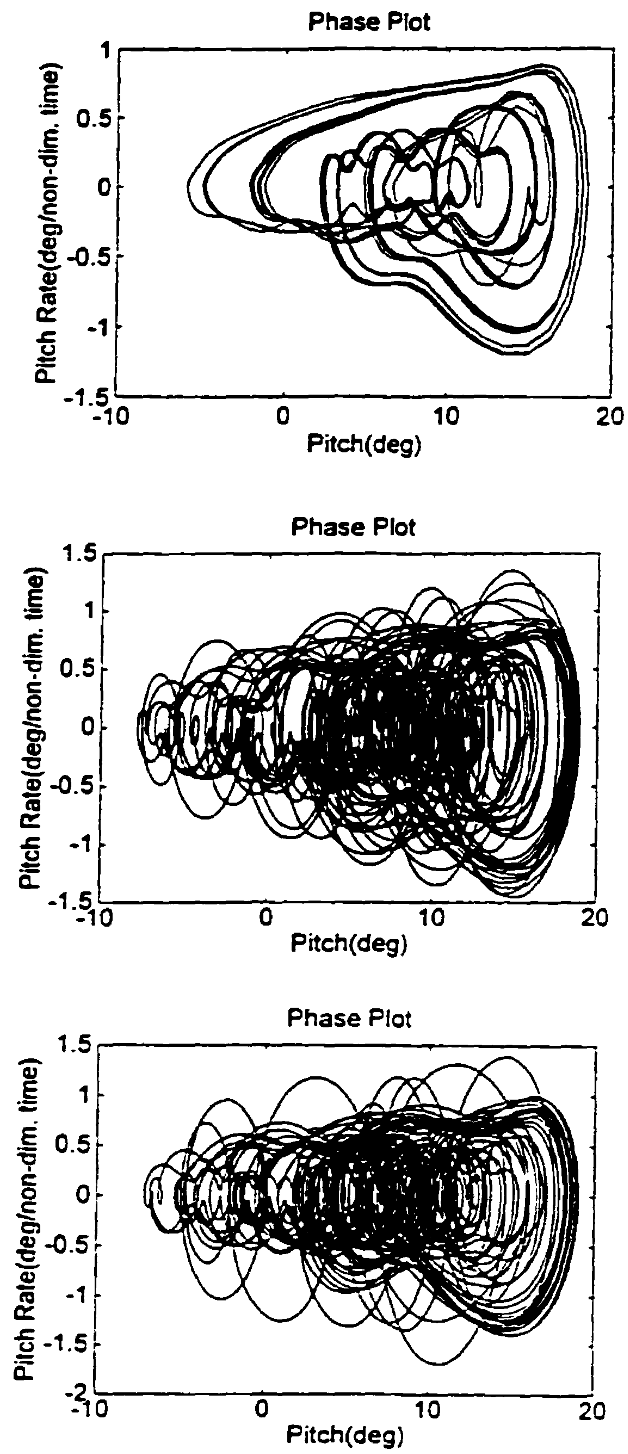

A)

B)

C)

Figure 5.7: Comparison of Pitch Response for Different Time-Step Sizes; Phase Plots: a) 128 iter./cycle b) 256 iter./cycle c) 512 iter./cycle: $\alpha_{mean} = 10$ deg, k=0.04, U^*=21, Qo=7x10^{-4}, $\varpi = 9$, M=0.4.

A)

B)

C)

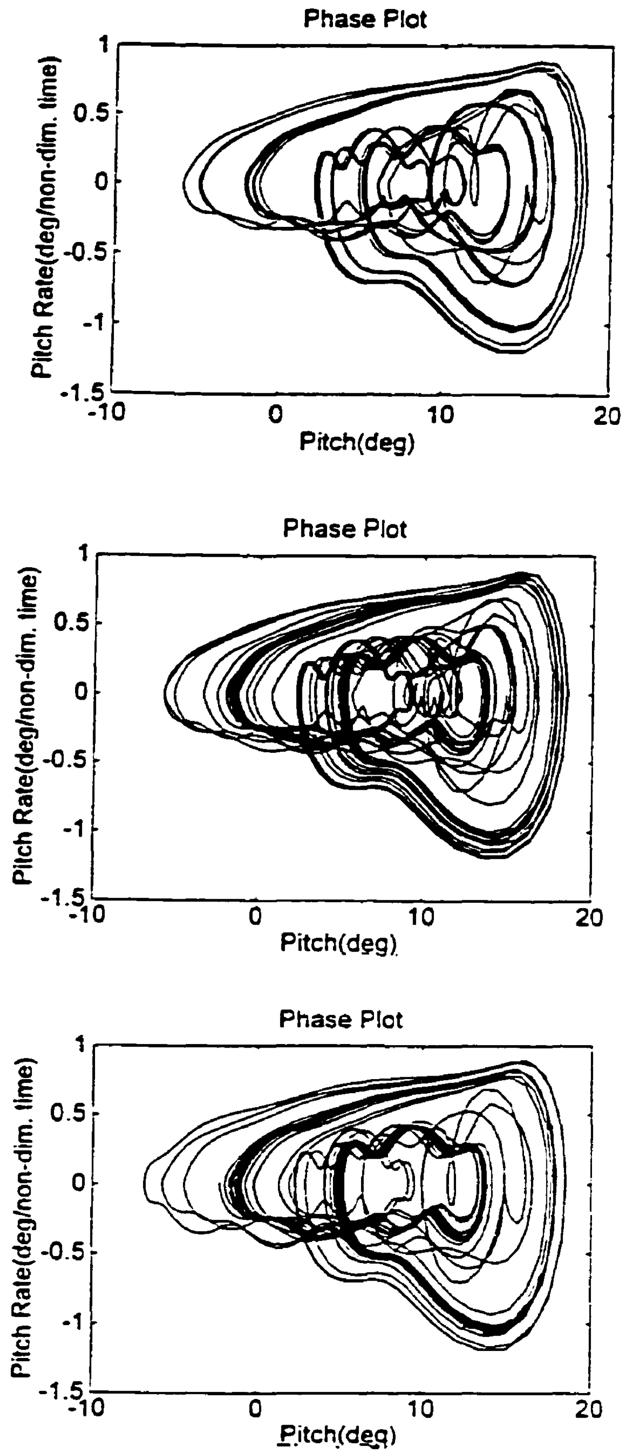

Figure 5.8: Comparison of Pitch Response for Different Values of the Predictor-Corrector Error; Phase Plots: a) P.C.E=1x10^{-6} b) P.C.E=1x10^{-8} c) P.C.E.=1x10^{-10}: $\alpha_{mean} = 10$ deg, k=0.04, U^*=21, Qo=7x10^{-4}, $\varpi = 9$, M=0.4.

Chapter 6

Non-Linear Analysis: The One-Degree -of-Freedom System

6.1 Introduction

Now that the model being used has been explained and scrutinized, it is necessary to analyze the output from this non-linear system. The most important aspect of the output is the possibility of chaos. This shall be the focus of the remainder of the thesis.

This chapter will study the one-degree of freedom system. Bifurcation plots using the amplitude of forcing *Qo* as the control parameter will allow the examination of pre-chaotic and post-chaotic changes of this system as the control parameter is varied. Once chaos is identified it will be verified through the use of the tools described in the first Chapter. The routes to and from each chaotic response will also be identified.

The ultimate objective of the latter part of the thesis is to identify and classify as many different types of motion that this system can produce in a broad range of system parameters. Another objective is to determine the route from which the motion changes from one type to another, as a system parameter is varied. The focus, of course, being chaotic motion and the route thereto. Comparisons with classical cases will be used as much as possible, and physical explanations will be used to explain some of the phenomena whenever possible.

6.2 Choice and Range of System Parameters

The choice and range of system parameters depends on many factors, which include accuracy, faithful representation of physical reality and constraints in computing power. Each choice was made according to experience, and does not necessarily follow a strict pattern.

The first variable that needs to be fixed is the Mach number. A Mach number of 0.4 is used throughout because the majority of data given by Leishman and Beddoes (1986, 1989) are at this Mach number; furthermore, it was this data that was used most extensively to verify the model developed for this thesis (Chapter 3). The elastic axis is chosen at the quarter chord, the center of mass is positioned at one-eighth of the chord in front of the mid point, the non-dimensional radius of gyration was given a value of 0.5, while the airfoil air-mass ratio was set at 100. These values were chosen in accordance with Lee and LeBlanc (1986). The structural damping was set to zero because the aerodynamic damping has been shown to be much larger than the structural damping in real situations; at least for cases below the flutter boundary. Three variables are chosen to be varied; these are: the amplitude of forcing (Qo), the frequency of forcing (k) and the non-dimensional velocity (U^*). Their respective ranges were determined through experience, and by comparing their magnitude with the aerodynamic forcing. The non-dimensional aerodynamic forcing term never surpasses 10^{-2}; therefore the amplitude of forcing was varied in this range. Qo is therefore varied between 0-0.002. The non-dimensional velocity term has no restrictions other than not being able to be equal to zero, however, non-dimensional velocities greater than 35 do not significantly change the response. U^* is therefore varied between 0 and 35. The forcing frequency was chosen to be varied between 0.04 and 0.2, which is no more than double, and no less than half the frequencies used by Leishman and Beddoes (1989).

Once the main variables are chosen the mean angle of attack is set at a value such that throughout the range under study the airfoil always enters the dynamic stall regime. If this is not done the airfoil is allowed to oscillate in its linear region, which defeats the purpose of a non-linear analysis. The last restriction made is that the angle of attack should not exceed 30 degrees and should not be less than -12.5 degrees. The minimum bound is chosen at the static stall angle in the negative direction for a Mach number of 0.4. This is done because the airfoil is not modeled to enter stall in the negative direction. The upper bound is chosen at 30 degrees because, in the model, assumptions were made that the sine of the pitch angle is approximately equal to its value in radians, while the cosine is equal to one. At 30 degrees there is an error of approximately 5% in the sine assumption and 13% in the cosine assumption, and so to maximize accuracy no more error than this should be allowed.

Therefore, the aforementioned ranges shall be used save when the angle restrictions have been surpassed or when there is no useful information past a particular value. The above choice of variables may be summarized as follows:

$$M = 0.4, a_h = -0.5, x_\alpha = 0.25, r_\alpha = 0.5, \mu = 100, \varsigma_\alpha = 0, 0 \le Qo \le 0.002, 0 < U^* \le 35$$
$$0.04 \le k \le 0.2, -12.5^\circ \le \alpha \le 30^\circ$$

Using these values and ignoring the plunge degree of freedom the aeroelastic equations (4-17) and (4-18) reduce to a single aeroelastic equation:

$$\alpha'' + \frac{1}{U^{*2}}\alpha = \frac{2}{\pi \mu r_\alpha^{\ 2}} C_m(s) + Qo(s) \qquad (6\text{-}1)$$

where $Qo(s)=Qo\ sin(ks)$

Equation (6-1) describes the non-linear one-degree of freedom system that will be studied in this chapter.

6.3 Procedure

The following procedure will be used to accomplish the objectives previously discussed

1- A bifurcation plot will be used to describe, in a general way, the behaviour of the system as the amplitude of forcing, Qo, is varied. This plot will use the maximum and minimum values of pitch.

2- The bifurcation plot will be dissected into regions of similar behaviour. Bifurcation points will separate these regions.

3- Each region will be classified according to its attractor on the Poincaré map and identified as periodic, quasi-periodic or chaotic.

4- If the region appears to be chaotic, tools will be used to further indicate whether or not the region is truly chaotic.

5- Once chaos has been established, the route to chaos will be established.

6.4 Physical Analysis Using Preliminary Examples

The analysis of the non-linear response of the system, using the analysis tools explored in the first Chapter, serves to identify the different types of motion that the system can produce (i.e.: periodic, quasi-periodic or chaotic). It does not, however, give any insight into the physical causes of the motion. An examination of the physical reality will shed light on the phenomena at work.

The oscillating airfoil enters different regimes of motion according to the range of angles it is oscillating in and its pitch rate. The most important angles are the static stall angle (for M=0.4 stall occurs at α = 12.5 deg) and the zero spring deflection angle (mean angle of attack). These angles are important because they determine the regions where each category of moment (i.e.: structural, inertial, aerodynamic and externally applied) works for or against one another.

Figure 6.1 shows the pitch response of the airfoil for two cycles (k=0.075, U*=20, Qo=0.0005, $\alpha_{mean} = 10\,\text{deg}$), the vectors correspond to the relative magnitude of the moments due to each category as described by equation (4-7) (i.e.: structural, inertial, aerodynamic and externally applied). These vectors are overlaid onto the pitch response of the airfoil. Figure 6.1(a) illustrates the aerodynamic moment at each point in the airfoil's motion. Most of the contribution of the aerodynamic moment in the linear region (i.e.: a few degrees below the static stall angle) comes from the impulsive loading. When the pitch rate is positive a compression wave is created on the upper surface of the airfoil, while a rarefaction wave is created on the lower. This means that in the linear regime when the pitch rate is positive (the slope of the pitch response is positive) the aerodynamic moment is negative and vice versa. Therefore, when the slope is positive in the linear region the aerodynamic moment is negative and vice versa as may be confirmed in Figure 6.1(a). The largest contribution of the aerodynamic moment comes during dynamic stall, (i.e.: a few degrees above the static stall angle) when the aerodynamic moment is non-linear and has its greatest influence over the other forces. In this regime the moment is negative. It is also important to note that in the linear regime the aerodynamic moment is working against the motion of the airfoil, while in the non-linear regime it is working with the motion of the airfoil. This means, that when the airfoil is oscillating about the static stall angle, for part of the cycle, the airstream is doing positive work and therefore supplying energy into the system. It is therefore possible to sustain a self-excited oscillation around the static-stall angle; this may be a precursor to flutter. Note that in Figure 6.1 all of the vectors **originating** from the pitch curve in the non-linear region represent non-linear moments, while those originating from the linear region represent linear moments.

Figure 6.1(b) illustrates the variation of structural moment with pitch angle. The structural moments work in a simpler fashion than the aerodynamic ones; when the angle is above the mean angle of attack (the line in Figure 6.1(b)) its influence is positive and vice versa. Figure 6.1(c) illustrates the variation of inertial moments, which work as time delays. They simply resist abrupt changes when the airfoil enters different regimes. More specifically, when the pitch acceleration is positive (the pitch response is concave up) this moment is negative, and vice versa. Therefore, when the curve is concave up the inertial moment is negative and vice versa; this may be confirmed in Figure 6.1(c). The inertial moment is at its highest value during dynamic stall, which characterizes the most abrupt change in the airfoil's motion. Figure 6.1(d) illustrates the externally applied moment. The externally applied moment works at its own pre-defined configuration (i.e.: a sine wave).

The above figures illustrate that once the response is known the various components of the system act in predictable ways. However, it is the coupling of the various forces with regards to the response and the non-linear nature of the aerodynamics when oscillating in stall that makes any qualitative attempts at predicting the response impossible. In other words there is a circular relation between the various components of the system and the response; the response of the system depends on the moments supplied from each component which depends on the response and so on. This was the entire reason for the predictor-corrector algorithm discussed in Chapter 5.

One way to try to create some kind of qualitative framework is to study each component separately, thus eliminating the coupling effect. For example, if the airfoil had only structural influences it would oscillate at its natural frequency $k=1/U^*$. If only the externally applied moment influenced it, it would oscillate at the externally applied frequency (k). The next example, illustrated in Figure 6.3, shows the system without the influence of structural or external forces (structural forces are very weak). This means that the system is simply a balance between inertial and aerodynamic forces. It may be described by the following equation:

$$\alpha''=\frac{2}{\pi\mu r_\alpha^{\,2}}Cm(s) \tag{6-2}$$

As can be seen in Figure 6.3, in this configuration the system is periodic of period two, with the main frequencies being 0.049 and 0.098 with a super-harmonic of 0.147, which is the addition of the first two frequencies. The most important conclusion from this example is that it is a self-excited oscillation. The possibility of this was examined earlier. Now, since there is no externally applied moment, the energy is supplied exclusively by the aerodynamics. Once again, the fact that it is oscillating in and out of stall, is necessary. Examples, with no external forcing, not oscillating about the static stall angle, cannot sustain a self-excited oscillation. Figure 6.2 shows a bifurcation plot with the non-dimensional velocity U^* as the control parameter. No external forcing is used. As can be seen, by not allowing the airfoil to oscillate in and out of stall (this is done by increasing the structural stiffness, which is accomplished by lowering the value of U^*), the aerodynamics supplies positive damping and the airfoil reaches an equilibrium point. By weakening the structural stiffness (increasing the value of U^*) the airfoil is allowed to oscillate at greater angles of attack, and, as can be seen, only when it is allowed to oscillate about the static stall angle can a self-excited oscillation take place. The reasons for this were discussed previously with Figure 6.1(a).

Dividing the system into its component forces gives insight into frequencies that are characteristic of the system. Although the various elements are highly coupled, the natural frequency of the system, the externally applied frequency and the frequencies discovered in Figure 6.3(c) recur many times as large peaks in the frequency spectrum in the responses that will be studied in this chapter. If these frequencies are not present, the frequencies of the response are always at least in proximity. This means that although it is impossible to predict the frequencies of the responses by some linear combination of the frequencies of the separate components, it is possible to determine a bound in which the frequencies will be found.

6.5 Case I

The first case that will be studied is characterized by the following parameters, k=0.088, U^*=23, $\alpha_{mean} = 5\,deg$, $0<Qo<0.001$. The structural natural frequency of this system is k=0.043, and the ratio of forcing to natural frequency is 2.0. This case represents a case of low structural stiffness relative to the other cases that will be studied. The bifurcation plot, seen in Figure 6.4(a), can be separated into five regions according to the qualitative features of the plot. A conceptual drawing of these five regions is given in

Figure 6.4(b), and the bifurcation points separating these regions are: 1) separating regions 1 and 2, $Qo=1.7x10^{-4}$, 2) separating regions 2 and 3, $Qo=3.83x10^{-4}$, 3) separating regions 3 and 4, $Qo=6.23x10^{-4}$, 4) separating regions 4 and 5, $Qo=7.4x10^{-4}$. Each region has its own characteristic attractor. The time history and frequency spectrum are computed using 50 cycles of forcing after 200 initial cycles, which are ignored so that there is no effect from transients. According to the frequency spectrum error defined in the first chapter (forcing frequency (*k)* / (# of cycles sampled)), the error in the frequency is +/-0.00176. When exact values of frequency are required, 200 cycles are sampled, thus reducing the error to +/-0.00044.

Region 1

This region is characterized by a quasi-periodic attractor, which has already undergone a breakdown towards a chaotic attractor. The first example ($Qo=5x10^{-5}$), which lies very near the beginning of this region, shows an almost periodic solution, whose amplitude is not constant throughout the airfoil's motion. The airfoil's motion does, however, reside within a region in the phase space with well-defined boundaries (Figure 6.5(a)). Limited or narrow-band chaos is present. This can be seen as limited broadening of the main frequencies in the spectrum (Figure 6.5(b)); the two main frequencies are $k=0.088$ and $k=0.099$. The Poincaré map shows a quasi-periodic attractor, which has already experienced some breakdown towards a chaotic attractor, via the quasi-periodic route (Figure 6.5(c)). This route is similar to the torus breakdown in the peroxidase-oxidase reaction illustrated in Figure 6.6, which is an example of a system that reaches chaos via the quasi-periodic route. Figure 6.5(c) resembles Figure 6.6(d), meaning that it is near the end of the quasi-periodic route towards chaos. In fact the next example studied in this region is chaotic.

Figure 6.7 shows the airfoil motion near the end of the first region (Qo=1.2333x10^{-4}). As can be seen, there are two main frequencies, k=0.042 and k=0.088, and make the motion almost period two (Figure 6.7(b)). Although, within the error of the frequency spectrum, this may primarily be a periodic solution, the Poincaré map shows a closed loop, which proves that the main frequencies are indeed incomensurate. The frequency spectrum of Figure 6.7(b) shows that a broad band of frequencies around k=0.04, (near the natural frequency) dominates the spectrum. The attractor, shown in Figure 6.7(c) indicates chaos.

To further test whether or not this is truly chaos a measure of the Lyapunov exponent, as seen in Figure 6.8(a), is calculated. This figure shows the separation of two initially neighbouring plots on the phase-plane as a function of non-dimensional time. The variable d is defined in the first chapter where the Lyapunov exponent is explained. As can be seen by this figure, a separation of initial conditions, d_o, of only 10^{-6} on the phase plane, separates within 1500 units of time to a difference, d, of 10^{+1}, which is the size of the attractor in the phase plane. The slope of this graph (Figure 6.8(a)) is an approximation of the Lyapunov exponent. For a more accurate measure of the Lyapunov exponent, the slope would have to be found starting from many different points on the phase-plane and averaged. This divergence between neighbouring plots can be seen more clearly in Figure 6.8(b). These plots show that the response is extremely sensitive to initial conditions and suggests a positive Lyapunov exponent. The final suggestion of chaos is the presence of fractal geometry in the Poincaré map, this is demonstrated in

Figure 6.9. In this figure one clearly sees complex patterns at two levels of magnification.This response therefore satisfies all of the aforementioned criteria of chaos, and is the first example of a response where chaos dominates.

Finally at the end of this region there is a periodic window (Qo=1.7x10^{-4}). Figure 6.10 shows an almost perfect periodic solution of period one and frequency k=0.088 (the externally applied frequency). This same frequency resides in the previous examples. This event has interrupted the route towards chaos.

Region 2

Region 2 seems to continue where Region 1 left off. The first example, which lies near the beginning of region 2 (Qo=2x10^{-4}), seems to be continuing the trend of quasi-periodic breakdown of Region 1. The attractor on the Poincaré map of Figure 6.11(b), looks almost identical to that of Figure 6.7(c). There is, however, a very distinct difference. Upon inspection of the long term behaviour (Figure 6.11(c)) one sees that for the first 5000 cycles of forcing the airfoil is in a periodic regime, which suddenly changes to a seemingly chaotic regime. This suggests that, on route to chaos, the second mechanism of intermittent transition, may be dominating the second region.

Figure 6.12 seems to show the first example of strong chaos. There is no repeatable pattern in the time history (6.12 (a)), the phase plane is filling (6.12 (b)), there is a broadband character in the frequency spectrum (Figure 6.12(c)), the attractor on the Poincaré map (Figure 6.12(d)) looks like a strange attractor, and there are no prolonged bursts of a stable periodic motion (Figure 6.12(e)). Once again, to try to show that chaos is present the same procedure of determining the sensitivity to initial conditions is undertaken, as for the response of Figure 6.7. This can be seen in Figure 6.13.Once again a positive slope in Figure 6.13(a) suggests a positive Lyapunov exponent, and fractal geometry is present at two levels of magnification (Figure 6.14). This response therefore satisfies all of the aforementioned criteria of chaos.

The last example in this region (Qo=3.8333x10^{-4}) shows how the chaotic attractor changes to an almost periodic attractor of period two (k=0.044, 0.088). Again, as can be seen in the time history of Figure 6.15(a), there are intermittent bursts of chaos from a period two oscillation, once again suggesting an intermittent transition. The attractor shown in Figure 6.15(c) shows vestiges of the chaotic attractor of the previous example (Figure 6.12(d)), but as can be seen in the long term behaviour (Figure 6.15(d)) the scatter has become more concentrated around two darker bands, which confirms a period two oscillation with intermittent bursts of chaos. This intermittent behaviour, however, varies from the previous case of intermittent behaviour (Figure 6.11(d)), because in this case there is no significant time period for which the period two oscillation is stable, whereas in the previous case the periodic oscillation was stable for 5000 cycles of forcing.

Region 3

This region is characterized by a period-2 oscillation with narrow-band chaos, which begins to destabilize and culminates in the creation of an almost stable period-4 oscillation in region four.

The first example (Qo=4.3667x10^{-4}) presented in Figure 6.16 shows an almost stable period-2 oscillation (k=0.044, 0.088), the frequency spectrum of Figure 6.16(b) confirms this. The Poincaré map of Figure 6.16(c) does show some chaotic behaviour, where, rather than showing two distinct points, which characterize a period-2 oscillation, it shows two distinct curves. This simply confirms the presence of narrow-band chaos.

The last two examples (Qo=5.4x10^{-4} (not shown), Qo=6.2333x10^{-4}) in this region simply continue this trend. Figure 6.17 (the last example), once again, shows an almost stable period two oscillation. However the variability in the amplitude has increased. Figure 6.17(c) shows even larger curves with more interesting fractal geometry. The last examples in this region show the growing emergence of two new frequencies. Along with the two main frequencies of k=0.044 and k=0.088, frequencies of k=0.022 and k=0.066 (Figure 6.17(b)) are emerging which will culminate in a period doubling bifurcation in region 4.

Note, Examples that are not shown were examples that were explored but that were too similar to a neighbouring example to be shown. They are mentioned because they are often used to determine a trend (e.g.: growing emergence of new frequencies).

Region 4

In Region 4 the system experiences a period-doubling bifurcation. The first two examples (Qo=6.5x10^{-4}, Qo=7.0333x10^{-4}), the second of which is shown in Figure 6.18, show the creation of an almost perfect period four oscillation at the frequencies, k=0.022, 0.044, 0.066, 0.088 (k=0.088 is the forcing frequency). The Poincaré map of 6.18(c), shows how the two fractal curves on the Poincaré map, of the period two oscillations, breakup into four fractal curves. Again narrow-band chaos is present.

The last example from this region (*Qo*=7.3667x10^{-4}) shows how the period four oscillation starts to degrade back to a period two oscillation very similar to that for region 2. The frequencies of k=0.022 and k=0.066 begin to disappear (Fig 6.19(b)), and the four curves on the Poincaré map merge once again to create two fractal curves (Fig 6.19(c)). This is an example of an incomplete period-doubling route to chaos. An example of incomplete period-doubling are the Feigenbaum trees, which are illustrated in Figure 6.20.

Region 5

This last region creates an almost perfect period two oscillation. The two curves of the Poincaré map shrink towards two distinct points, to make a period two oscillation of the same frequencies of that in region 2 (Figures 6.21, 6.22). This change can be seen on the Poincaré maps of three examples (*Qo*=7.7333x10^{-4}, *Qo*=9.0333x10^{-4}, *Qo*=7.3667x10^{-4}) (Figure 6.21,6.22(c)). As *Qo* is increased past that shown on the bifurcation plot, no new bifurcations occur and the system remains at this configuration. The final response can be seen in Figure 6.22. The main frequencies, once again, are k=0.044, 0.088 (Figure 6.22(b)).

Summary

For Case I, more than one route towards and away from chaos is present as the control parameter *Qo* is varied. The first region represents an example of the quasi-periodic route. The second represents an intermittence route, while the third, fourth and fifth represent incomplete period-doubling. There were no typical routes, it was often a combination. Chaos is almost always present in a narrow-band form. There were only a few cases of strong chaos, and it was for these cases that further tests were used to indicate chaos. Frequencies that appeared in the frequency spectra were always near the natural frequency or the forcing frequency. Coincidentally the natural frequency and forcing frequency were very close in value to the frequencies found when the airfoil was oscillating under the influence of aerodynamic and inertial forces only, as discussed in section 6.4.

6.6 Case II

The second case is characterized by the following system parameters: k=0.15, U^*=13.5, $\alpha_{mean} = 5\,\deg$, 0<Qo<0.001. The structural natural frequency of this system is k=0.074, and the ratio of forcing to natural frequency is 2.0. This is the same ratio as the first case. Although the first case has a higher value of U^* it has a lower value of k, thus maintaining the same ratio. This case represents a case of high structural stiffness relative to the other cases (i.e.: U* is low relative to the other cases). The bifurcation plot, seen in Figure 6.23(a), can be separated into four regions, according to the qualitative features of the plot. These four regions can be seen in the conceptual drawing of Figure 6.23(b), and the bifurcation points separating these regions are: 1) separating regions 1 and 2, Qo=2.5x10^{-4}, 2) separating regions 2 and 3, Qo=4.3x10^{-4}, 3) separating regions 3 and 4, Qo=6.7x10^{-4}. The frequency spectrum error in this case is +/-0.003. Once again when exact values of frequencies are required 200 cycles were sampled to reduce the error to +/-0.00075.

Region 1

The first region is characterized by a quasi-periodic attractor, which unravels via a quasi-periodic route towards a chaotic attractor. Figure 6.24 shows the time history and the phase-plane of the response at Qo=0. As can be seen, for the most part, the solution is periodic, and since there is no forcing term it is an example of a self-excited oscillation. There is also a single burst of non-periodic motion. As mentioned in the discussion of self-excited oscillations in section 6.4, the oscillation should be about the stall angle. Looking at the time history confirms this fact. Upon inspection of the frequency spectrum of Figure 6.24(c), besides the large spike at k=0.1 there are other spikes, most of which lie near zero. This simply reflects the fact that the burst is seen only once among the many cycles that are sampled in the time-history plot, the frequency of this burst is therefore naturally near zero. When looking at the Poincaré map of Figure 6.24(d), one sees that it resembles the phase-plane. This underlies the problem of using a Poincaré map when the forcing amplitude is zero. The Poincaré map uses the forcing frequency to sample the data. When forcing is present (i.e.: non-zero amplitude) this frequency is also present in the frequency spectrum of the response. When forcing is not present, chances are that the forcing frequency (which is technically meaningless with zero forcing amplitude) is not present in the response. This makes the Poincaré map meaningless. It resembles the phase-plane because the map encounters every different point that makes up the cycle of the response. The long-term behaviour (Figure 6.24(e)) shows that the burst that is seen in the time history does not last past a few thousand cycles and may therefore be considered transient chaos. This means that the response becomes periodic after a few thousand cycles. The Poincaré map, indicates quasi-periodicity (closed loop), in contrast to the other plots. This result is meaningless for the reasons mentioned before. The case of Qo=0 will therefore not be studied for the remainder of the cases.

The second example in this region ($Qo=7\times10^{-5}$) is much easier to classify. We see that in this case, the misleading conclusion of quasi-periodicity of the previous example is no longer misleading. This is because the forcing frequency of k=0.15 is a component of the response, as can be seen from the small spike at this frequency in the frequency spectrum of Figure 6.25(b). As can be seen by the Poincaré map of Figure 6.25(c), it is a quasi-periodic attractor which has already undergone unraveling towards a chaotic attractor. Looking at the Fourier Spectrum of Figure 6.25(b), the forcing frequency is present, and the low frequency end has a broad-band character introducing chaos via the quasi-periodic route. This quasi-periodic route is qualitatively different from the previous case: it is not like the peroxidase-oxidase reaction, illustrated in Figure 6.6, it is more like the quasi-periodic transition of the Rayleigh-Bénard thermal convection system, illustrated in Figure 6.26.

The last two examples ($Qo=1.4\times10^{-4}$ (not shown), $Qo=2.1\times10^{-4}$) continue the trend towards a chaotic attractor, which culminates in the attractor seen in Figure 6.27(c). The last example in this region (Figure 6.27) may be considered chaotic, and must be further studied. The attractor (Figure 6.27(c)) shows the same type of folding at the top of the broken torus as in Figure 6.26(b), which further points out the similarities between this case and the Rayleigh-Bénard thermal convection system. Figure 6.27 shows that this is indeed chaotic. Again, the time history is unpredictable, the frequency spectrum has a broad-band character, the Poincaré plot reveals a strange attractor, there is a sensitivity to initial conditions and hence indications of a positive Lyapunov exponent (Figure 6.28) as well as fractal geometry (Figure 6.29).

Region 2

The second region has been differentiated from the first region because, instead of continuing the trend established in the first region, a window of more stable, almost periodic, motion appears, and a new intermittence route to chaos is introduced.

The first example in this region (Qo=2.8x10^{-4}) is very interesting because it represents a stable periodic solution with nine individual frequencies in the frequency spectrum (Figure 6.30)! The Poincaré section and long term behaviour (Figure 6.30 (d), and (e)) show that this period nine oscillation is stable for almost the entire 30 000 cycles. Intermittent bursts of chaos are present.

The second and third (last) examples (Qo=3.5x10^{-4}, Qo=4.2x10^{-4}) show how through an intermittence route, the response becomes chaotic Figure (6.31). The last example shows all of the characteristics of chaos. It does, however, have a window of stability in the long term behaviour (Figure 6.31(c)). The first example of the third region shows the fully chaotic response.

The intermittence behaviour in this region show relaminarization channels in the first and second return maps. These channels in the return maps are indicators of intermittency in many classical examples. Figure 6.32 shows the first and second return maps of the pitch responses in this region, relaminarization channels in these maps can clearly be seen below the identity line.

Region 3

This region begins with an excellent example of chaos (*Qo*=4.9x10^{-4}), which was created through the intermittence route described in region 2. This example is illustrated in Figure 6.33 Further investigation of this chaos is done, as in the previous case, seen in Figures 6.34 and 6.35. All the criteria of chaos are satisfied.

The last two examples in this region (*Qo*=5.6x10^{-4}, *Qo*=6.3x10^{-4}) show the unraveling of the chaotic attractor via an intermittence route. This intermittence nature is best identified in the long-term behaviour of Figures 6.36(c) and 6.37(c). The effects of this intermittence transition away from chaos on the Fourier spectrum may be seen in Figure 6.38. The broad-band of frequencies near zero become less strong as *Qo* is increased.

Region 4

The unraveling continues in the first example of this region (*Qo*=7x10^{-4}), as can be seen by the Poincaré map of Figure 6.39(b). The stable oscillation now dominates the long-term behaviour, seen in Figure 6.39(c).

The second example (*Qo*=7.7x10^{-4}) shows a stable oscillation of period three. Figure 6.40 shows the most perfect example of a stable periodic solution thus far. It is unusual to find such a stable solution surrounded by chaos. It is stable for all 30000 cycles (Figure 6.40(e)) and represents three concise dots on the Poincaré map (Figure 6.40(d)). The route taken to this periodic solution is difficult to identify, it seems to be a periodic window.

Similar periodic windows appear until the end of this region. Three more examples are studied in this region (Qo=8.4x10^{-4}, Qo=9.1x10^{-4}, Qo=9.8x10^{-4}). Either a perfect period three oscillation (Qo=7.7x10^{-4}, 9.1x10^{-4}: Figures 6.40, 6.41(b)) or an attractor with intermittent chaos (Qo=7x10^{-4}, 8.4x10^{-4}, 9.8x10^{-4}: Figures 6.39,6.41(a),6.41(c)) characterizes this region.

Summary

This case, unlike the previous one, shows no clear period-doubling bifurcations. It is dominated, for the most part, by an intermittence mechanism, which can be compared to classical cases due to the presence of a relaminarization channel in the return maps. Besides this, a quasi-periodic route is taken in the first region similar to that observed in the first case. This quasi-periodic route is qualitatively different from the quasi-periodic route in the first case and resembles the Rayleigh-Bénard system. Another interesting feature of this case is the appearance of stable periodic oscillations with many constituent frequencies. As many as nine individual frequencies were found in one example.

6.7 Case III

The third case was chosen with similar parameters to the first case. It will therefore be compared and contrasted with that case. This case is characterized by the following system parameters, k=0.1, U^*=20, $\alpha_{mean} = 5\,deg$, 0<Qo<0.001. The natural frequency of this system is k=0.05 and the ratio of forcing to natural frequency is 2.0. The bifurcation plot, seen in Figure 6.42 can be separated into five regions according to the qualitative features of the plot. A conceptual drawing of these five regions can be seen in

Figure 6.42(b), and the bifurcation points separating these regions are: 1) separating regions 1 and 2, Qo=4x10^{-4}, 2) separating regions 2 and 3, Qo=6x10^{-4}, 3) separating regions 3 and 4, Qo=6.933x10^{-4}, 4) separating regions 4 and 5, Qo=8.233x10^{-4}. The frequency spectrum error is +/-0.002 or +/-0.0005 when 200 cycles are sampled.

Region 1

As in the other cases the first region is characterized by a quasi-periodic attractor, which has already undergone a breakdown towards a chaotic attractor. Figure 6.43 lies near the beginning of this region (Qo=1x10^{-4}) and shows what seems to be a chaotic response. The Fourier spectrum of Figure 6.43(b) further indicates chaos by its broad-band nature. The Poincaré map (Figure 6.43(c)) shows a chaotic attractor, which is similar to the chaotic attractor found in the second example of the first region of the first case (Figure 6.7). In other words it is a quasi-periodic attractor that has undergone substantial breakdown towards a chaotic attractor. It is reasonable that the first region of the third case be similar to the first region of the first case. This is because the effects of the externally applied moment are low in this region (low amplitude in Region 1) and the remaining parameters such as the natural frequencies in both cases are near to each other (Case I, k=0.043; Case III, k=0.05).

The second example in this region (Qo=1.9x10^{-4}) continues the quasi-periodic route to chaos, very much like in the first case. In this region, however, the chaos that is present is intermittent in nature. This can be seen clearly in the long-term behaviour of Figure 6.44(c). Similar to the previous example there is a broad-band of frequencies near k=0.05, and a strong peak at k=0.1 (Figure 6.44(a)). This example is very similar to the first example of the second region of the first case (Figures 6.11). Again, it makes sense that the two examples are similar, as they have similar parameters. The similarities between the responses in the two cases decrease as the forcing amplitude is increased.

The last example in this region (Qo=3.7x10^{-4}) is the first good example of chaos. The time history is unpredictable, the frequency spectrum is broad-band in nature, while the Poincaré section reveals a chaotic attractor (Figure 6.45). The extra tests were performed similarly to the other cases and further indicated chaos (not shown).

Region 2

This region begins approximately where the third region of the first case begins. The reason why the boundaries of the regions in this case do not coincide to those of the first case is due to the lack of a periodic window in the first region in this case. The first region was therefore not split into two separate ones as in the first case. Once again there are similarities between the cases. This region, as for the third region of the first case, is characterized by a period two oscillation with narrow-band chaos, which begins to disappear and culminates in the creation of an almost stable period four oscillation.

Three examples are studied in this region: (Qo=4.3x10^{-4}, Qo=5.3x10^{-4}, Qo=5.77x10^{-4}). The narrow-band chaos present in the first example slowly disappears to create a more stable, mainly period-two oscillation, as can be seen on the phase plots in this region (Figure 6.46). The narrow-band of frequencies around k=0.05 become less pronounced (Figure 6.47). The Poincaré sections transform into two solid curves attached by a dashed curve (Figure 6.48). These are the same events that characterize region 3 of the first case. However the two curves, which indicate a period-2 oscillation with narrow band chaos, look different in this case. In this region these two fractal curves are connected by less pronounced curves, indicating that the narrow-band chaos in this region is stronger than in its counterpart of the first case. The differences between the cases are starting to become more significant.

Region 3

In Region 3 the system experiences two incomplete period-doubling bifurcations. Its counterpart in region 4 of the first case only experiences one. The first example (Qo=6.3x10^{-4}) of Figure 6.49 shows the creation of an almost perfect period 4 oscillation at the frequencies, k=0.025, 0.05, 0.075, 0.1. This is double the number of frequencies than for the previous example. This example is very similar to the second example of Region 4 in the first case, which has an almost perfect period four oscillation at the frequencies k=0.022, 0.044, 0.066, 0.088 (Figure 6.18). In both cases these frequencies are multiples of the forcing and natural frequencies of the respective cases. The Poincaré map of 6.49(c) shows how the two fractal curves of the period two oscillation, present in the previous region, breakup into four curves. Again narrow-band chaos is present and more so than its counterpart in case I.

In the first case the four curves become smaller, almost forming four points for the almost perfect period four oscillation of Figure 6.18. The last example from this region (Qo=6.7x10^{-4}) shows how the period four oscillation begins another period-doubling bifurcation. This bifurcation is incomplete, however. The incomplete period-doubling can be seen in the third region of the bifurcation plot and conceptual drawing of Figure 6.42. The phase-plane shows the beginning of a period-doubling bifurcation

(Figure 6.50(a)), the Poincaré map of Figure 6.50(c) shows the creation of twice as many fractal curves as the previous example. The frequency spectrum shows new peaks at k=0.0125, 0.0375, 0.0625, 0.0875, which is in addition to the frequencies of k=0.025, 0.05, 0.075, 0.1, the frequencies of the period four oscillation (Figure 6.50(b)). These new frequencies appear symmetrically around the frequencies of k=0.025 and 0.075 at +/- 0.0125 of these frequencies (all the frequencies are multiples of 0.00125).

Region 4

Two examples are studied in this region (Qo=7.3x10^{-4}, Qo=7.7x10^{-4}). This region returns to the period four oscillation of region 3 but has weaker narrow-band chaos and the four curves shrink, creating an almost perfect period four oscillation. This trend can be seen in Figure 6.51.

Region 5

Two examples are studied in this region (Qo=8.8x10^{-4}, Qo=9.9x10^{-4}). This region, similar to region 5 of case I, returns to an almost stable period-two oscillation. This trend can be seen in Figure 6.52. The last example of this region is a very interesting example of a periodic solution with narrow-band chaos. Upon inspection of the fractal geometry of the attractor, one may find in this example a great complexity as seen in Figure 6.53. This type of intricate fractal geometry is not present in the first case.

Summary

More than one route towards and away from chaos is present. The first region represents an example of the quasi-periodic route. The second represents an intermittence route, while the third represents incomplete period doubling. There were no typical routes, it was often a combination. This case was very similar to the first case, having similar routes to and from chaos and similar attractors on the Poincaré map. Some notable differences were present, however. No periodic windows were present in this case. On the bifurcation plot (Figure 6.42(a)) there is apparently a periodic window at the end of Region 2 at (Qo=0.000577), but this is simply an example of the bifurcation plot sampling the solution in the stable region of an intermittently chaotic response. The incomplete period-doubling cascade took an extra period-doubling bifurcation, ending up with a period-8 oscillation before returning back to the final period two oscillation. The attractors were similar for the two cases but become more dissimilar as Qo was increased. The difference was most pronounced in the last example, which showed very complex fractal geometry not present in the first case.

6.8 Case IV

The fourth and last case studied is similar to the second case, and is characterized by the following system parameters, k=0.15, U^*=15, $\alpha_{mean} = 6$ deg, $0<Qo<0.001$. The natural frequency of this system is k=0.067 and the ratio of forcing to natural frequency is 2.25. In fact the only difference between case IV and case II is that U^*=15 not 13.5. The bifurcation plot, seen in Figure 6.54, can be separated into six distinct regions according to the qualitative features of the plot. These six regions can be seen in figure 6.54(b), and the bifurcation points separating these regions are: 1) separating regions 1 and 2, *Qo*=3.4×10^{-4}, 2) separating regions 2 and 3, *Qo*=6.466×10^{-4}, 3) separating regions 3 and 4, *Qo*=9.33×10^{-4}2) separating regions 4 and 5, *Qo*=1.346×10^{-4}, 3) separating regions 5 and 6, *Qo*=1.64×10^{-4}. More regions are chosen in this case than in any other because the bifurcations continue past *Qo*=0.001, which does not happen in the other cases. The frequency spectrum error is +/-0.003 or +/-0.00075 when 200 cycles are sampled.

Region 1

Once again the first region is characterized by a quasi-periodic attractor, which unravels itself via the quasi-periodic route towards a chaotic attractor. The first example in this region (*Qo*=1×10^{-4}) lies near the same point as the second example of the first region in the second case. The attractors on the Poincaré map are very similar, this can be seen by comparing Figure 6.25 and Figure 6.55. The attractor reveals a quasi-periodic response, already unraveling towards a chaotic attractor (Figure 6.55).

The second example (*Qo*=2.5×10^{-4}) shows a continuation of the quasi-periodic route towards chaos (Figure 6.56). The only major difference between this and the first example is that, among the broad-band of frequencies in the frequency spectrum, two frequencies stand out more, these are k=0.045 and k=0.15 (Figure 6.56(b)).

The last example (*Qo*=3.3×10^{-4}) in this region reveals exactly the same event which caused the separation of the first two regions of the second case (Figure 6.57), this being a periodic window. This periodic window is very similar to that of the second case (Figure 6.30). The attractors of Figures 6.30(d) and Figure 6.57(d) are similar. The main difference being that instead of having nine main frequencies, in this case there are only four (Figure 6.57(b)). Once again this periodic window introduces an intermittence route towards the chaotic attractor, that will be found in the second region

Region 2

As in the second case, the second region has been differentiated from the first region because, instead of continuing the trend established in the first region, a window of more stable, almost periodic, motion appears and a new intermittence route to chaos is introduced. This intermittence route continues until the end of the bifurcation plot but is interrupted by periodic windows. Once again the similarities between this case and the second one become less as *Qo* is increased. In the second case relaminarization channels were revealed in the first and second return maps (Figure 6.32). In this case relaminarization channels are also present, however, in this case they are present only in the first return maps and bear a remarkable resemblance to a classical case of a type I intermittence transition towards chaos. This will be shown later.

The first example in this region (Qo=3.3x10^{-4}) is the first example, for this case, of strong chaos. The top right portion of its attractor in Figure 6.58(c) resembles the attractor of the first example of the third region of the second case (Figure 6.33). Once again the extra tests further indicate chaos (not shown).

The last example in this region (Qo=6.4x10^{-4}) shows another similar chaotic attractor, (Figure 6.59). This case is less chaotic than the previous one. As can be seen from the frequency spectrum (Figure 6.59(a)), three main frequencies have emerged, which are revealed in the long term behaviour as three darker bands (Figure 6.59(c)). The intermittence behaviour in this region reveals relaminarization channels in the first maps.

These channels, along with others in this case, will later be shown to resemble a classical example of type I intermittency.

Region 3

This region begins with one of the few examples of a perfectly stable periodic response (Qo=7.3x10^{-4}) with a period three oscillation of frequencies k=0.05,0.1, 0.15 (Figure 6.60(b)). This oscillation is stable for all 30 000 cycles and appears as three distinct points on the Poincaré map (Figure 6.60(c)).

The last example of this region (Qo=8.5x10^{-4}) reveals another chaotic attractor, similar to the ones in region 2 (Figure 6.60(e)). Once again a relaminarization channel is revealed in the first return map, which will later be compared to a classical example.

Region 4

The similarities between this case and the second case end in this region. This region actually coincides with the end of the bifurcation plot of the second case.

The example from this region (Qo=1x10^{-3}) reveals a periodic solution as shown by the time history and frequency plot (Figure 6.61(a)). However, the amplitude of this period one oscillation is not constant throughout all 30000 cycles. A myriad of points on the Poincaré map further indicates this (Figure 6.61(c)).

Region 5

This region begins with a chaotic attractor shown in Figure 6.62 (Qo=1.35x10^{-3}). There are two main frequencies: k=0.075 and k=0.15, on the frequency spectrum (Figure

6.62(b)). This implies a period-doubling bifurcation, since the previous example from the previous region had only one main frequency. In fact, there is also the emergence of two new frequencies: k=0.03 and 0.045, which are present as smaller spikes on the Fourier spectrum, implying the beginning of another period doubling bifurcation. As can be seen by the Poincaré map (Figure 6.62(c)), this chaotic attractor is simply two fractal curves, which implies that the chaos is narrow-band.

The last example of this region shows the emergence of an almost stable period four oscillation, and is shown in Figure 6.63 ($Qo=1.5\times10^{-3}$). The Poincaré map (Figure 6.63(c)) shows four small curves. This period-doubling route is incomplete, because the next region reveals an almost stable period two oscillation with narrow-band chaos.

Region 6

The last example of this case ($Qo=1.88\times10^{-3}$) reveals a period-two oscillation at frequencies k=0.075 and k=0.15 (Figure 6.64(b)), which are the two main frequencies of the chaotic attractor of region five.

Comparison to Type I Intermittent Transition

Figure 6.65 shows the first return maps of the chaotic attractors found starting in region two and ending in region five (Region 2, Example 3: $Qo=6.4\times10^{-4}$, Region 3, Example 2: $Qo=8.5\times10^{-4}$, Region 5, Example 1: $Qo=1.35\times10^{-3}$). These are compared to the classical example of the type I transition shown in Figure 6.65(a),(b),(c). As can be seen the trend is identical except for the fact that the curves lie above the identity line in the classical example rather than below. This fact has no bearing on the theory behind relaminarization channels, and is a compelling proof that the intermittence route to chaos in this case is of Type I.

Summary

This case is very similar to the second case, regardless of the fact that the bifurcation plots are dissimilar. The first three regions followed the identical route as in case II. The attractors even resembled each other. As in case II, a quasi-periodic route began for low *Qo*, was interrupted by a periodic window which then introduced an intermittence route. The difference in case IV, compared with cae II, was the appearance of an incomplete period-doubling route for *Qo*>0.001. Relaminarization channels were present, but only the first return map. These channels indicated an intermittent transition of type I.

6.9 Effects of Changing Initial Conditions and Basins of Attraction

A basin of attraction is the range of initial conditions for which the motion of a system, in this case the airfoil, tends towards an attractor. Every response that was studied in this thesis had the initial conditions of $\alpha_o = \alpha_{mean}, \alpha_o' = 0$. Hence, it is possible that there exist competing attractors that will attract other responses beginning with different initial conditions. It is therefore necessary to determine the size and boundaries of the basins of attraction of chaotic attractors found in each case. One example of chaos was chosen from each case. Figures 6.66 reveals the attractors found when starting from several different initial conditions. A grid of initial conditions was studied. A total of

1600 different initial conditions were explored. The attractors shown in Figure 6.66 describe the Poincaré maps sampled for 20 cycles after 200 cycles have passed, for each response starting from its respective initial condition. This means that 20 cycles for each of the 1600 responses gives a total of 32000 points on each Poincaré map. As can be seen in these figures the resulting attractors are identical to the Poincaré maps, which were sampled for 29 000 cycles after 1000 cycles starting from a single initial condition. These attractors may be found in Figures 6.12(d), 6.33(b), 6.48(b), 6.58(c). Hence, for the basin of attraction sampled there are no competing attractors. Figure 6.67 reveals the path of a response starting from one of the initial conditions for one of the examples. It also reveals the entire grid of initial conditions that were used for all the examples of Figure 6.66.

A)

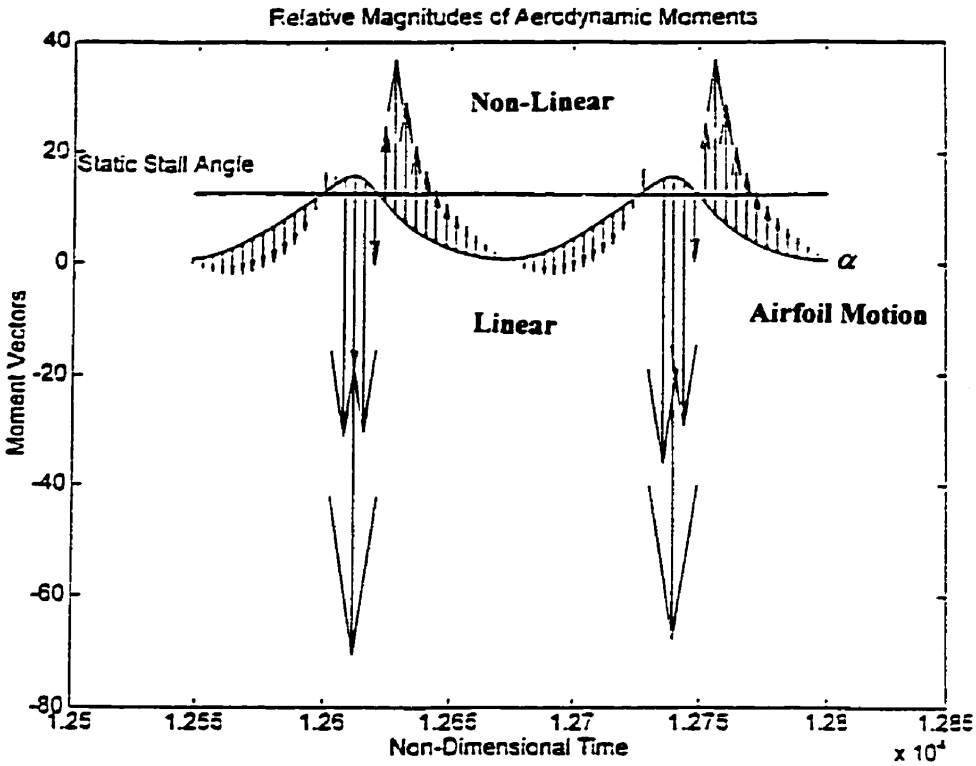

B)

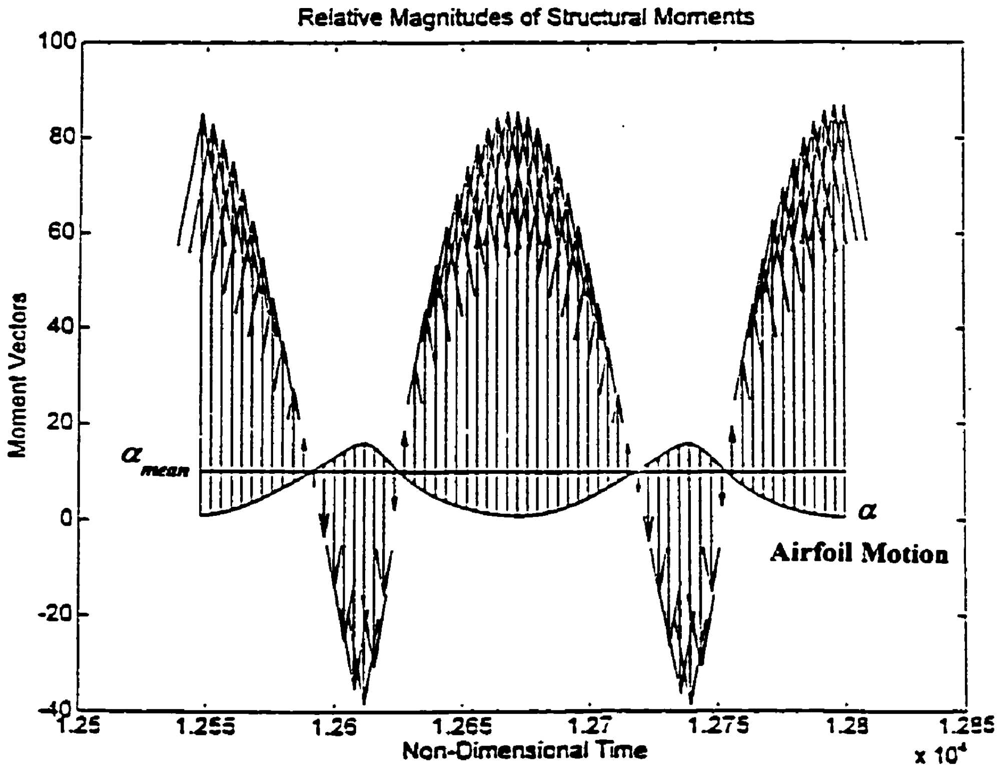

Figure 6.1: Vector Plot; a) Aerodynamic Moment b) Structural Moment c) Inertial Moment d) Externally Applied Moment: k=0.075, $\alpha_{mean} = 6$ deg, U^*=20, Qo=5x10^{-4}.

C)

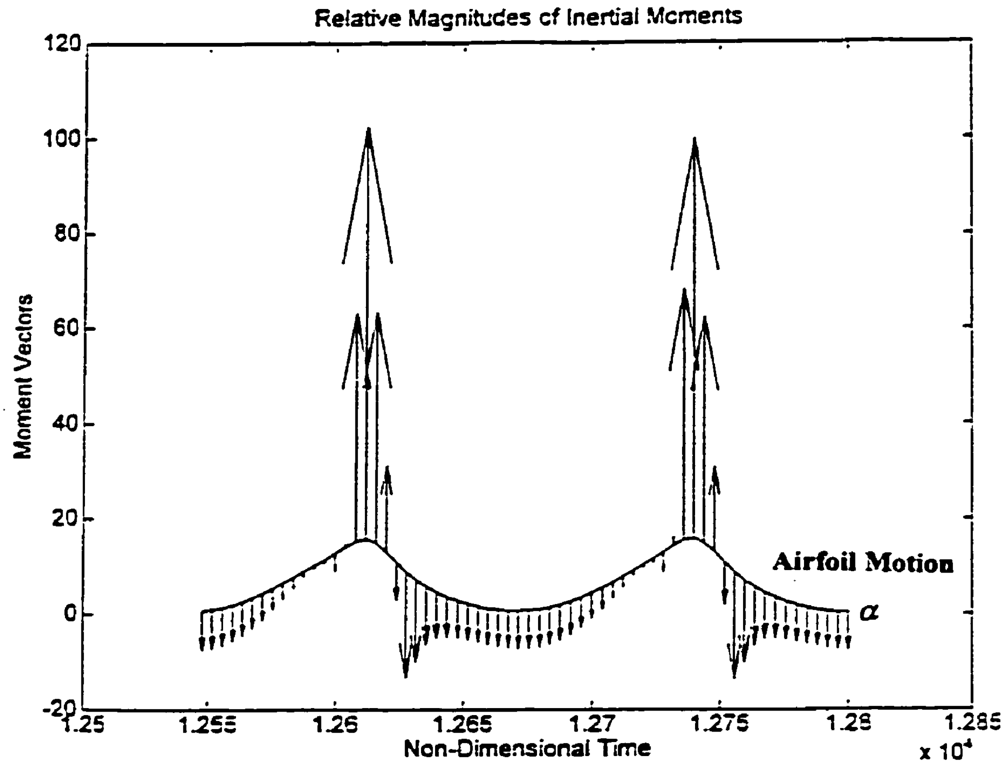
Relative Magnitudes of Inertial Moments
Moment Vectors
Non-Dimensional Time
x 10^4
Airfoil Motion
α
120
100
80
60
40
20
0
-20
1.25
1.255
1.26
1.265
1.27
1.275
1.28
1.285

D)

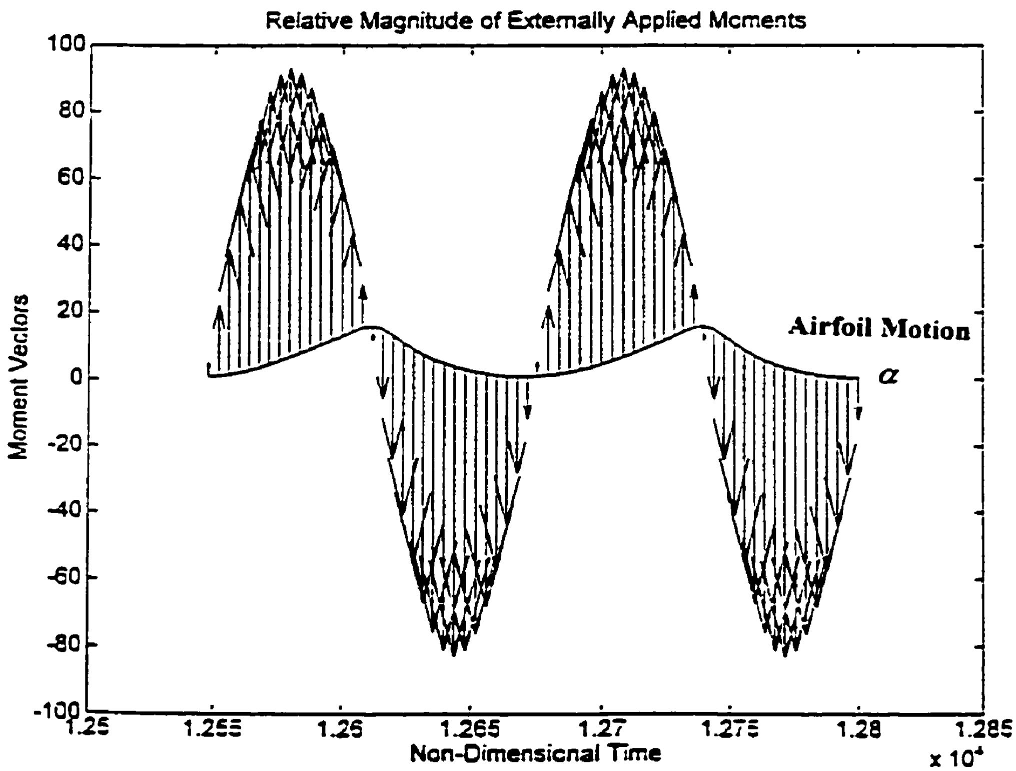
Relative Magnitude of Externally Applied Moments
Moment Vectors
Non-Dimensional Time
x 10^4
Airfoil Motion
α
100
80
60
40
20
0
-20
-40
-60
-80
-100
1.25
1.255
1.26
1.265
1.27
1.275
1.28
1.285

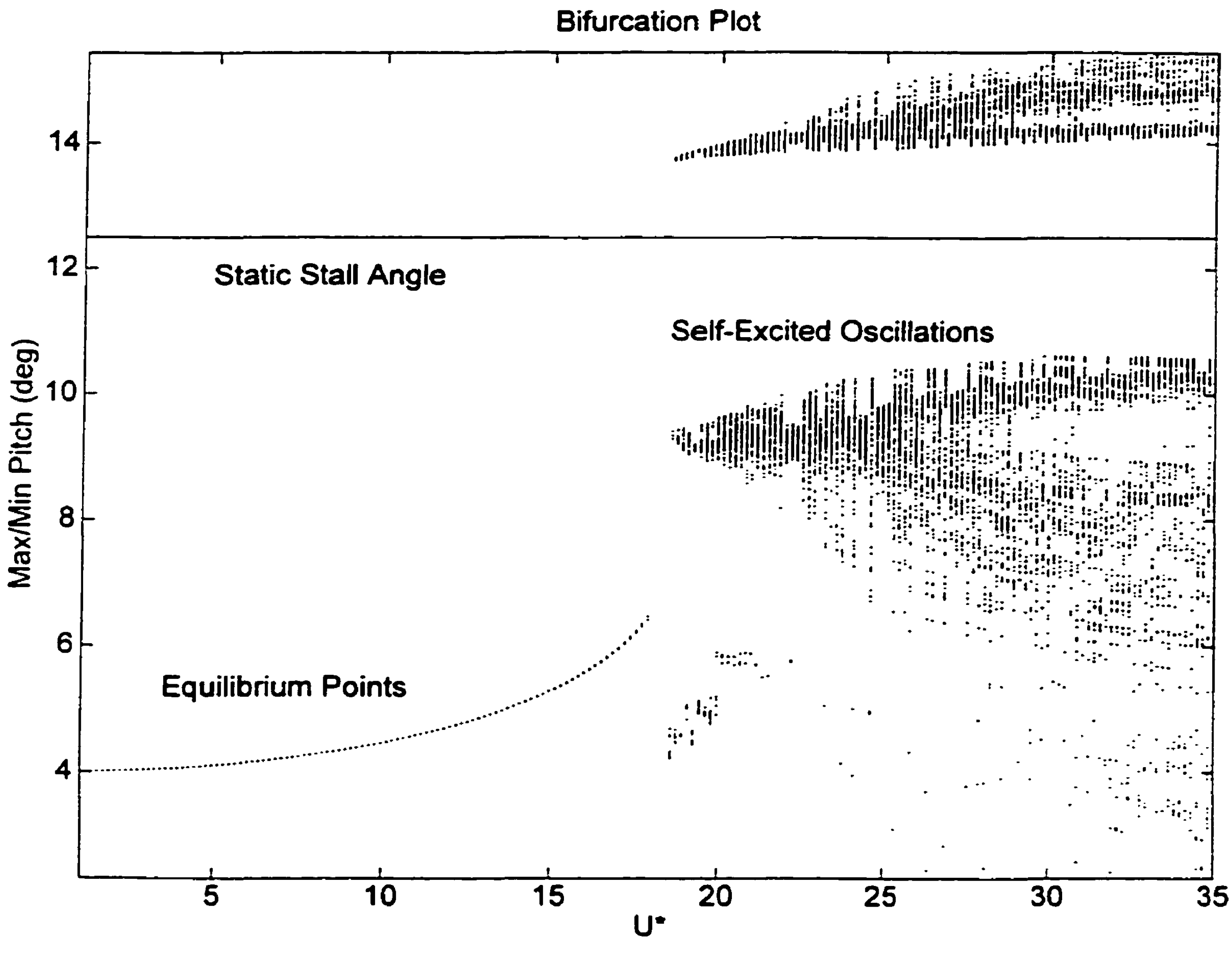

Figure 6.2: Bifurcation Plot with U^* as the Control Parameter Showing a Transition Between Equilibrium Points and Self-Excited Oscillations: Qo=0, k=N/A, $\alpha_{mean} = 4$ deg, $0<U^*<35$.

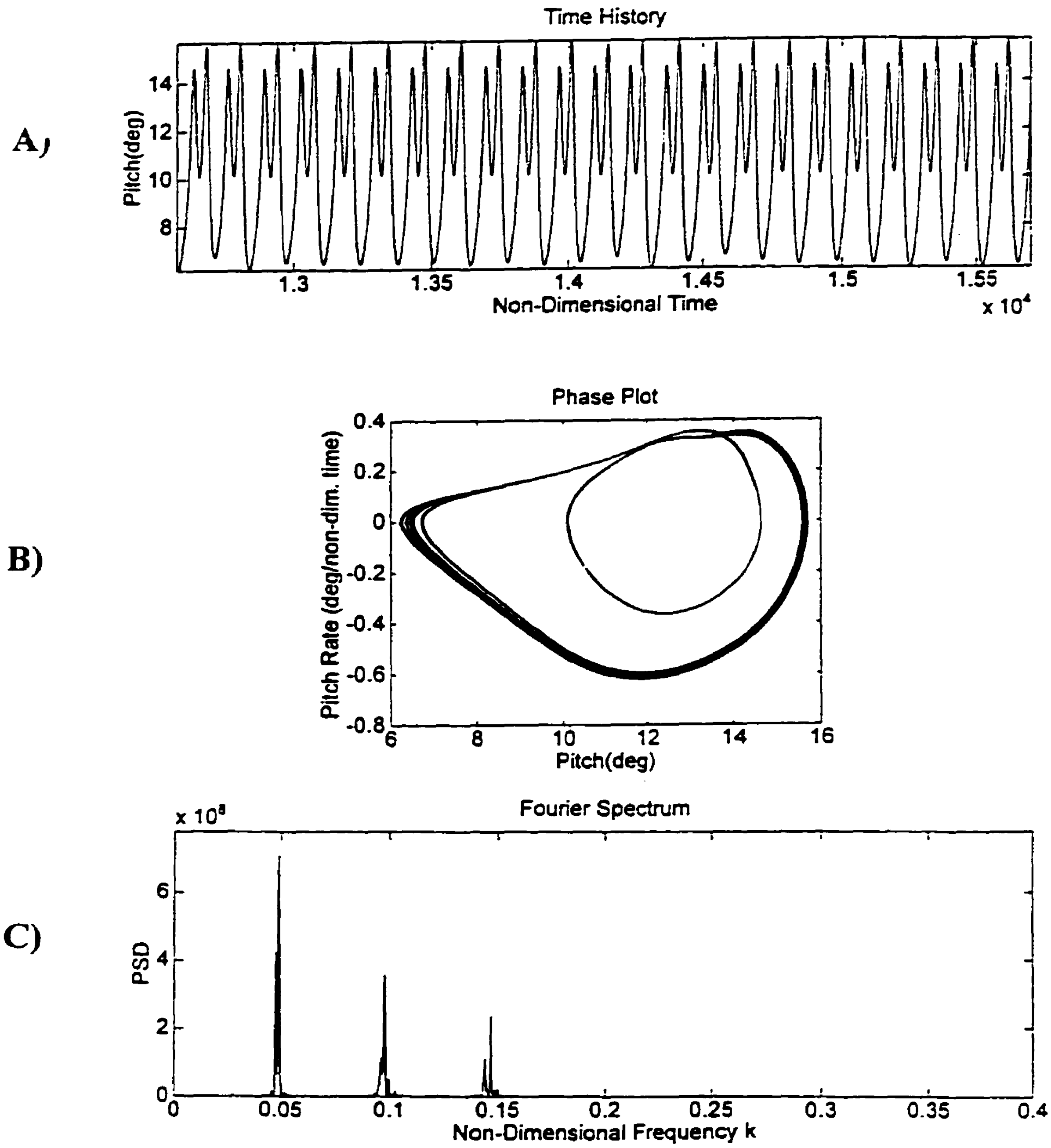

Figure 6.3: Airfoil Response Without the Influence of Structural or Externally Applied Moments; a) Time History b) Phase Plot c) Fourier Spectrum: k=N/A, α_{mean}=N/A, $U^*=\infty$, Qo=0.

A)

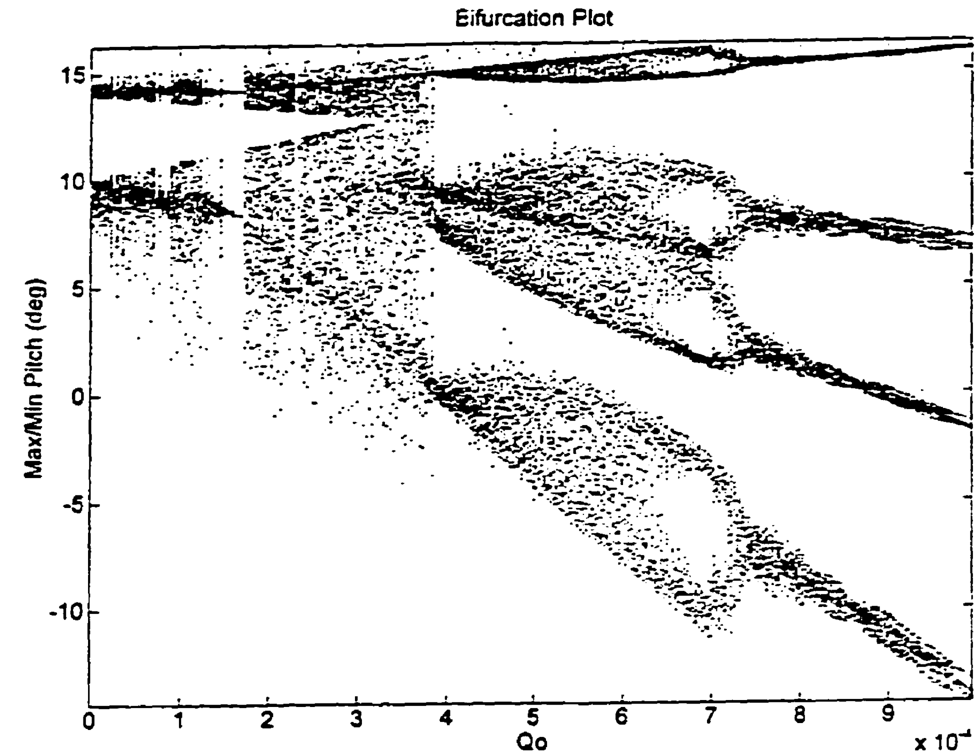

Case I

B)

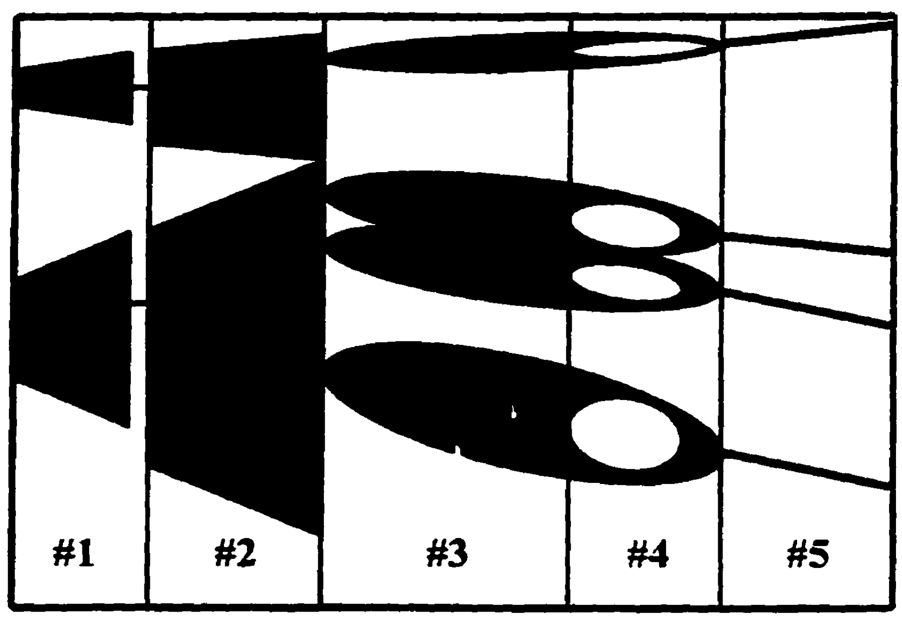

Figure 6.4: Case I; a) Bifurcation Plot b) Conceptual Drawing: k**=0.088,** α_{mean} = 5 deg, U^***=23, 0<**Qo**<0.001.**

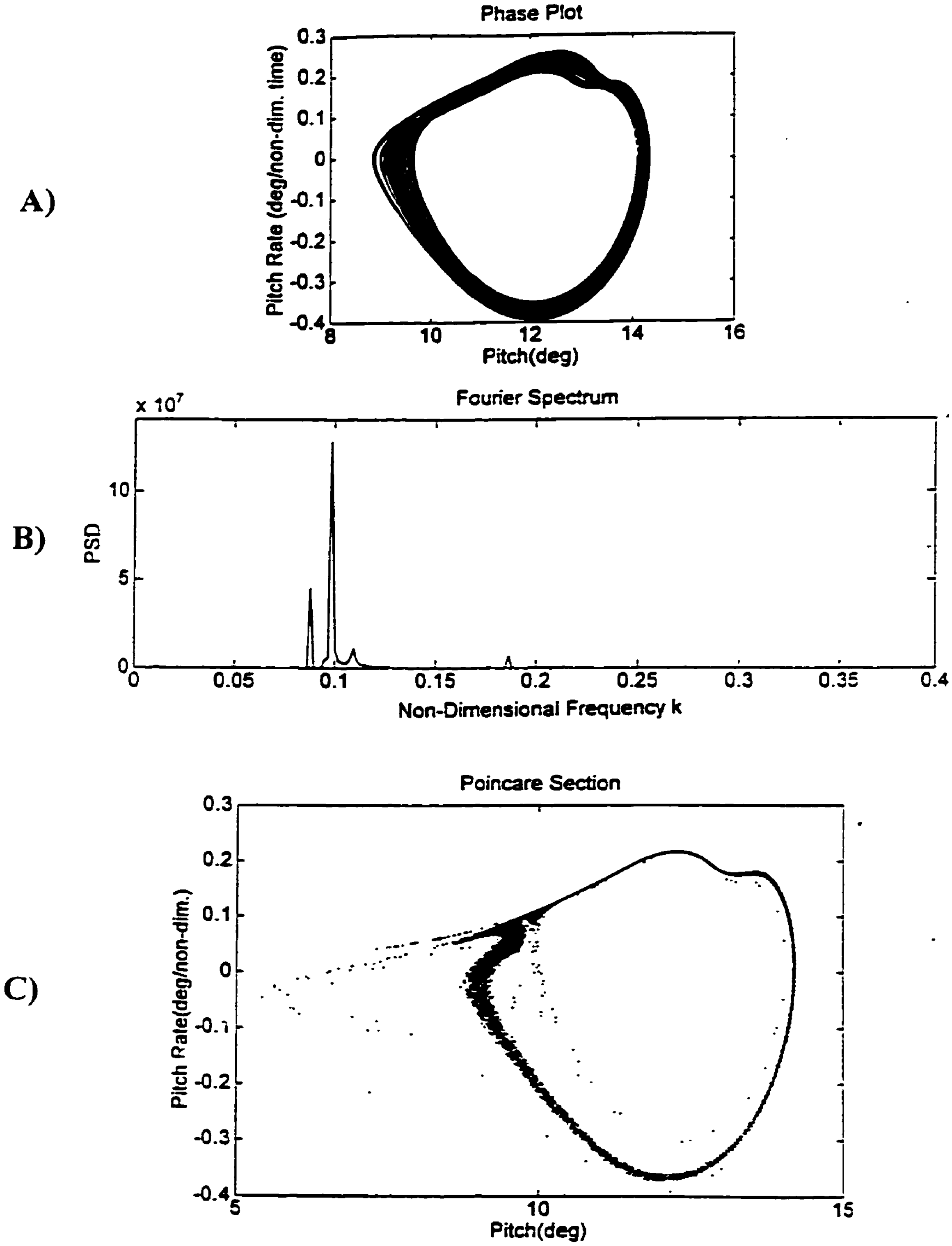

Figure 6.5: Case I, Region 1, Example 1; a) Phase Plot b) Fourier Spectrum c) Poincaré Section: *k*=0.088, $\alpha_{mean} = 5$ deg, *U=23, *Qo*=0.5x10^{-4}.**

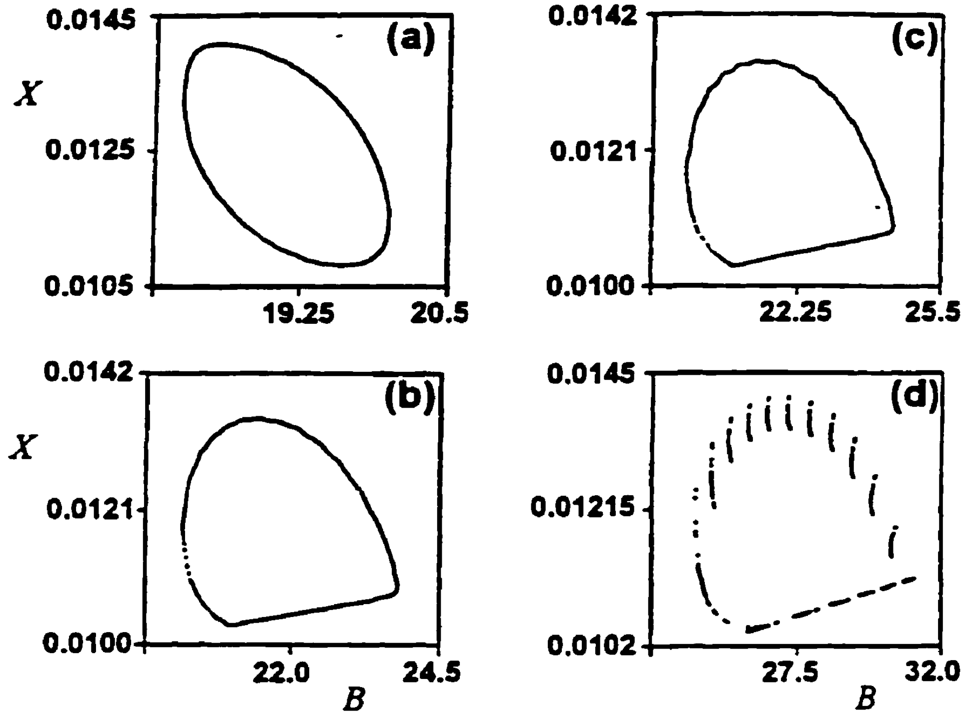

Figure 6.6: Quasi-Periodic Route Towards Chaos in the Peroxidase-Oxidase Reaction; Poincaré Sections: a) Undistorted Torus b) Wrinkled Torus c) Fractal Torus d) Broken Torus. Reproduced from Nayfeh and Balachandran (1995).

A)

B)

C)

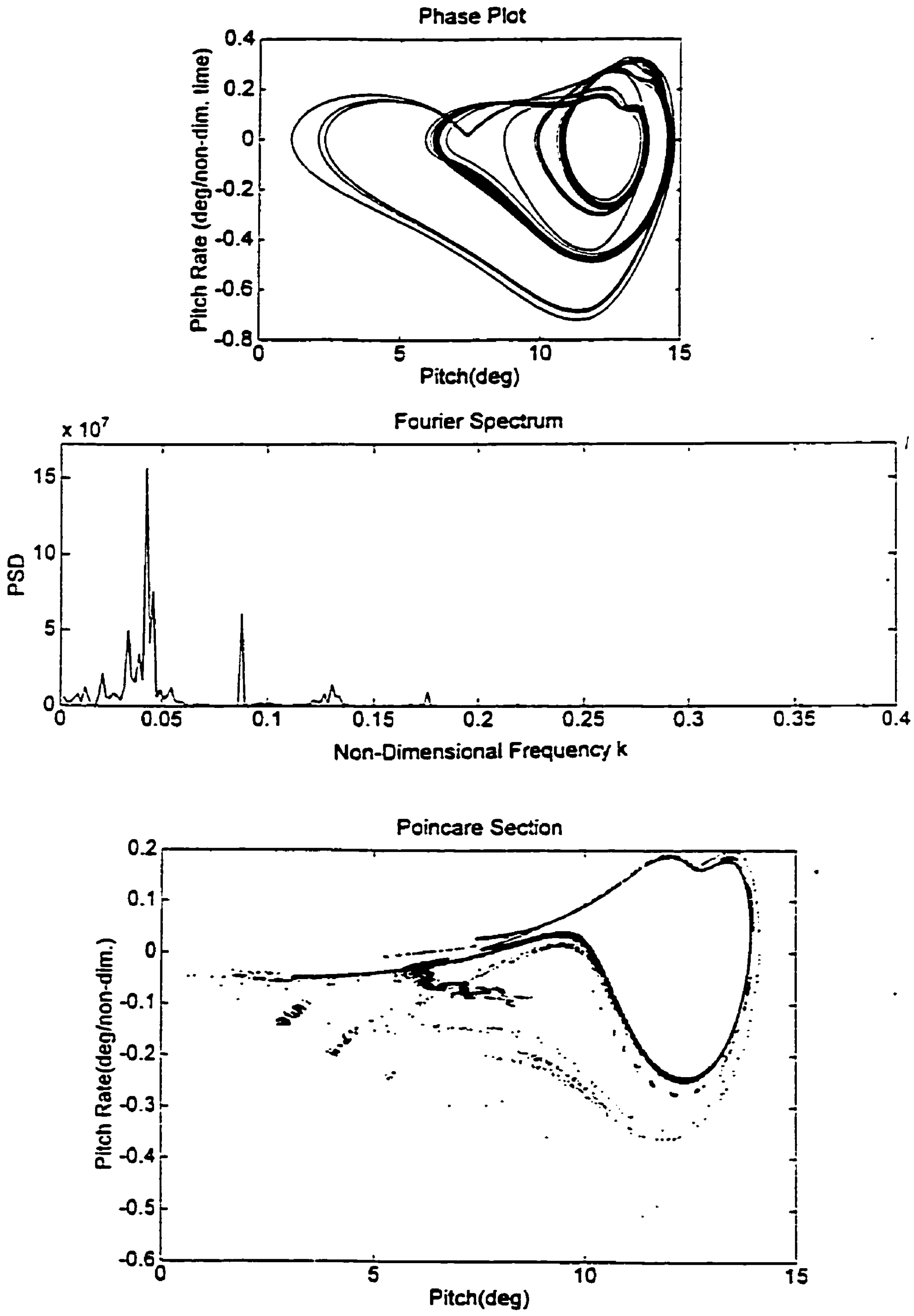

Figure 6.7: Case I, Region 1, Example 2; a) Phase Plot b) Fourier Spectrum c) Poincaré Section: k=0.088, $\alpha_{mean} = 5$ deg, U^*=23, Qo=1.2333x10^{-4}.

A)

B)

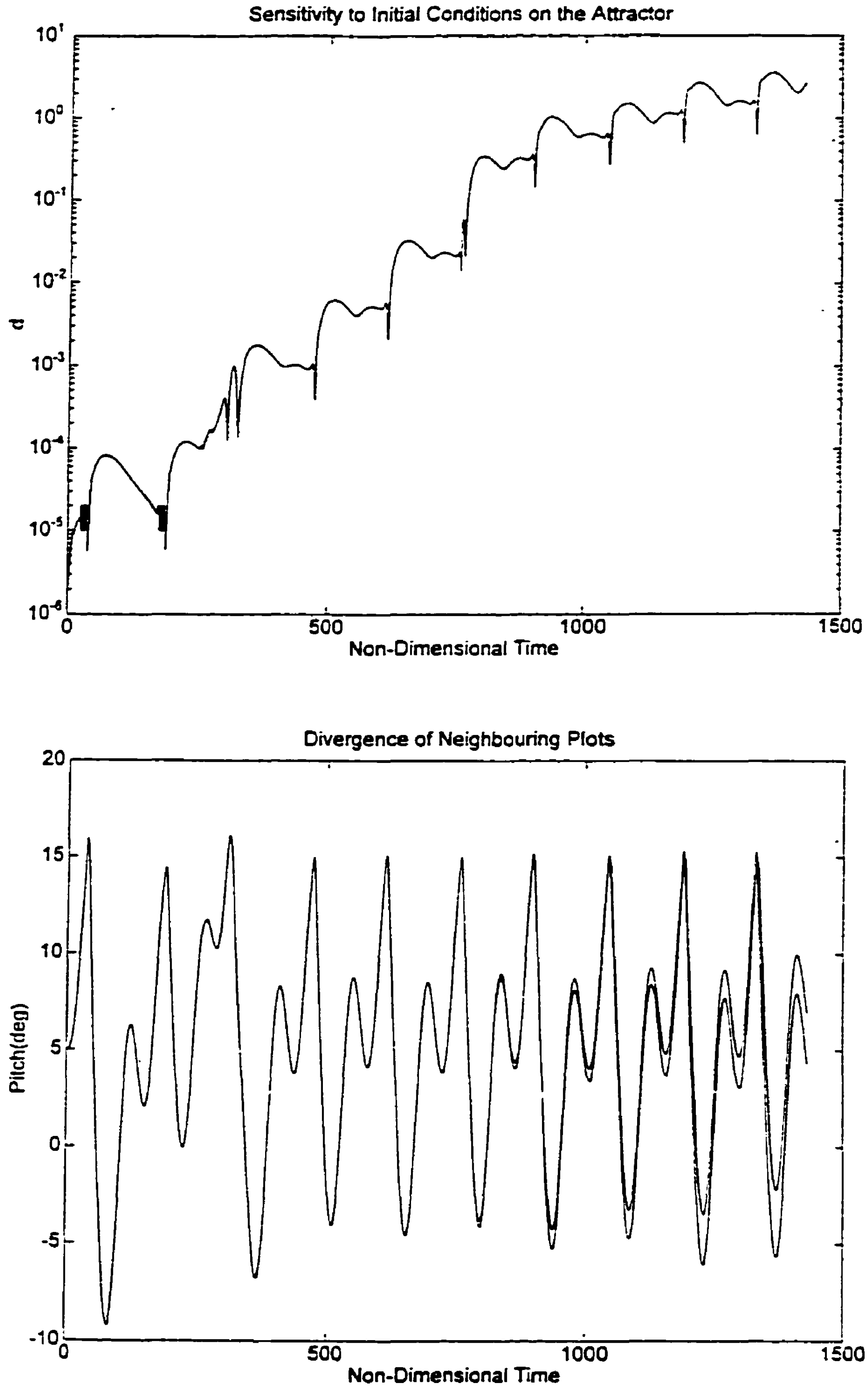

Figure 6.8: Case I, Region 1, Example 2; a) Sensitivity to Initial Conditions (Lyapunov Exponent) b) Divergence of Neighbouring Plots: k=0.088, α_{mean} = 5 deg, U^*=23, Qo=1.2333x10^{-4}.

A)

B)

C)

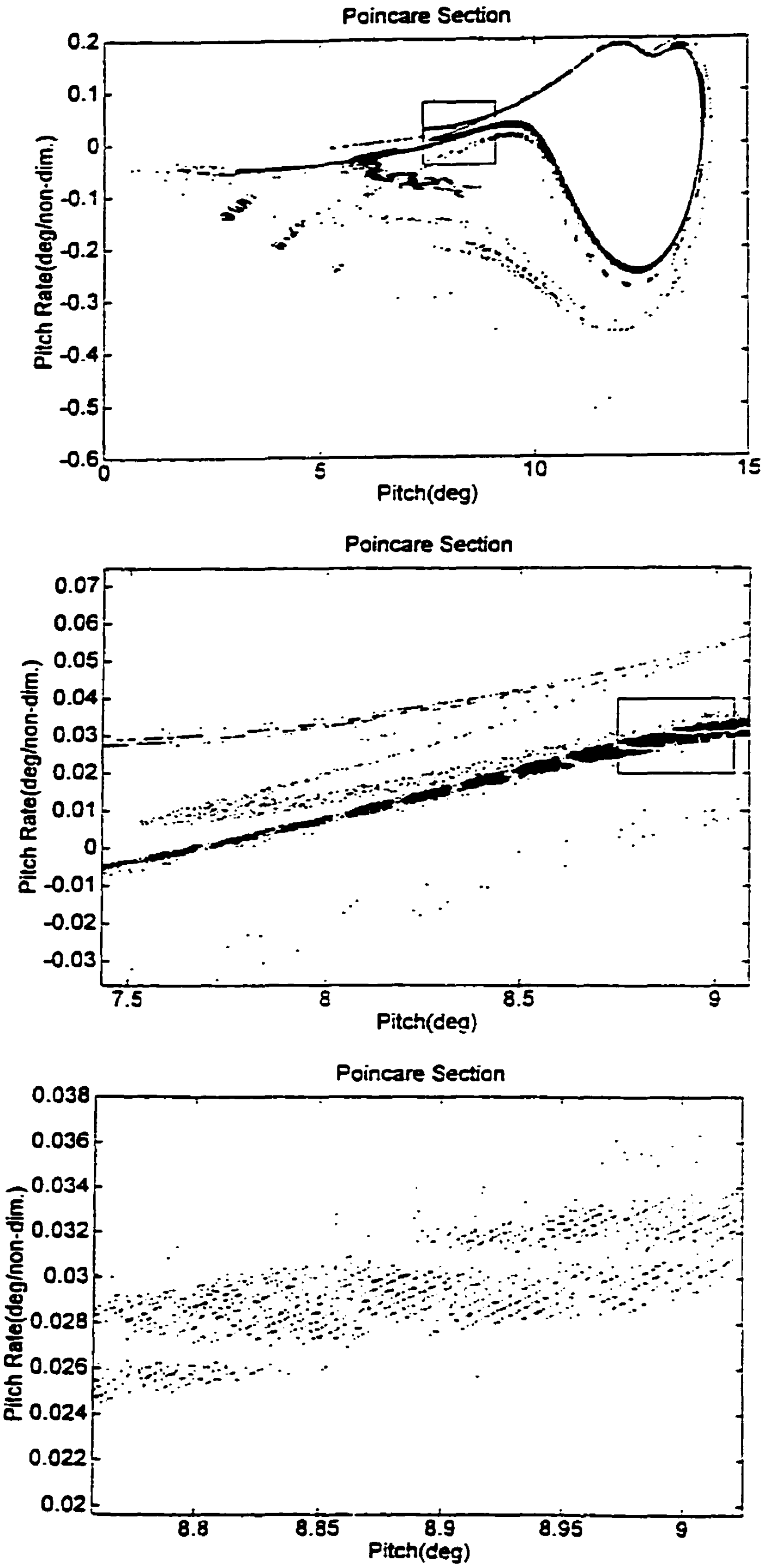

Figure 6.9: Case I, Region 1, Example 2; Magnified Poincaré Section a) Regular b) Level 1 c) Level 2: k=0.088, α_{mean} = 5 deg, U^*=23, Qo=1.2333x10^{-4}.

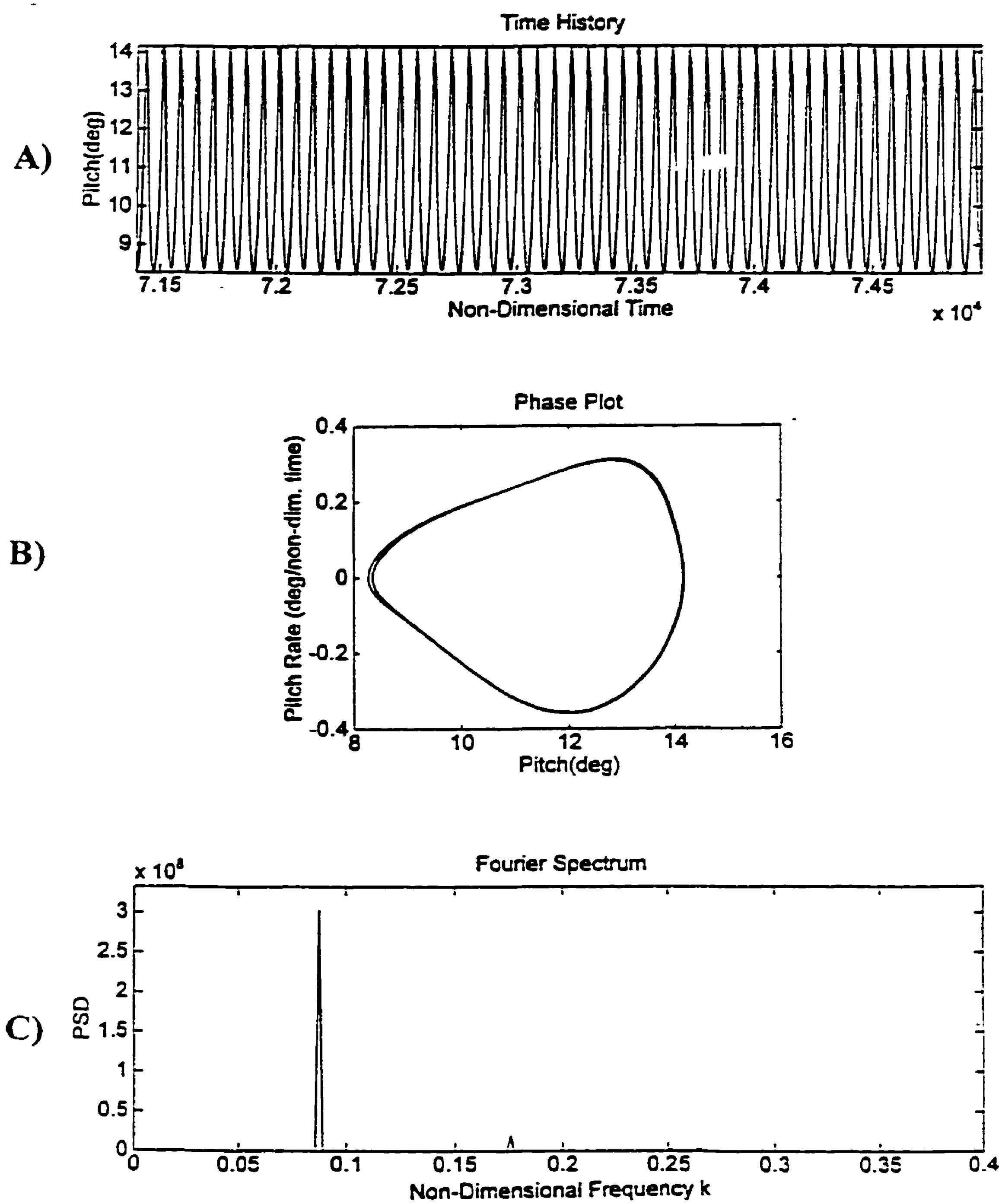

Figure 6.10: Case I, Region 1, Example 3; a) Time History b) Phase Plot c) Fourier Spectrum: k=0.088, $\alpha_{mean} = 5$ deg, U^*=23, Qo=1.7x10^{-4}.

A)

B)

C)

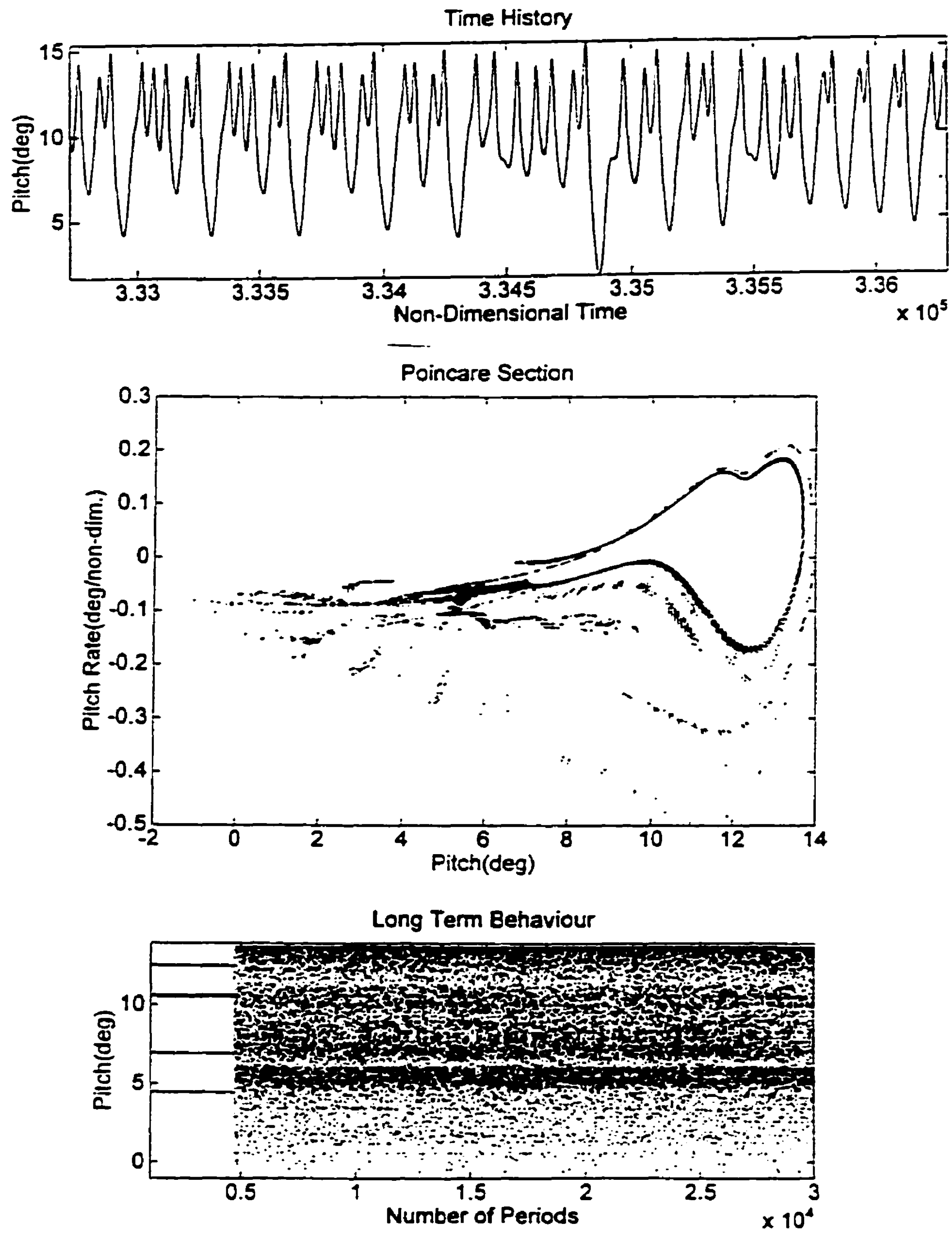

Figure 6.11: Case I, Region 2, Example 1; a) Time History b) Poincaré Section c) Long Term Behaviour: *k*=0.088, $\alpha_{mean} = 5$ deg, *U=23, *Qo*=2x10^{-4}.**

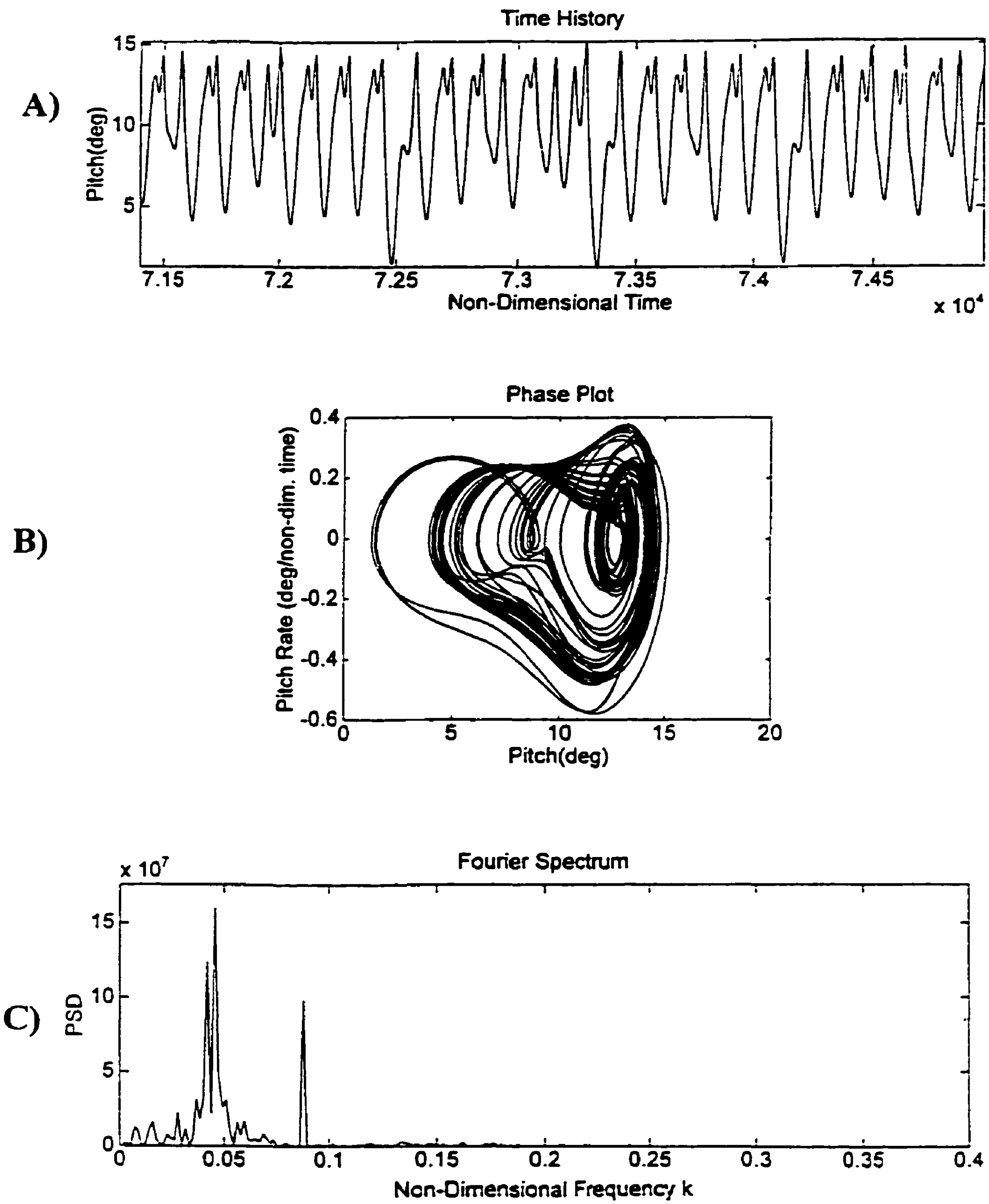

Figure 6.12: Case I, Region 2, Example 2; a) Time History b) Phase Plot c) Fourier Spectrum d) Poincaré Section e) Long Term Behaviour: k=0.088, $\alpha_{mean} = 5$ deg, U^*=23, Qo=2.8x10^{-4}.

D)

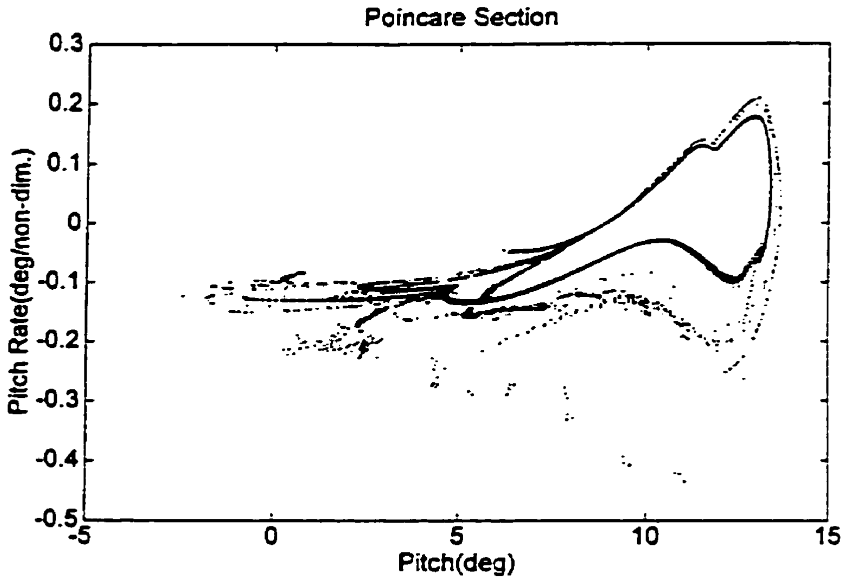
Poincare Section
Pitch Rate(deg/non-dim.)
Pitch(deg)
0.3
0.2
0.1
0
-0.1
-0.2
-0.3
-0.4
-0.5
-5
0
5
10
15

E)

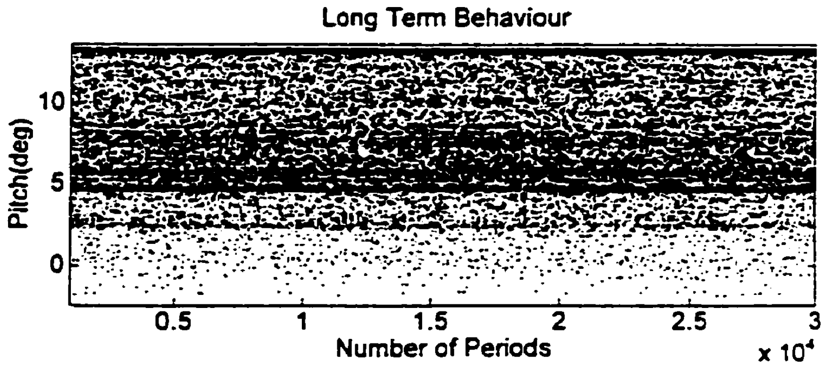
Long Term Behaviour
Pitch(deg)
Number of Periods
10
5
0
0.5
1
1.5
2
2.5
3
x 10^4

A)

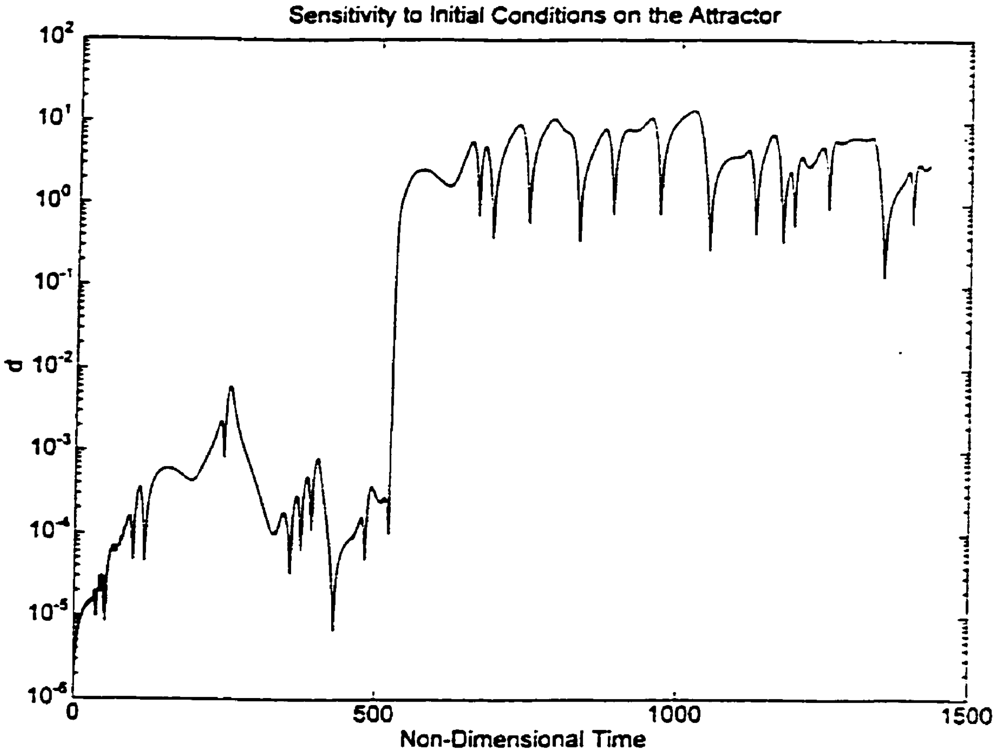

B)

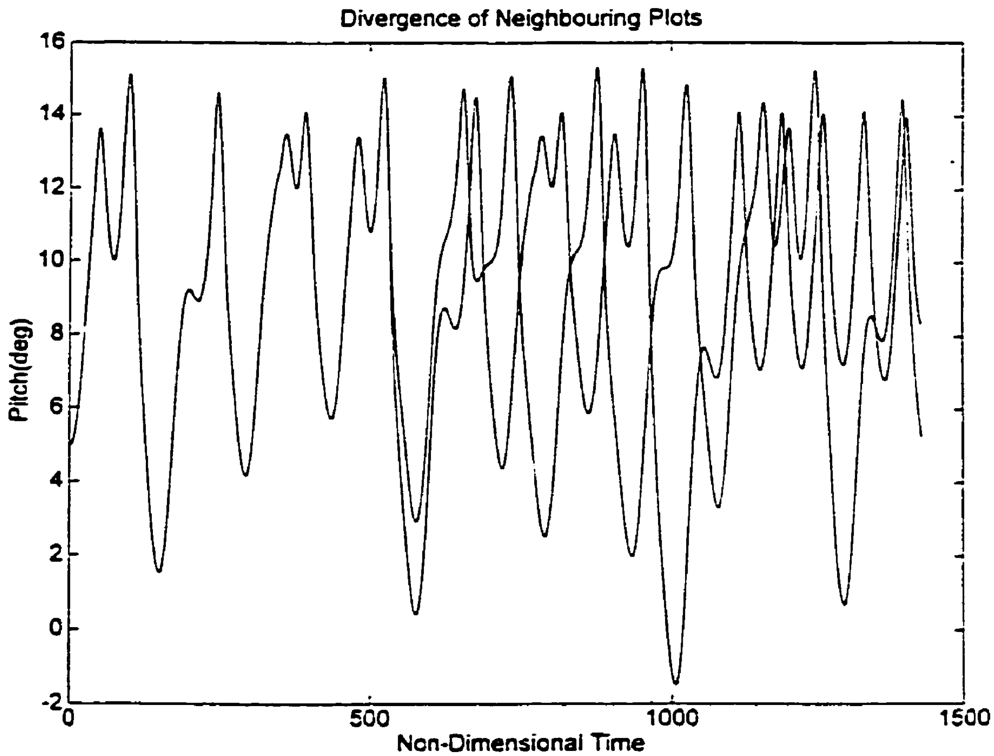

Figure 6.13: Case I, Region 2, Example 2; a) Sensitivity to Initial Conditions (Lyapunov Exponent) b) Divergence of Neighbouring Plots: k=0.088, $\alpha_{mean}=5$ deg, U*=23, Qo=2.8x10^{-4}.

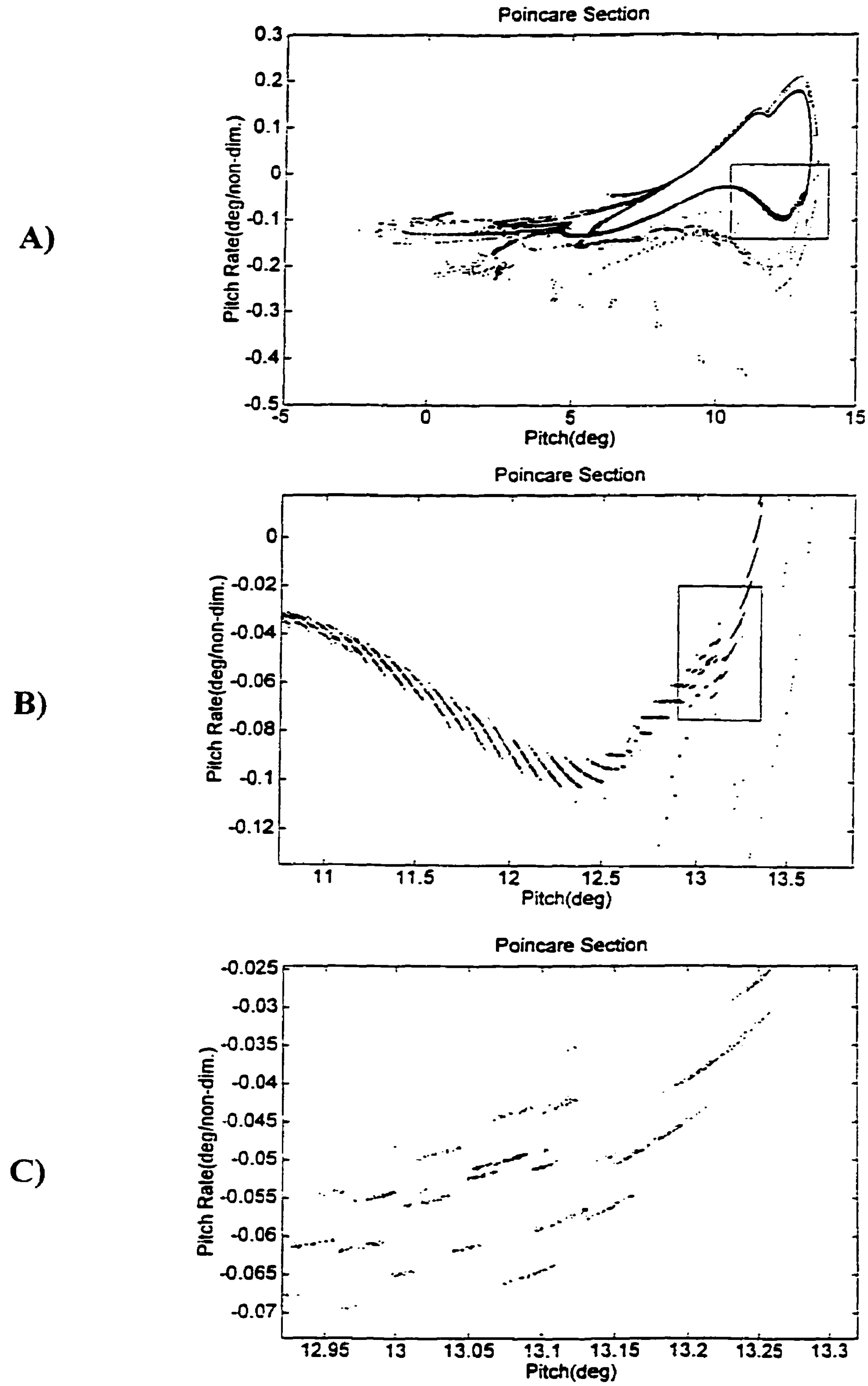

Figure 6.14: Case I, Region 2, Example 2; Magnified Poincaré Section a) Regular b) Level 1 c) Level 2: k=0.088, $\alpha_{mean}=5$ deg, U^*=23, Qo=2.8x10^{-4}.

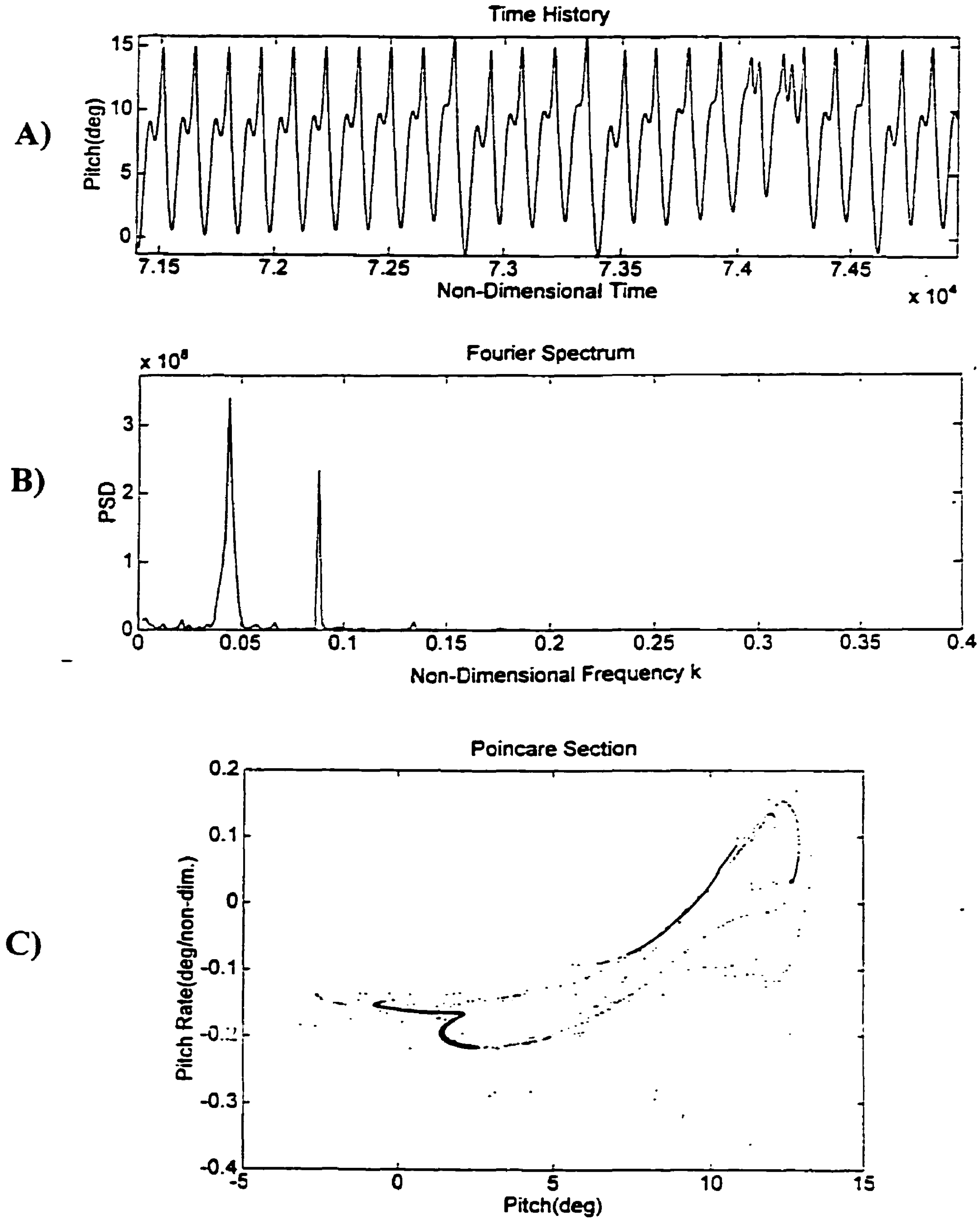

Figure 6.15: Case I, Region 2, Example 3; a) Time History b) Fourier Spectrum c) Poincaré Section d) Long Term Behaviour: k=0.088, $\alpha_{mean} = 5$ deg, U^*=23, Qo=3.8333x10^{-4}.

D)

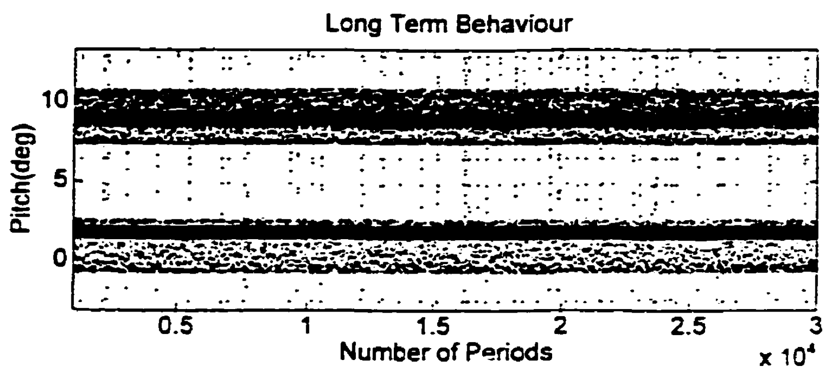
Long Term Behaviour
Pitch(deg)
10
5
0
0.5
1
1.5
2
2.5
3
Number of Periods
x 10^4

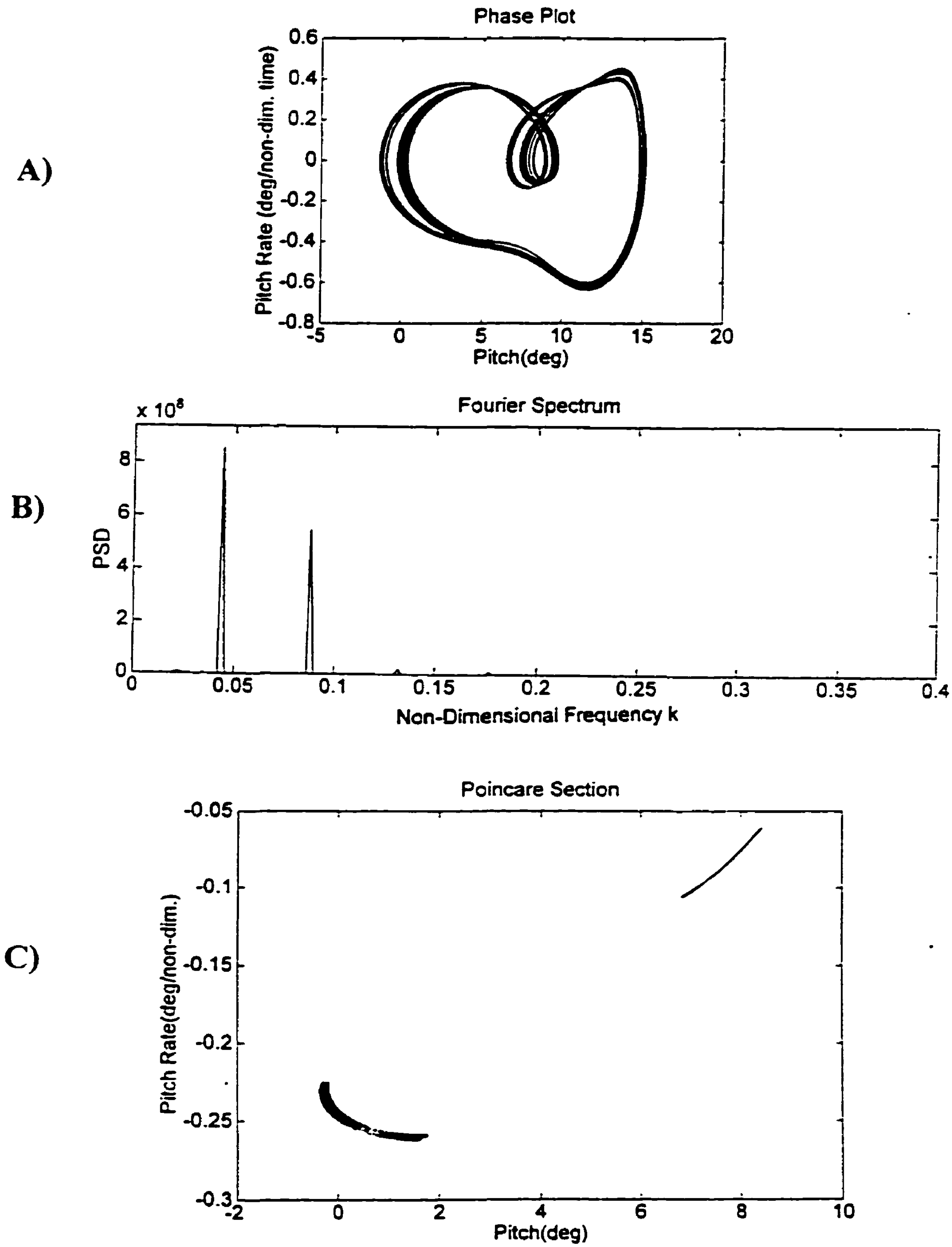

Figure 6.16: Case I, Region 3, Example 1; a) Phase Plot b) Fourier Spectrum c) Poincaré Section: k=0.088, $\alpha_{mean} = 5$ deg, U^*=23, Qo=4.3667x10^{-4}.

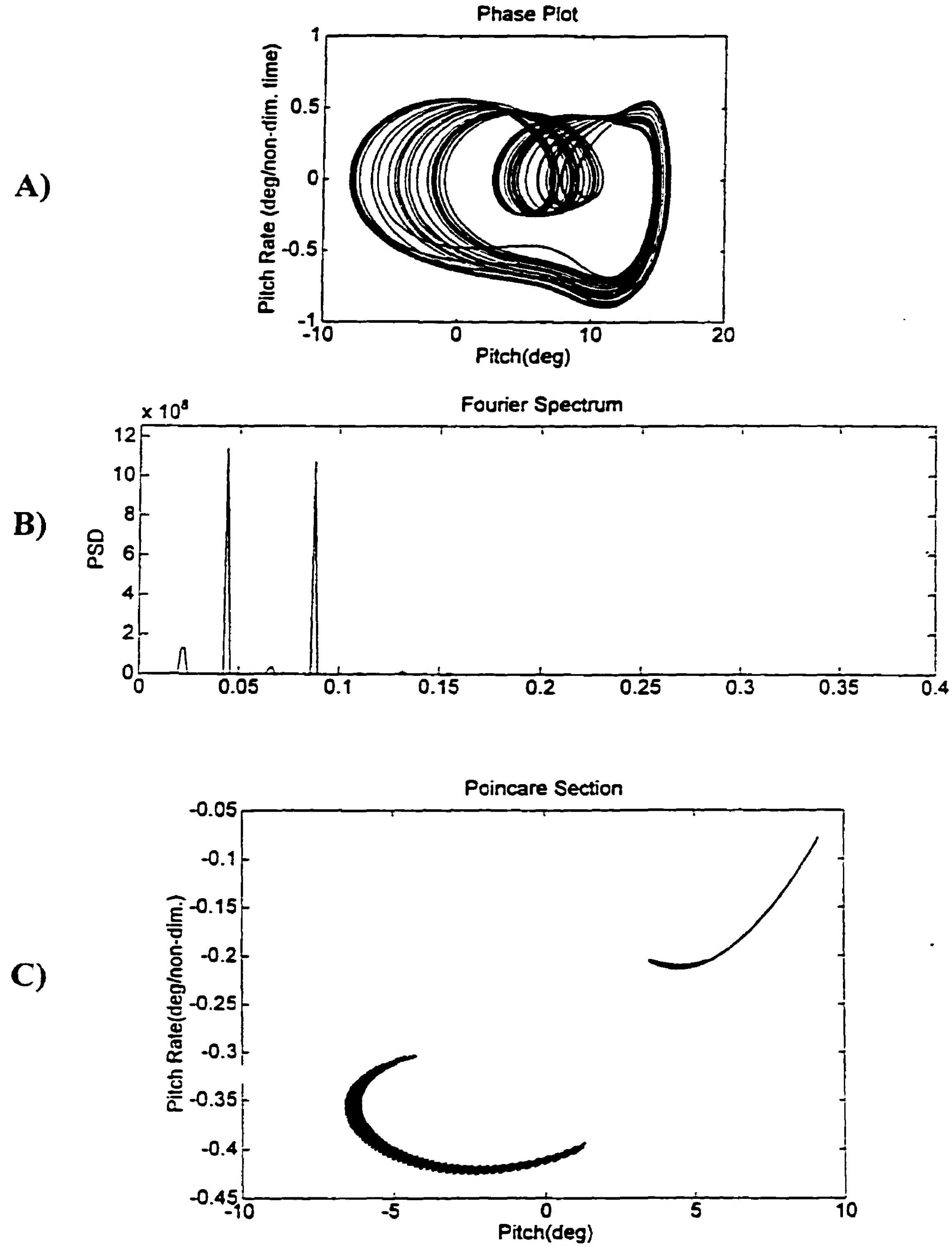

Figure 6.17: Case I, Region 3, Example 3; a) Phase Plot b) Fourier Spectrum c) Poincaré Section: k=0.088, $\alpha_{mean} = 5$ deg, U^*=23, Qo=6.2333x10^{-4}.

A)

B)

C)

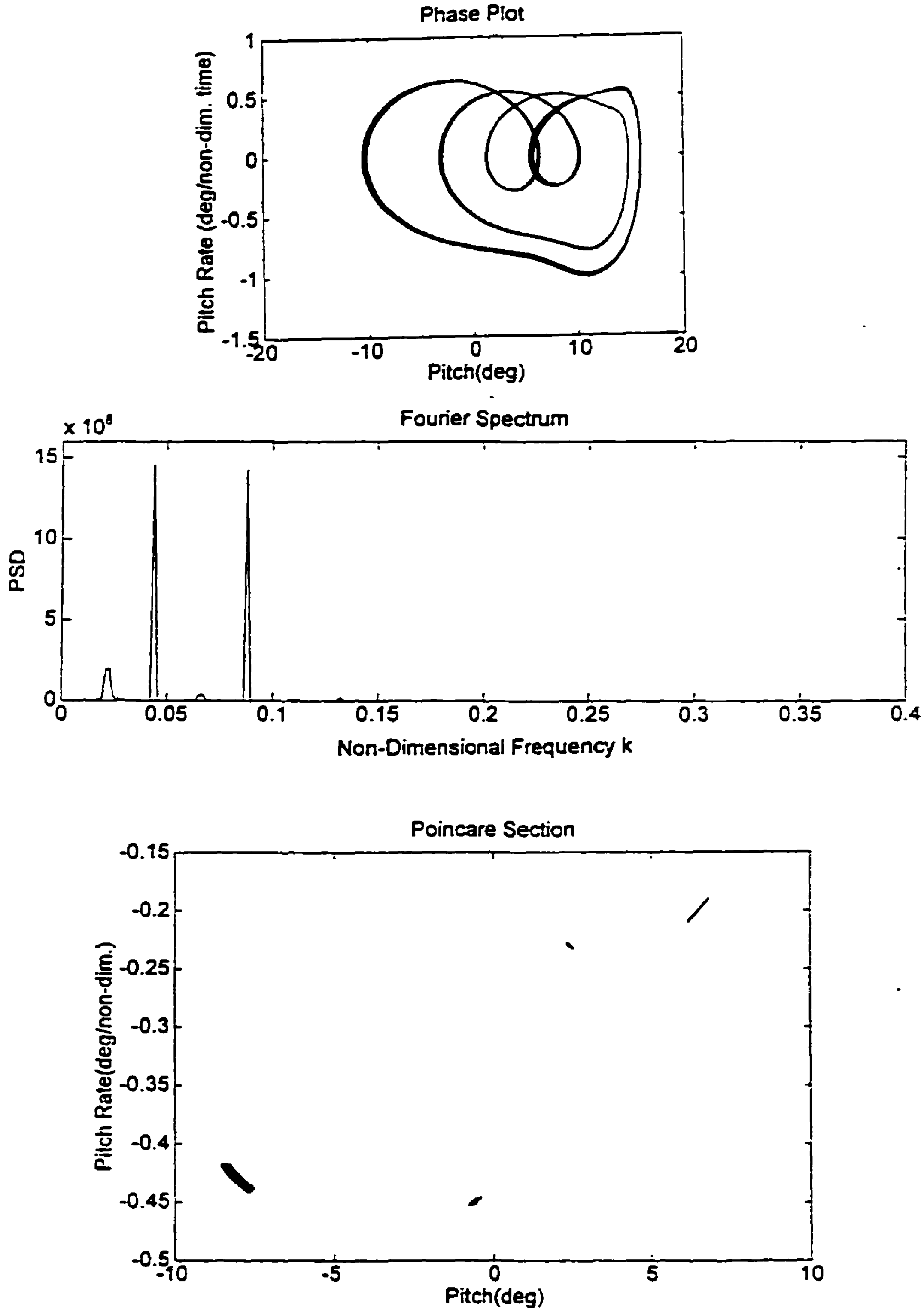

Figure 6.18: Case I, Region 4, Example 2; a) Phase Plot b) Fourier Spectrum c) Poincaré Section: k=0.088, $\alpha_{mean} = 5$ deg, U^*=23, Qo=7.0333x10^{-4}.

A)

B)

C)

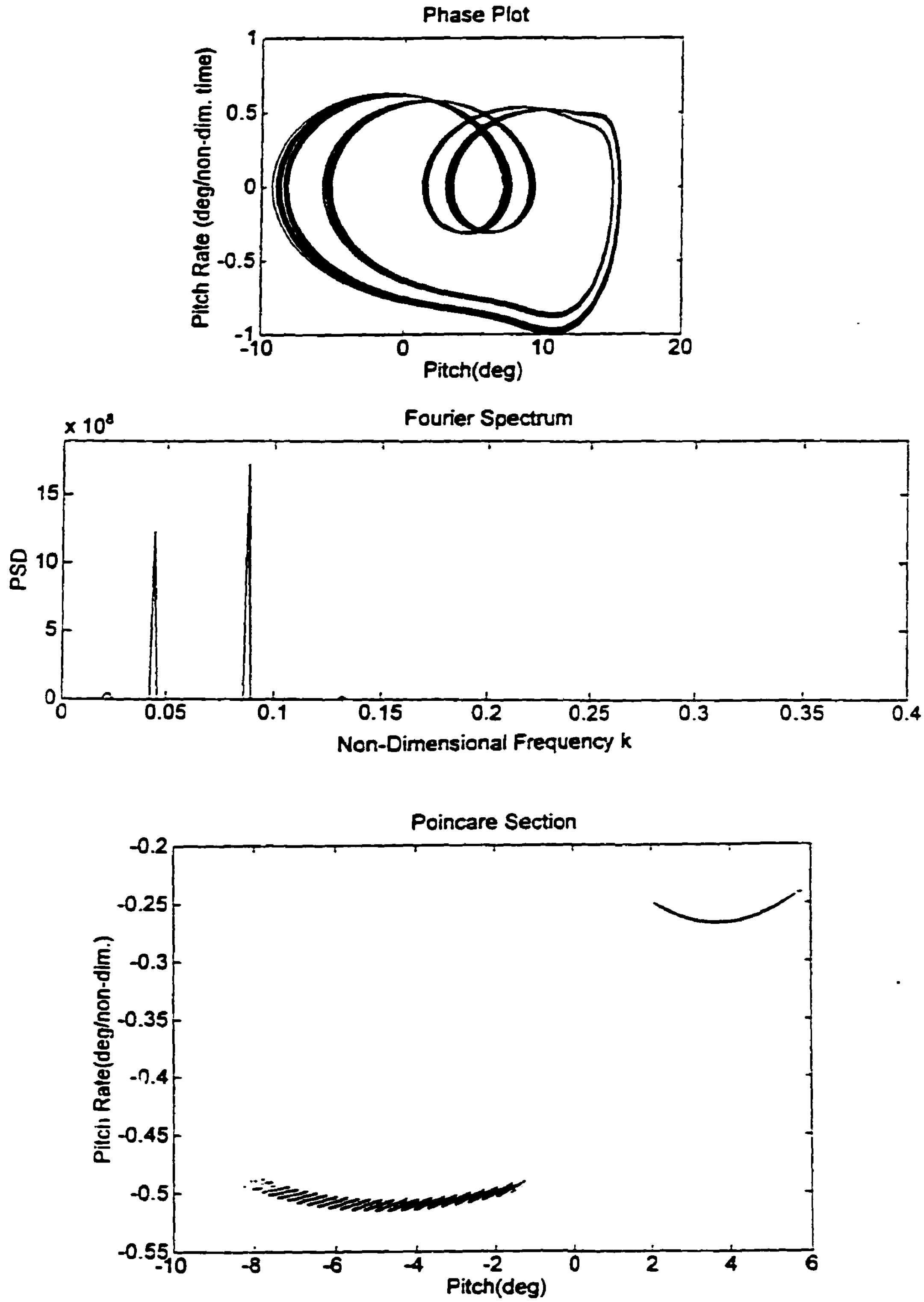

Figure 6.19: Case I, Region 4, Example 3; a) Phase Plot b) Fourier Spectrum c) Poincaré Section: k=0.088, $\alpha_{mean}=5$ deg, U^*=23, Qo=7.3667x10^{-4}.

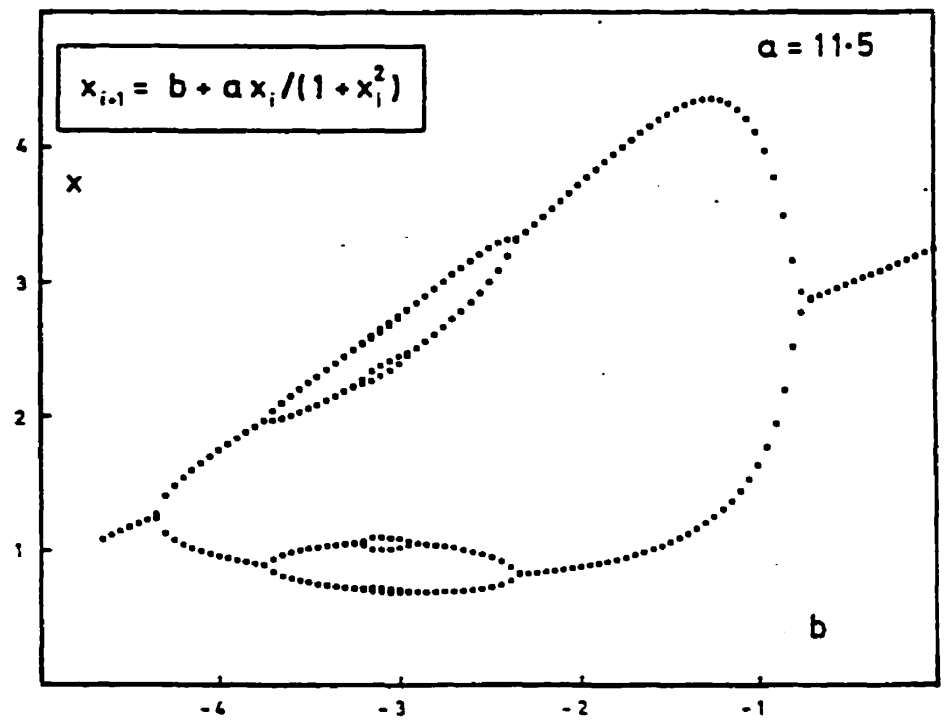

Figure 6.20: Feigenbaum Trees: an Example of an Incomplete Period-Doubling Cascade. Reproduced from Thompson and Stewart (1986).

A)

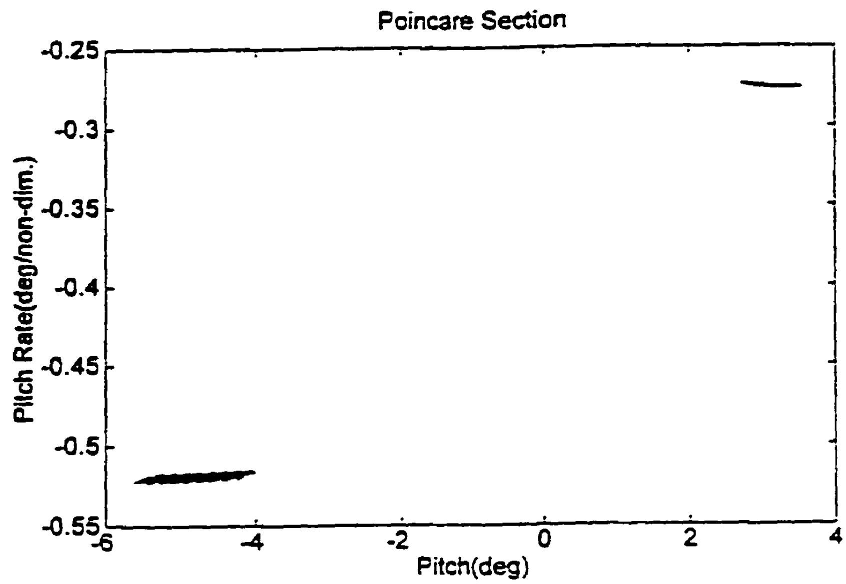

B)

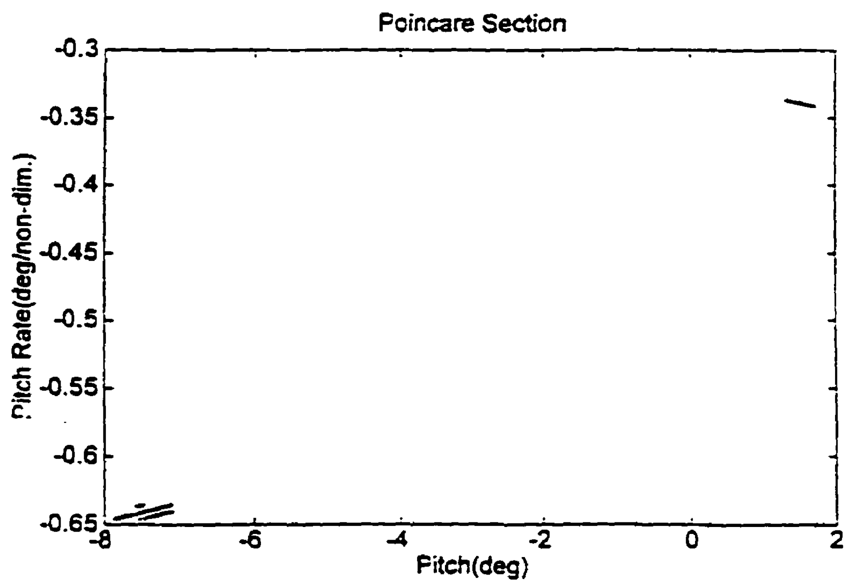

Figure 6.21: Case I, Region 5, Example 1 & 2; a) Example 1; Poincaré Section b) Example 2;Poincaré Section: *k*=0.088, $\alpha_{mean} = 5$ deg, *U=23, a) *Qo*=7.7333x10^{-4}, b)*Qo*=9.0333x10^{-4}.**

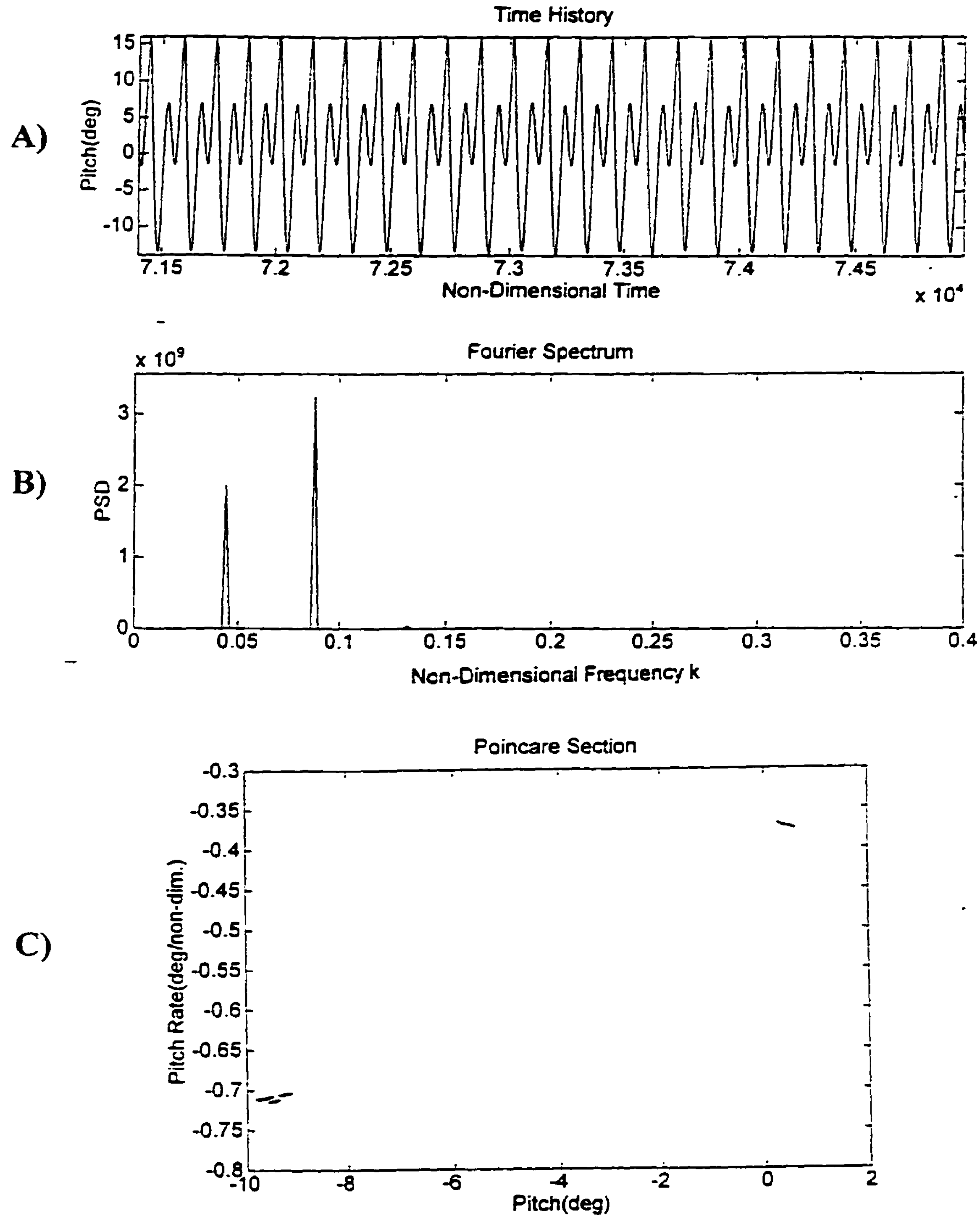

Figure 6.22: Case I, Region 5, Example 3; a) Time History b) Fourier Spectrum c) Poincaré Section: k=0.088, $\alpha_{mean} = 5$ deg, U^*=23, Qo=9.9x10^{-4}.

A)

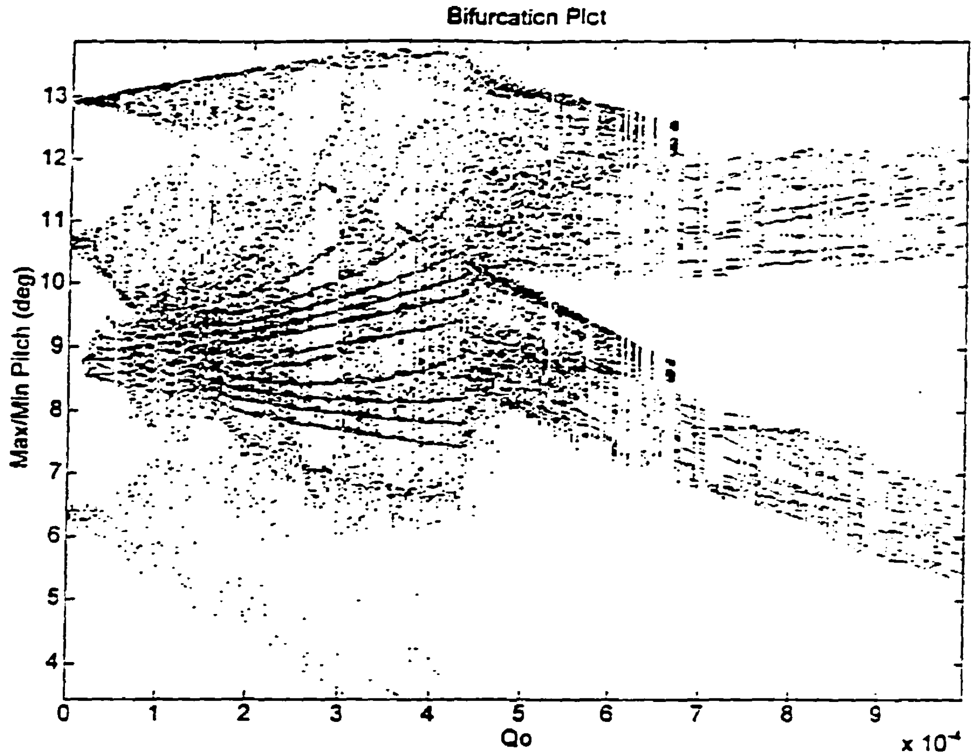

Case II

B)

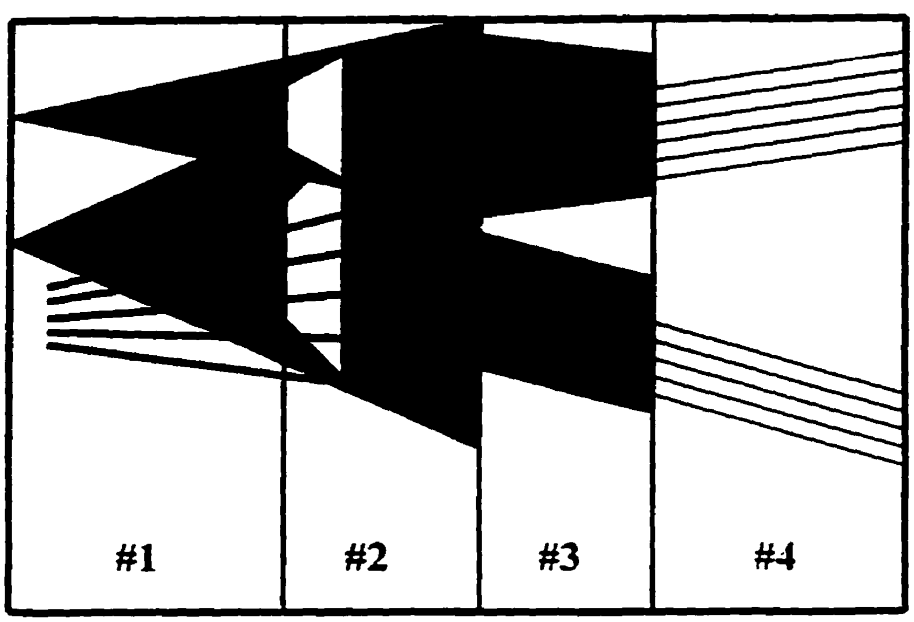

Figure 6.23: Case II; a) Bifurcation Plot b) Conceptual Drawing: k=0.15, $\alpha_{mean} = 6$ deg, U^*=13.5, 0<Qo<0.001.

A)

B)

C)

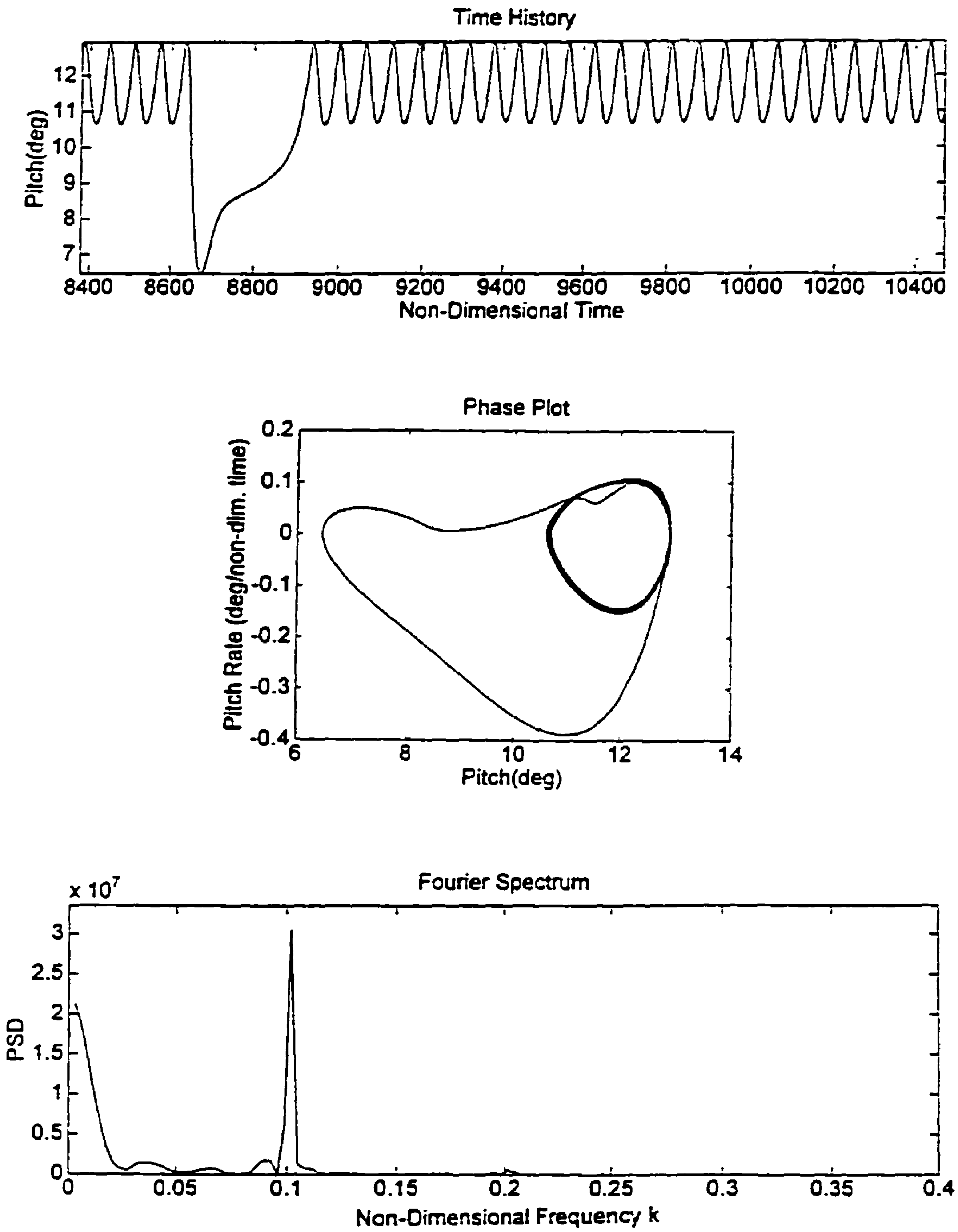

Figure 6.24: Case II, Region 1, Example 1; a) Time History b) Phase Plot c) Fourier Spectrum d) Poincaré Section e) Long Term Behaviour: k=0.15, $\alpha_{mean} = 6$ deg, U^*=13.5, Qo=0.

D)

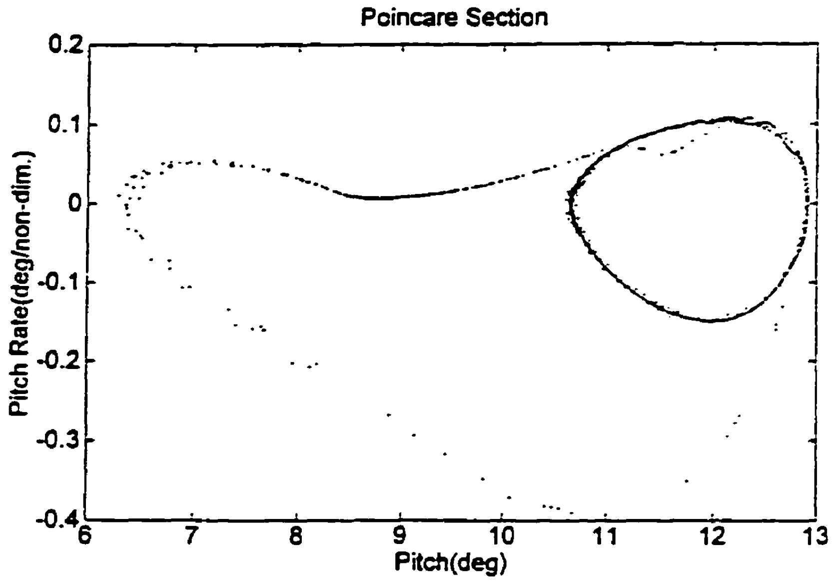
Poincare Section
Pitch Rate(deg/non-dim.)
Pitch(deg)
0.2
0.1
0
-0.1
-0.2
-0.3
-0.4
6
7
8
9
10
11
12
13

E)

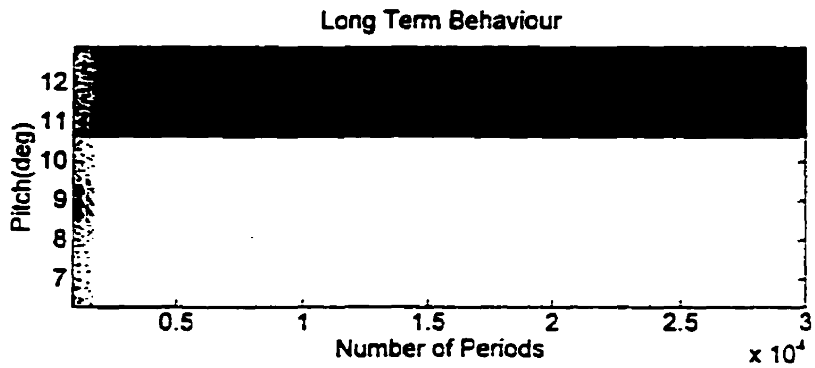
Long Term Behaviour
Pitch(deg)
Number of Periods
x 10^4
12
11
10
9
8
7
0.5
1
1.5
2
2.5
3

A)

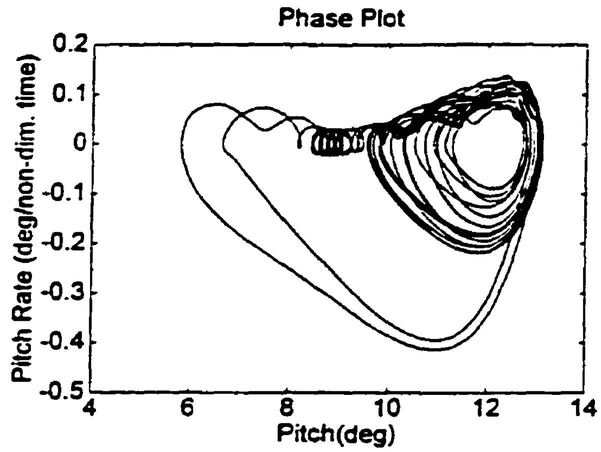

B)

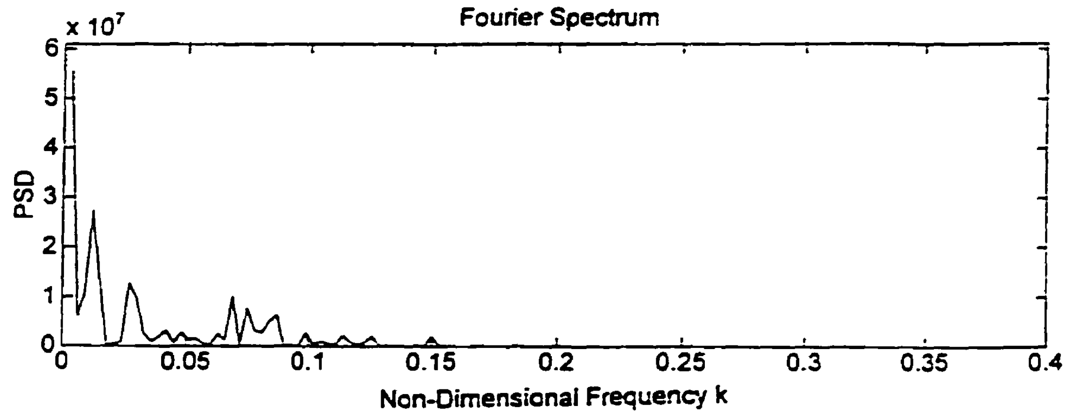

C)

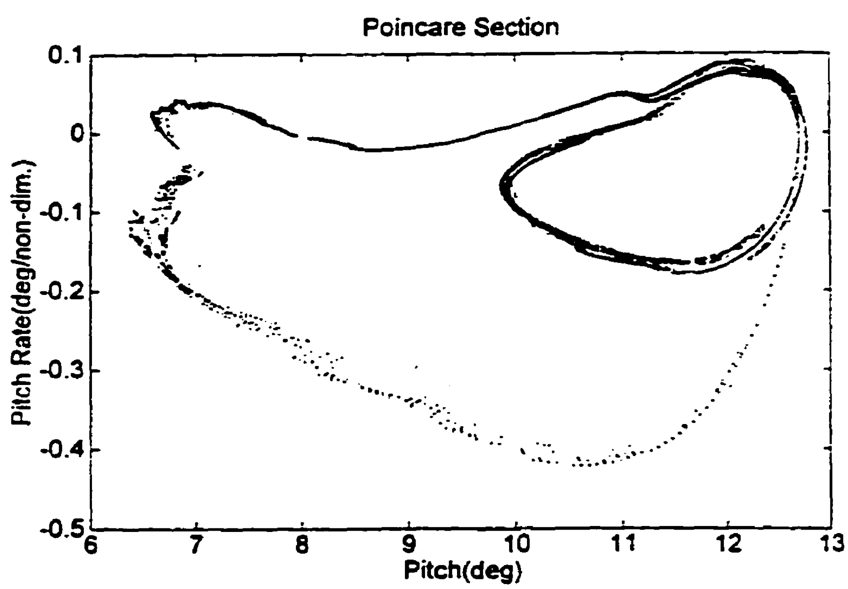

Figure 6.25: Case II, Region 1, Example 2; a) Phase Plot b) Fourier Spectrum c) Poincaré Section: k=0.15, $\alpha_{mean}=6$ deg, U^*=13.5, Qo=7x10^{-4}.

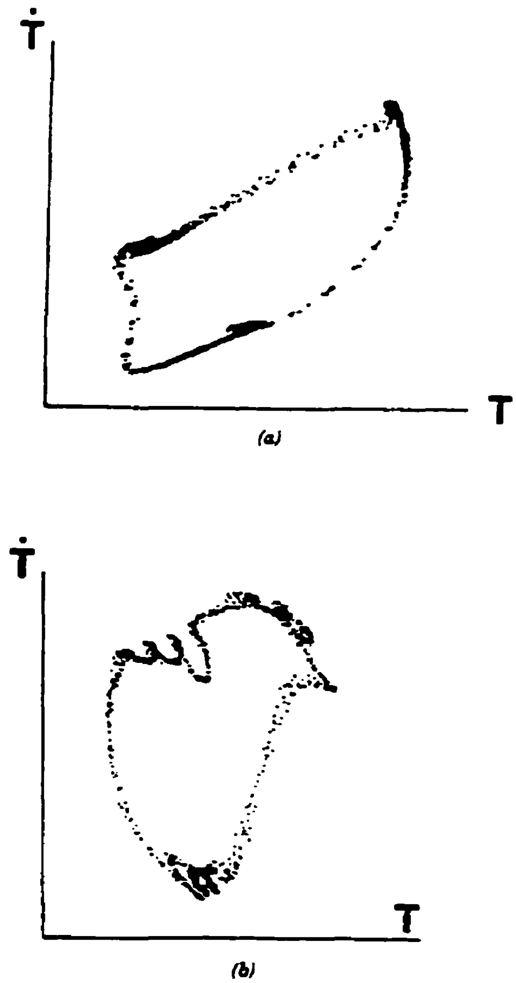

Figure 6.26: Quasi-Periodic Route Towards Chaos in Rayleigh-Benard Thermal Convection; Poincaré Sections: a) Quasi-Periodic Motion d) Broken Torus. Reproduced from Moon (1987).

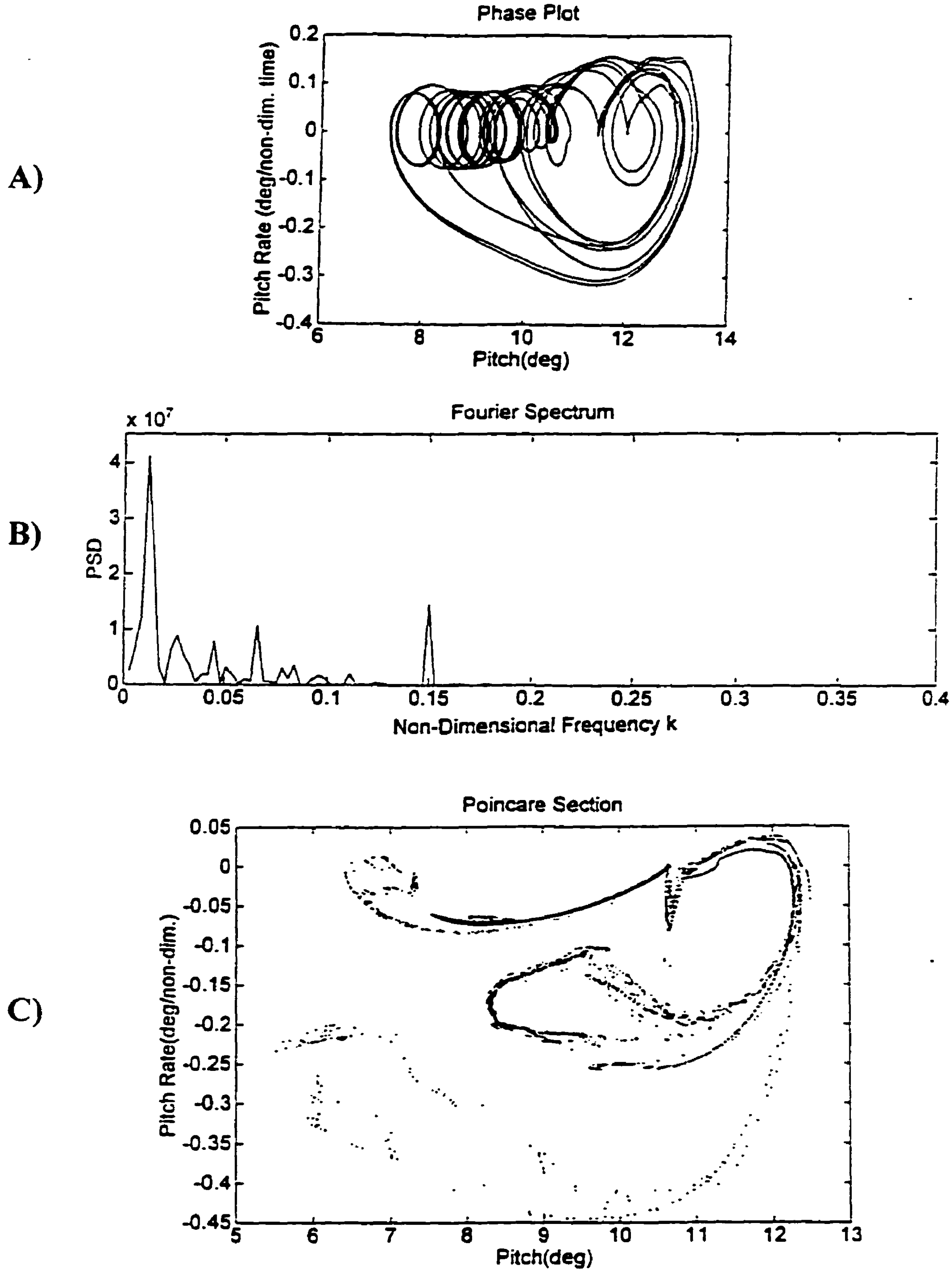

Figure 6.27: Case II, Region 1, Example 4; a) Phase Plot b) Fourier Spectrum c) Poincaré Section: k=0.15, $\alpha_{mean} = 6$ deg, U^*=13.5, Qo=2.1x10^{-4}.

A)

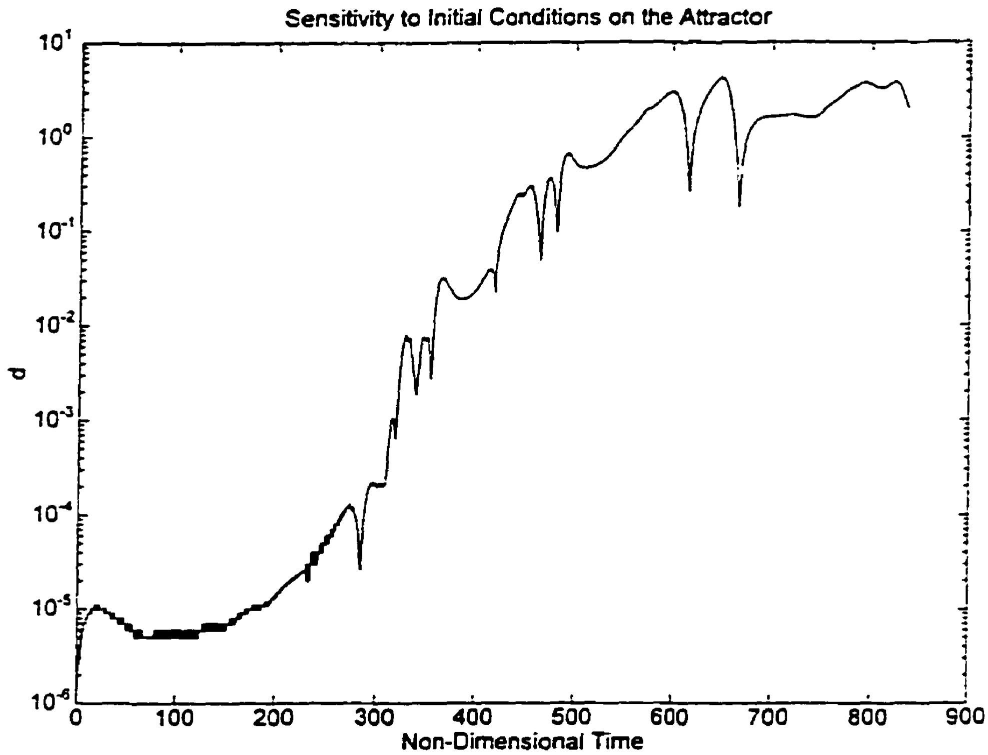

B)

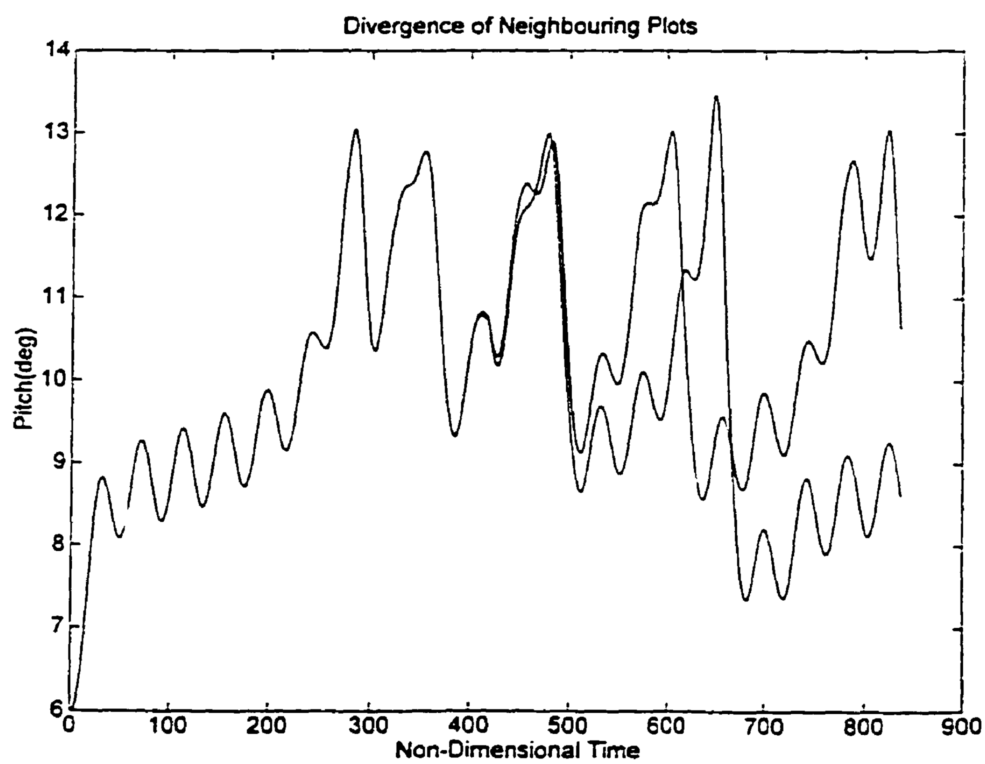

Figure 6.28: Case II, Region 1, Example 4; a) Sensitivity to Initial Conditions (Lyapunov Exponent) b) Divergence of Neighbouring Plots: k=0.15, $\alpha_{mean} = 6$ deg, U^*=13.5, Qo=2.1x10^{-4}.

A)

B)

C)

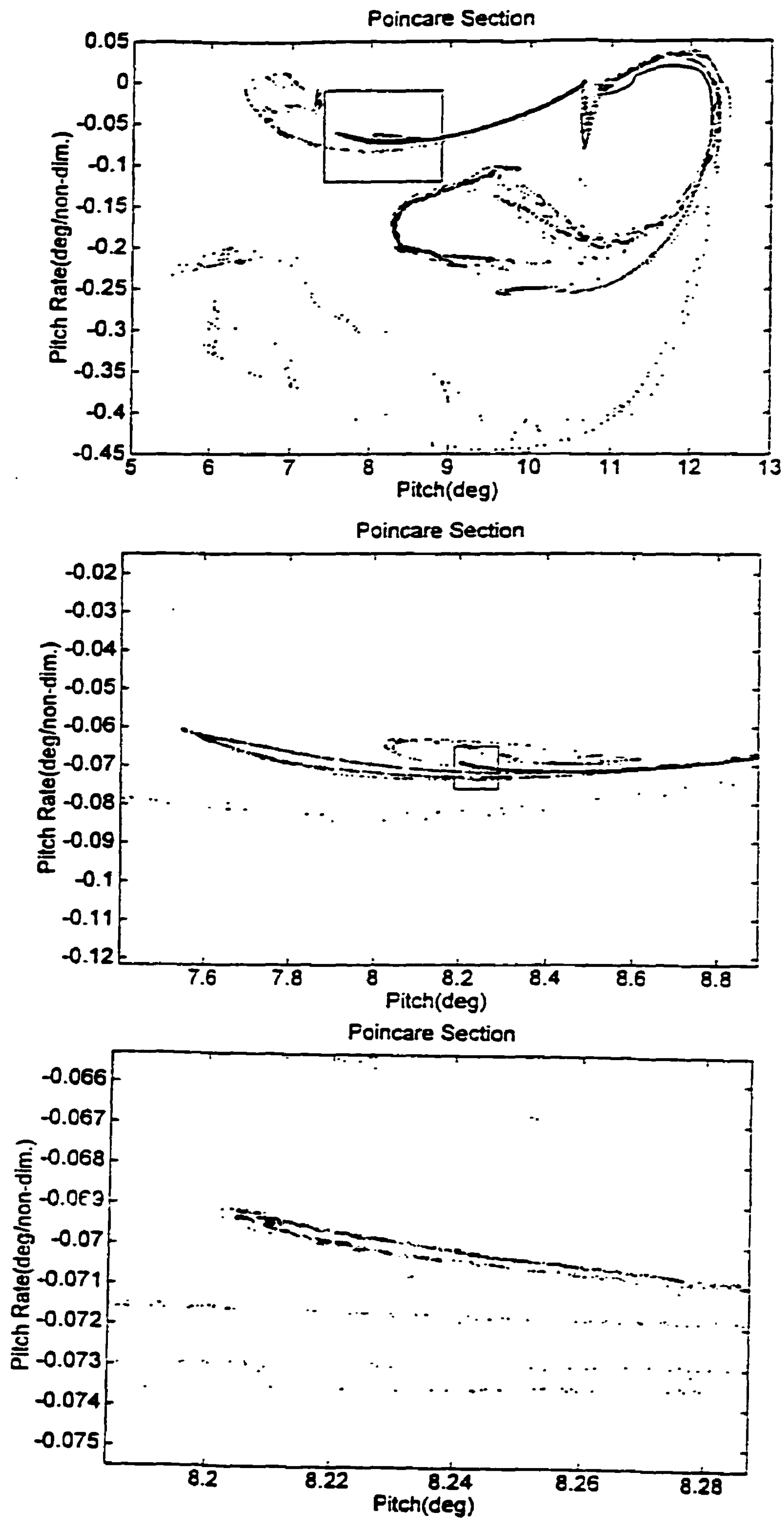

Figure 6.29: Case II, Region 1, Example 4; Magnified Poincaré Section a) Regular b) Level 1 c) Level 2: k=0.15, $\alpha_{mean}=6$ deg, U^*=13.5, Qo=2.1x10^{-4}.

A)

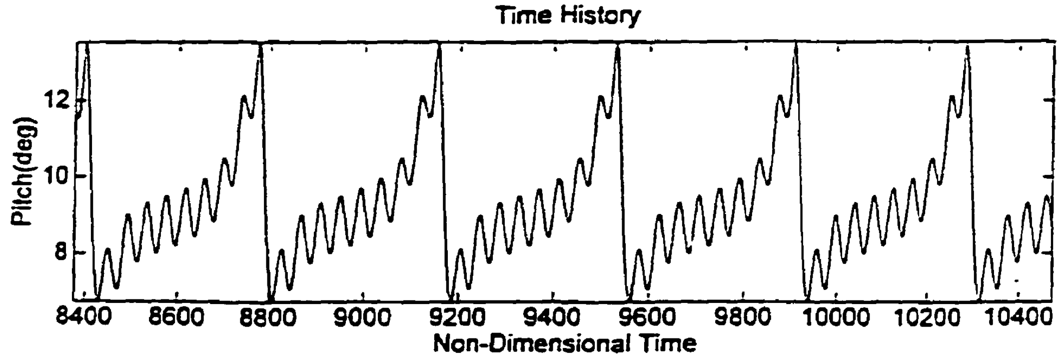

B)

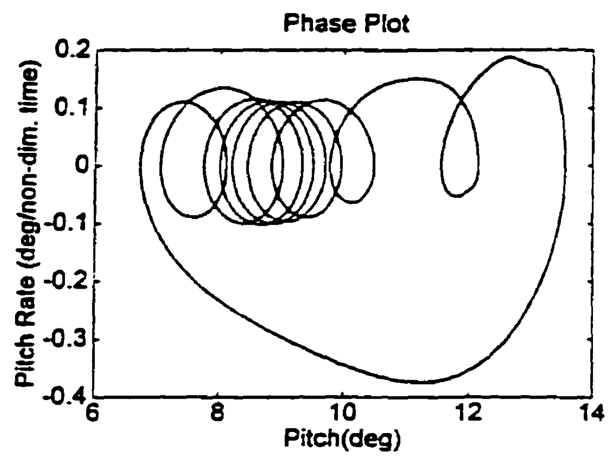

C)

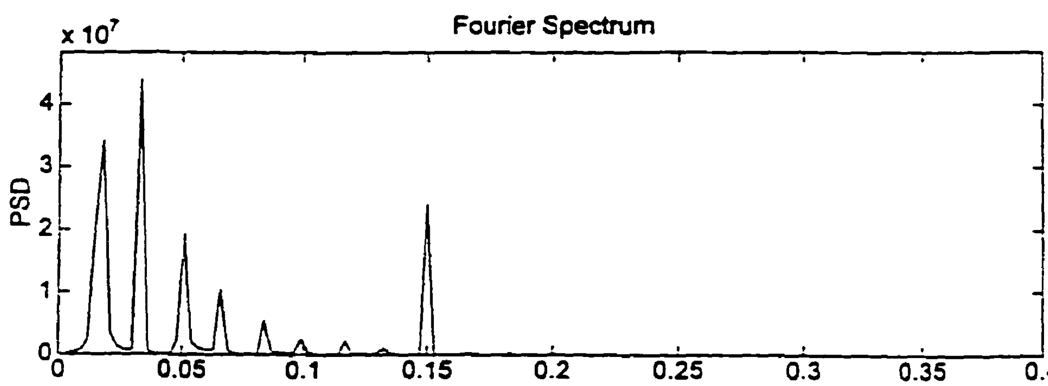

Figure 6.30: Case II, Region 2, Example 1; a) Time History b) Phase Plot c) Fourier Spectrum d) Poincaré Section e) Long Term Behaviour: k=0.15, $\alpha_{mean} = 6$ deg, U^*=13.5, Qo=2.8x10^{-4}.

D)

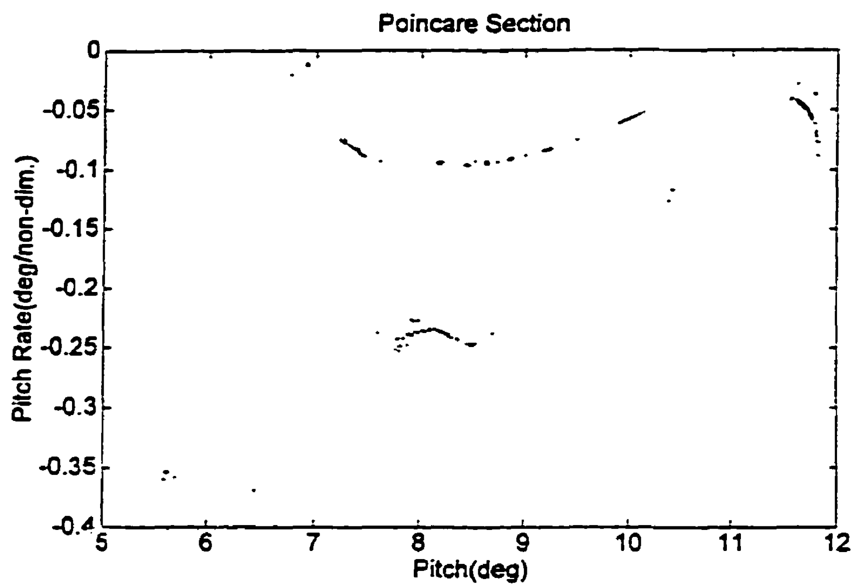
Poincare Section
Pitch Rate(deg/non-dim.)
0
-0.05
-0.1
-0.15
-0.2
-0.25
-0.3
-0.35
-0.4
5
6
7
8
9
10
11
12
Pitch(deg)

E)

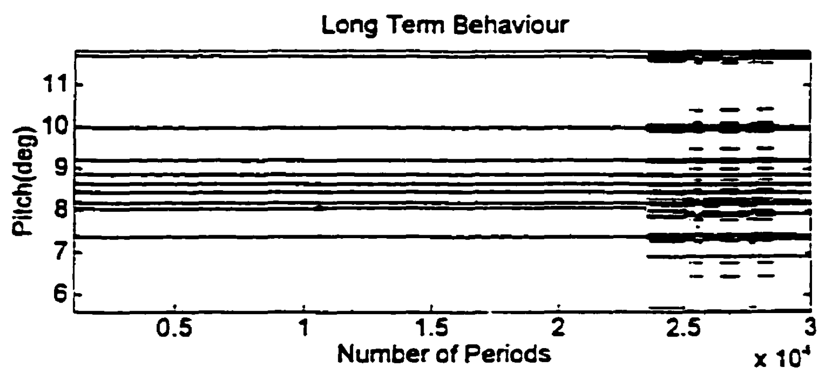
Long Term Behaviour
Pitch(deg)
11
10
9
8
7
6
0.5
1
1.5
2
2.5
3
Number of Periods
x 10⁴

A)
B)
C)

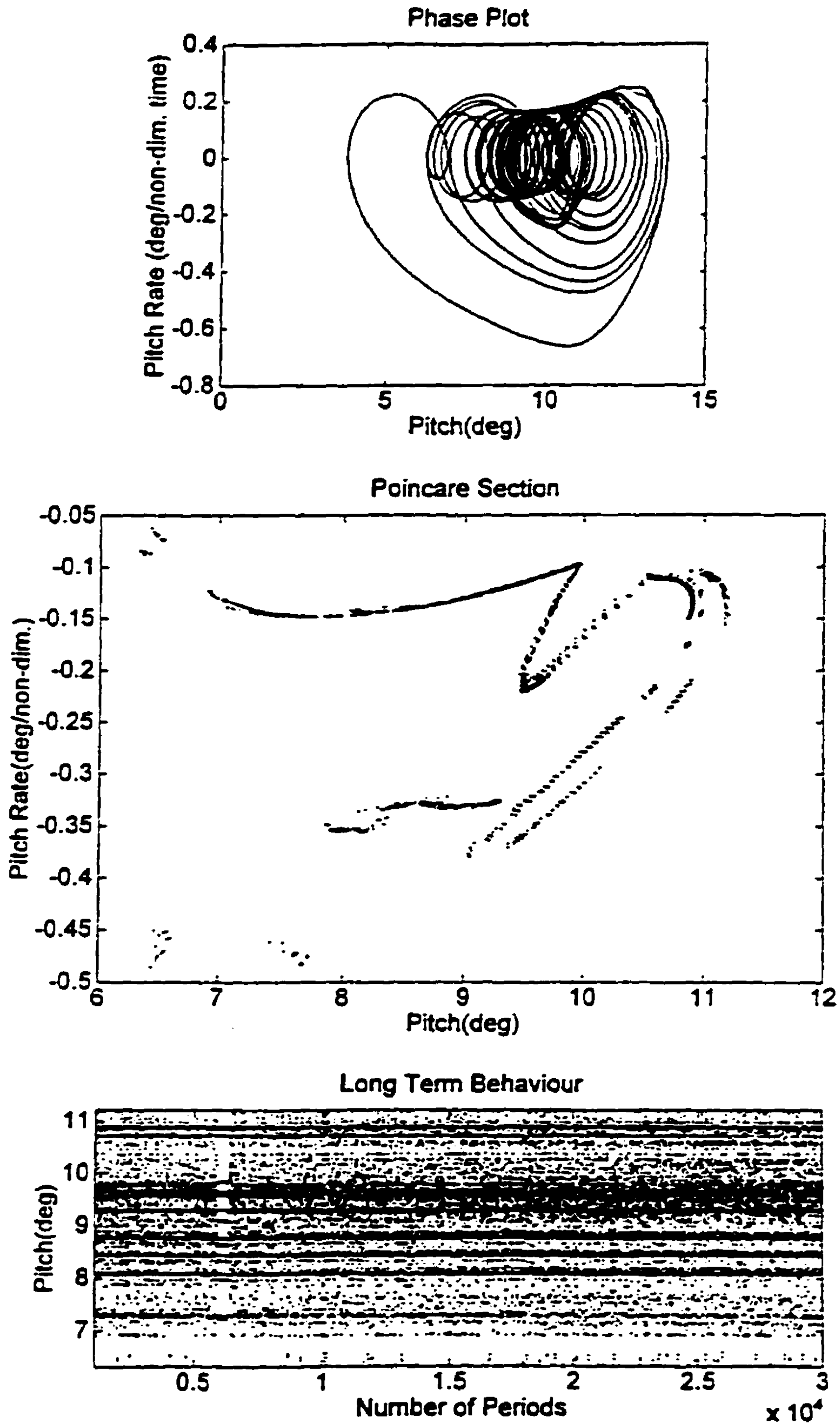

Figure 6.31: Case II, Region 2, Example 3; a) Phase Plot b) Poincaré Section c) Long Term Behaviour: k=0.15, $\alpha_{mean}=6$ deg, U^*=13.5, Qo=4.2x10^{-4}.

A)

B)

C)

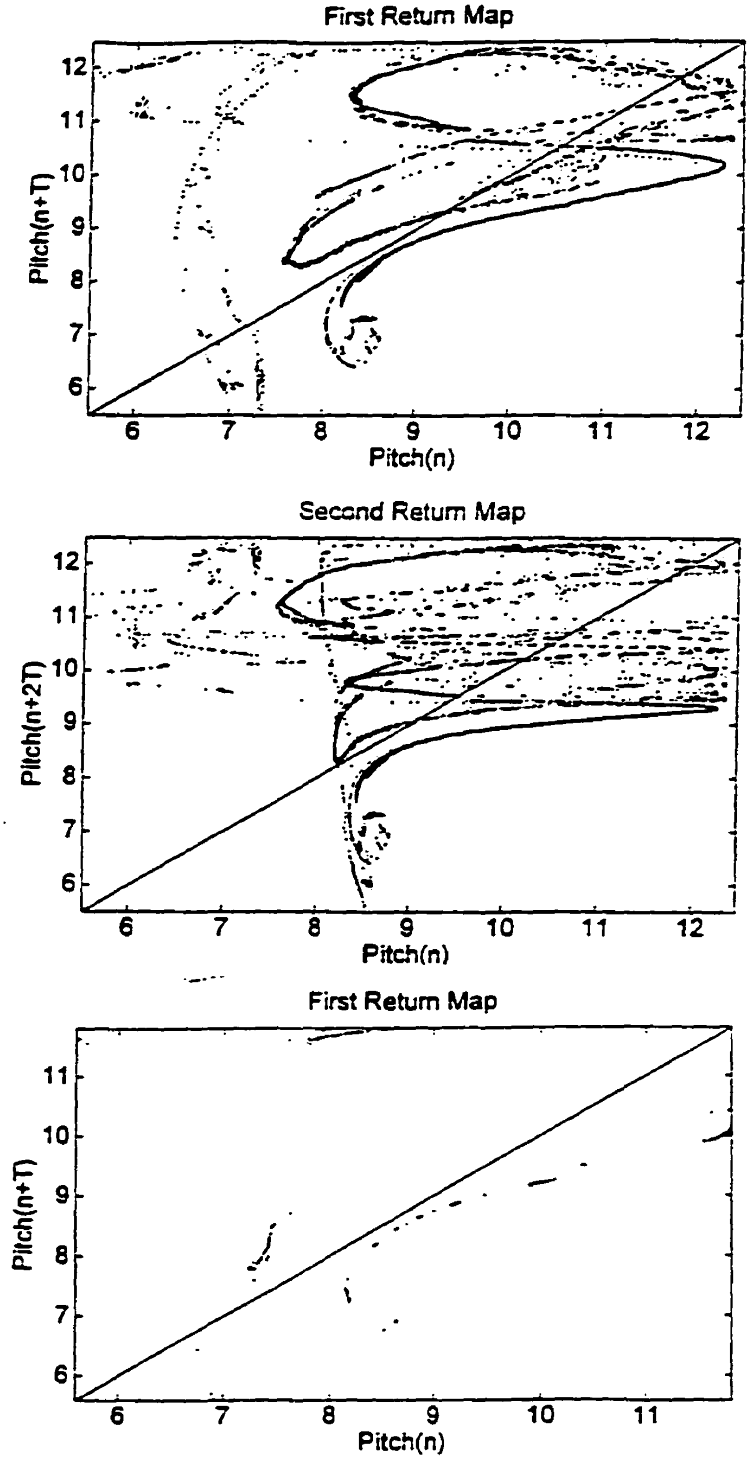

Figure 6.32: Case II, Return Maps; Region 1, Example 4: a) First b) Second; Region 2, Example 1: c) First d) Second; Region 2, Example 3: e) First f) Second; k=0.15, α_{mean} = 6 deg, U^*=13.5, Qo=2.1x10^{-4}, Qo=2.8x10^{-4}, Qo=4.2x10^{-4}.

D)

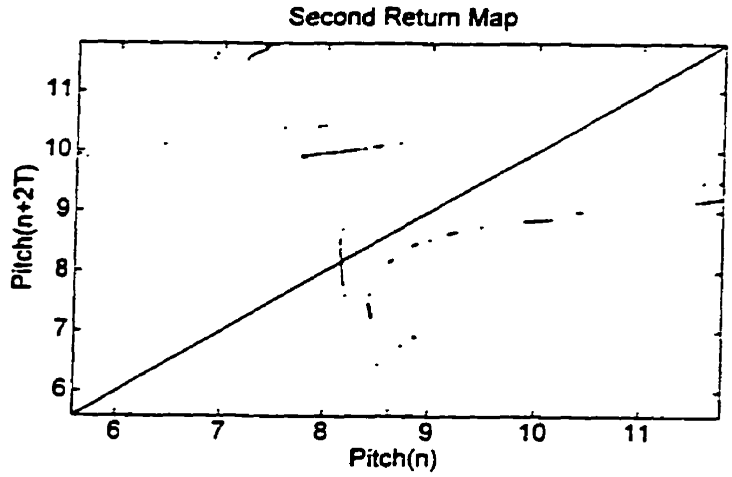
Second Return Map
Pitch(n+2T)
11
10
9
8
7
6
6
7
8
9
10
11
Pitch(n)

E)

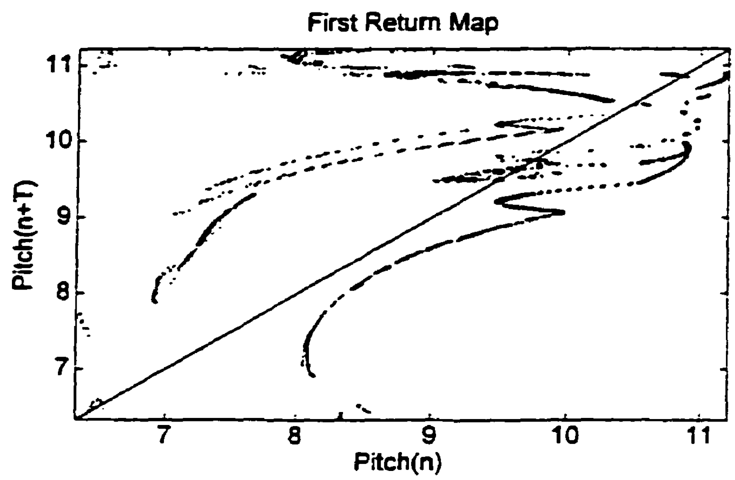
First Return Map
Pitch(n+T)
11
10
9
8
7
7
8
9
10
11
Pitch(n)

F)

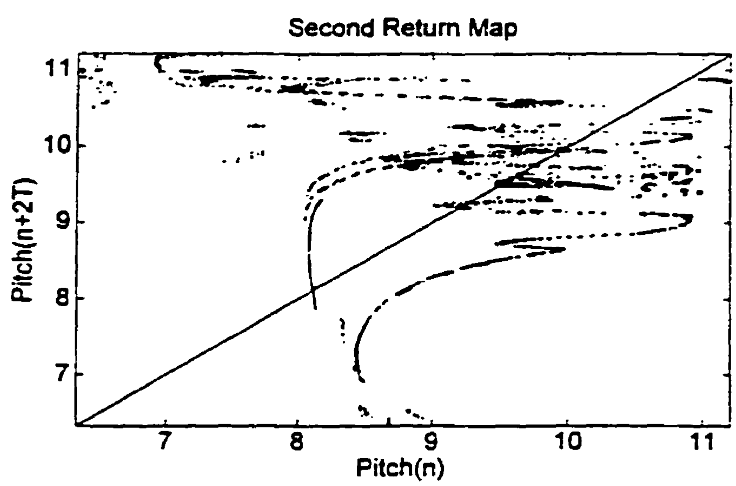
Second Return Map
Pitch(n+2T)
11
10
9
8
7
7
8
9
10
11
Pitch(n)

A)

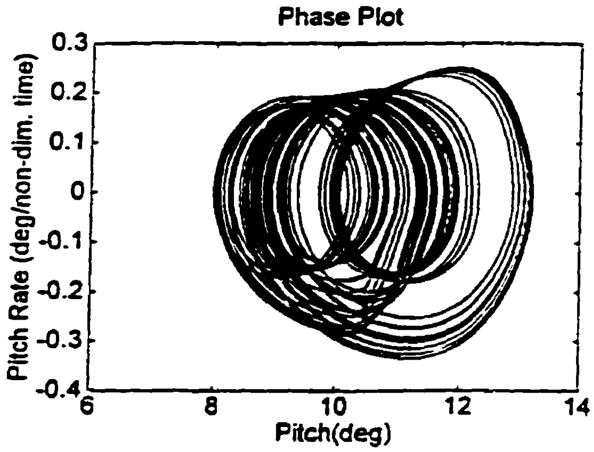

B)

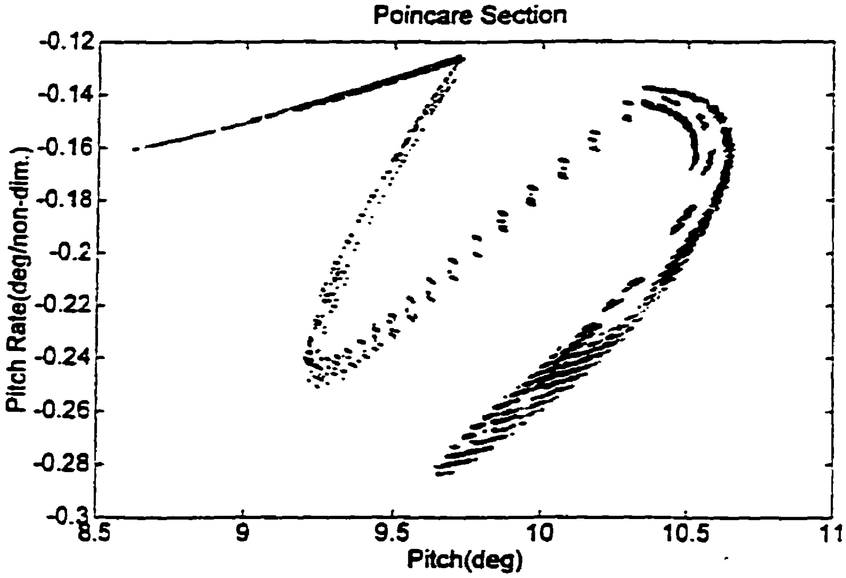

C)

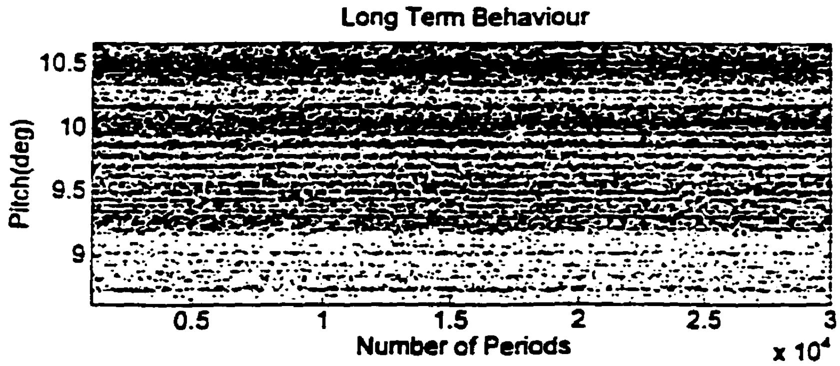

Figure 6.33: Case II, Region 3, Example 1; a) Phase Plot b) Poincaré Section c) Long Term Behaviour: k=0.15, $\alpha_{mean} = 6$ deg, U*=13.5, Qo=4.9x10^{-4}.

A)

B)

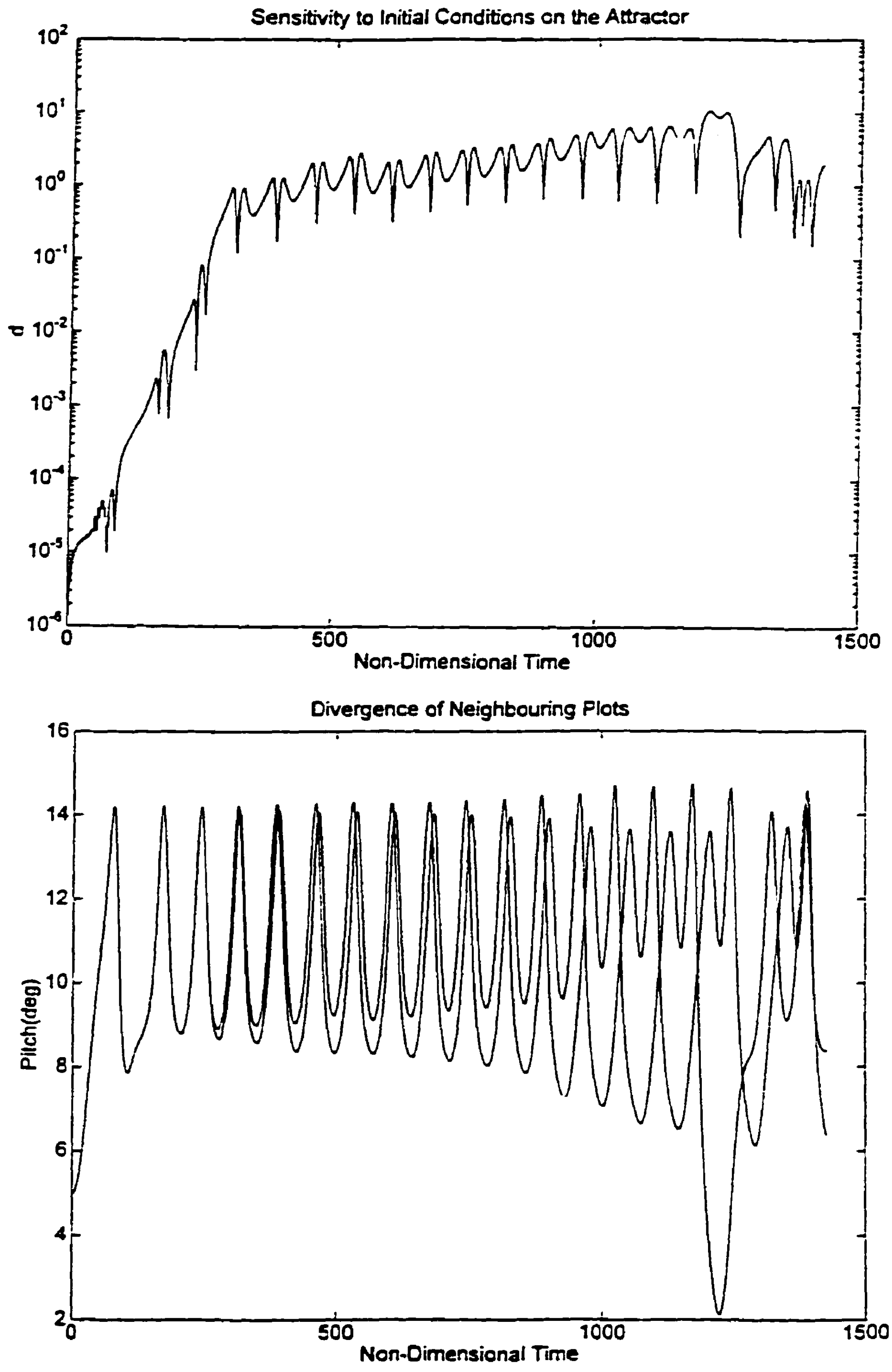

Figure 6.34: Case II, Region 3, Example 1; a) Sensitivity to Initial Conditions (Lyapunov Exponent) b) Divergence of Neighbouring Plots: k=0.15, $\alpha_{mean} = 6$ deg, U^*=13.5, Qo=4.9x10^{-4}.

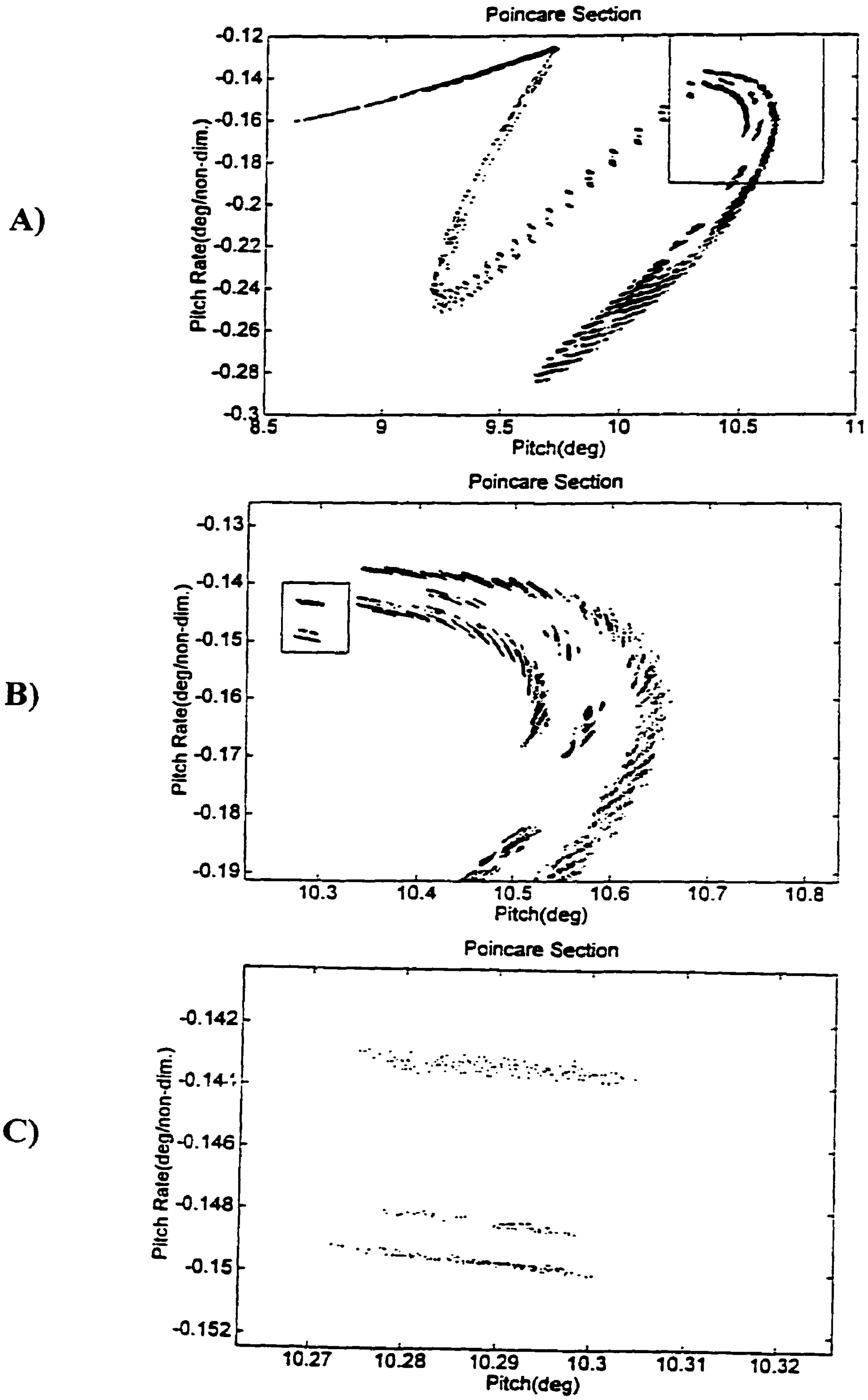

Figure 6.35: Case II, Region 3, Example 1; Magnified Poincaré Section a) Regular b) Level 1 c) Level 2: k=0.15, $\alpha_{mean}=6$ deg, U^*=13.5, Qo=4.9x10^{-4}.

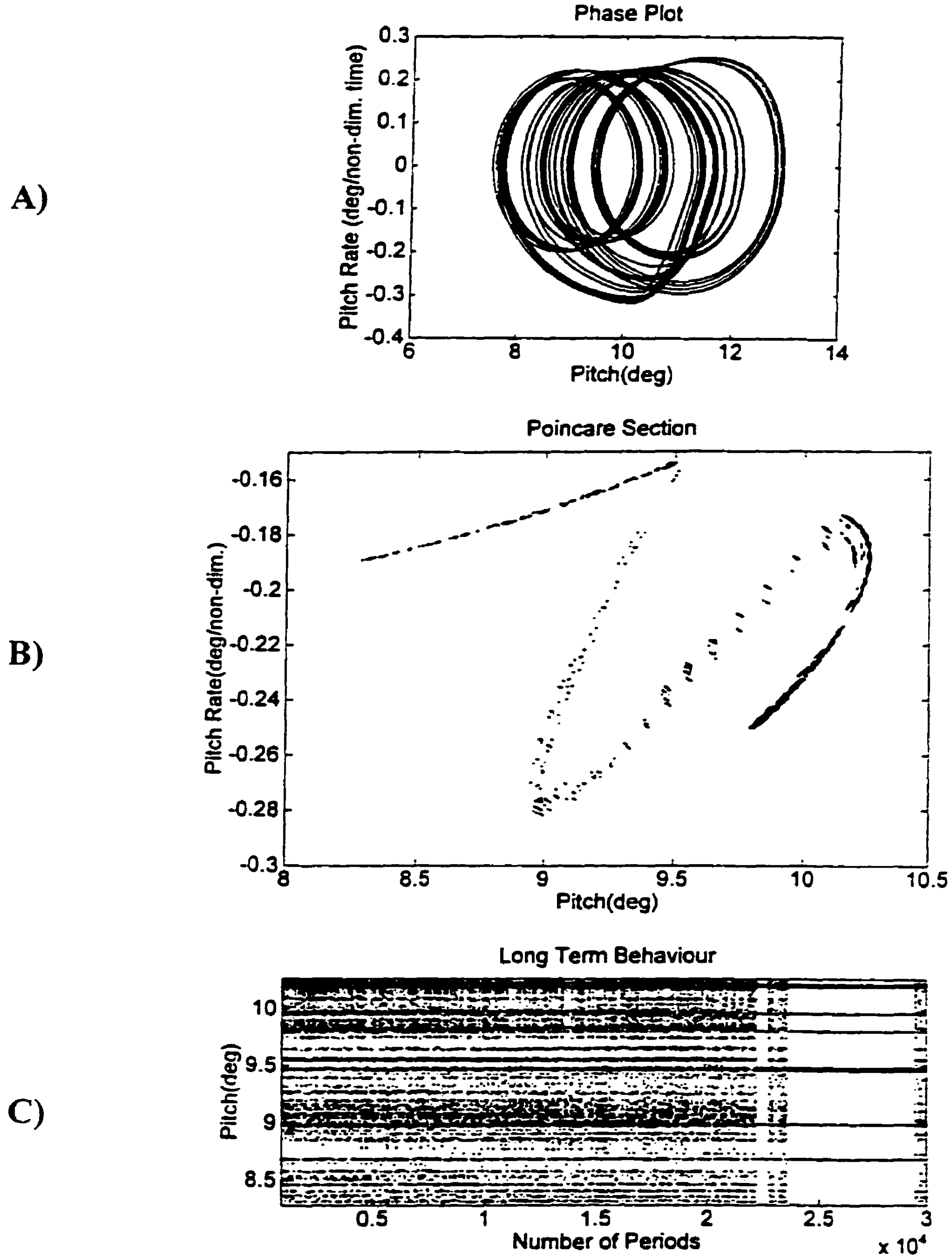

Figure 6.36: Case II, Region 3, Example 2; a) Phase Plot b) Poincaré Section c) Long Term Behaviour: k=0.15, $\alpha_{mean}=6$ deg, U^*=13.5, $Qo=5.6\text{x}10^{-4}$.

A)

B)

C)

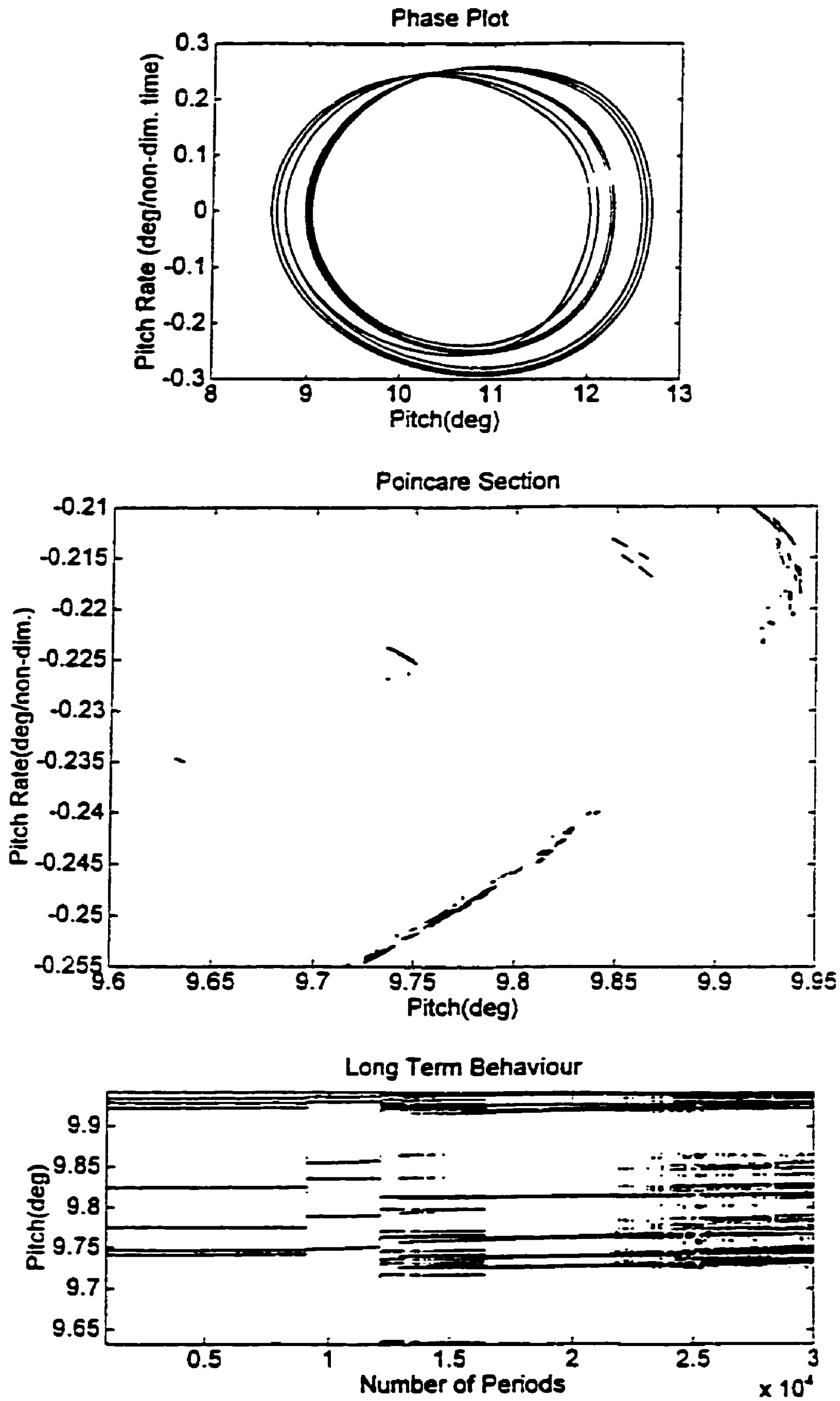

Figure 6.37: Case II, Region 3, Example 3; a) Phase Plot b) Poincaré Section c) Long Term Behaviour: k=0.15, $\alpha_{mean}=6$ deg, U^*=13.5, Qo=6.3x10^{-4}.

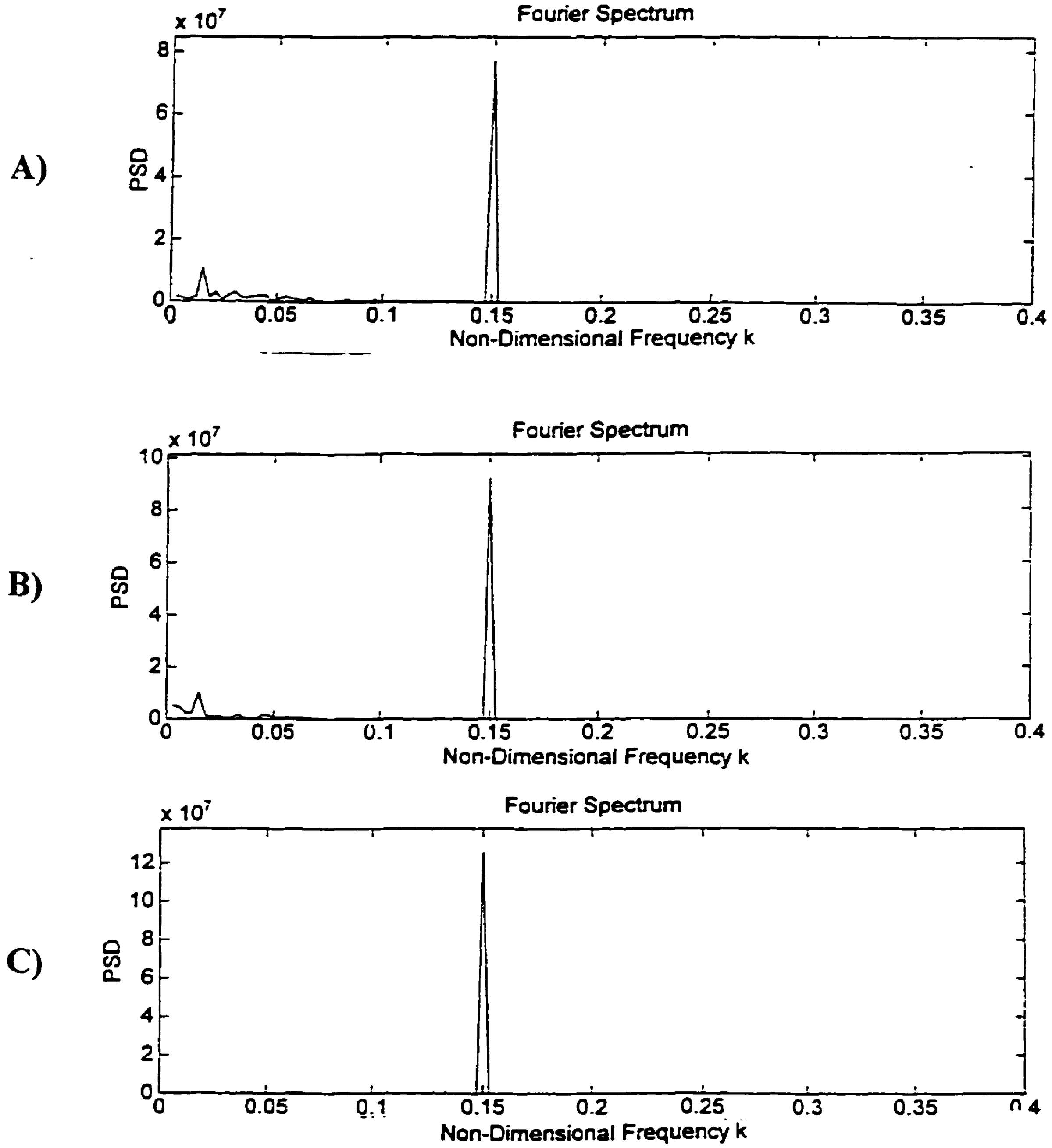

Figure 6.38: Case II, Region 3, Examples 1,2,3; Fourier Spectra a) Example 1 b) Example 2 c) Example 3: k=0.15, $\alpha_{mean} = 6$ deg, U^*=13.5, Qo=4.9x10^{-4}, Qo=5.6x10^{-4}, Qo=6.3x10^{-4}.

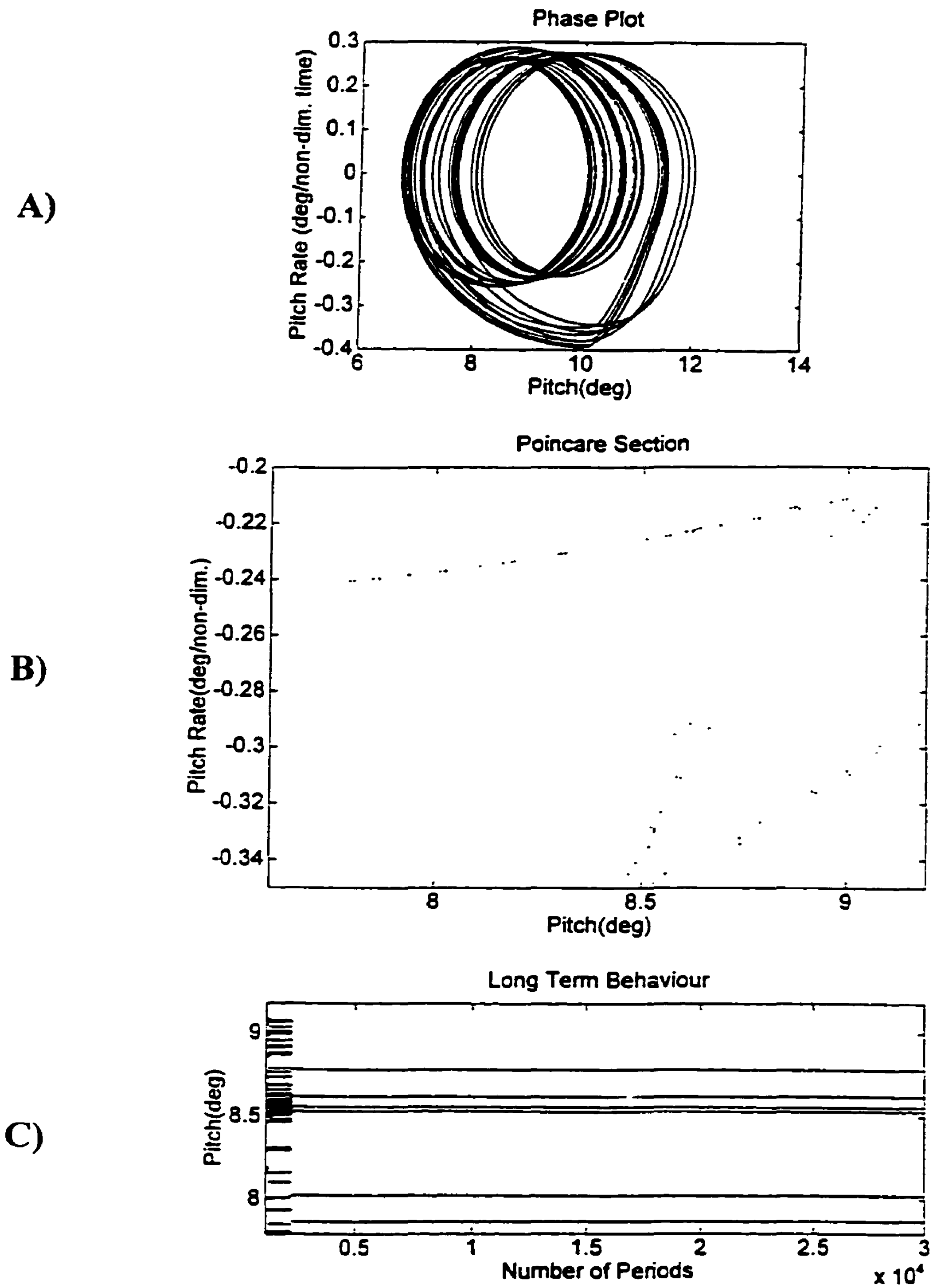

Figure 6.39: Case II, Region 4, Example 1; a) Phase Plot b) Poincaré Section c) Long Term Behaviour: k=0.15, $\alpha_{mean} = 6$ deg, U^*=13.5, Qo=7x10^{-4}.

A)

B)

C)

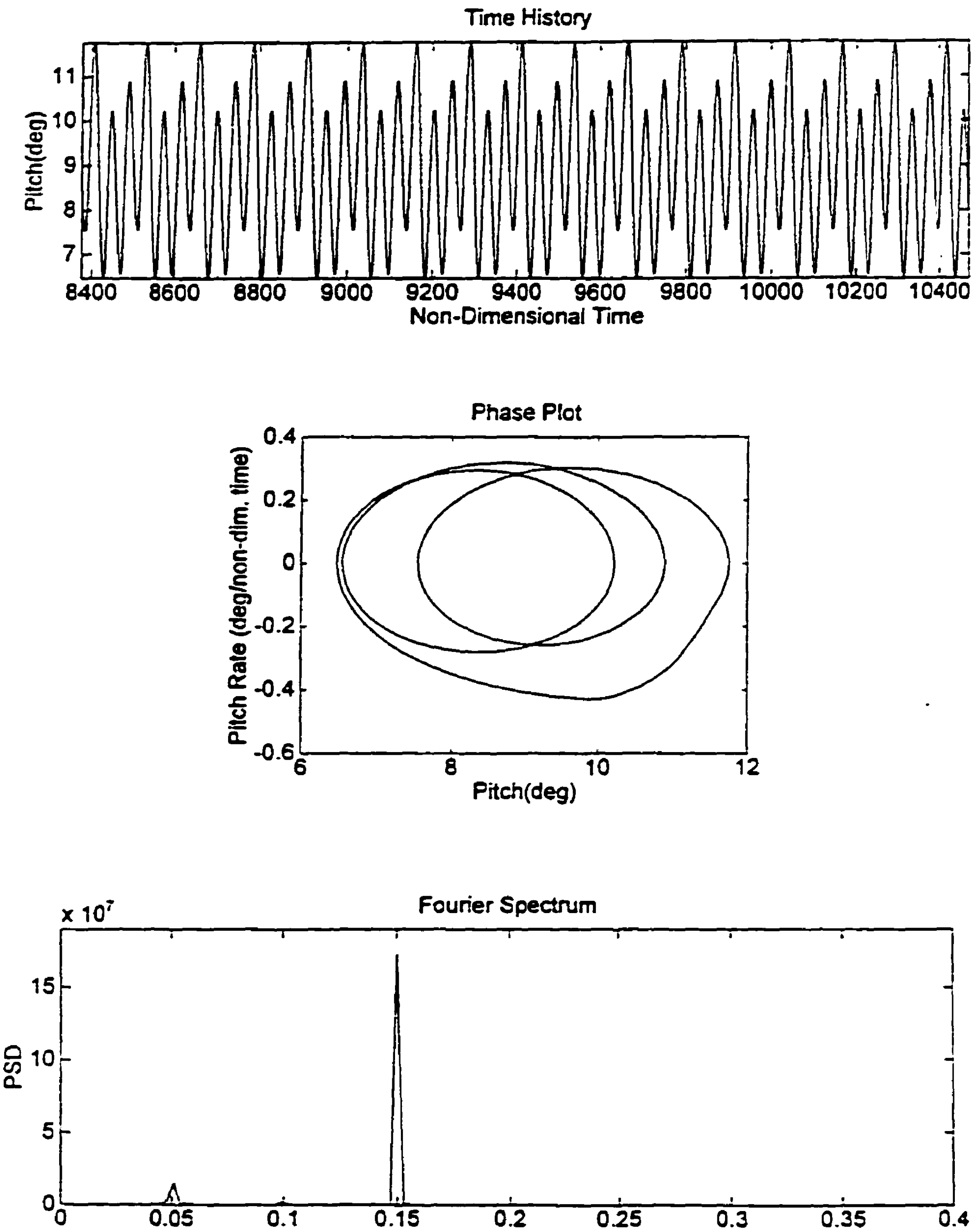

Figure 6.40: Case II, Region 4, Example 2; a) Time History b) Phase Plot c) Fourier Spectrum d) Poincaré Section e) Long Term Behaviour: k=0.15, $\alpha_{mean} = 6$ deg, U^*=13.5, Qo=7.7x10^{-4}.

D)

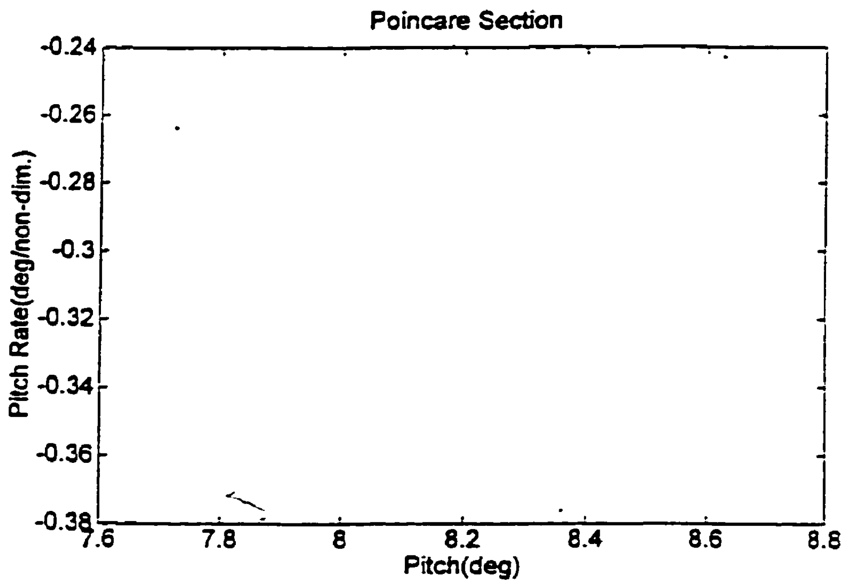
Poincare Section
-0.24
-0.26
-0.28
-0.3
-0.32
-0.34
-0.36
-0.38
Pitch Rate(deg/non-dim.)
7.6
7.8
8
8.2
8.4
8.6
8.8
Pitch(deg)

E)

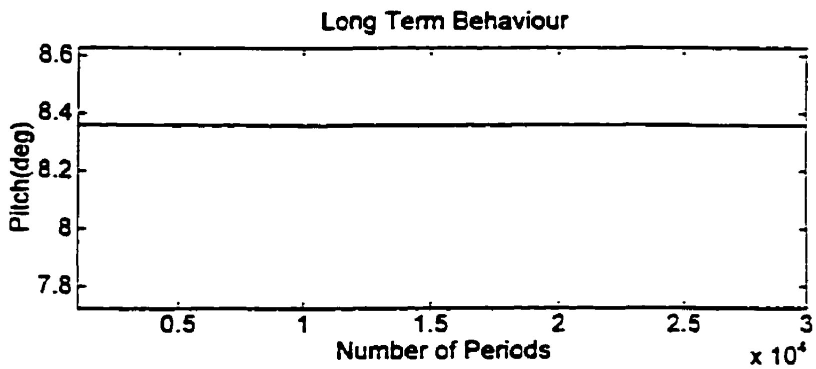
Long Term Behaviour
8.6
8.4
8.2
8
7.8
Pitch(deg)
0.5
1
1.5
2
2.5
3
Number of Periods
x 10^4

A)

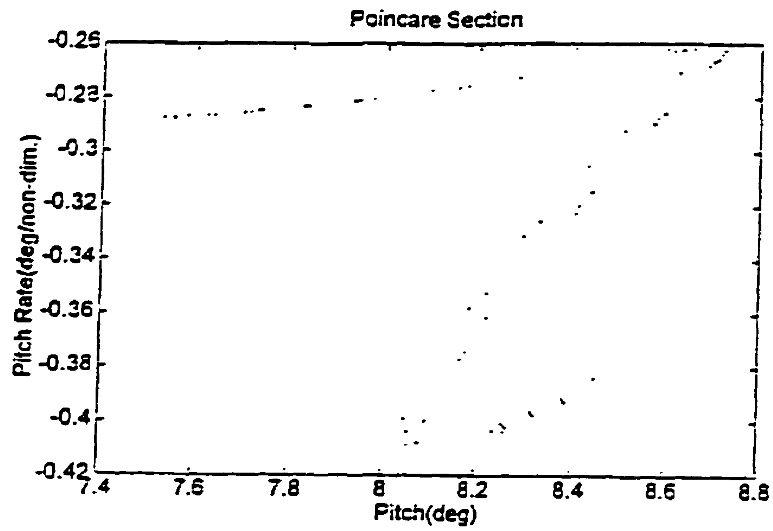

B)

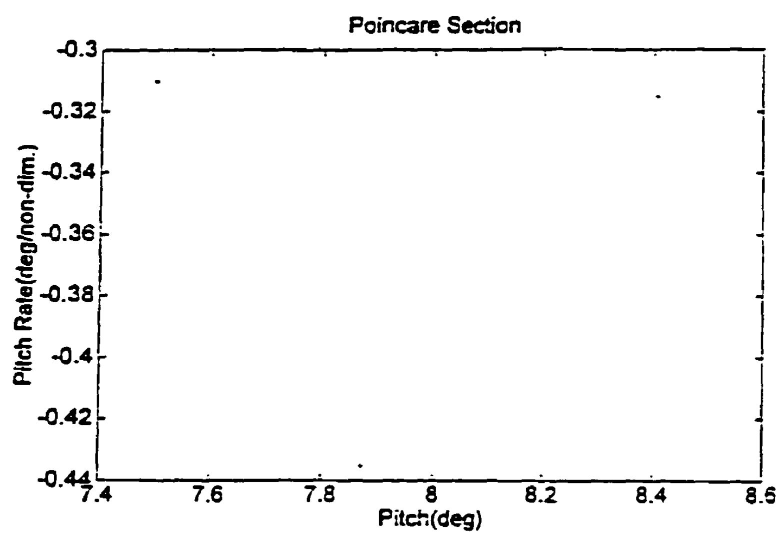

C)

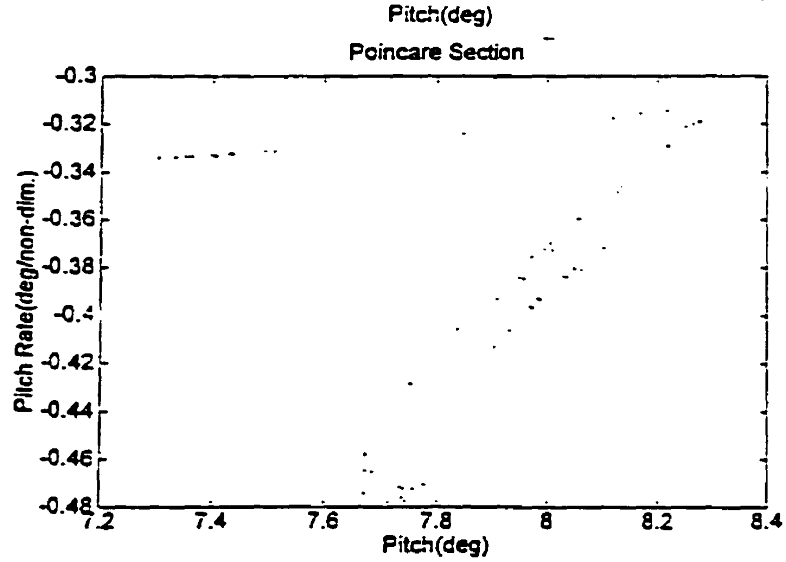

Figure 6.41: Case II, Region 4, Examples 3,4,5; Poincaré Sections a) Example 3 b) Example 4 c) Example 5: k=0.15, $\alpha_{mean} = 6$ deg, U^*=13.5, Qo=8.4x10^{-4}, Qo=9.1x10^{-4}, Qo=9.8x10^{-4}.

A)

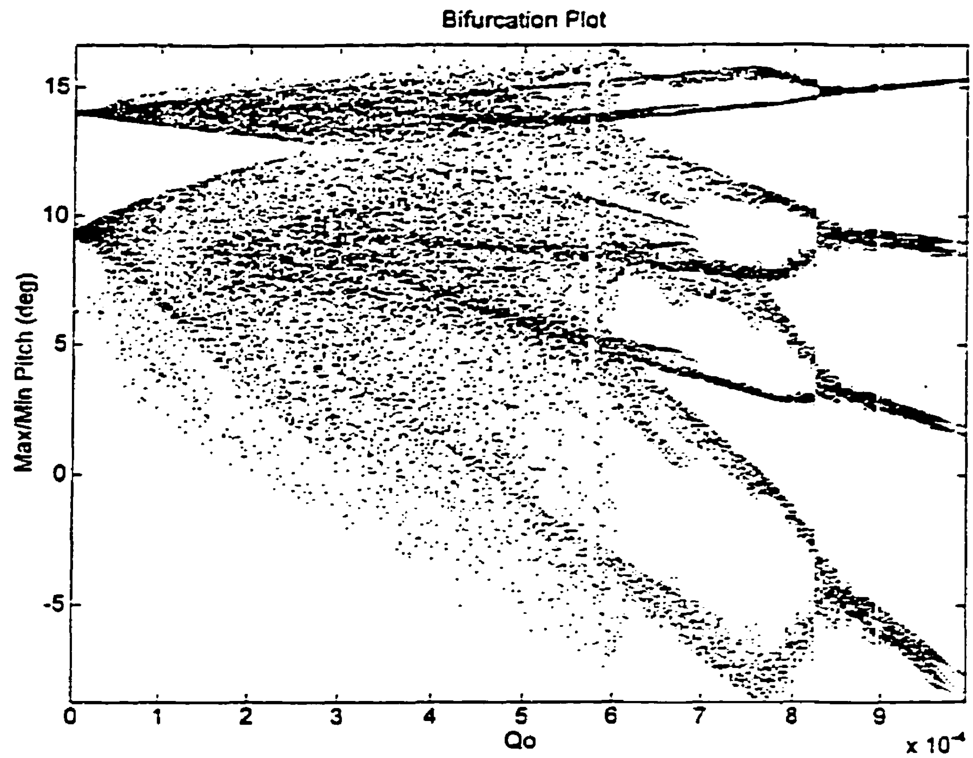

Case III

B)

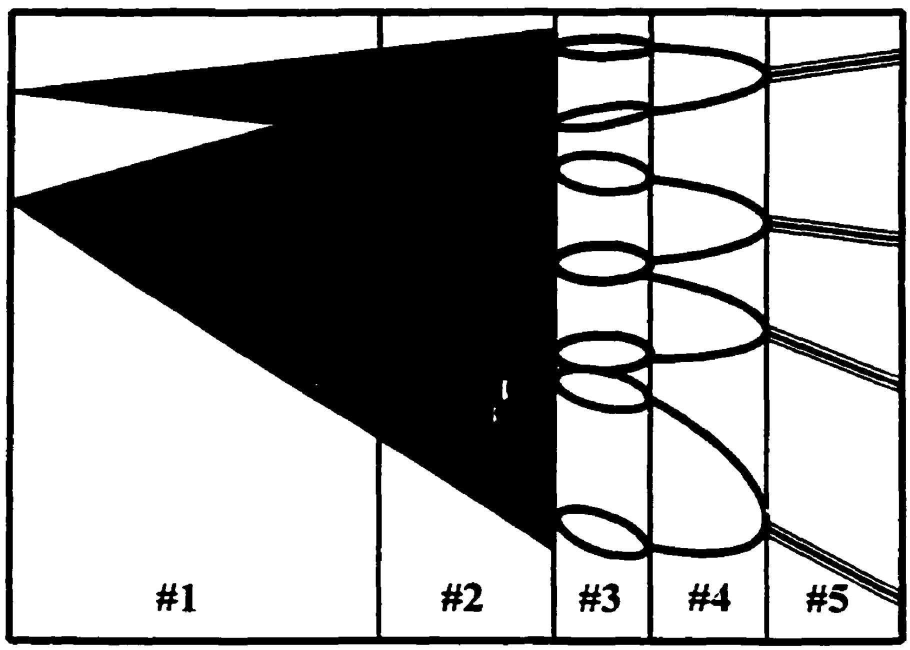

Figure 6.42: Case III; a) Bifurcation Plot b) Conceptual Drawing: k=0.1, α_{mean} = 5 deg, U*=20, 0<Qo<0.001.

A)

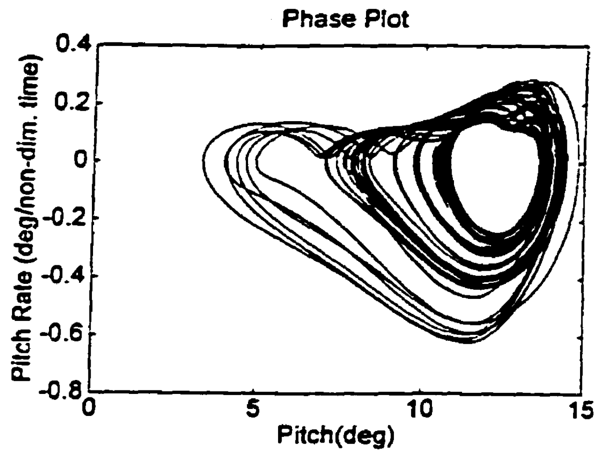

B)

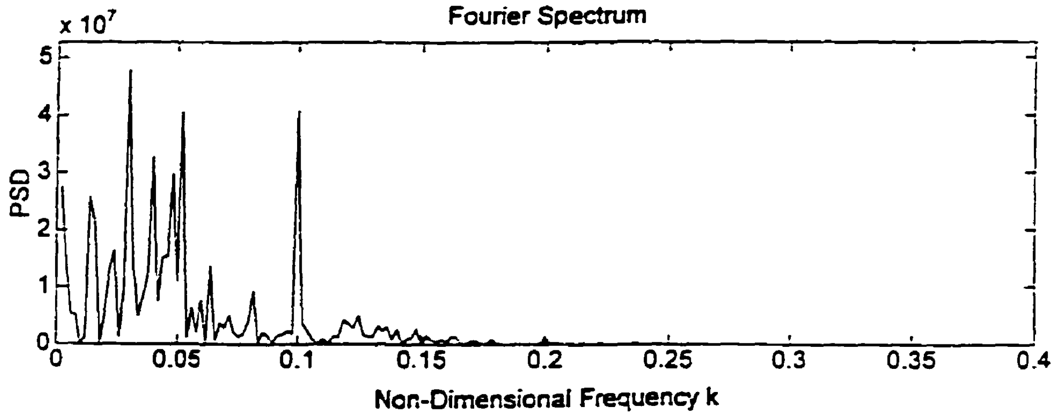

C)

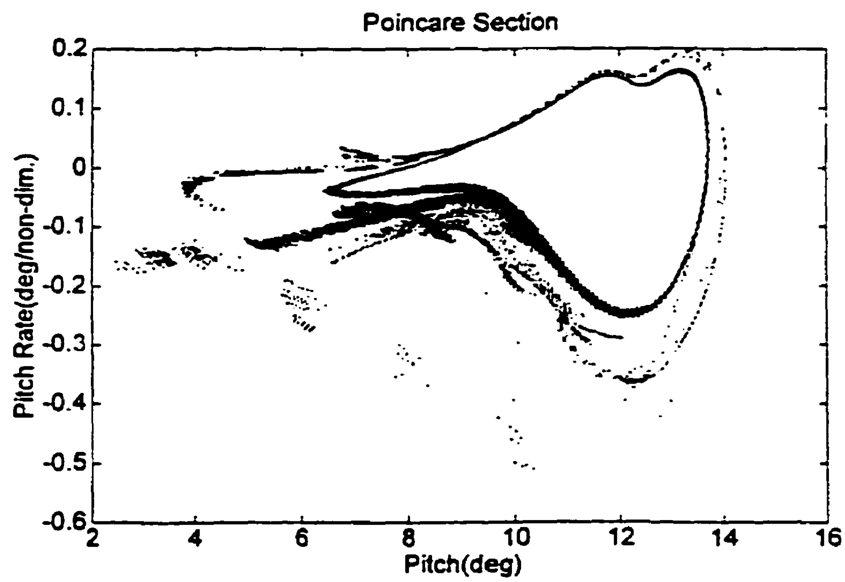

Figure 6.43: Case III, Region 1, Example 1; a) Phase Plot b) Fourier Spectrum c) Poincaré Section: *k*=0.1, $\alpha_{mean}=5$ deg , $U^*=20$, $Qo=1\times10^{-4}$.

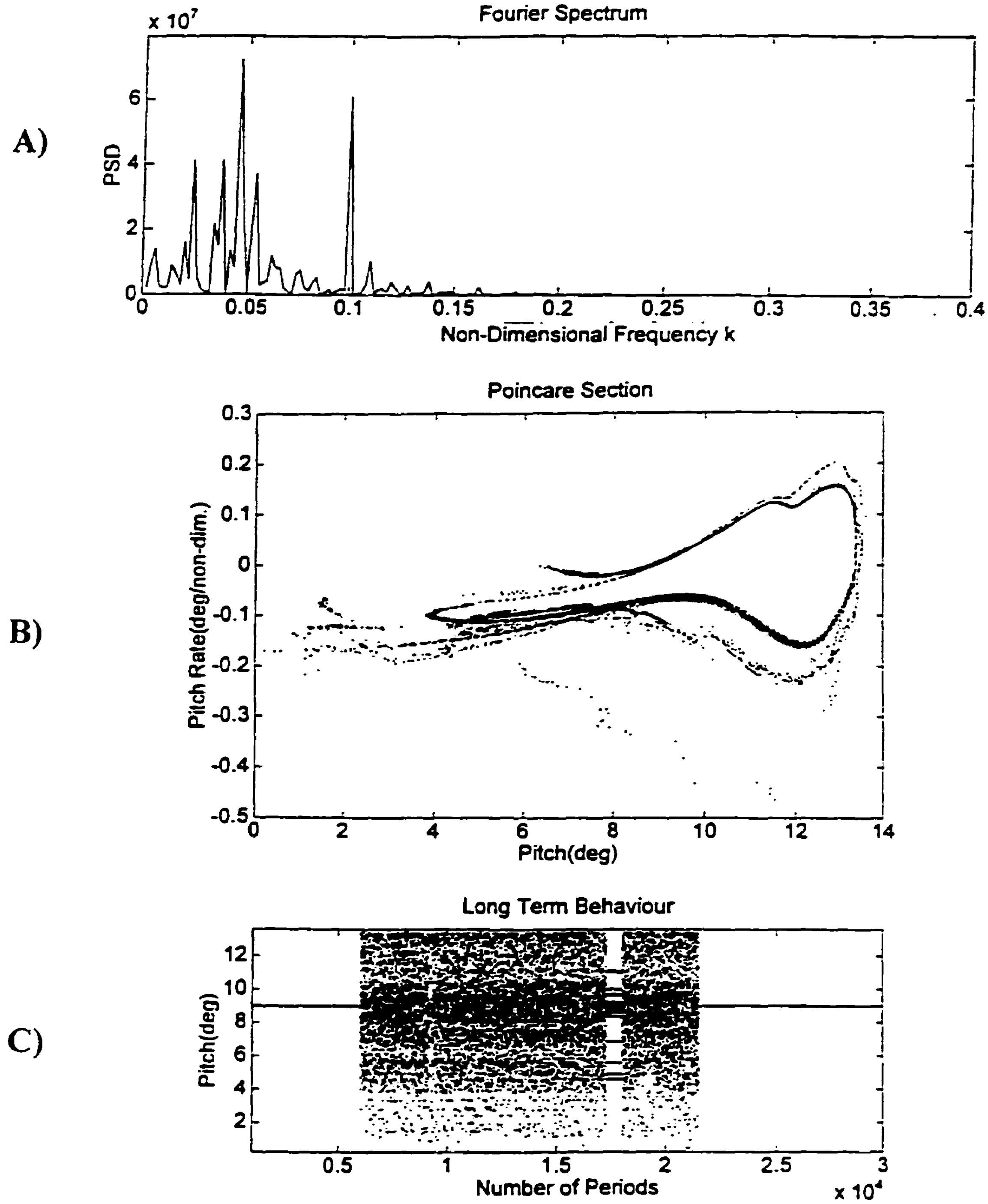

Figure 6.44: Case III, Region 1, Example 2; a) Fourier Spectrum b) Poincaré Section c) Long Term Behaviour: k=0.1, α_{mean}=5 deg , U^*=20, Qo=1.9x10^{-4}.

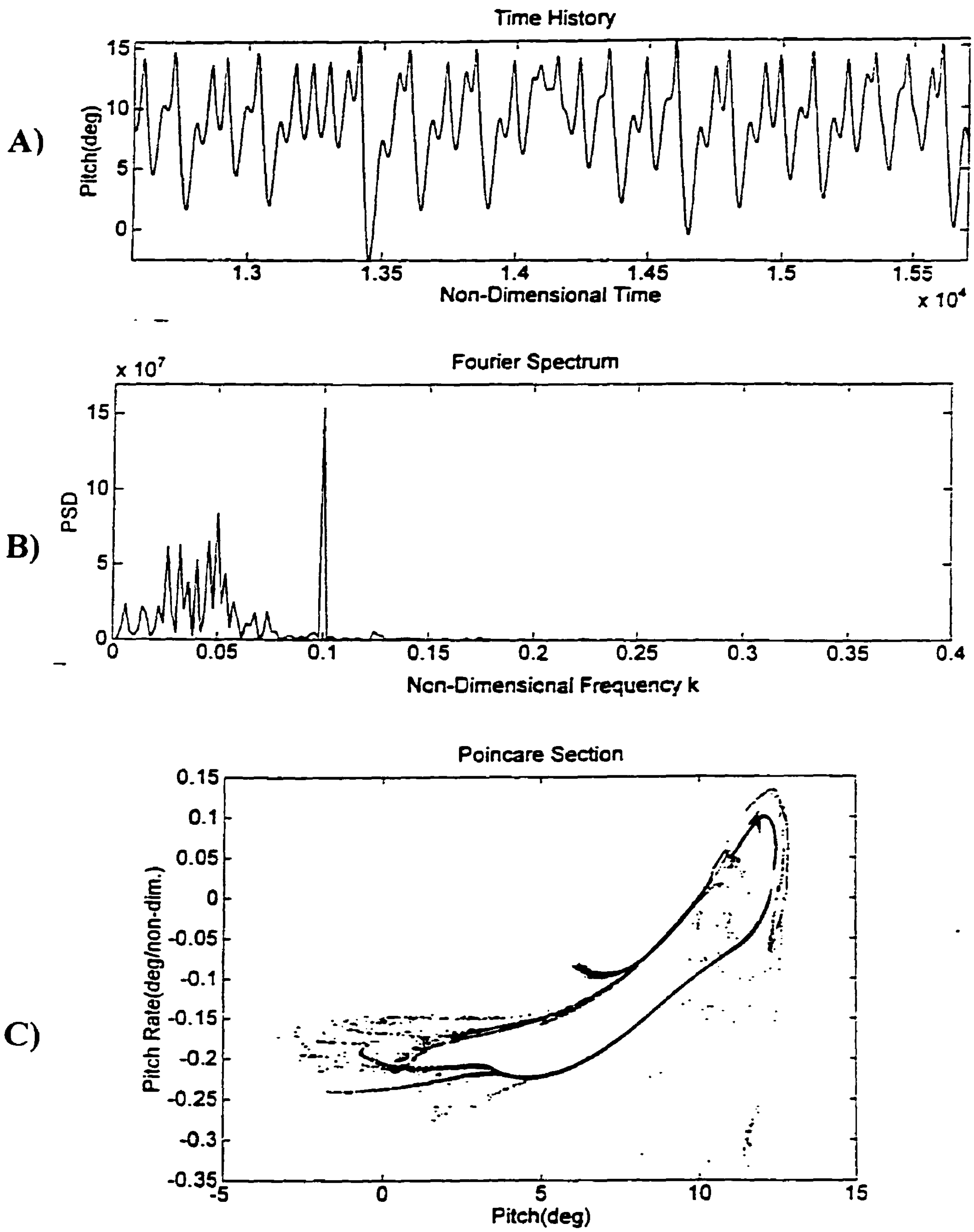

Figure 6.45: Case III, Region 1, Example 3; a) Time History b) Fourier Spectrum c) Poincaré Section: k=0.1, α_{mean}=5 deg, U^*=20, Qo=3.7x10^{-4}.

A)

B)

C)

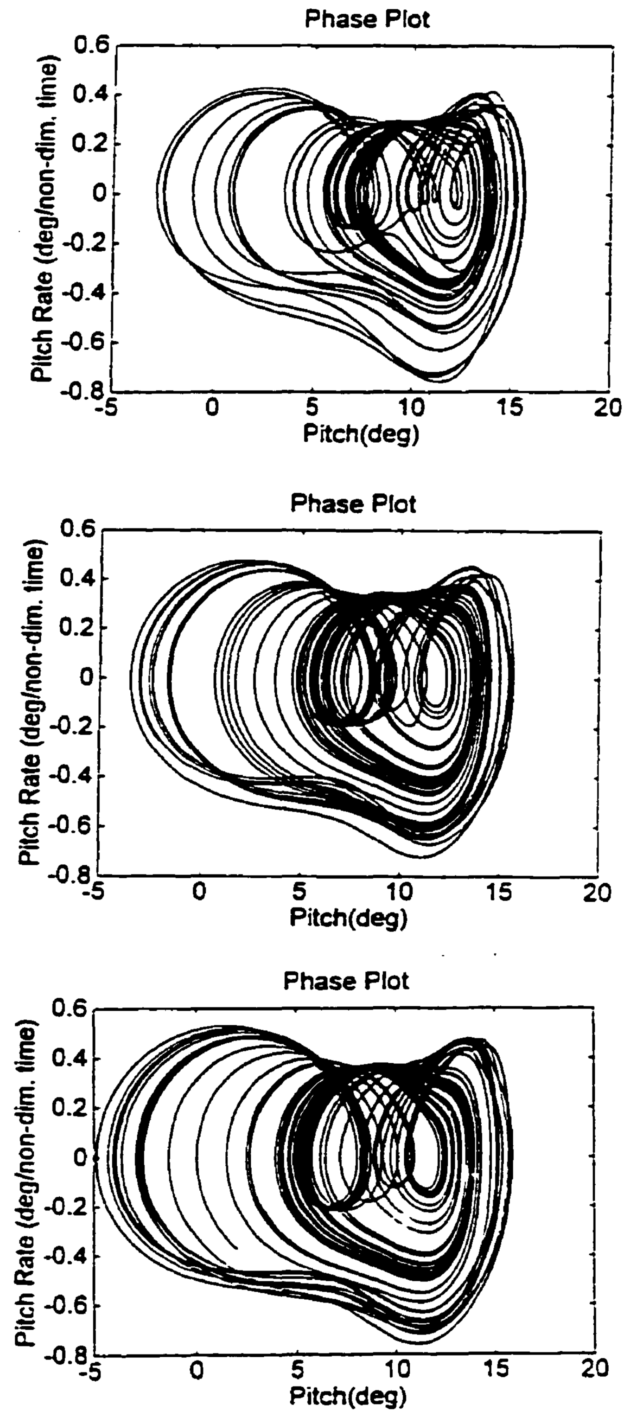

Figure 6.46: Case III, Region 2, Examples 1,2,3; Phase Plots a) Example 1 b) Example 2 c) Example 3: *k*=0.1, $\alpha_{mean}=5$ deg, *U=20, *Qo*=4.3x10^{-4}, *Qo*=5.3x10^{-4}, *Qo*=5.77x10^{-4}.**

A)

B)

C)

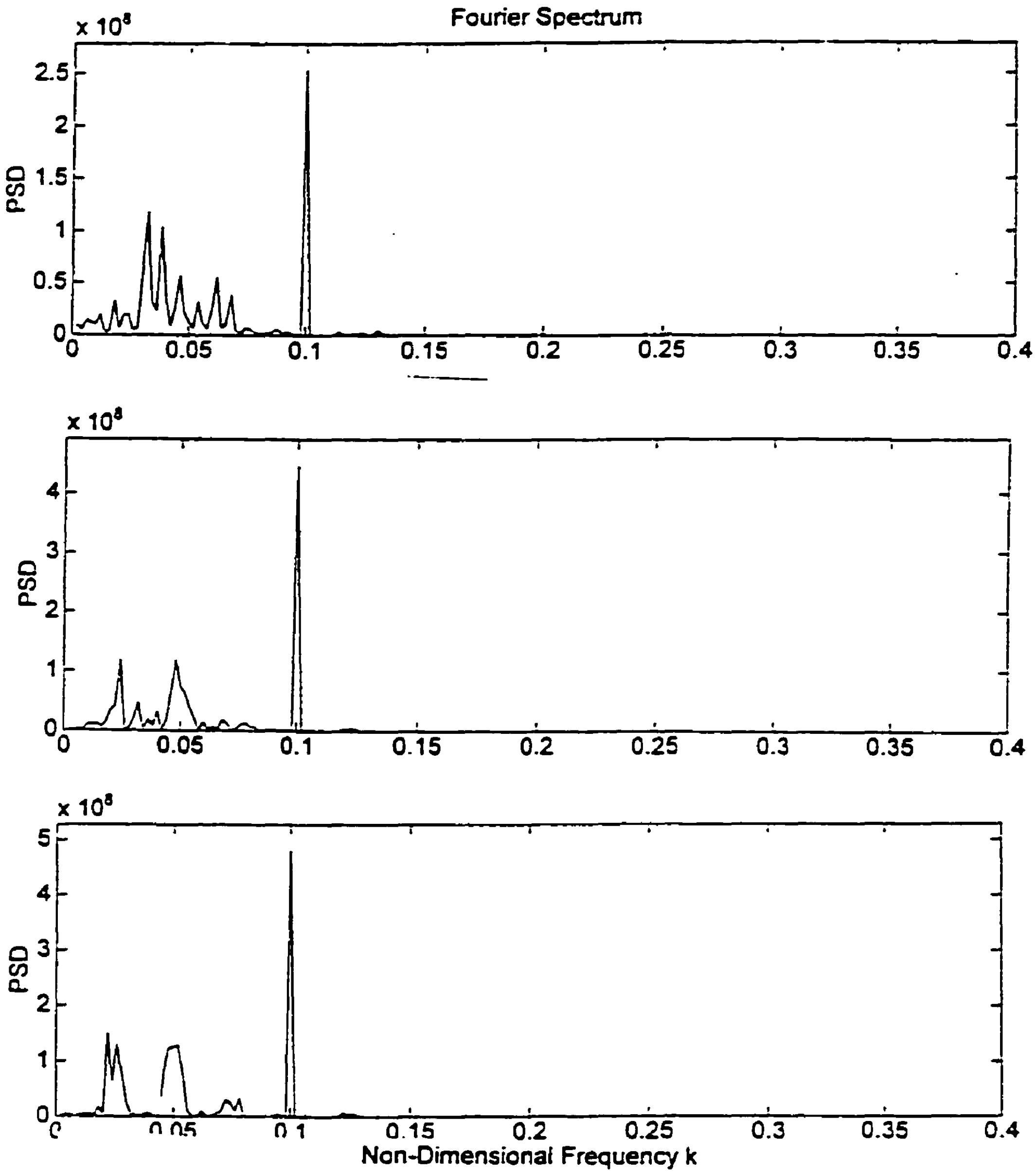

Figure 6.47: Case III, Region 2, Examples 1,2,3; Fourier Spectra a) Example 1 b) Example 2 c) Example 3: k=0.1, α_{mean}=5 deg, U^*=20, Qo=4.3x10^{-4}, Qo=5.3x10^{-4}, Qo=5.77x10^{-4}.

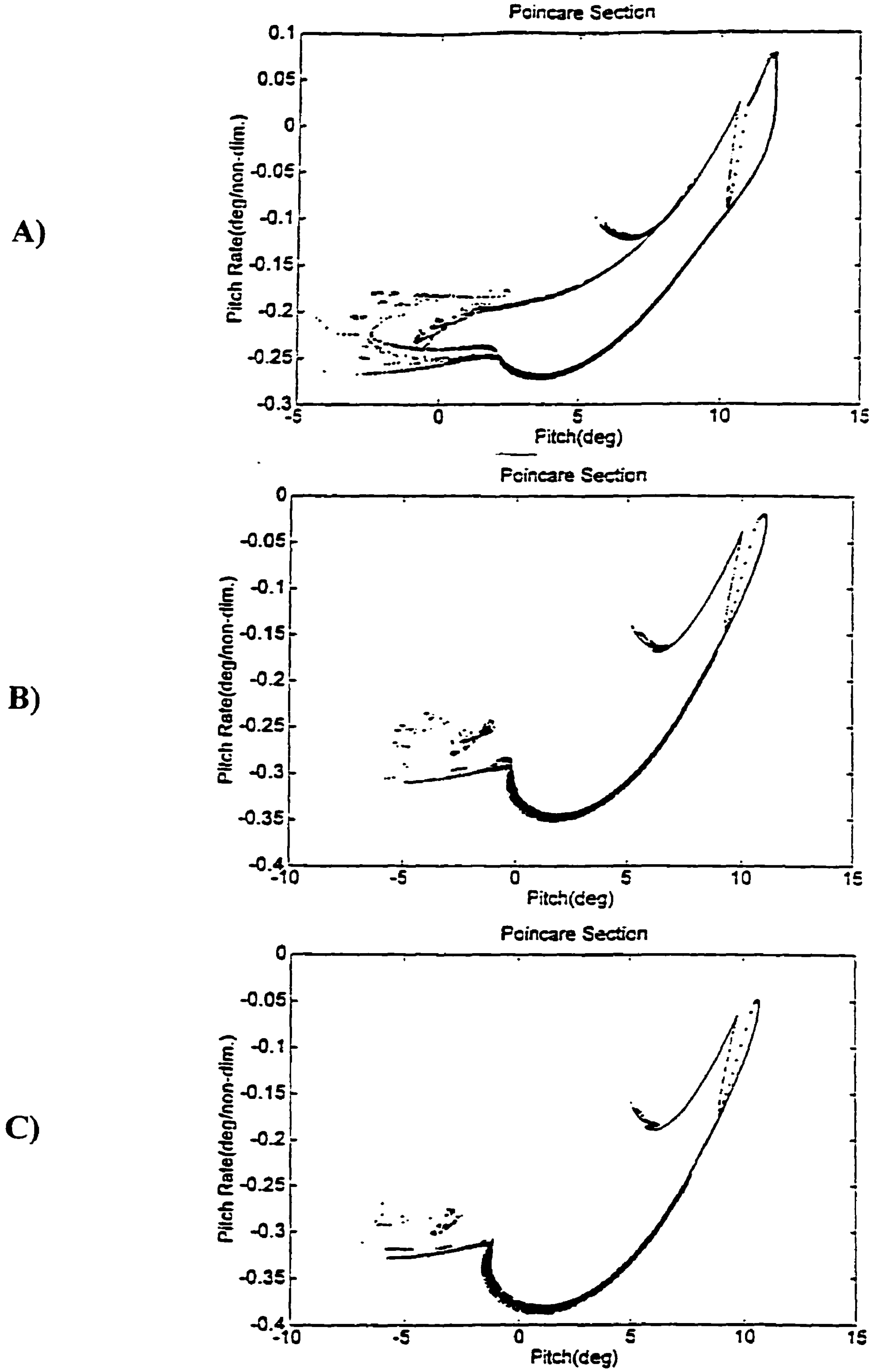

Figure 6.48: Case III, Region 2, Examples 1,2,3; Poincaré Sections a) Example 1 b) Example 2 c) Example 3: k=0.1, α_{mean}=5 deg, U^*=20, Qo=4.3x10^{-4}, Qo=5.3x10^{-4}, Qo=5.77x10^{-4}.

A)

B)

C)

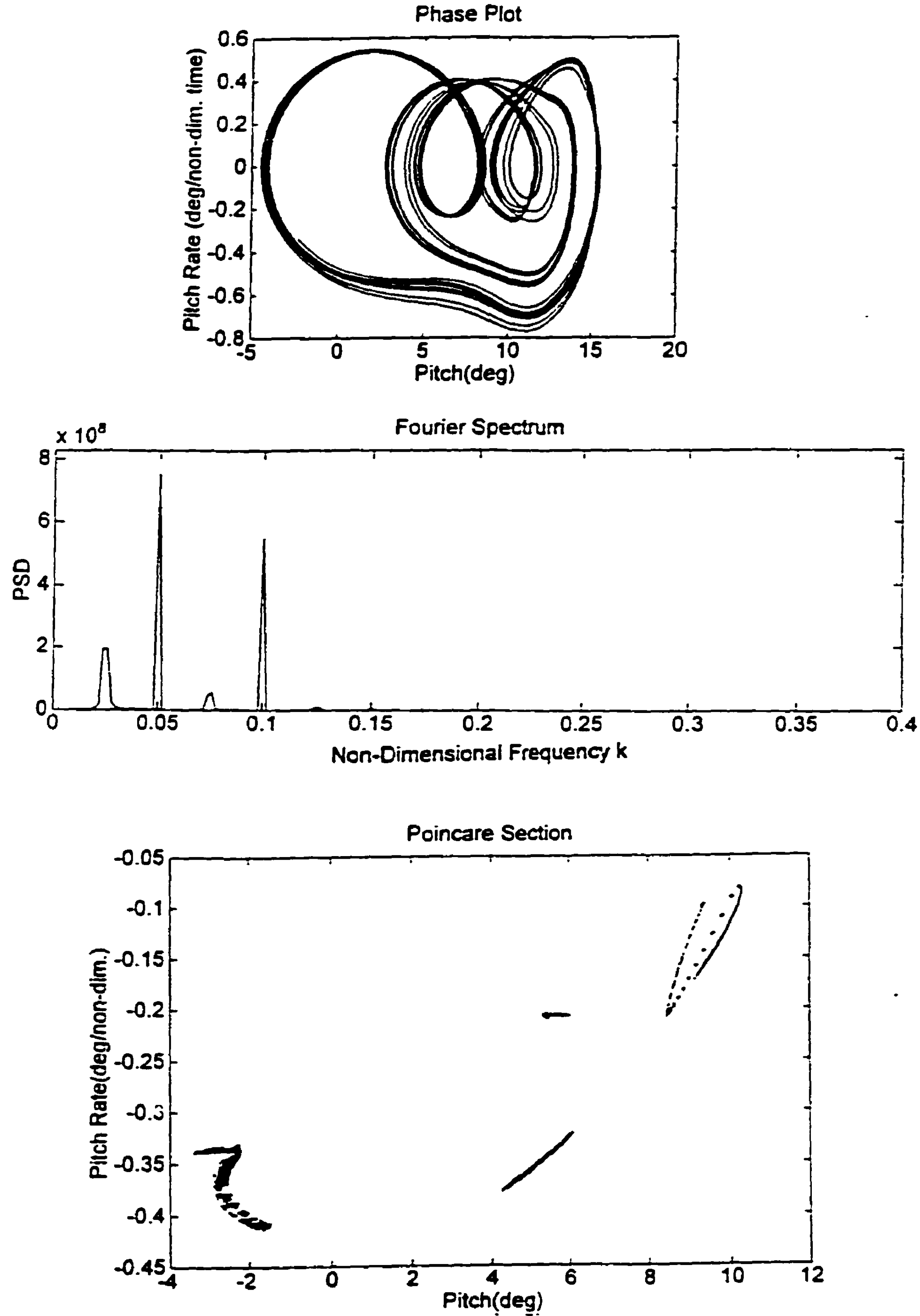

Figure 6.49: Case III, Region 3, Example 1; a) Phase Plot b) Fourier Spectrum c) Poincaré Section: *k*=0.1, $\alpha_{mean}=5$ deg, *U=20, *Qo*=6.3x10^{-4}.**

A)

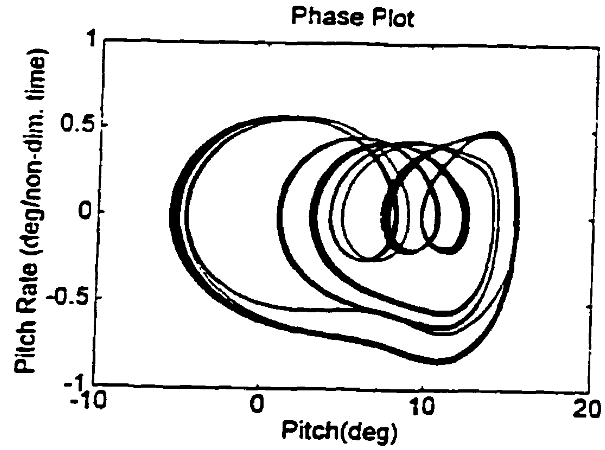

B)

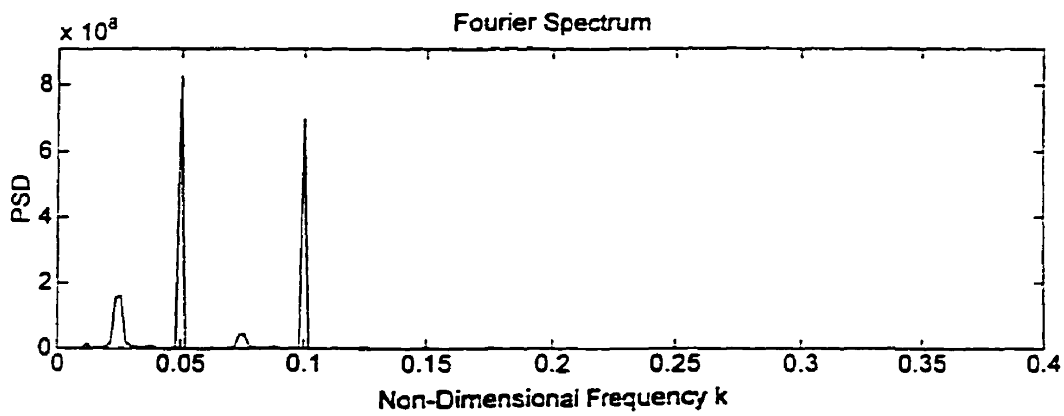

C)

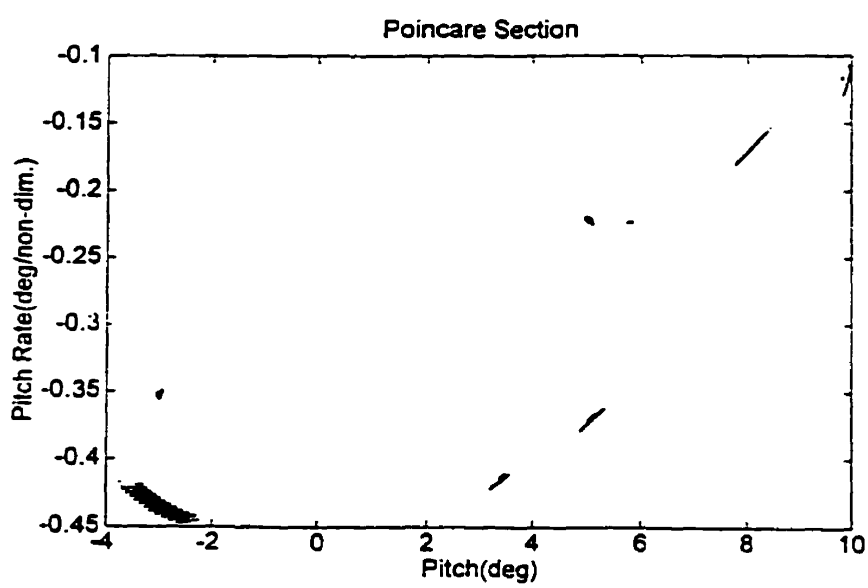

Figure 6.50: Case III, Region 3, Example 2; a) Phase Plot b) Fourier Spectrum c) Poincaré Section: k=0.1, $\alpha_{mean}=5$ deg, U^*=20, Qo=6.7x10^{-4}.

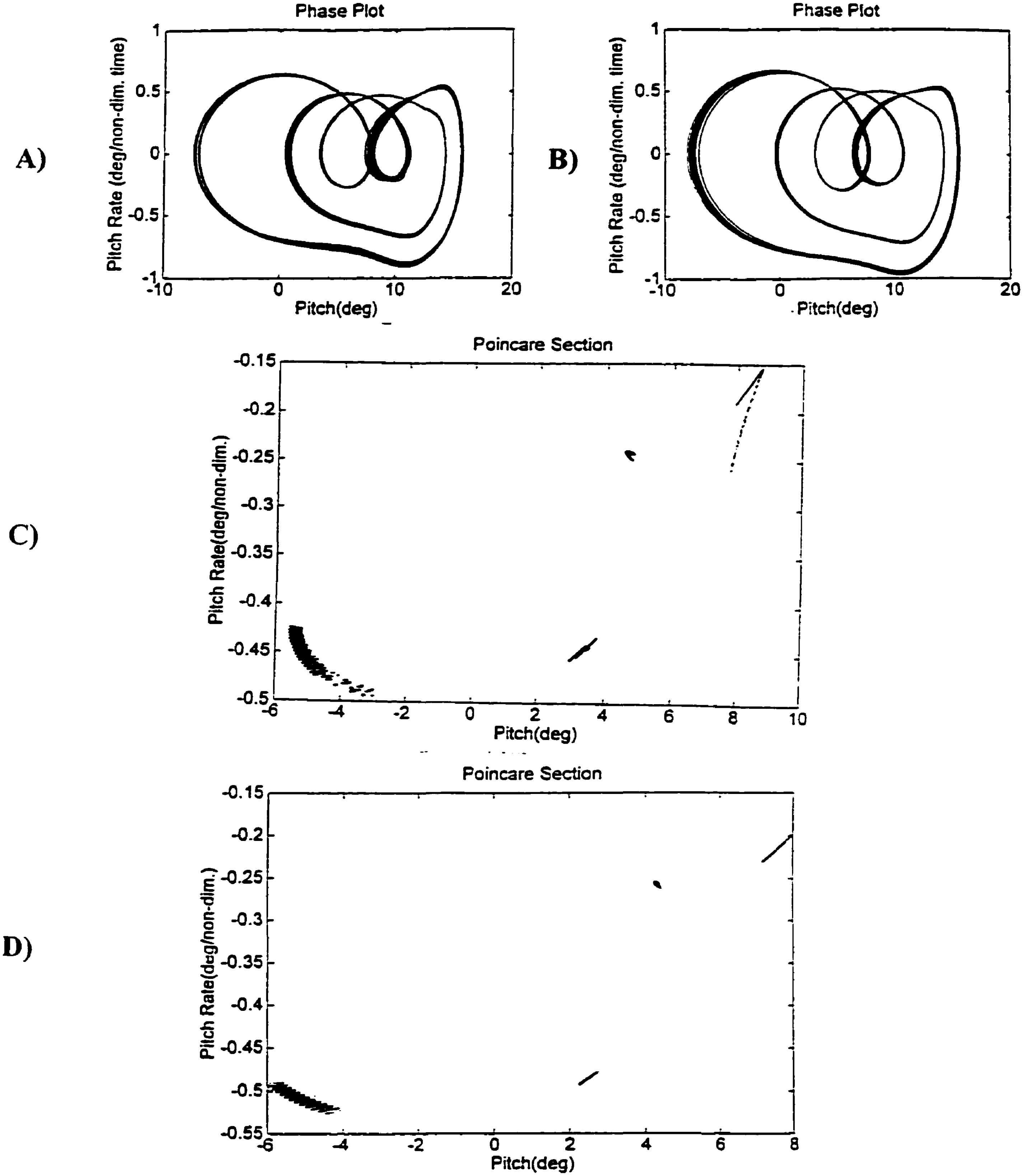

Figure 6.51: Case III, Region 4, Examples 1,2; Phase Plots a) Example 1 b) Example 2, Poincaré Sections c) Example 1 d) Example 2: *k*=0.1, $\alpha_{mean}=5$ deg, *U=20, *Qo*=7.3x10^{-4}, *Qo*=7.7x10^{-4}.**

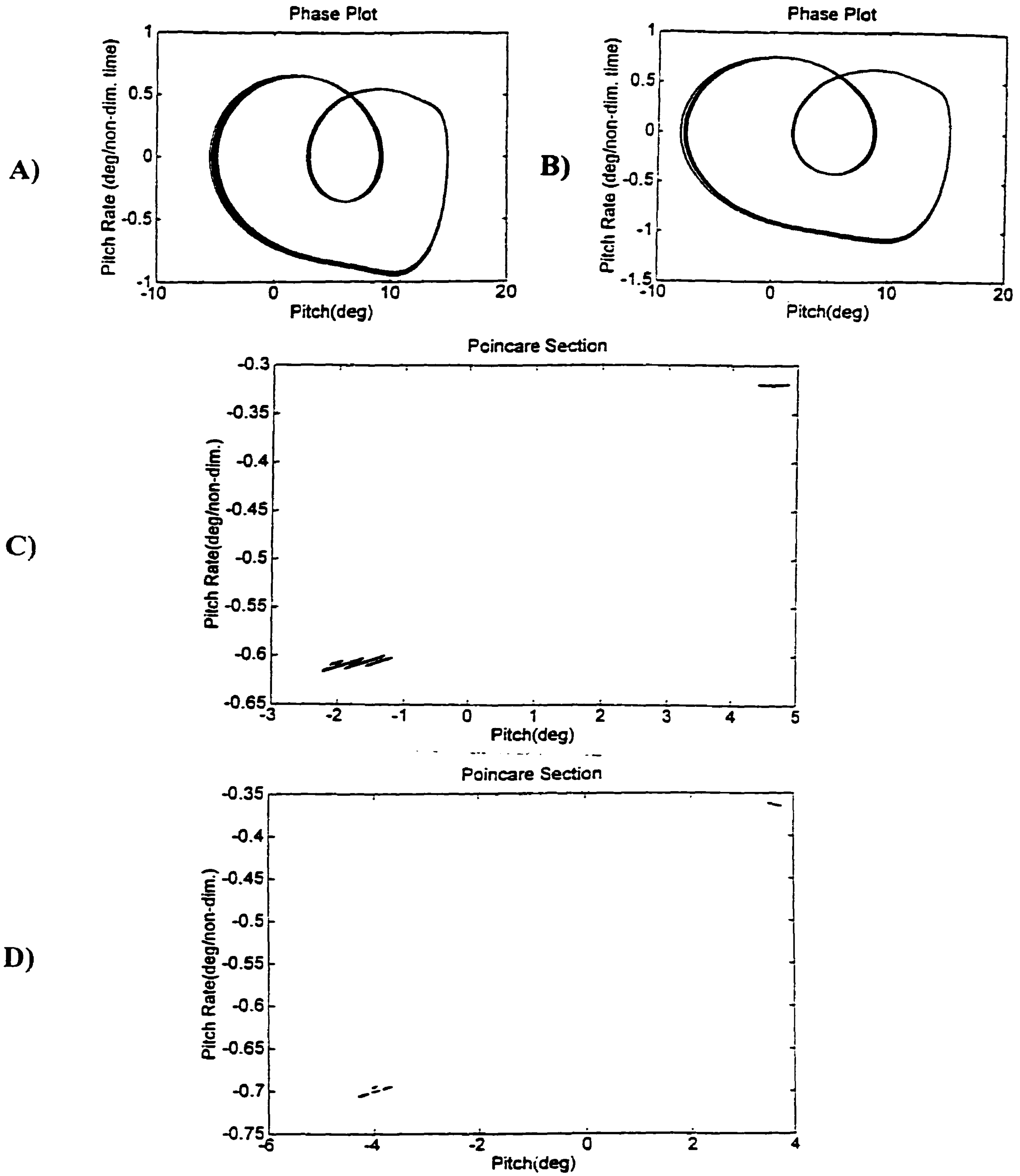

Figure 6.52: Case III, Region 5, Examples 1,2; Phase Plots a) Example 1 b) Example 2, Poincaré Sections c) Example 1 d) Example 2: k=0.1, α_{mean} = 5 deg, U^*=20, Qo=8.8x10^{-4}, Qo=9.9x10^{-4}.

A)

B)

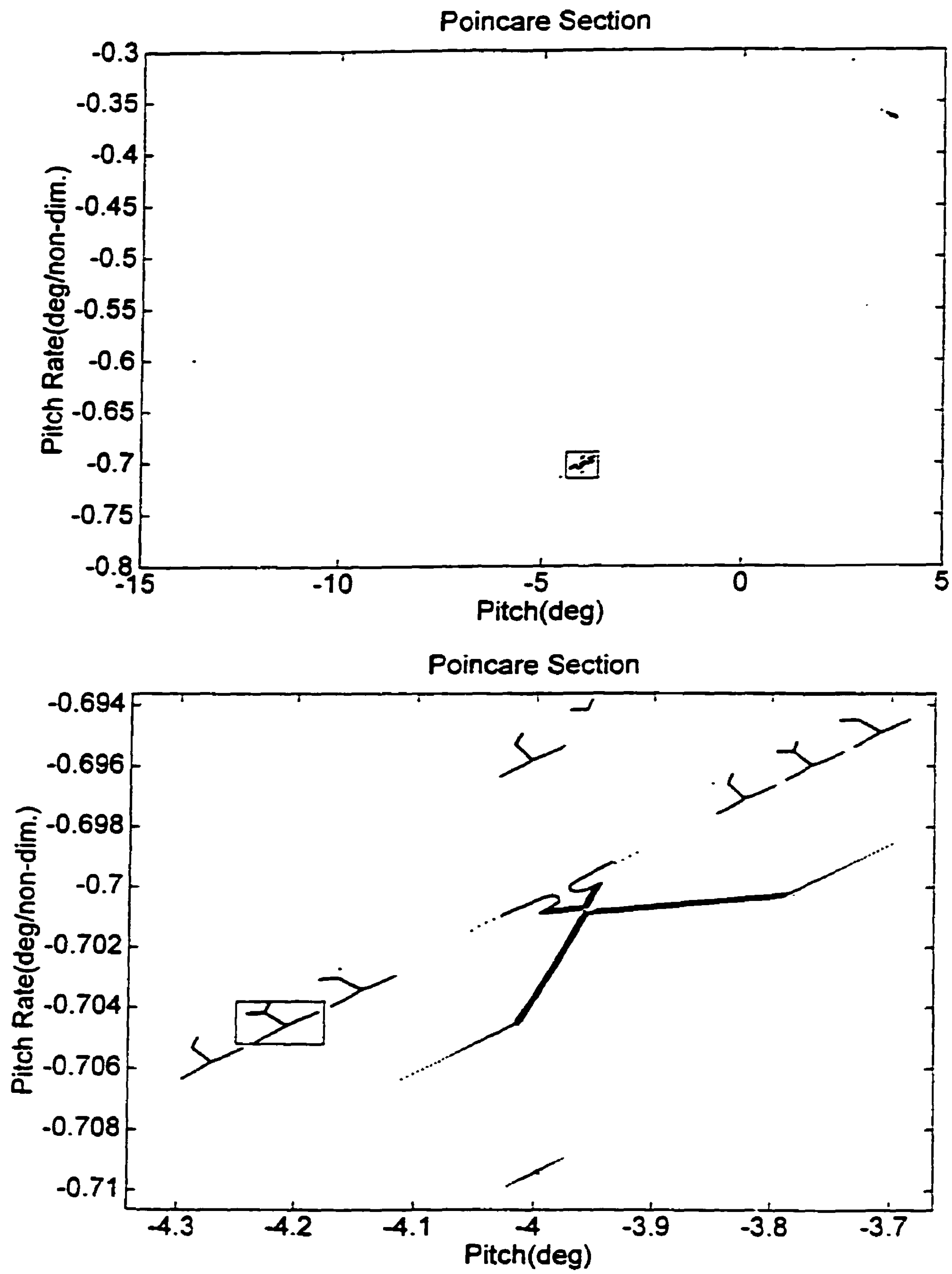

Figure 6.53: Case III, Region 5, Example 2; Magnified Poincaré Section a) Regular b) Level 1 c) Level 2 d) Level 3: *k*=0.1, $\alpha_{mean} = 5$ deg, *U=20, *Qo*=9.9x10^{-4}.**

C)

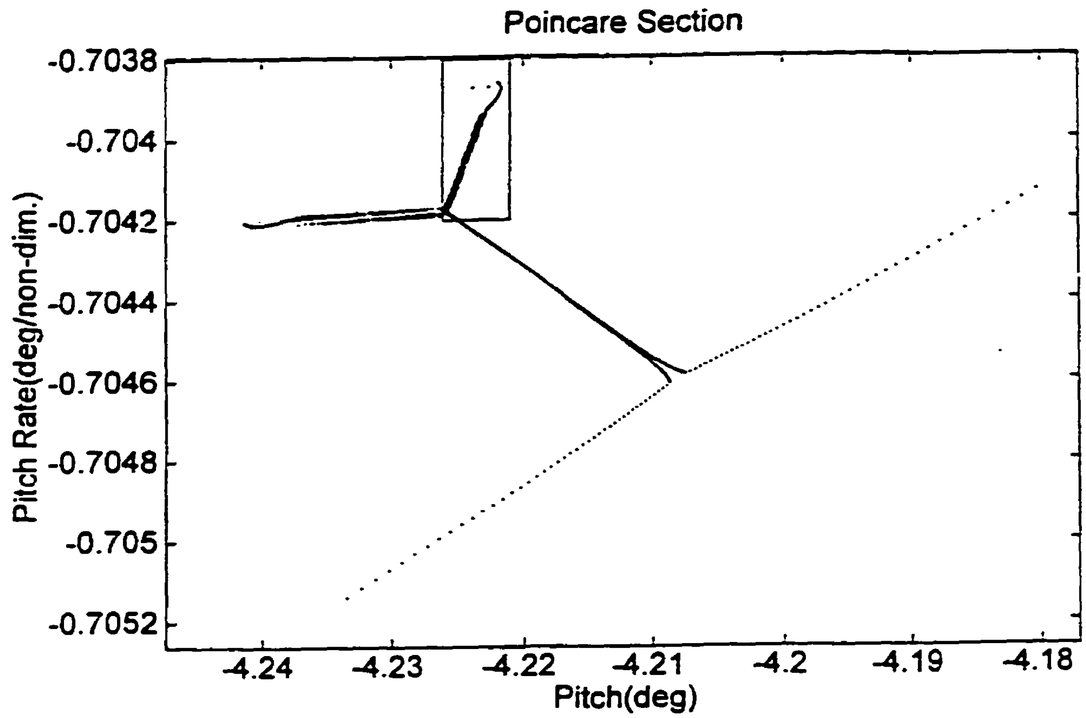
Poincare Section
-0.7038
-0.704
-0.7042
-0.7044
-0.7046
-0.7048
-0.705
-0.7052
Pitch Rate(deg/non-dim.)
-4.24
-4.23
-4.22
-4.21
-4.2
-4.19
-4.18
Pitch(deg)

D)

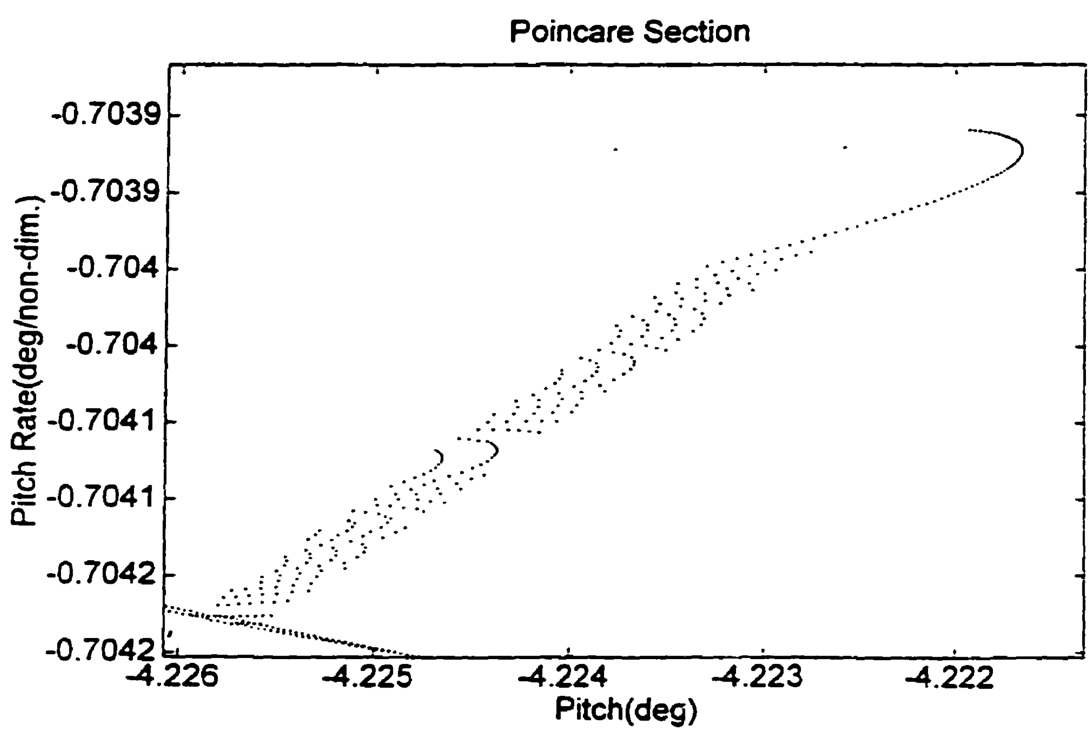
Poincare Section
-0.7039
-0.7039
-0.704
-0.704
-0.7041
-0.7041
-0.7042
-0.7042
Pitch Rate(deg/non-dim.)
-4.226
-4.225
-4.224
-4.223
-4.222
Pitch(deg)

A)

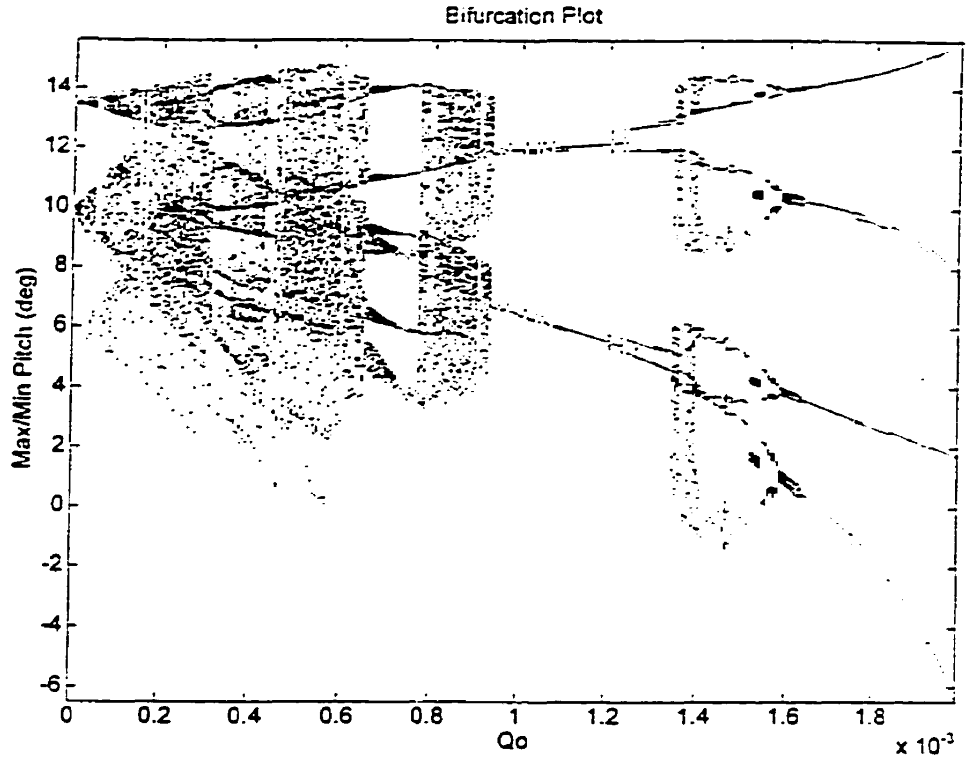

Case IV

B)

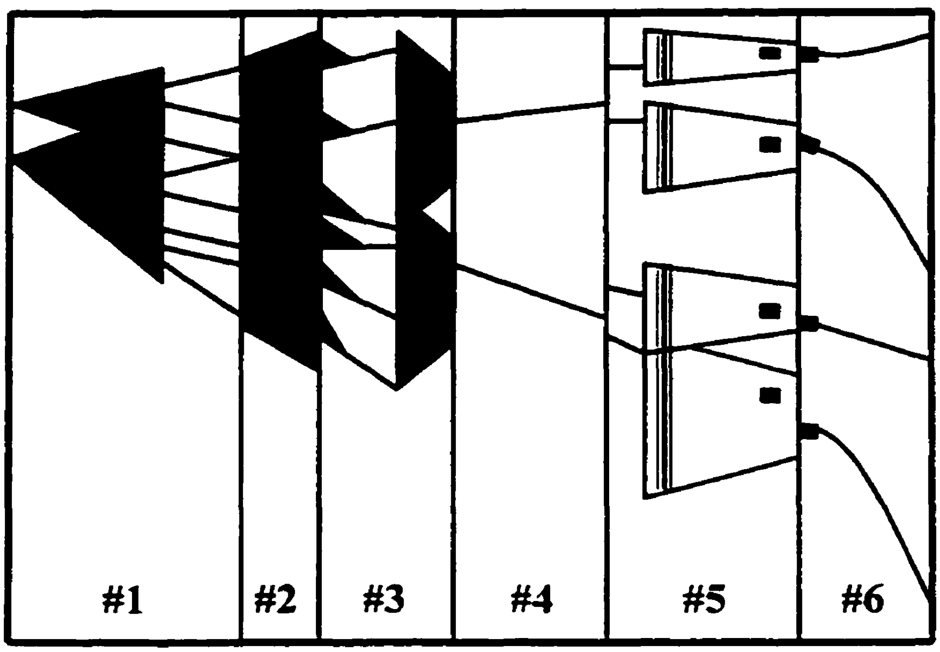

Figure 6.54: Case IV; a) Bifurcation Plot b) Conceptual Drawing: k=0.15, $\alpha_{mean}=6$ deg, U^*=15, 0<Qo<0.002.

A)

B)

C)

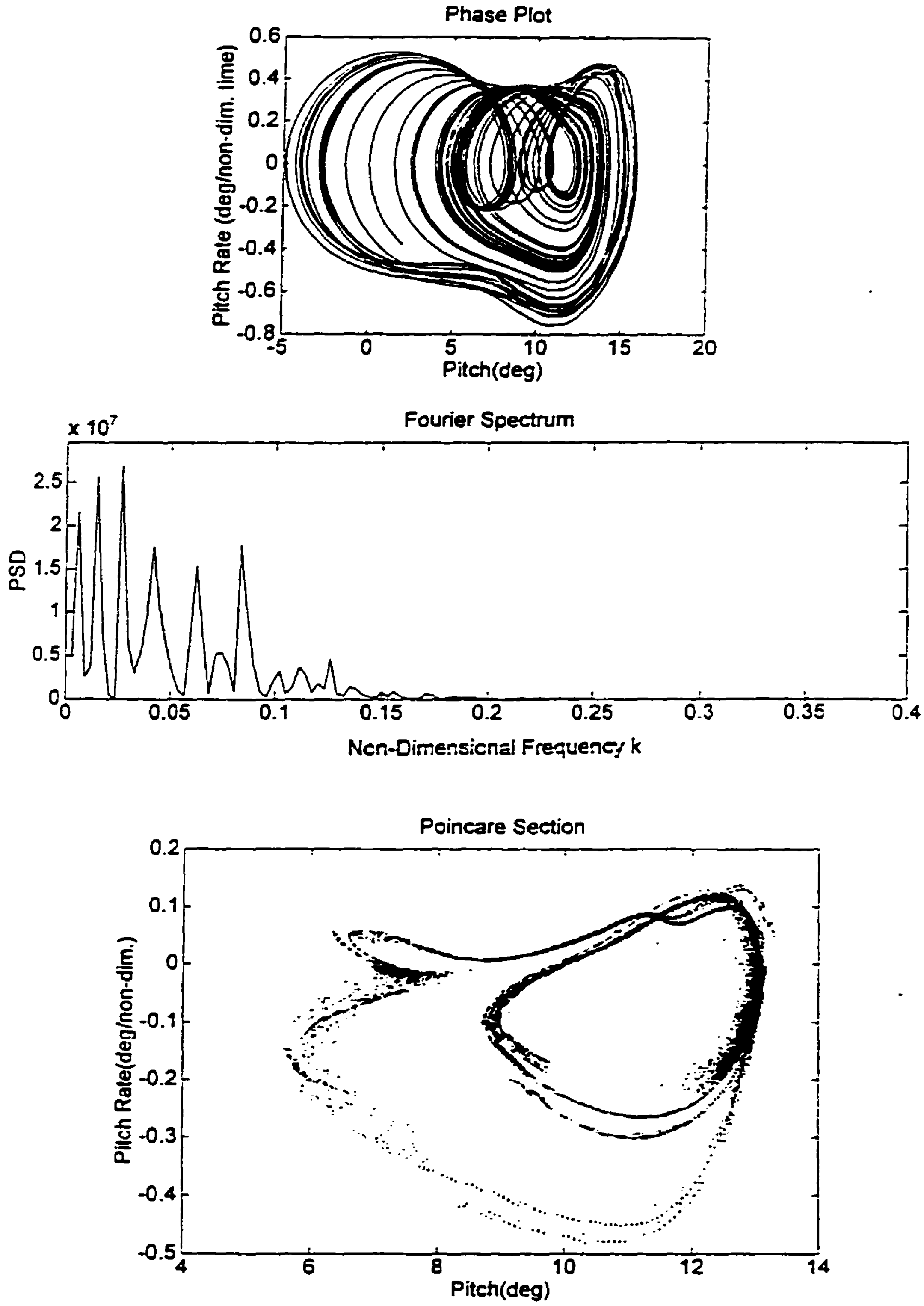

Figure 6.55: Case IV, Region 1, Example 1; a) Phase Plot b) Fourier Spectrum c) Poincaré Section: *k*=0.15, $\alpha_{mean} = 6$ deg, *U=15, *Qo*=1x10^{-4}.**

A)

B)

C)

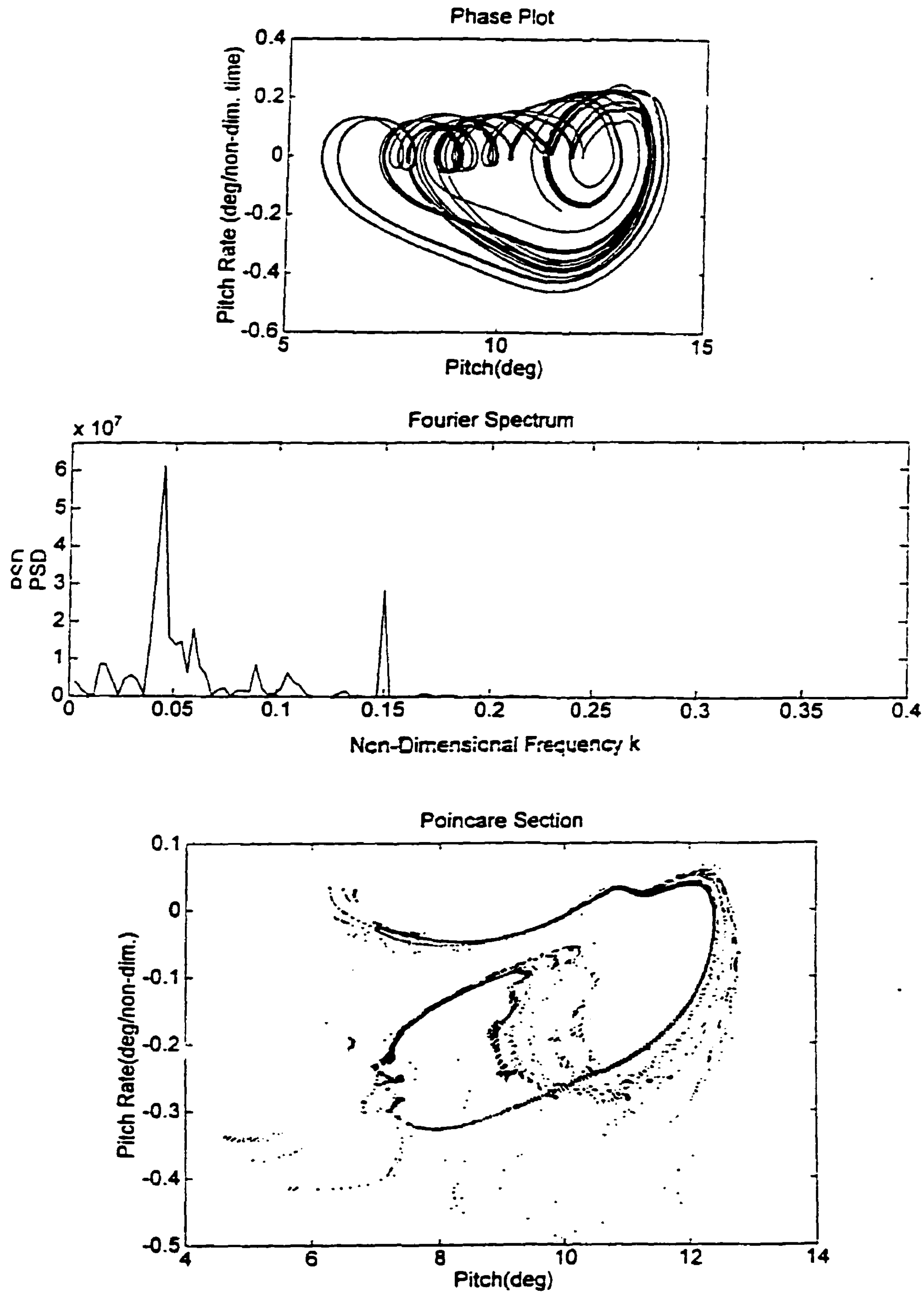

Figure 6.56: Case IV, Region 1, Example 2; a) Phase Plot b) Fourier Spectrum c) Poincaré Section: k=0.15, $\alpha_{mean}=6$ deg, U^*=15, Qo=2.5x10^{-4}.

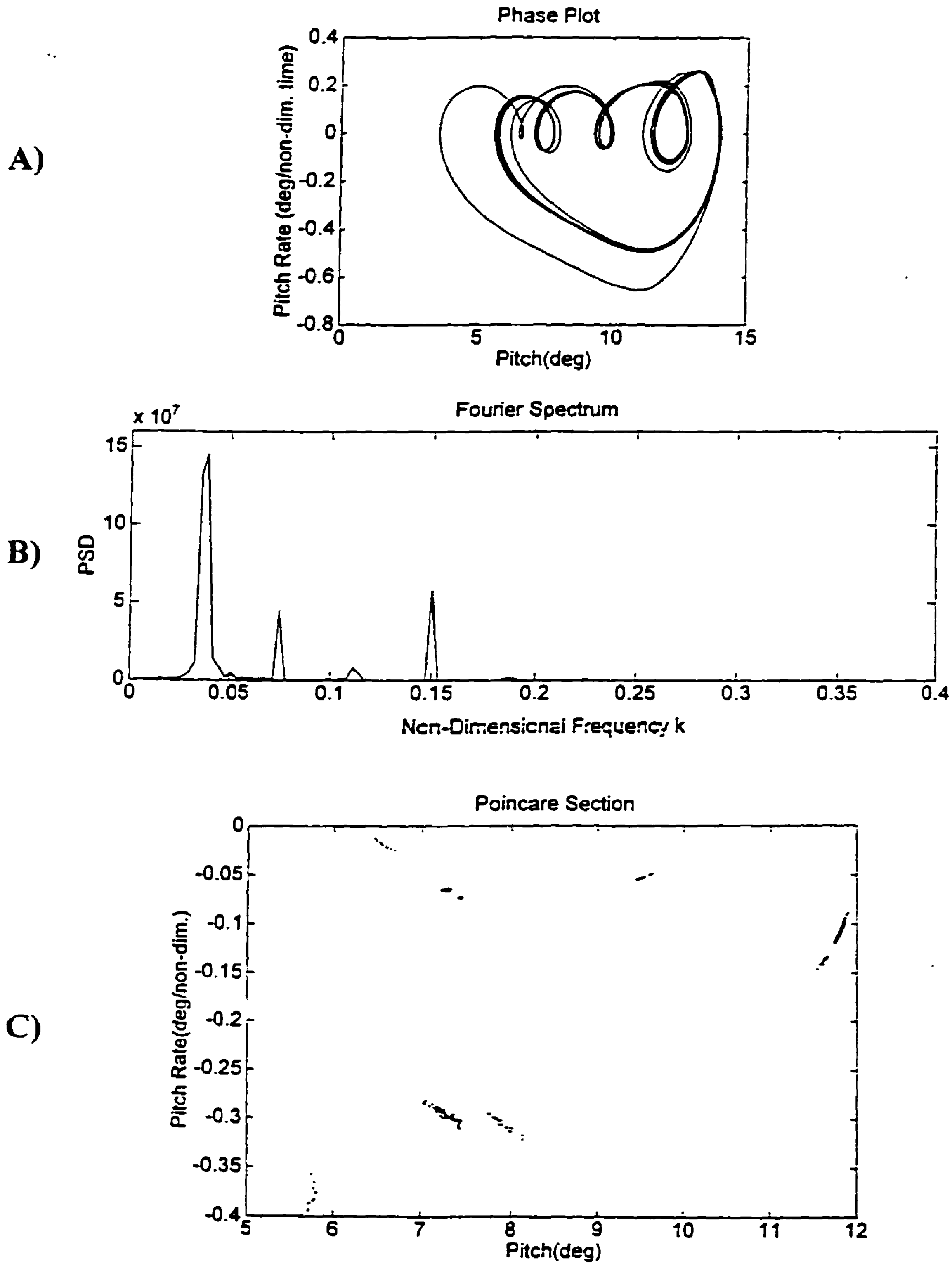

Figure 6.57: Case IV, Region 1, Example 3; a) Phase Plot b) Fourier Spectrum c) Poincaré Section: k=0.15, $\alpha_{mean}=6$ deg, U^*=15, Qo=3.3x10^{-4}.

A)

B)

C)

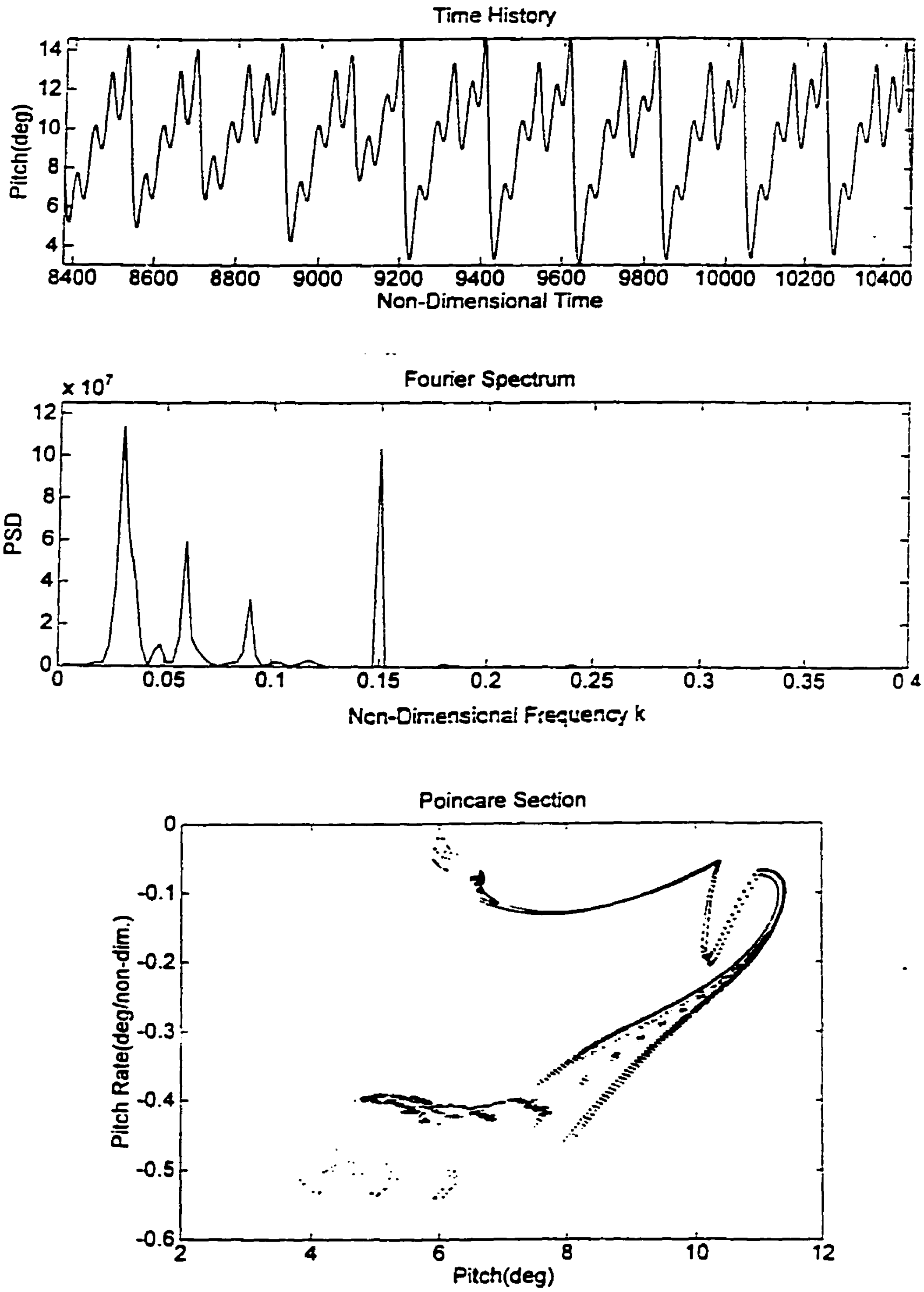

Figure 6.58: Case IV, Region 2, Example 1; a) Time History b) Fourier Spectrum c) Poincaré Section: k=0.15, $\alpha_{mean}=6$ deg, U^*=15, Qo=4.7x10^{-4}.

A)

B)

C)

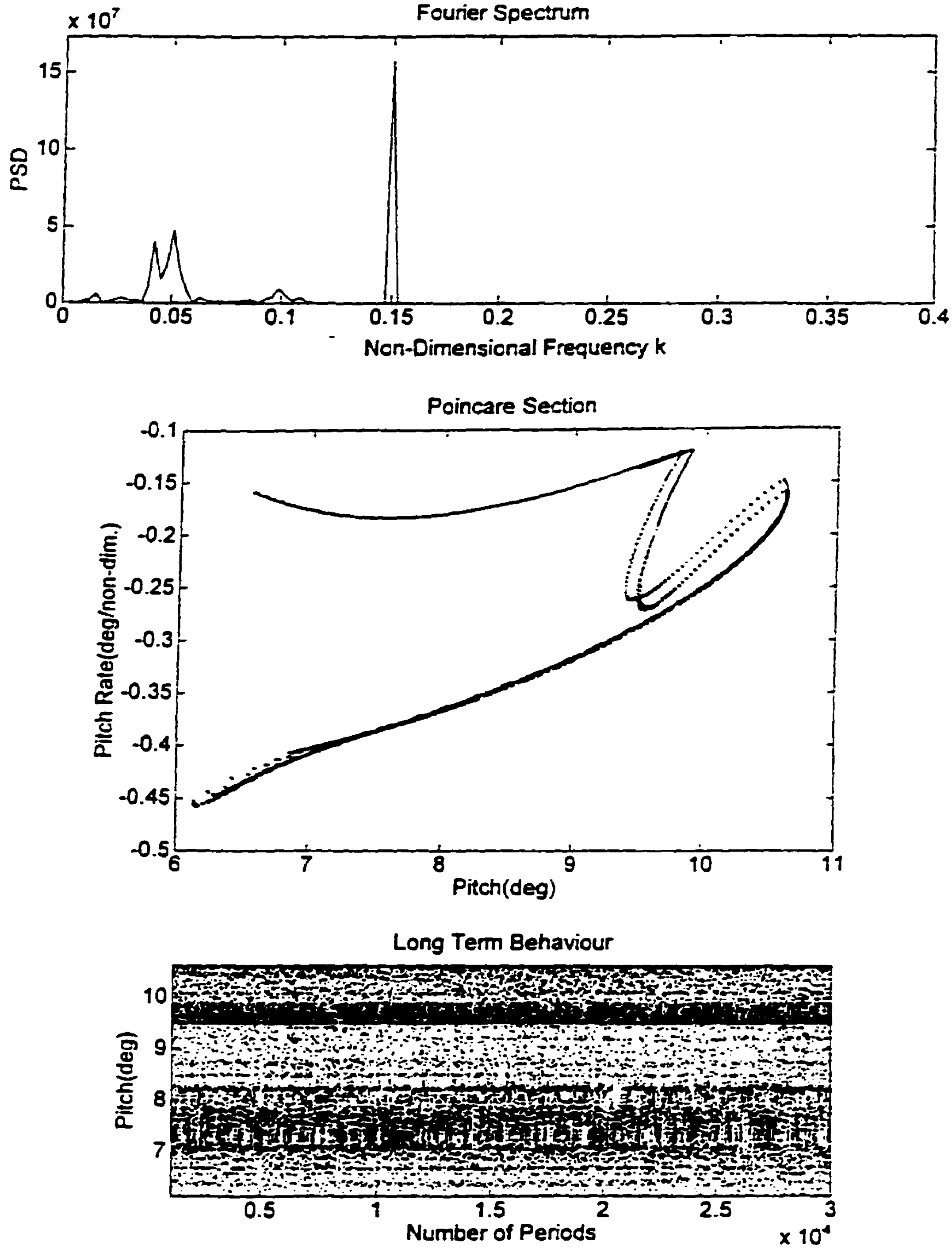

Figure 6.59: Case IV, Region 2, Example 2; a) Fourier Spectrum b) Poincaré Section c) Long Term Behaviour: k=0.15, $\alpha_{mean} = 6$ deg, U^*=15, Qo=6.4x10^{-4}.

A)

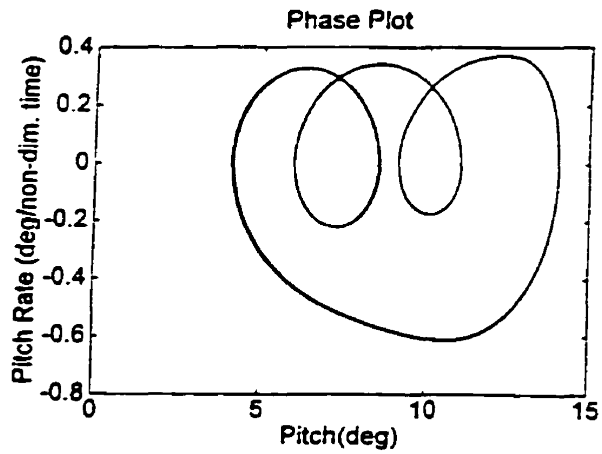

B)

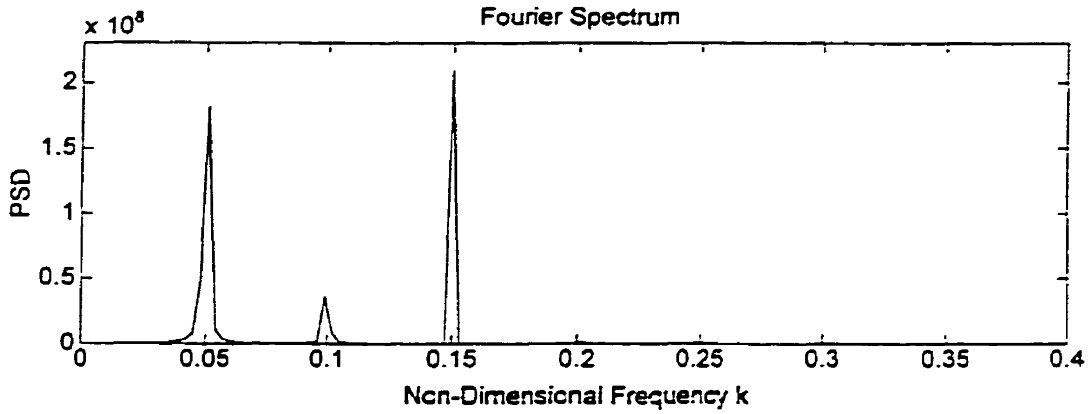

C)

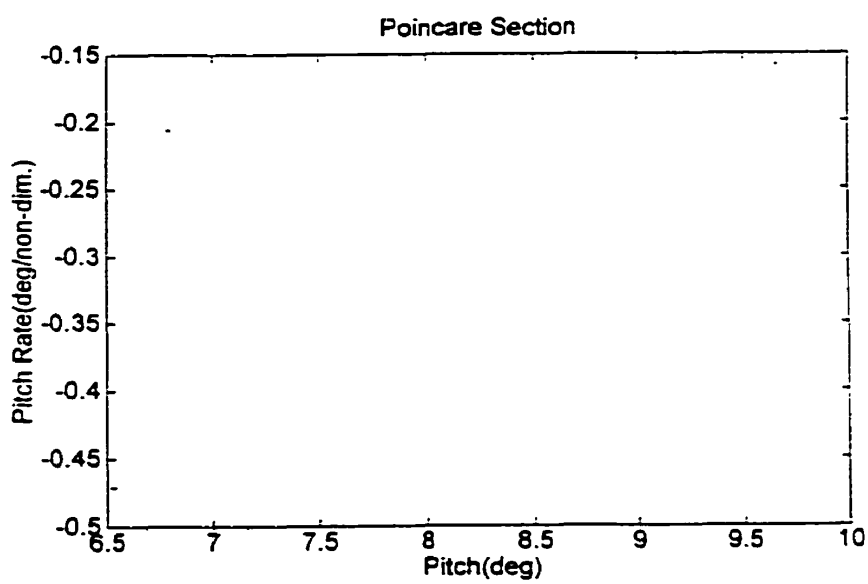

Figure 6.60: Case IV, Region 3, Examples 1,2; Example 1 a) Phase Plot b) Fourier Spectrum c) Poincaré Section d) Long Term Behaviour, Example 2 e) Poincaré Section: k=0.15, α_{mean} = 6 deg, U^*=15, Qo=7.3x10^{-4}, Qo=8.5x10^{-4}

D)

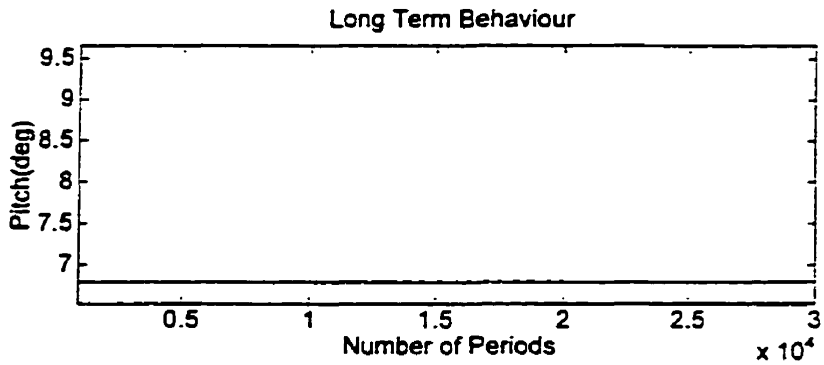
Long Term Behaviour
Pitch(deg)
9.5
9
8.5
8
7.5
7
0.5
1
1.5
2
2.5
3
Number of Periods
x 10^4

E)

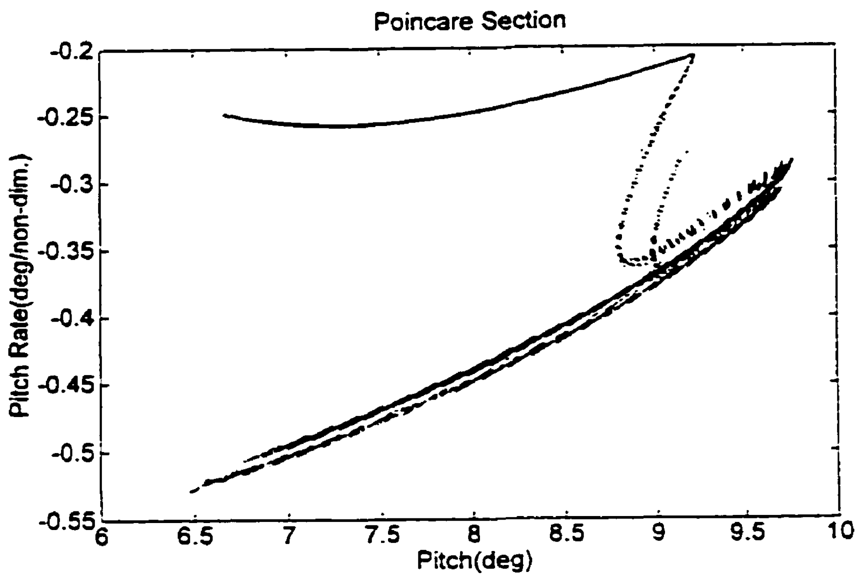
Poincare Section
Pitch Rate(deg/non-dim.)
-0.2
-0.25
-0.3
-0.35
-0.4
-0.45
-0.5
-0.55
6
6.5
7
7.5
8
8.5
9
9.5
10
Pitch(deg)

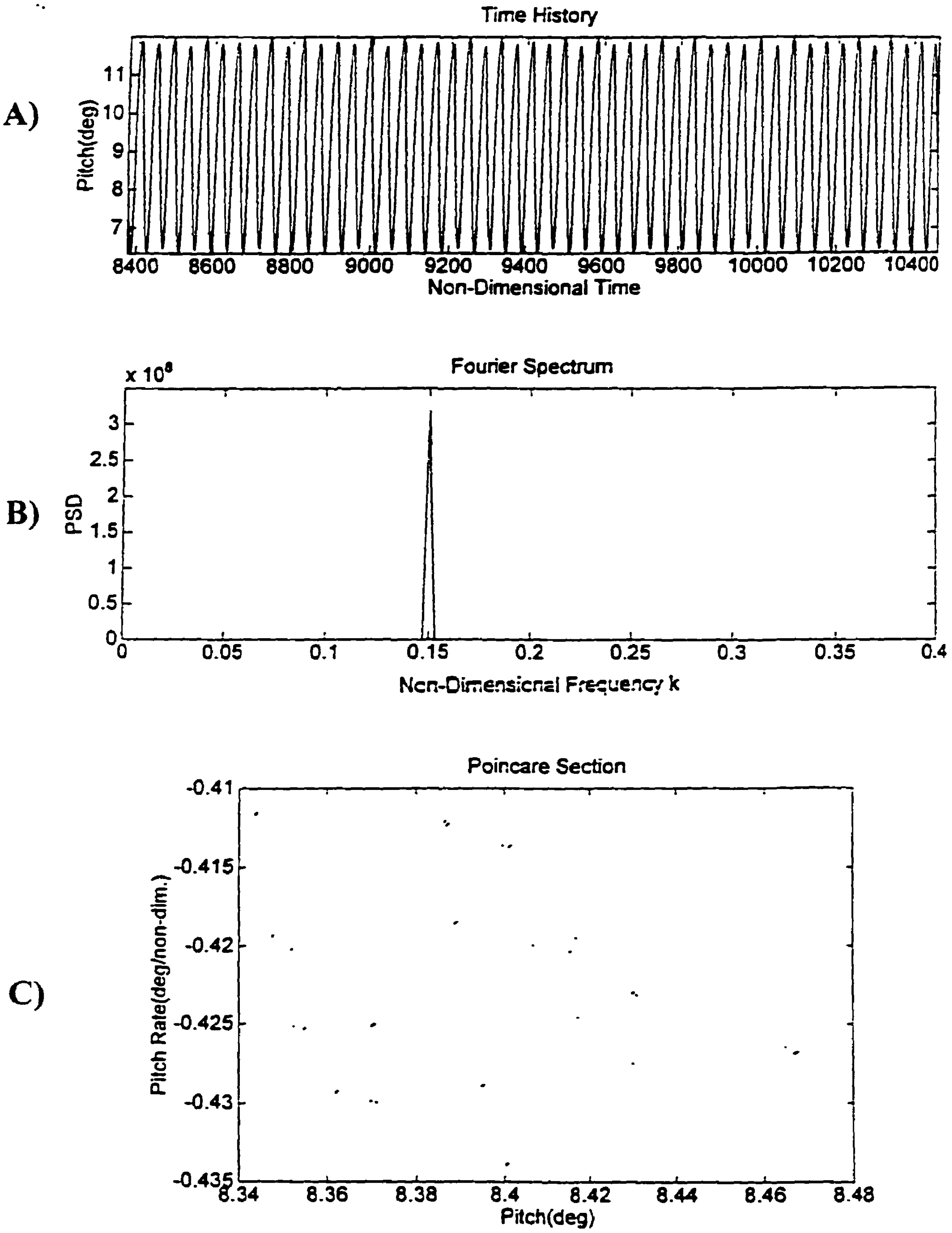

Figure 6.61: Case IV, Region 4, Examples 1; a) Time History b) Fourier Spectrum c) Poincaré Section: k=0.15, $\alpha_{mean}=6$ deg, U^*=15, Qo=1x10^{-3}.

A)

B)

C)

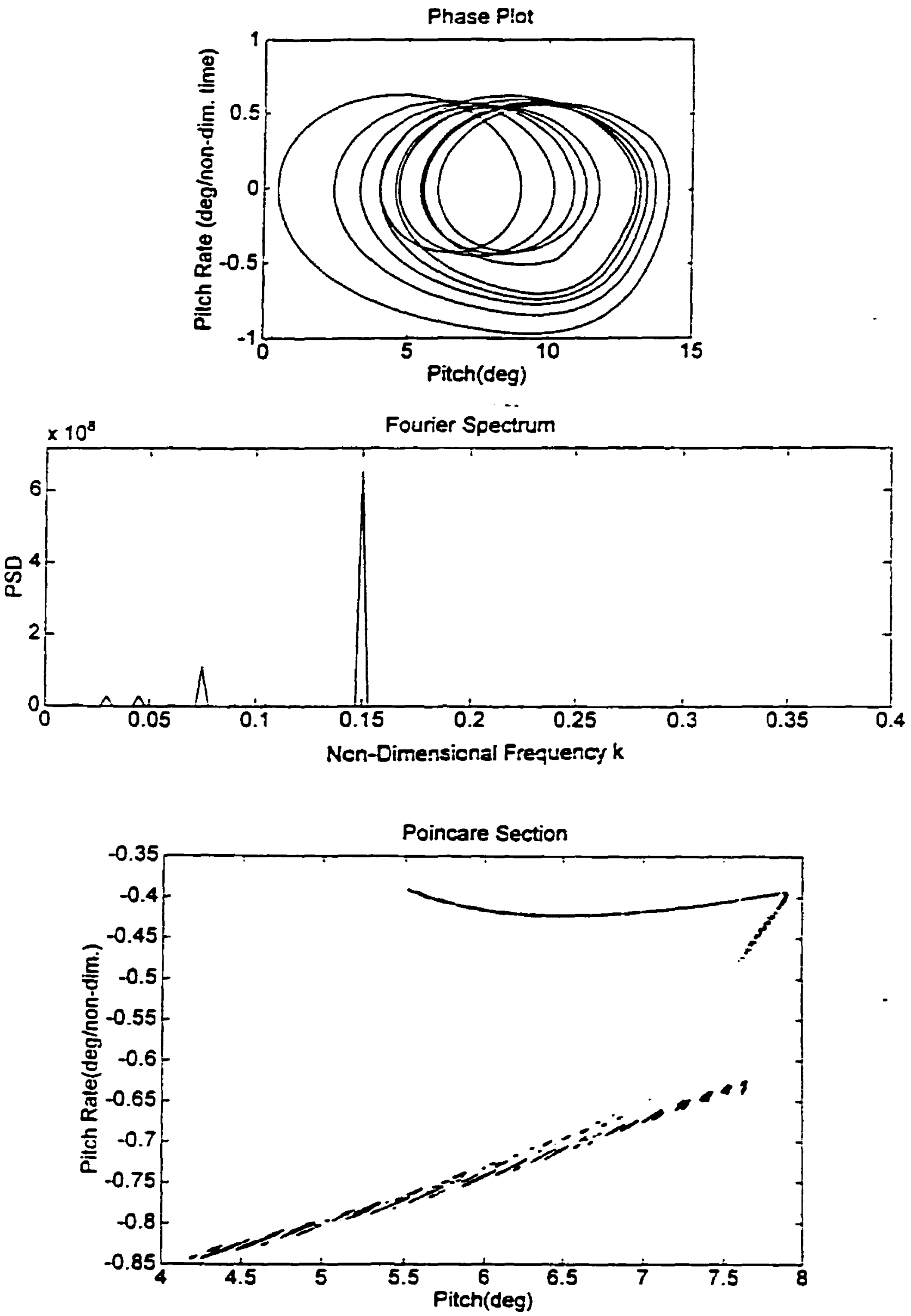

Figure 6.62: Case IV, Region 5, Examples 1; a) Phase Plot b) Fourier Spectrum c) Poincaré Section: *k*=0.15, $\alpha_{mean} = 6$ deg, *U=15, *Qo*=1.35x10^{-3}.**

A)

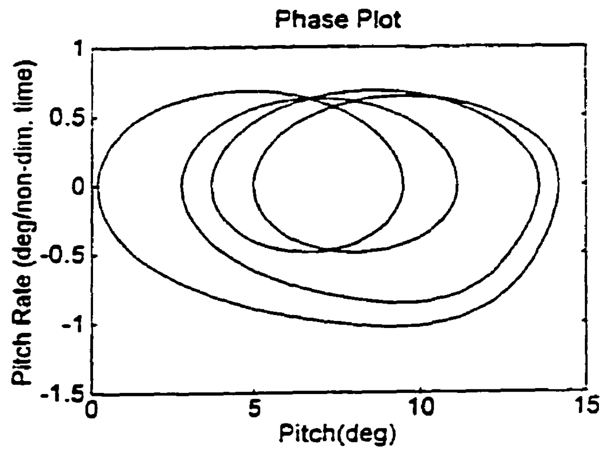

B)

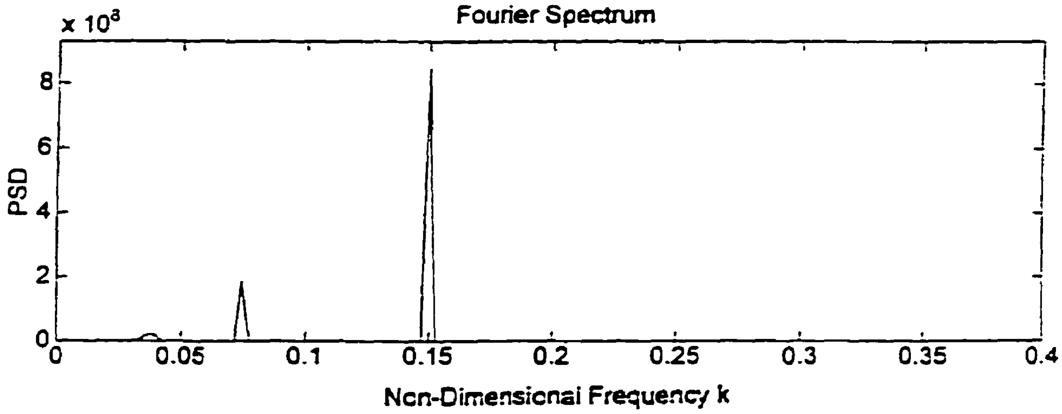

C)

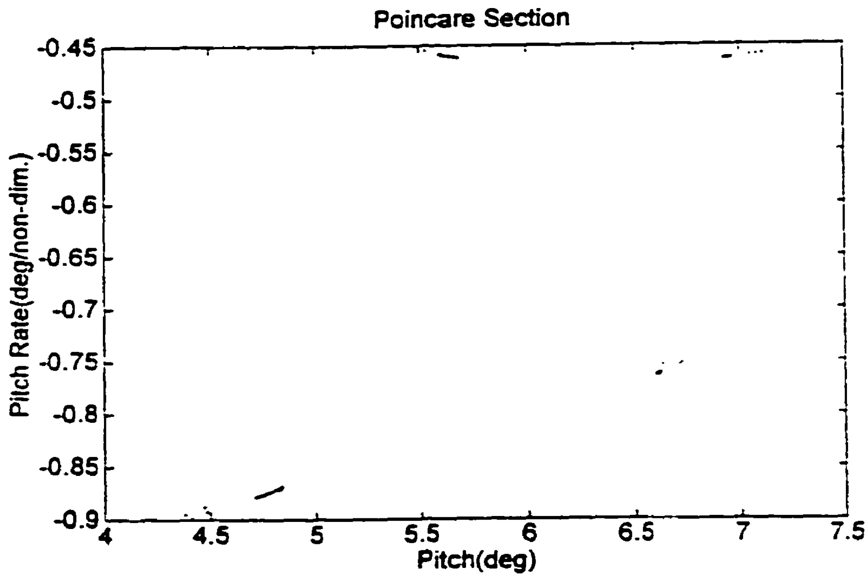

Figure 6.63: Case IV, Region 5, Example 2; a) Phase Plot b) Fourier Spectrum c) Poincaré Section: k=0.15, $\alpha_{mean}=6$ deg, U^*=15, Qo=1.5x10^{-3}.

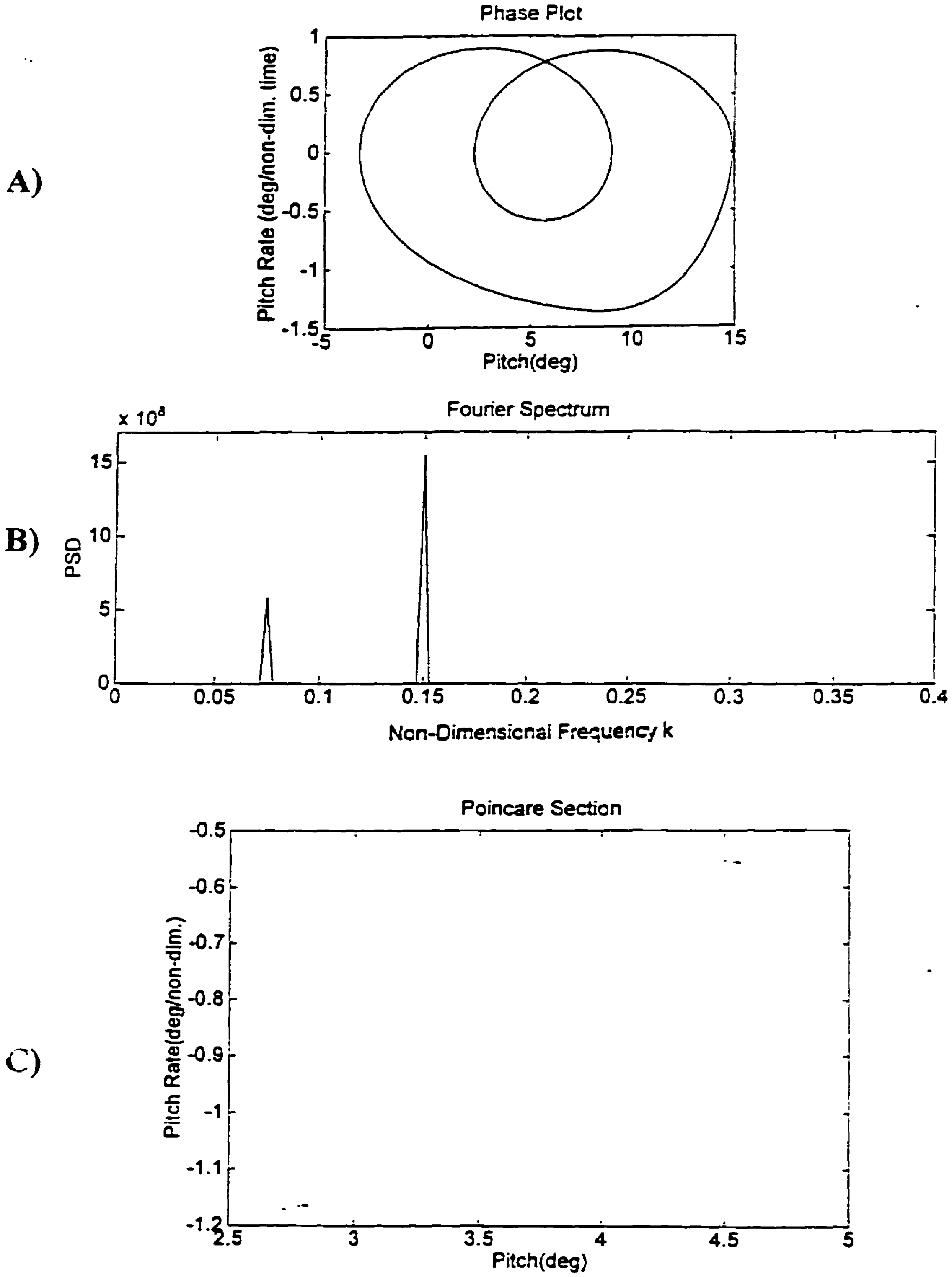

Figure 6.64: Case IV, Region 6, Example 1; a) Phase Plot b) Fourier Spectrum c) Poincaré Section: k=0.15, α_{mean} = 6 deg, U^*=15, Qo=1.88x10^{-3}.

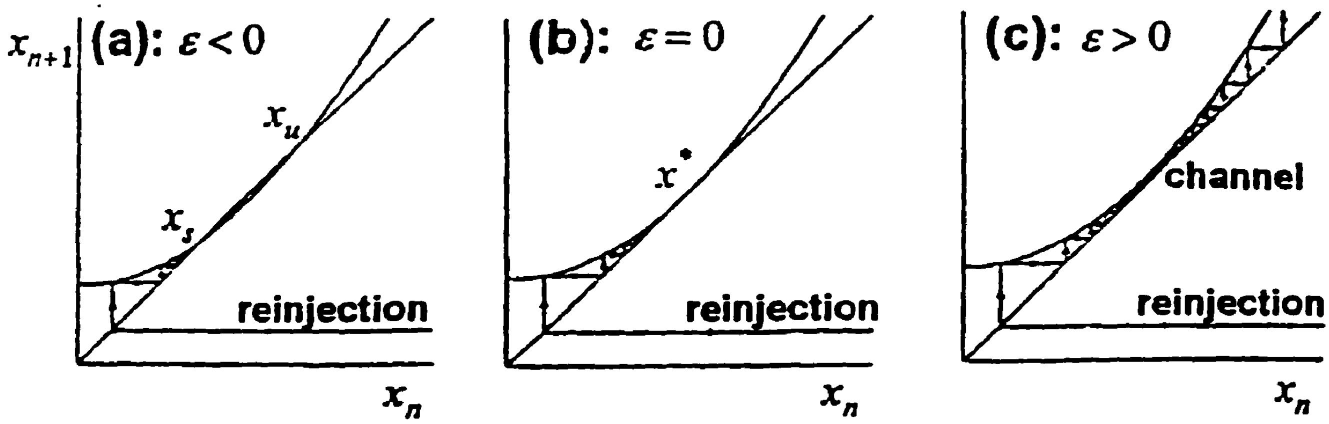

D)

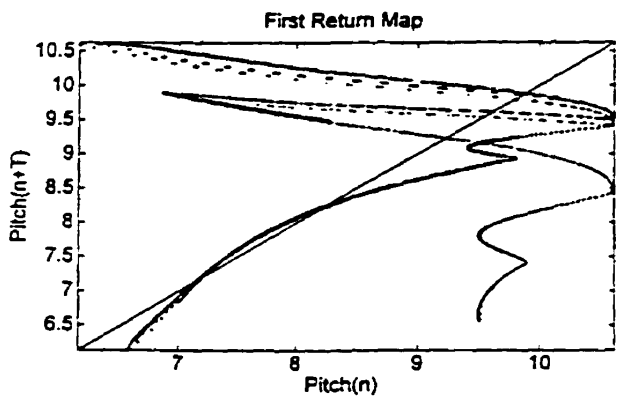

E)

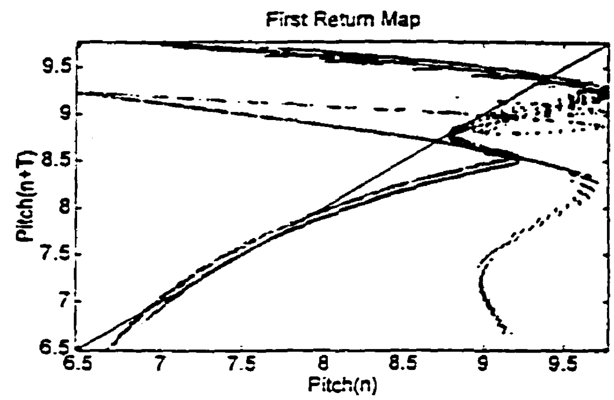

F)

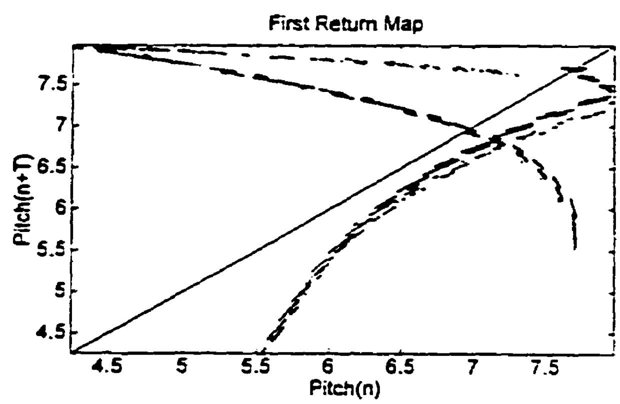

Figure 6.65: Comparison to Type I Intermittent Transition; Classical Example, First Return Maps: a),b),c); First Return Maps from Case IV: d) Region 2, Example 2 e) Region 3, Example 2 f) Region 5, Example 1: k=0.15, $\alpha_{mean}=6$ deg, U^*=13.5, Qo=6.4x10^{-4}, Qo=8.5x10^{-4}, Qo=1.35x10^{-3}. Classical Example Reproduced from Nayfeh and Balachandran (1995).

A)

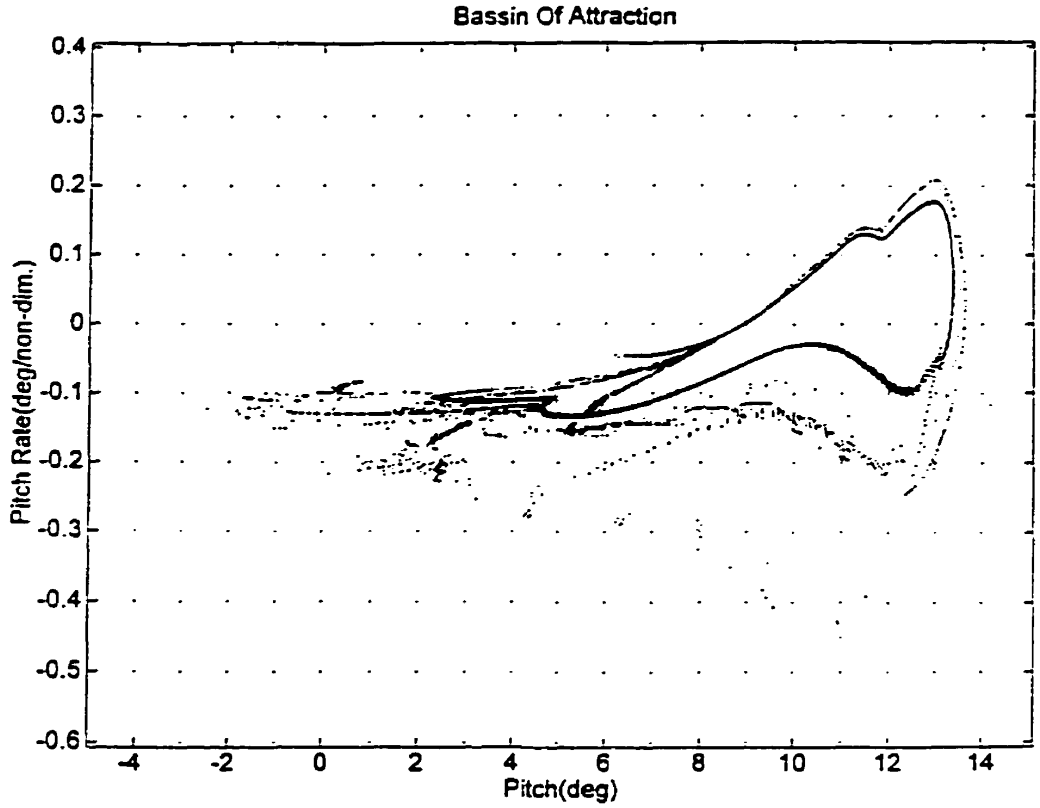

B)

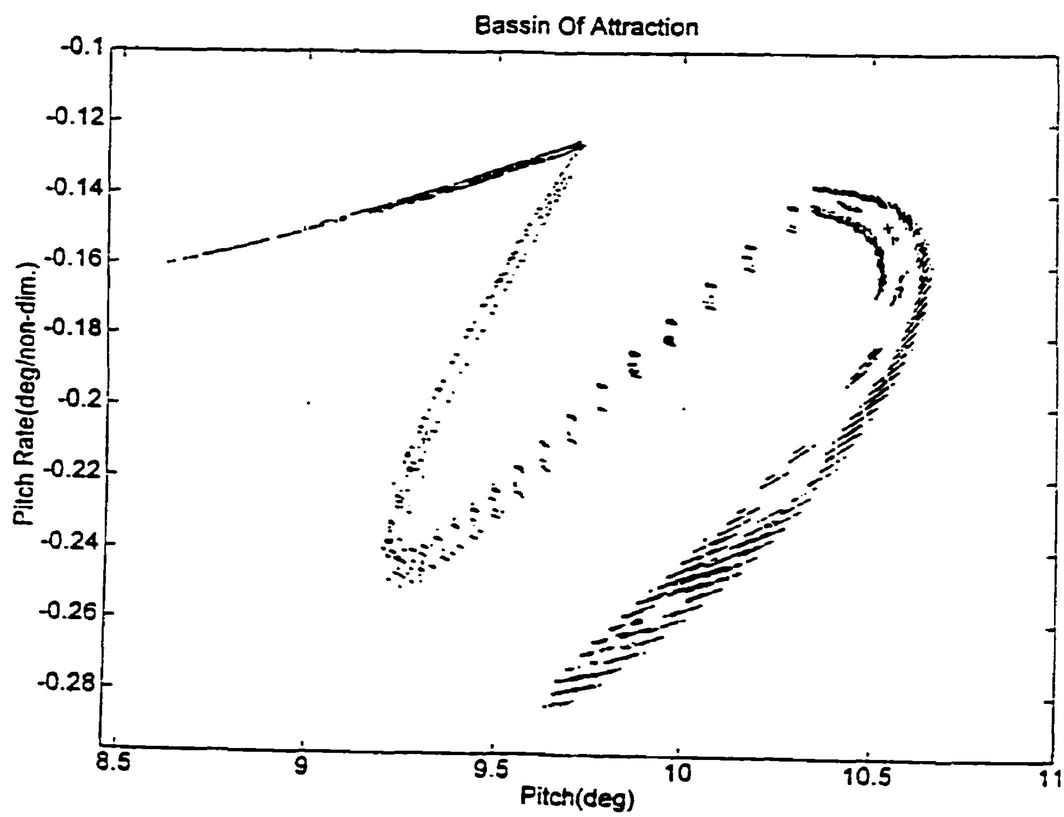

Figure 6.66: Basin of Attraction: a) Case I, Region 2, Example 2 b) Case II, Region 3, Example 1 c) Case III, Region 2, Example 2 d)Case IV, Region 2, Example 1.

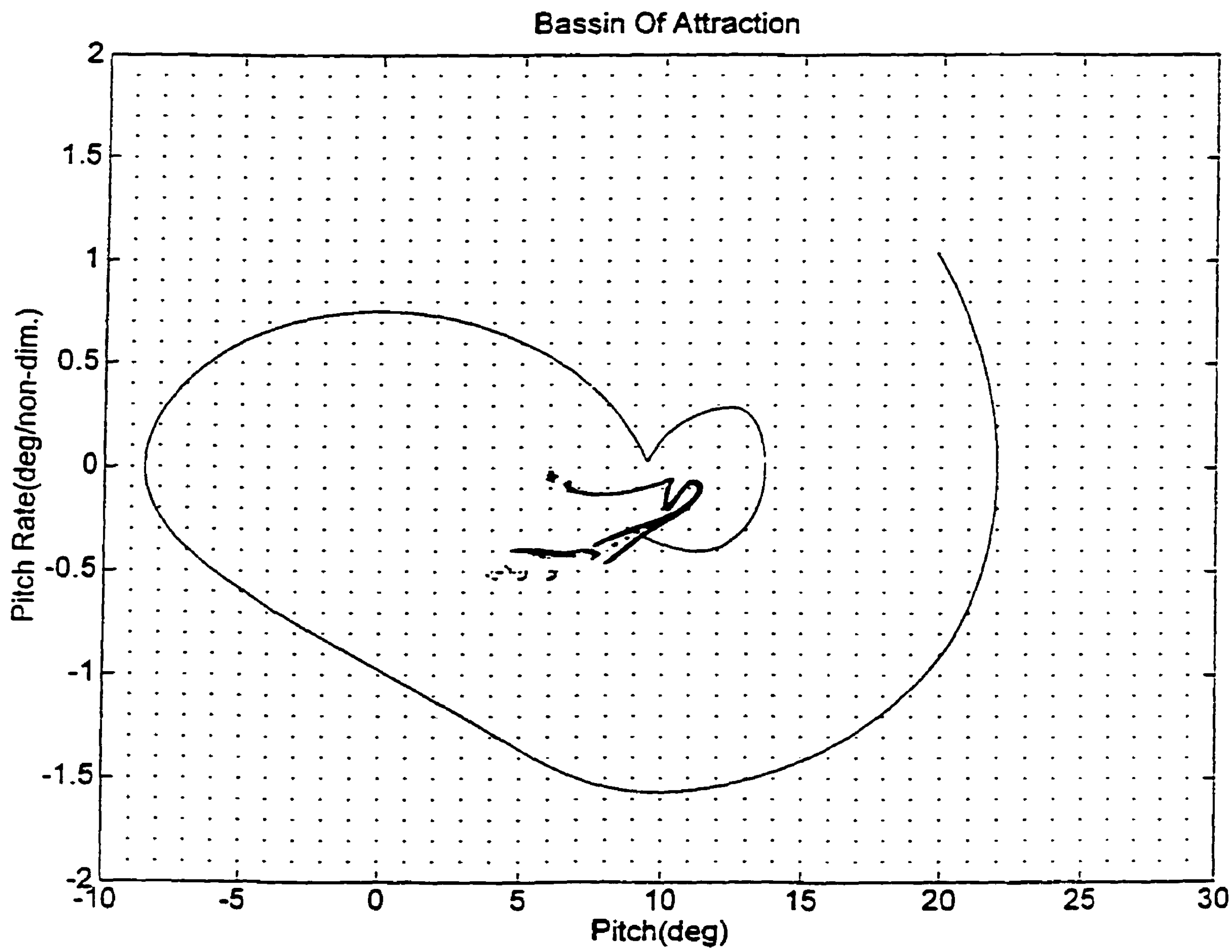

Figure 6.67: Basin of Attraction; Path Followed by Response to Attractor and Grid of Initial Conditions: Case IV, Region 2, Example 1.

Chapter 7

Non-Linear Analysis: The Two-Degree -of-Freedom System

7.1 Introduction

The previous chapter used all of the various tools discussed in the first chapter to examine the one-degree-of-freedom system. The purpose of this chapter will be to examine the two-degree-of-freedom system. The addition of the plunge degree-of-freedom will introduce the possibility of binary flutter. This will be the main focus of this chapter.

Bifurcation plots will be used in conjunction with time-histories, phase-plots and frequency spectra to see how the behaviour of the system changes as the plunge degree-of-freedom is introduced into the system. The variable of interest in this section is the ratio of natural frequencies, discussed in Chapter 5. As this variable is increased the effect of plunge diminishes. Therefore, the lower the value of this variable, the greater the effect of this new degree-of-freedom as this variable approaches infinity the system reverts to the one-degree-of-freedom scenario.

Flutter is an instability whereby an airfoil oscillates without any external forcing. It is therefore extracting energy from the steady airstream. Under certain conditions this self-excited oscillation may be violent. This condition is possible in the one-degree of freedom case because of unsteady or non-linear effects (stall flutter). In these cases negative damping arises due to the nature of the aerodynamics. These types of flutter were not encountered in the one-degree-of-freedom case, although case II of chapter 6 did show how oscillations near the stall angle can have enough negative damping to sustain a self-excited harmonic oscillation. The negative damping does not last throughout the entire cycle of the oscillation, however, and flutter does not occur. Flutter was encountered, however, in the two-degree-of freedom case; this is categorized as binary flutter (other forms of flutter are also possible). Binary refers to the fact that the flutter is caused by the coupling of two degrees-of-freedom; in this case, pitch and plunge. This type of flutter is also referred to as classical flutter. Once again, energy is being extracted from the airstream, but this time it is caused by the way the two modes of motion interact. This binary flutter occurs when the plunge motion acts to add energy in unison with the pitch, they therefore reinforce each other and cause the airfoil to oscillate violently.

The system parameters pertaining to the pitch degree-of-freedom will take the same values as defined in Section 6.2. The remaining system parameters, pertaining to the newly added plunge degree-of-freedom must therefore be set. The plunge damping ratio is assumed to be zero, just like the pitch damping ratio ($\varsigma_h = 0$), and no plunge degree-of-freedom forcing is used ($Po(s)$=0). Under these circumstances the aeroelastic equations (4-17) and (4-18) reduce to the following equations:

$$\xi'' + x_\alpha \alpha'' + \frac{\varpi^2}{U^{*2}}\xi = \frac{-1}{\pi\mu} C_n(s) \tag{7-1}$$

$$\frac{x_\alpha}{r_\alpha^2}\xi'' + \alpha'' + \frac{1}{U^{*2}}\alpha = \frac{2}{\pi\mu r_\alpha^2} C_m(s) + Qo(s) \tag{7-2}$$

where $Qo(s)=Qo\sin(ks)$

Equations (7-1) and (7-2) are the non-linear equations that will be studied in this chapter.

7.2 Flutter

The analytical determination of the non-linear flutter boundary is beyond the scope of this thesis; however, a linear analysis can be done and will be shown to be quite accurate nonetheless. The non-dimensional two-degree-of-freedom equations (Equations (7-1) and (7-2)) can be rewritten in matrix form in the following way:

$$[M]z''+[C]z'+[E]z=[Q]z+[F] \tag{7-3}$$

where $z=[\xi\ \alpha]^T$, [Q] is the aerodynamic matrix, [F] is the forcing matrix and the prime denotes differentiation with respect to non-dimensional time.

All of the structural damping terms are considered to be zero, and therefore [C]=[0]. The next step is to choose a solution. A simple harmonic solution of the following form is assumed:

$$z=z_o e^{ik_r s} \tag{7-4}$$

where k_r refers to the reduced frequency of the harmonic response.

Now that the form of the solution is known, the linear aerodynamic solution must be found. This solution may be found through the use of the reciprocal relation. This relation will allow the linear solution for a harmonically oscillating airfoil to be found from the indicial response that was used in this thesis. All of the indicial responses to the various step inputs were approximated with exponential functions, and had the following form:

$$\phi(s, M) = A(B + C\exp(-as) + D\exp(-bs)) \tag{7-5}$$

where ϕ is the indicial function, which when multiplied by the step input gives the indicial response and s is non-dimensional time.

The response to a harmonic input takes the following form:

$$H(k_r, M) = F + iG \tag{7-6}$$

where H is the harmonic function, which when multiplied by the harmonic input of equation (7-4) will give the harmonic response.

In chapter two the reciprocal relation of equation (2-18) was used to convert the harmonic response of Theodorsen to the indicial response of Wagner. An alternative form of the reciprocal relation will allow the indicial response of the linear portion of the model to be converted to the linear harmonic response. The reciprocal relation and its solution are:

$$H(k_r, M) = F + iG = ik\int_0^\infty \phi(s, M)\exp(-ik_r s)ds \tag{7-7}$$

Using the indicial function of equation (7-5), the solution for the harmonic response is:

$$F = A(B + \frac{Ck_r^{\,2}}{a^2 + k_r^{\,2}} + \frac{Dk_r^{\,2}}{b^{-} + k_r^{\,2}})$$

$$G = A(\frac{Cak_r}{a^2 + k_r^{\,2}} + \frac{Dbk_r}{b^2 + k_r^{\,2}}) \tag{7-8}$$

Using the above relations the linear indicial response of equations (2.39)-(2.42) can be converted to the linear harmonic response, which takes the following form:

<u>Harmonic Pitch Response Function</u>

$$C_{n\alpha}(k_r, M) = [(\mathrm{Re}\, C_{n\alpha}) + i(\mathrm{Im}\, C_{n\alpha})]$$

$$C_{nq}(k_r, M) = [(\mathrm{Re}\, C_{nq}) + i(\mathrm{Im}\, C_{nq})]$$

Harmonic Pitch Rate Response Function

$$C_{m\alpha}(k_r, M) = [(\mathrm{Re}\, C_{m\alpha}) + i(\mathrm{Im}\, C_{m\alpha})]$$

$$C_{mq}(k_r, M) = [(\mathrm{Re}\, C_{mq}) + i(\mathrm{Im}\, C_{mq})] \tag{7-9}$$

where "Re" refers to the real part, "Im" refers to the imaginary part.

When these harmonic functions are multiplied by the appropriate harmonic inputs the linear harmonic solution is obtained. These functions must now be incorporated into the complex aerodynamic matrix [Q]. The following inputs are used:

Pitch Input (Includes Pitch Equivalent)

$$\alpha + \frac{q}{2} + \frac{\dot{h}}{U_\infty} = \alpha + 2\alpha' + \xi' = \alpha - 2ik_r\alpha - ik_r\xi$$

Pitch Rate Input

$$q = 2\alpha' = -2ik_r\alpha \tag{7-10}$$

where the first equality converts the variables used in the aerodynamic model to those used in the aeroelastic model via Table (4-25), and the second equality converts the variables when the response is known to be harmonic.

Using the above inputs with the harmonic functions, the complex aerodynamic matrix may now be found:

$$Q = \frac{1}{\pi\mu}\begin{bmatrix} \{[(\mathrm{Im}C_{n\dot{\alpha}})k_r] - i[k_r(\mathrm{Re}C_{n\dot{\alpha}})]\}, & \{[2(\mathrm{Im}C_{nq})k_r - (\mathrm{Re}C_{n\alpha})] - i[(\mathrm{Im}C_{n\alpha}) + 2(\mathrm{Re}C_{nq})k_r]\} \\ 2\{[(-\mathrm{Im}C_{m\dot{\alpha}})k_r] + i[k_r(\mathrm{Re}C_{m\dot{\alpha}})]\}, & 2\{[-2(\mathrm{Im}C_{mq})k_r + (\mathrm{Re}C_{m\alpha})] + i[(\mathrm{Im}C_{m\alpha}) + 2(\mathrm{Re}C_{mq})k_r]\} \end{bmatrix}$$

(7-11)

A method using artificial damping is then used for the flutter analysis. This method commences by adding an artificial damping in complex form as follows:

$$[M]z''+\frac{(1+ig)}{U*^2}[E]z=[Q]z \tag{7-12}$$

The theory is that when g is negative the system is stable because external forcing is required to maintain simple harmonic motion. Therefore when g is positive, the opposite is true and the system is unstable. The flutter boundary is when g=0. When applied to the model used in this thesis the matrices take the following form:

$$M=\begin{bmatrix} 1 & x_\alpha \\ x_\alpha & r_\alpha^2 \end{bmatrix} \qquad E=\begin{bmatrix} \varpi^2 & 0 \\ 0 & r_\alpha^2 \end{bmatrix} \tag{7-13}$$

and $[Q]$ is defined above.

Inputting the solution of equation (7-4) into equation (7-12) yields

$$\{-k_r{}^2[M]-[Q]+\frac{(1+ig)}{U*^2}[E]\}z_o=[0] \tag{7-14}$$

This equation is an eigenvalue problem, whose eigenvalue is equal to $\frac{(1+ig)}{U*^2}$.

The following procedure is taken to determine the flutter boundaries: 1) the value of k_r is set; 2) all of the matrices are calculated; 3) eigenvalue analysis reveals two eigenvalues; 4) the real portion of each eigenvalue allows U^* to be obtained while the imaginary portion allows the determination of g. By setting the value of k_r at many different values, two curves of g versus U^* may be obtained. When one of the curves gives g greater than zero the airfoil experiences linear flutter. Many pertinent flutter boundary graphs may be found.

The first graph that may be obtained is the variation of artificial damping (g) with the non-dimensional velocity (U^*). An example of this is shown in Figure 7.1(a) (Qo=0, 0.04< k_r <0.2, $\alpha_{mean} = 0\,\text{deg}, \varpi = 3)$. Two curves are obtained because of the two eigenvalues. One of those curves always has negative values of g, while the other changes between negative and positive values. This latter curve is the one that determines the flutter boundary (Figure 7.1(b)). These curves are found for a constant value of the ratio of natural frequencies (ϖ), which for the above example was 3. The non-dimensional frequency of the harmonic response (k_r) is varied from 0.04 to 0.2, in accordance with the boundaries set in Chapter 6.

By varying the ratio of natural frequencies between 0 and 6 a family of curves of g versus U^* may be generated. Some of the curves from this family can be seen in Figure 7.2(a). The lengths of these curves vary because of the boundaries set for k_r and U^* (U^* should be less than 35 according to chapter 6). By determining the value of non-dimensional velocity (U^*) at which the artificial damping (g) is equal to zero, which is the value of U^* where the curves of Figure 7.2(a) cross the dotted identity line, a flutter boundary may be created between the ratio of natural frequencies and non-dimensional velocity. This can be seen in Figure 7.2(b), and is the curve labeled L, to denote that it corresponds to the linear system. To verify the usefulness of the flutter boundary plot, which was derived from linear analysis, it must be compared to the non-linear system.

The non-linear flutter boundary may be found by studying the non-linear response of the airfoil with the following values for the airfoil parameters: $\alpha_{mean} = 0\,\text{deg}$, Qo=0, the ratio of natural frequencies is varied between 0 and 6 incremented by 0.2, while the value of the non-dimensional velocity is increment by 0.1 starting below the linear flutter boundary (Figure 7.2(b)) until such a point where the non-linear system experiences divergent oscillations, corresponding to flutter. The presence of flutter may be verified by examining the time-histories of the responses. Plotting the points where flutter first occurs produces the non-linear boundary as approximated by the model. The non-linear curve, labeled N-L, is shown in comparison to the linear curve in Figure 7.2(b). Figure 7.2(b) shows that the linear prediction is close, but always under-estimates, the value of U^* at which flutter occurs. This under-estimation increases as U^* increases. Another interesting feature of the plot is that the value of U^* at which flutter occurs increases as the ratio of natural frequencies decreases below the point where both frequencies are equal. If the airfoil is experiencing flutter, it may possibly be avoided by decreasing the non-dimensional velocity or by increasing the ratio of natural frequencies to greater than one or in some cases by decreasing the ratio of natural frequencies to less than one. The non-dimensional velocity may be decreased by increasing the torsional stiffness or by decreasing the airspeed.

One example of flutter will be studied (Qo=0,$\alpha_{mean} = 0, U^* = 17.5, \varpi = 3$). According to Figure 7.2(b) this airfoil is experiencing flutter. The time histories of both the pitch and plunge motions (Figure 7.3) show that the airfoil is indeed experiencing flutter. The frequency spectra of the two degrees-of-freedom show one main frequency at k_r=0.127 for both degrees-of-freedom. The difference between the pitch and plunge motion is in their phase. The plunge oscillation is almost 90 degrees out-of-phase with the pitch oscillation. This means that the plunge rate is almost in phase with the pitch. Under this scenario the airfoil is extracting the maximum energy from the airstream, and because of the fact that the frequencies for both degrees of freedom are identical, this phase difference between pitch and plunge is maintained; thus, causing the oscillations to continue growing in amplitude. This fact is described as "frequency coalescence", and was assumed for the linear flutter analysis. Note: The reduced frequency k_r in this section refers to the frequency of the harmonic response, and should not be confused with the reduced frequency in every other section, k, which refers to the pitch forcing frequency.

7.3 Introduction of Chaos by the Addition of the Plunge Degree -of-Freedom

A reasonable range for the ratio of natural frequencies is between 0.5 and 4 (Lee and LeBlanc (1986) do not surpass a value of 10 in their analysis). According to the flutter boundary graph of Figure 7.2(b), however, the airfoil experiences flutter in the lower end of this range for values of U^* greater than 4.8. The non-dimensional velocity may be lowered below this value in two ways. One way is to increase the torsional stiffness until U^* goes below this threshold. The other way is to decrease the airspeed (U_∞) to achieve the same goal. If the airspeed is decreased, however, the model no longer falls within the range of system parameters that were used in the paper by Leishman and Beddoes (1989), on which this thesis is based. The torsional stiffness is therefore increased. Figure 7.4 shows a bifurcation plot for the following airfoil parameters: Qo=0.001, k=0.1, $\alpha_{mean} = 10\,\text{deg}$, $U^* = 5, 0.5 < \varpi < 4$. Because of the fact that the torsional stiffness is so high there is only a particular range of ϖ where non-periodic oscillations are present. This is around where the ratio of natural frequencies is equal to one. Around this value, the airstream supplies sufficient energy to the system to overcome the strong structural stiffness and allows for larger oscillations and thus larger excursions into stall, a region dominated by non-linear forces. This can be seen in Figure 7.4. The one-degree-of-freedom scenario, which is the situation for large values of the ratio of natural frequencies, shows small non-chaotic oscillations around the mean angle of attack. This may be seen in Figure 7.5. The situation shown in Figure 7.5 prevails for values of the ratio of natural frequencies greater than 2.4 as can be seen in the bifurcation plot of Figure 7.4(a). Chaotic oscillations may be found in the range of $1.2 < \varpi < 2.3$. This range can be seen in Figure 7.4(b). An example of a seemingly chaotic oscillation may be seen in Figure 7.6 (pitch response) and 7.7 (plunge response) for airfoil parameters: (Qo=0.001, $\alpha_{mean} = 10\text{deg}, U^* = 5, \varpi = 1.41$). Existing within the same range ($1.2 < \varpi < 2.3$) are examples of non-chaotic oscillations, an example of which, may be seen in Figure 7.8 (pitch response) and 7.9 (plunge response) for the following airfoil parameters: Qo=0.001, $\alpha_{mean} = 10\text{deg}, U^* = 5, \varpi = 2.285$. The time-histories and phase plots of both examples resemble responses that were studied in Chapter 6. Similarities lie between the two degrees-of-freedom, however. When chaos is present in one degree of freedom it is also present in the other and when the pitch oscillation is periodic so is the plunge. This is because the two degrees of freedom are coupled. This is the reason why Figure 7.6 and 7.7 are both chaotic (seemingly), while Figure 7.8 and 7.9 are both periodic. Another interesting comparison is in the frequency spectra. They are very similar for both degrees of freedom. The main peaks align perfectly. This may be described as frequency coalescence and is a necessary condition for binary flutter.

7.4 Summary

Although the determination of the theoretical non-linear flutter boundary was not done, the linear analysis correlated well with the approximate non-linear flutter boundary obtained from the model used in this thesis. When flutter was shown to occur it could be avoided by: 1) increasing the torsional (pitch) stiffness; 2) lowering the airspeed; 3) increasing the ratio of natural frequencies; and, 4) decreasing the ratio of natural frequencies below one (in some cases). When chaos occurs in the two-degree-of-freedom system, it occurs in both degrees-of-freedom; and conversely when chaos is not present it is not present in both degrees-of-freedom. This makes sense because the two degrees of freedom are both structurally and aerodynamically coupled. Finally, the frequency spectra for both degrees-of-freedom were very similar during flutter and near the flutter boundary, having the same frequencies. This phenomenon is known as frequency coalescence and it is a necessary condition for binary flutter.

All of these conclusions are consistent with both theoretical and experimental studies of flutter from many different sources (e.g.: Fung (1993)).

A)

B)

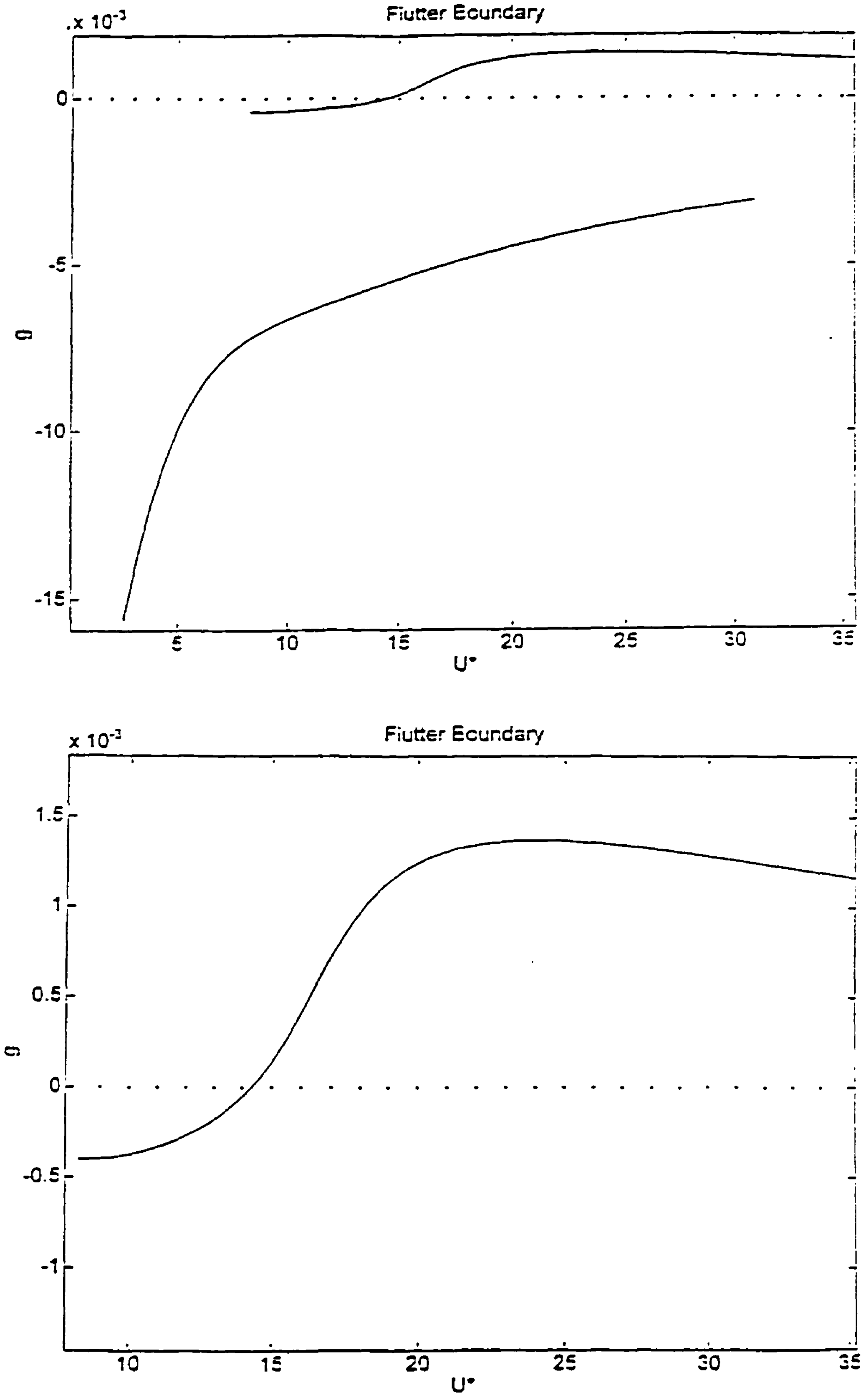

Figure 7.1: Flutter Boundary: g vs U^*; a) Using both Eigenvalues b) Focusing on Curve that Crosses Identity Line: $\alpha_{mean}=0$ deg, $Qo=0$, $0.04<k_r<0.2$, $\varpi=3$.

A)

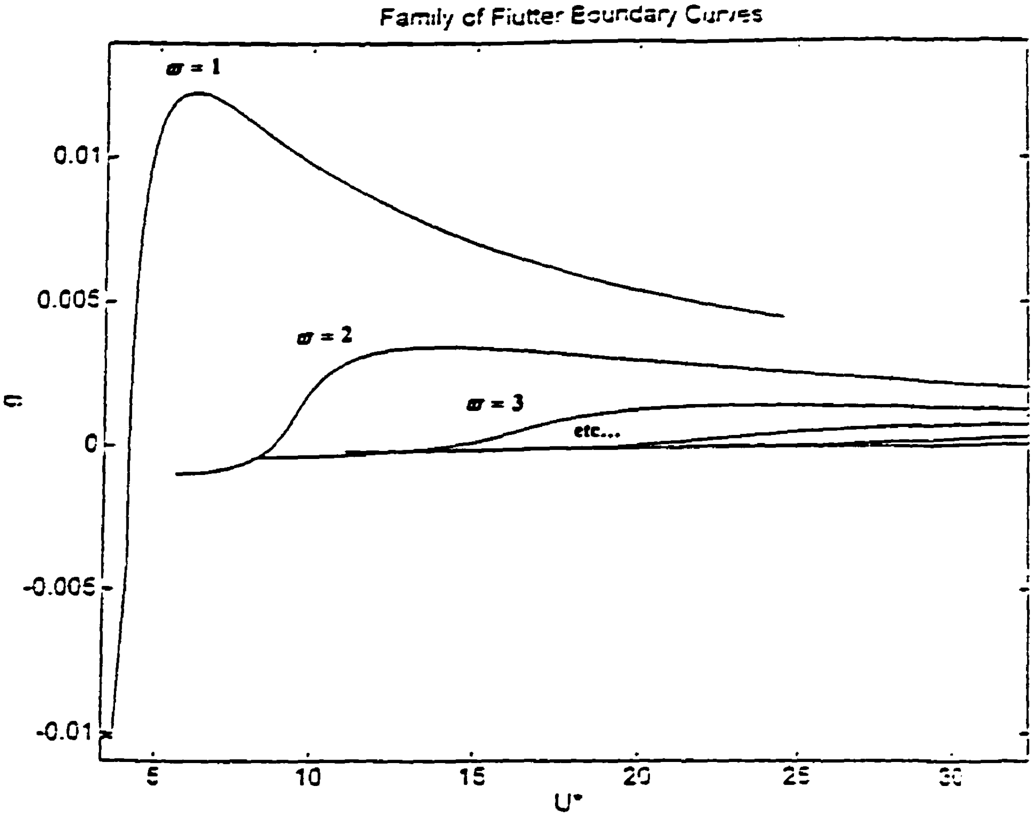

B)

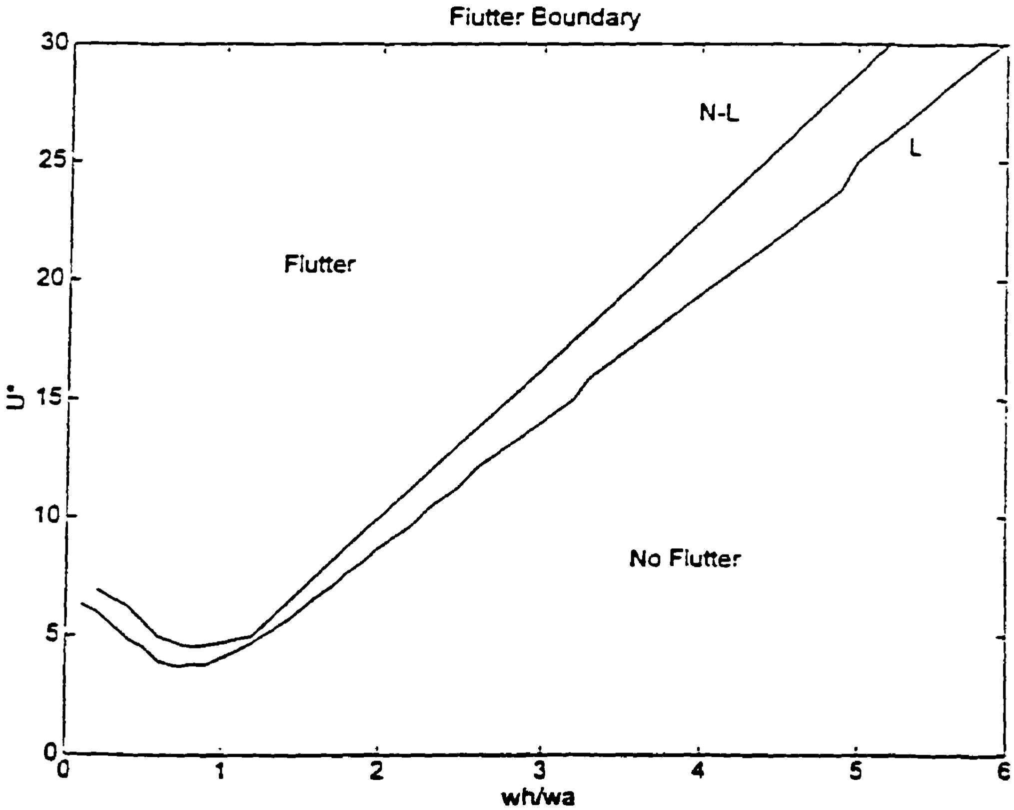

Figure 7.2: Flutter Boundary; a) Family of g vs U^* Curves b) U^* vs ϖ U^*, L: Linear, N-L: Non-Linear: $\alpha_{mean} = 0$, Qo=0, 0.04<k_r<0.2, $0 < \varpi < 6$.

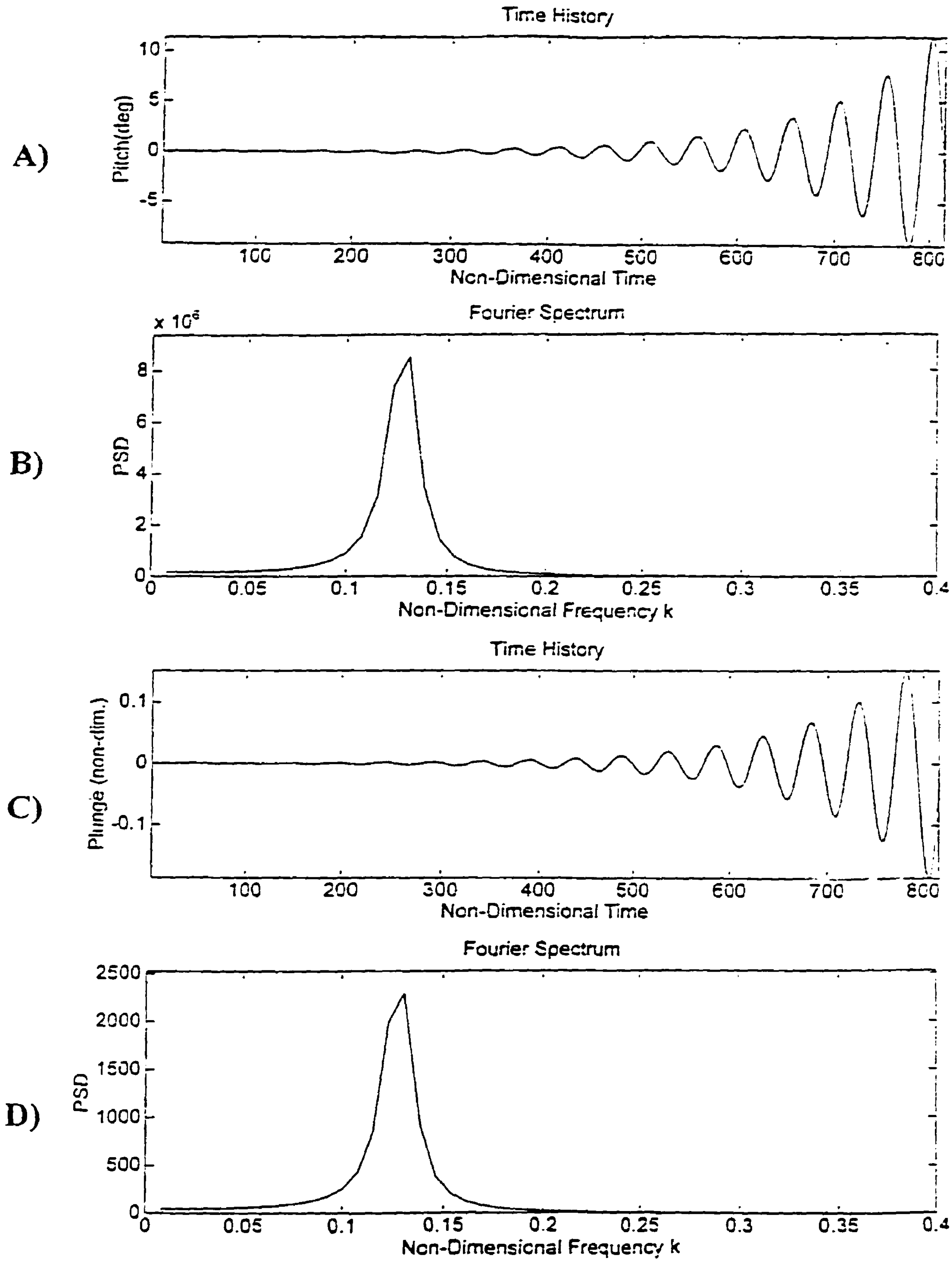

Figure 7.3: Example of Flutter; Pitch: a) Time History b) Fourier Spectrum, Plunge: c) Time History d) Fourier Spectrum: $\alpha_{mean} = 0$ deg, ***Qo*=0, *U**=17.5,** $\varpi = 3$.

A)

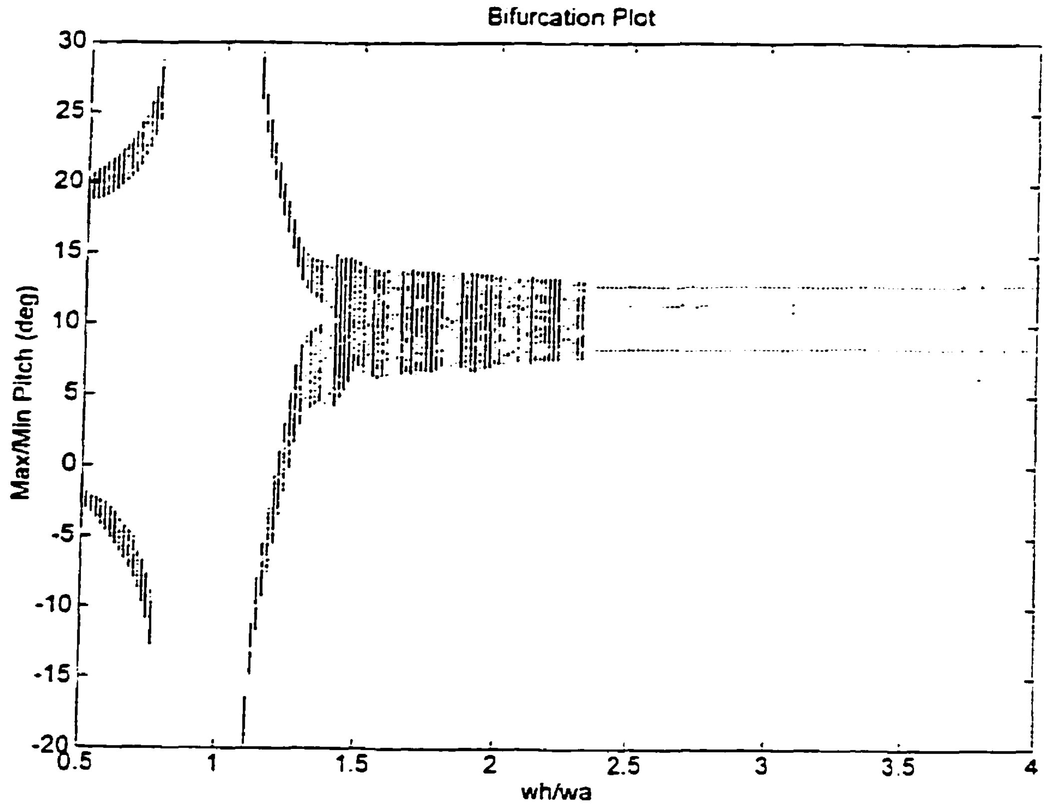

B)

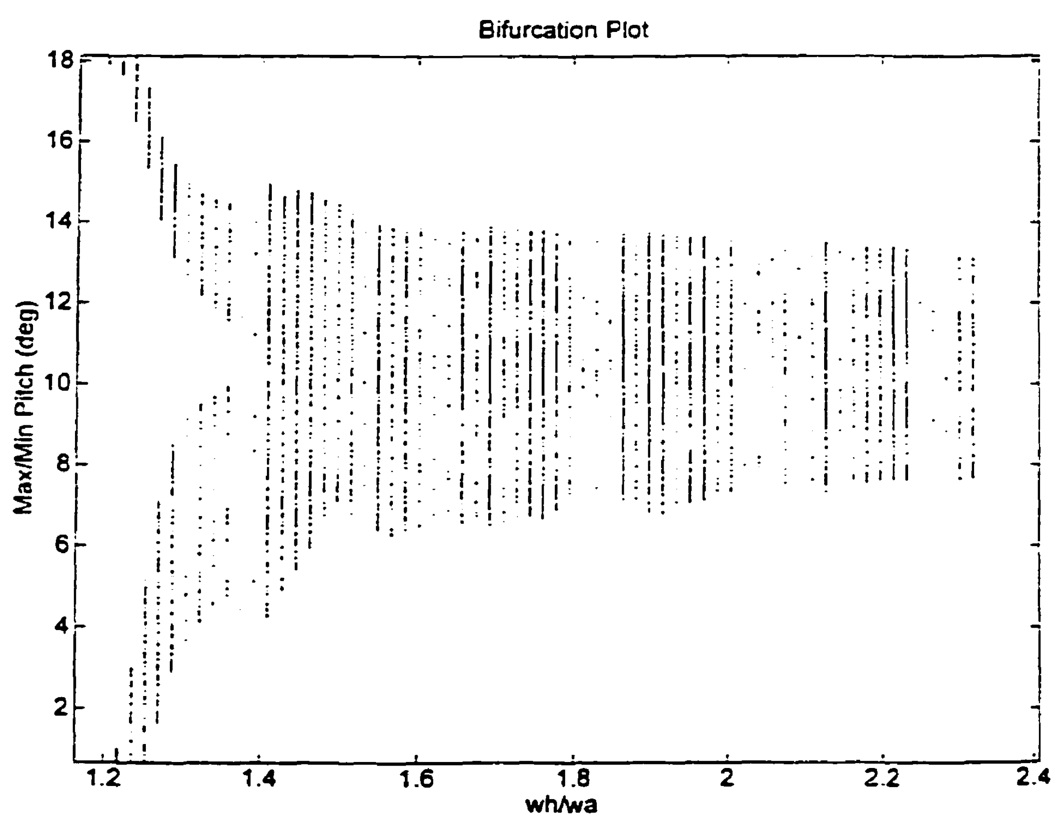

Figure 7.4: Bifurcation Plot: Plunge Degree of Freedom; a) $0.5 < \varpi < 4$ b) $1.2 < \varpi < 2.4$: $\alpha_{mean} = 10$ deg, *Qo*=0.001, *k*=0.1, *U=5.**

A)

B)

C)

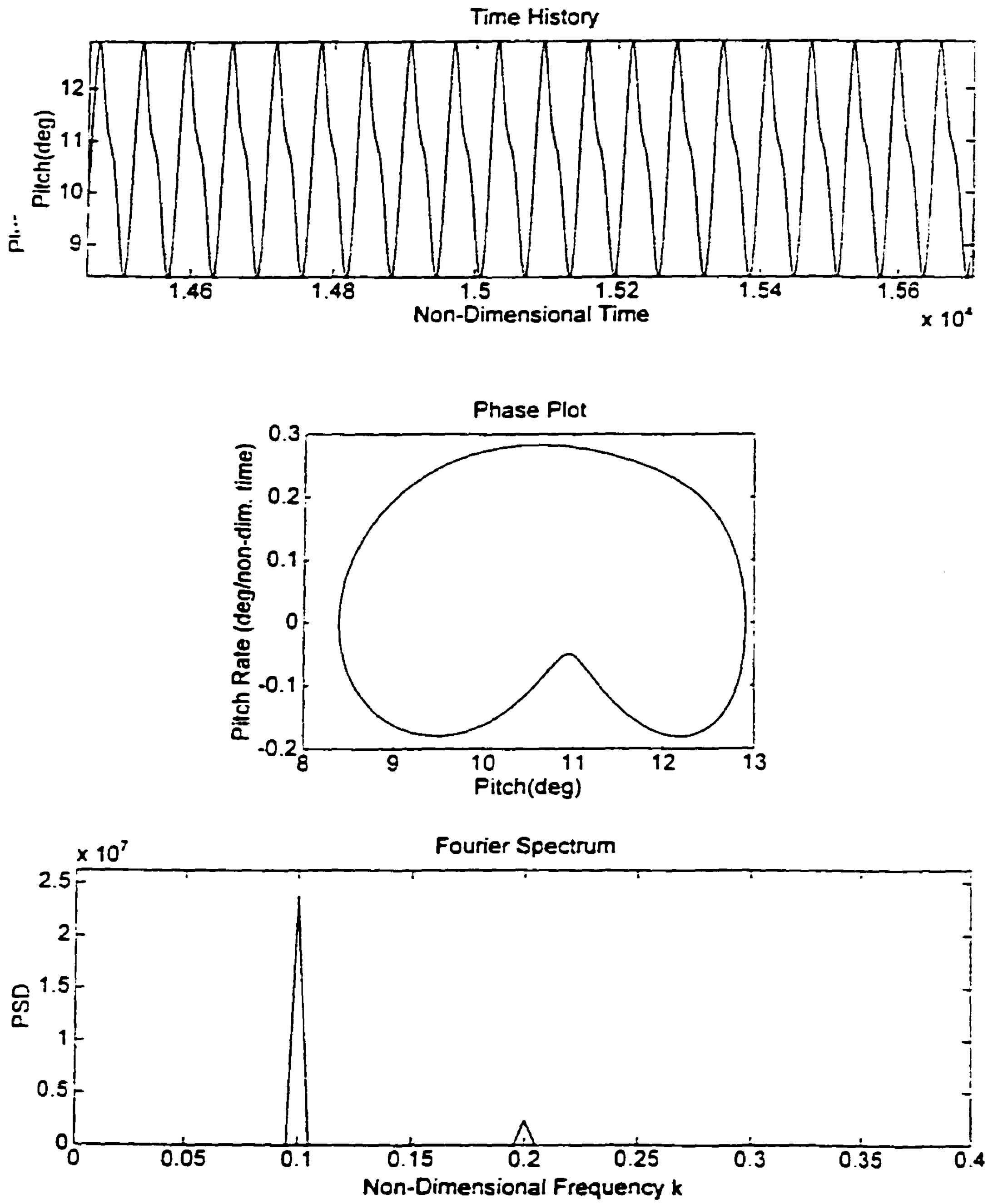

Figure 7.5: Airfoil Response (1-D.O.F.): Pitch Degree of Freedom; a) Time History b) Phase Plot c) Fourier Spectrum (Log Scale): Qo=0.001, k=0.1, α_{mean} = 10 deg, U^*=5, $\varpi = \infty$.

A)

B)

C)

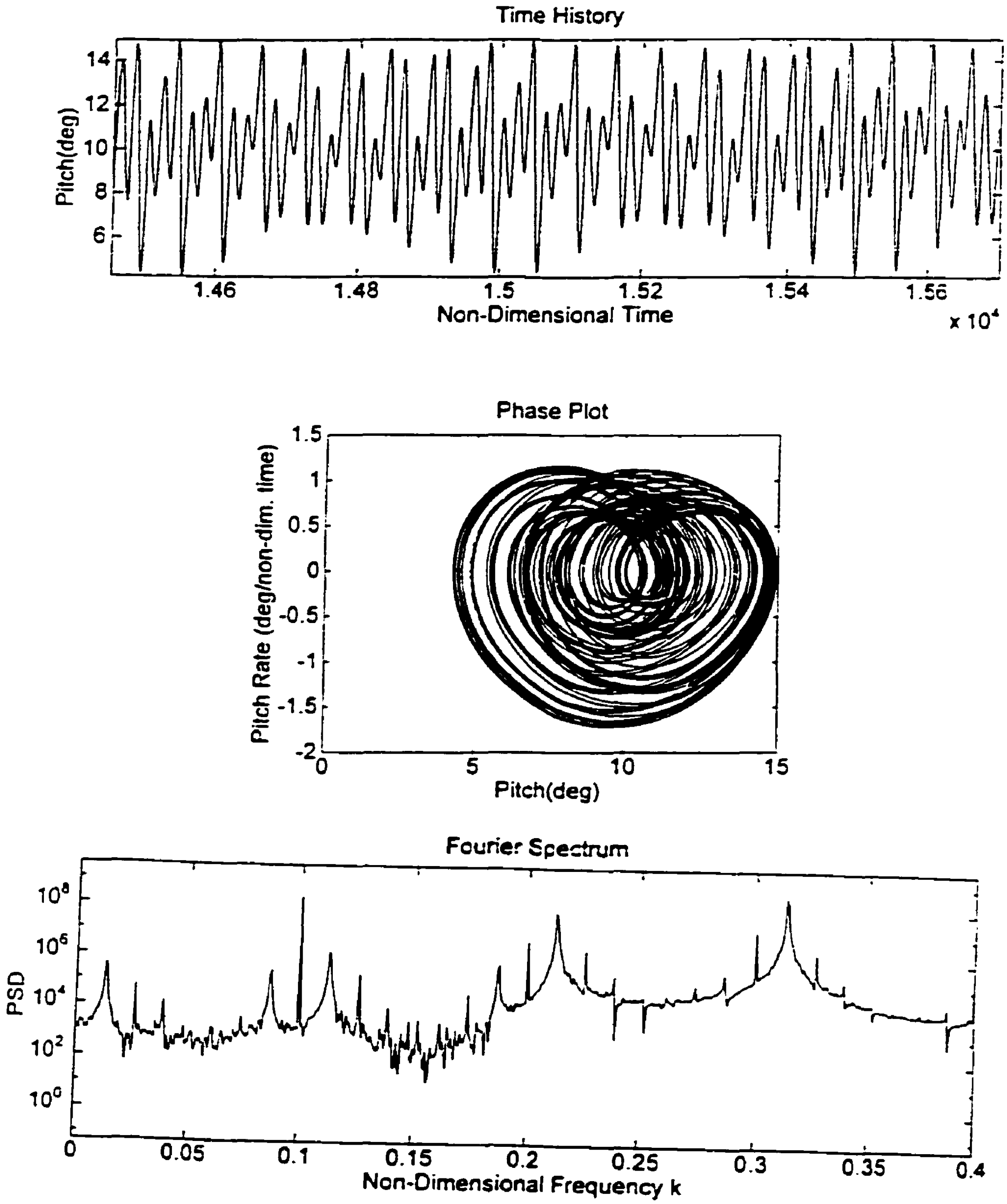

Figure 7.6: Airfoil Response: Pitch Degree of Freedom; a) Time History b) Phase Plot c) Fourier Spectrum (Log Scale): Qo=0.001, k=0.1, α_{mean} = 10 deg, U^*=5, ϖ = 1.41.

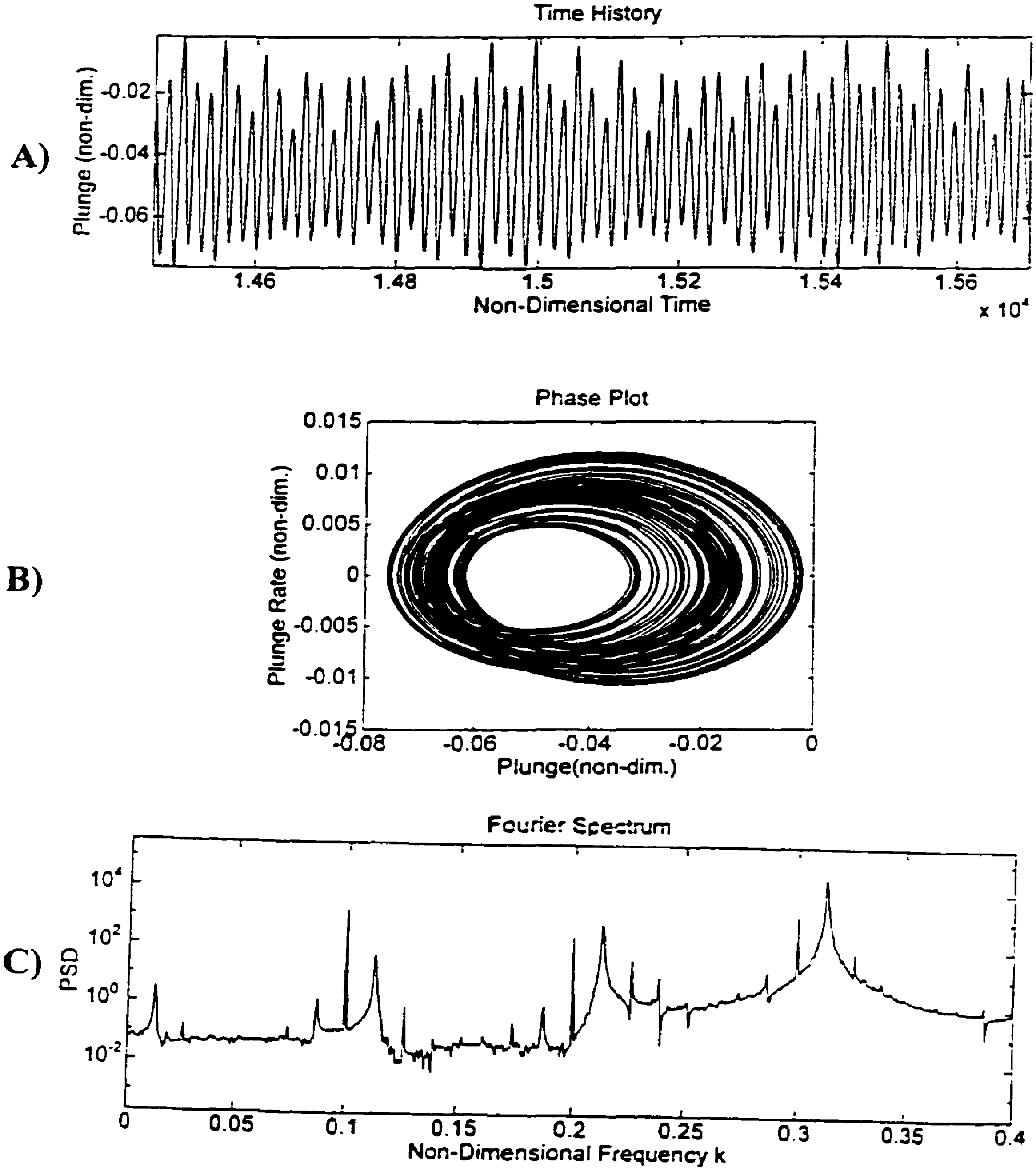

Figure 7.7: Airfoil Response: Plunge Degree of Freedom; a) Time History b) Phase Plot c) Fourier Spectrum (Log Scale): *Qo*=0.001, *k*=0.1,α_{mean} = 10 deg, *U=5, ϖ = 1.41.**

A)

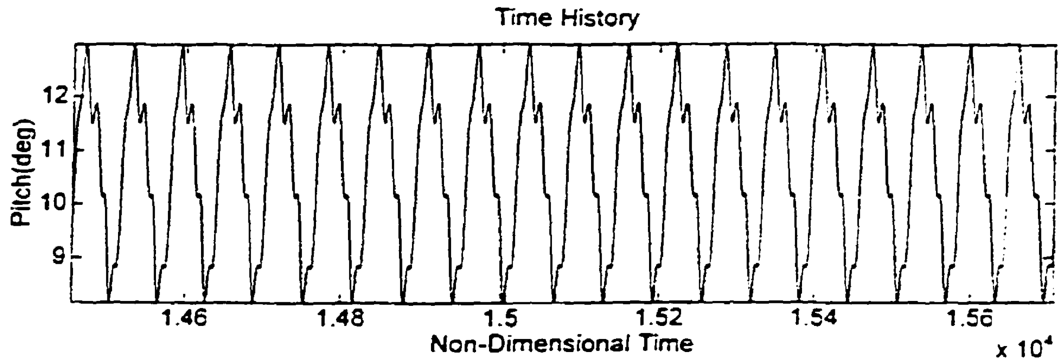

B)

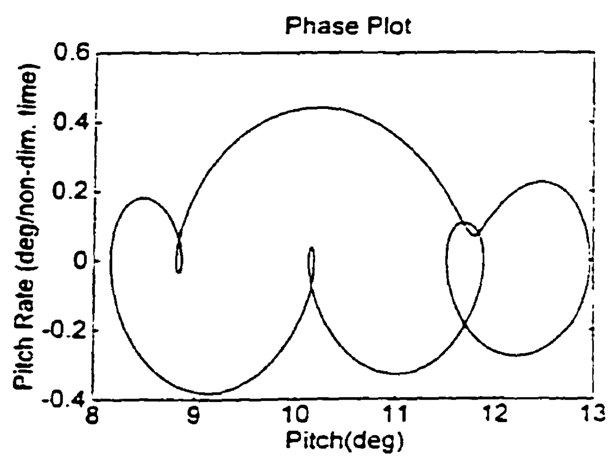

C)

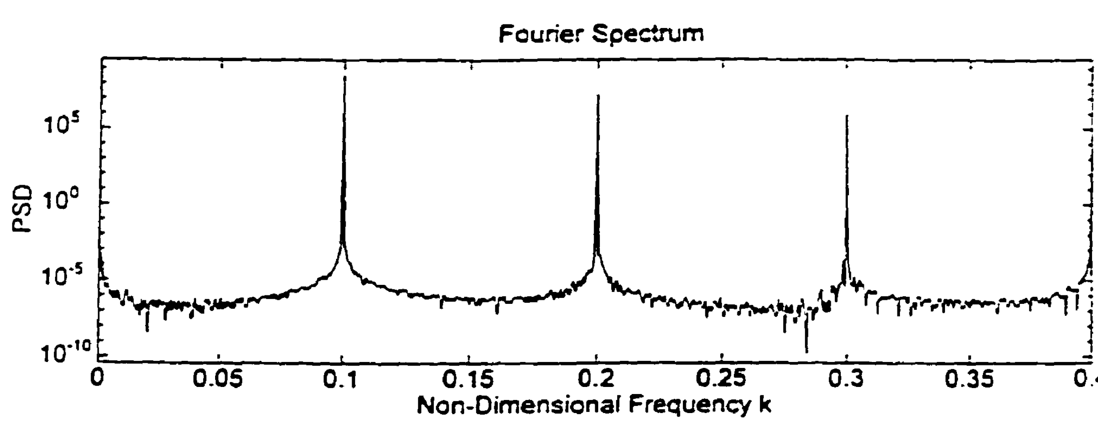

Figure 7.8: Airfoil Response: Pitch Degree of Freedom; a) Time History b) Phase Plot c) Fourier Spectrum (Log Scale): Qo=0.001, k=0.1, $\alpha_{mean} = 10$ deg, U^*=5, $\varpi = 2.285$.

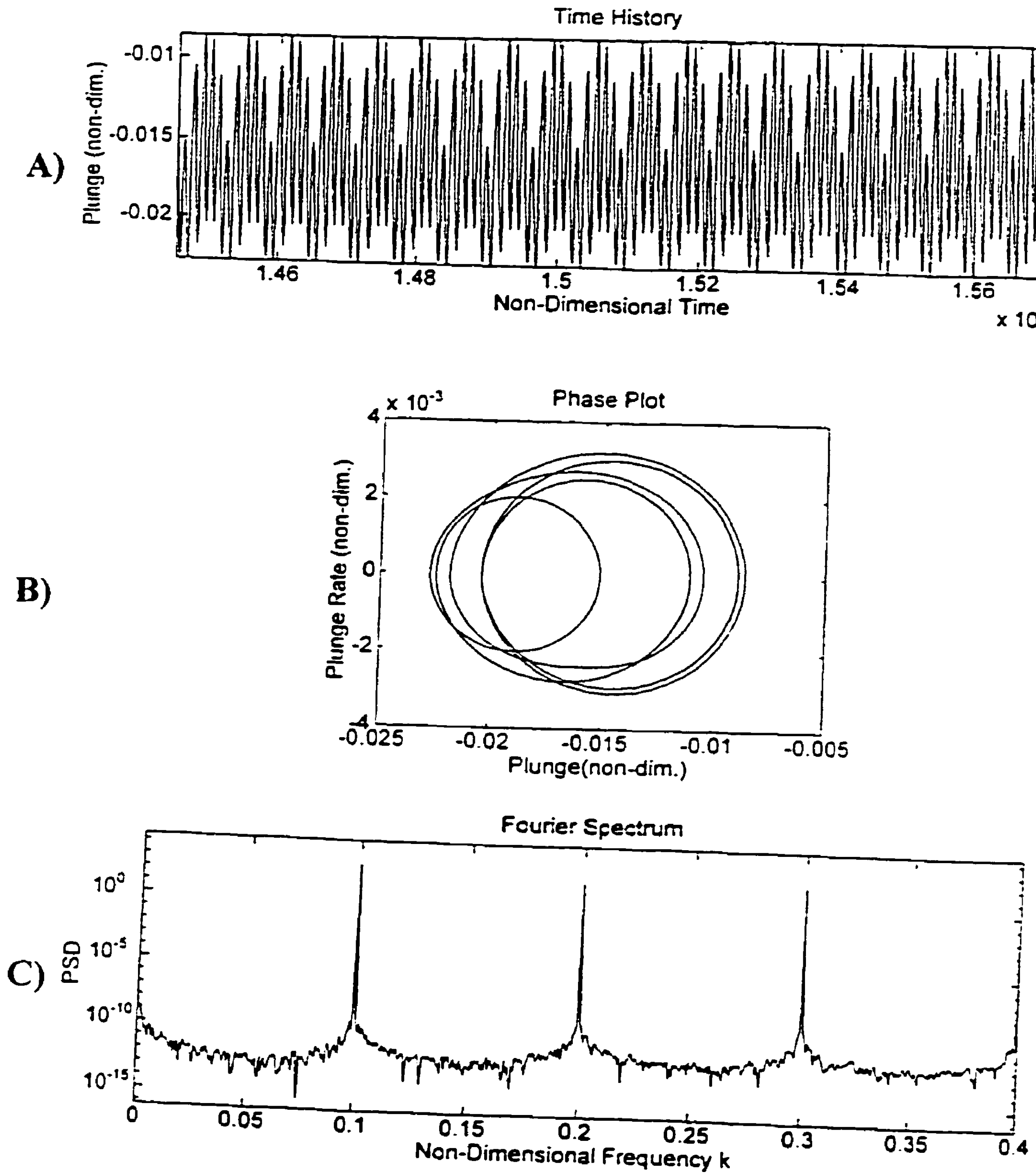

Figure 7.9: Airfoil Response: Plunge Degree of Freedom; a) Time History b) Phase Plot c) Fourier Spectrum (Log Scale): Qo=0.001, k=0.1, $\alpha_{mean} = 10$ deg, U^*=5, $\varpi = 2.285$.

Chapter 8

Conclusions and Recommendations

8.1 Introduction

The non-linear response and instabilities of a two-degree-of-freedom airfoil oscillating in dynamic stall was examined in this thesis. Many conclusions were drawn referring to the limitations of the semi-empirical model used, while others referred to the classes of motion produced by the non-linear system, and to the existence of instabilities. The main focus was the possibility of chaos and the route thereto. In this chapter, the main conclusions of this thesis are summarized and recommendations are given towards improving the model.

8.2 Conclusions

The Dynamic Stall Model

1) The dynamic stall model used in this thesis correlated well with the model derived by Leishman and Beddoes, which was presented at the 42^{nd} Annual Forum of the American Helicopter Society (Leishman and Beddoes, 1986). When comparing the data obtained by Leishman and Beddoes for both harmonic and ramp inputs with the results obtained from the model used in this thesis, they were found to be almost identical.

2) The plunge degree-of-freedom was incorporated into the model, taking into account non-linear plunge effects. This was done in accordance with the work of Leishman and Tyler (1992). The only thing that was done differently was the altering of the pressure lag time constant (T_p). This constant was not altered because the experiments used to determine the altered time constant, did not match the experiments used by Leishman and Beddoes.

3) Errors were discovered in the paper by Leishman and Beddoes (1986). They ignored the circulatory contribution due to pitch-rate in the moment coefficient. There were also typographical errors in some of the constants used in their model. These errors were discovered while cross-checking the paper with other papers written by Leishman and/or Beddoes.

The Aeroelastic Model

4) The aeroelastic model was based on the work of Lee and LeBlanc (1986) and was easily implemented into the overall model. The only difficulty arose with the possibility of feed-back loops. Perturbing the response during such a loop solved this problem.

The One-Degree-of-Freedom System

5) Instability was discovered when the airfoil oscillated about the static stall angle. Under this condition the airfoil was able to sustain a self-excited oscillation.

6) Every class of motion was produced by the non-linear system. Periodic, quasi-periodic and chaotic responses were found in every case studied, while equilibrium points

were found when the airfoil had no external forcing and was not oscillating around the static-stall angle. Limited or narrow-band chaos was very often present.

7) Several routes to chaos were discovered. The quasi-periodic route, period-doubling route and intermittence route were all discovered and almost always worked in combination. Some of these routes were compared to classical examples. Quasi-periodic routes similar to those taken by the Peroxidase-Oxidase Reaction and the Rayleigh-Bénard Thermal Convection System were found, while a type I intermittency route very similar to a classical example was also found.

The Two-Degree-of-Freedom-System

8) Binary flutter was discovered in the two-degree-of-freedom system. A linear analysis was done, which correlated well with the non-linear model.

9) The frequency spectrum around the flutter boundary was found to have almost the same frequencies for both degrees-of-freedom. This is known as frequency coalescence.

10) When flutter was encountered it could be avoided by increasing the torsional stiffness, decreasing the airspeed, increasing the ratio of natural frequencies or, in some cases, by decreasing the ratio of natural frequencies below one.

8.3 Recommendations

In light of the conclusions summarized above there are ways in which the model may be improved. There are also capabilities that were incorporated into model that were not explored, which may be possible avenues for future research.

To improve the aerodynamic model one must perform a new set of experiments incorporating both degrees-of-freedom using well defined inputs. Once this is done, curve-fitting techniques may be used to re-determine all of the time constants used in the model. The circulatory contribution due to pitch-rate to the moment coefficient should be added before the re-evaluation of the time constants so that the aerodynamic model is complete. Doing this would maximize the accuracy of the aerodynamic model. To improve the numerical scheme used for the aeroelastic model one may wish to incorporate a relaxation scheme so as to avoid feed-back loops. To improve the non-linear analysis would require the use of more complex tools. The determination of the Lyapunov exponents is one such tool. The application of such tools on the response produced by the model used in this thesis could be the basis of further research.

The capabil'ties of the model used were not all explored. Mach number and many of the structural parameters were not varied. The Mach number could have been varied between 0.3 and 0.8. An interpolation algorithm, which was incorporated into the computer program, assured that all of the Mach-number-dependent constants could be evaluated throughout the entire range between 0.3 and 0.8. By varying the Mach number and the structural parameters (e.g.: position of the center of gravity), new conditions where instabilities occur, and new routes to chaos may be discovered.

References

1. Beddoes, T.S., **A Qualitative Discussion of Dynamic Stall.** A Special Course on Unsteady Aerodynamics, AGARD Rep. 678, 1979.

2. Beddoes, T.S., **Application of Indicial Aerodynamic Functions.** A Special Course on Unsteady Aerodynamics, AGARD Rep. 679, 1980.

3. Beddoes, T.S., **Practical Computation of Unsteady Lift.** Vertica, Vol. 7, No. 2, pp.55-71, 1983.

4. Beddoes, T.S., **Representation of Airfoil Behaviour.** Vertica, Vol. 7, pp. 183-197, 1983.

5. Bergé, P., Pomeau, Y., Vidal, C., **Order Within Chaos.** John Wiley & Sons, New York, 1986.

6. Bielawa R.L., Johnson S.A., Chi, R.M., Gangwani, S.T., **Aeroelastic Analysis for Propelers.** NASA Contractor Rept. 3719, 1983.

7. Bisplinghoff, R.L., Ashley, H. and Halfman, R.L. , **Aeroelasticity.** Addison-Wesley, Cambridge, MA, 1955.

8. Carr, L.W., **Progress in Analysis and Prediction of Dynamic Stall.** AIAA Journal of Aircraft, Vol. 25, No. 1, pp. 6-17, Jan 1988.

9. Ericsson, L.E. and Reding, J.P., **Fluid Mechanics of Dynamic Stall.** Journal of Fluids and Structures 2, 1988.

10. Fung, Y.C., **An Introduction to the Theory of Aeroelasticity.** Dover Publications, New York, 1993.

11. Hauenstein, A.J., Zara, J., Eversman, W., Qumei, I., **Chaotic and Nonlinear Dynamic Response of Aerosurfaces with Structural Nonlinearities.** Proceedings of the 33rd AIAA/ASME/ASCE/AHS/ASC Structures, Structural Dynamics and Materials Conference, Part 4: Structural Dynamics II, pp. 2367-2375, Dallas, 1992.

12. Houbolt, J.C., **A Recurrence Matrix Solution for the Dynamic Response of Elastic Aircraft.** Journal of Aeronautical Sciences, Vol. 17, pp. 540-550, 1950.

13. Lee, B.H.K. and LeBlanc, P., **Forced Oscillation of a Two-Dimensional Airfoil with Non-Linear Aerodynamic Loads.** NRC, Rep. LR-617, No. 25411, Ottawa, Jan 1986.

14. Lee, B.H.K., Tron, A., **Effects of structural Nonlinearities on Flutter Characteristics of the CF-18 Aircraft.** Journal of Aircraft, Vol. 26, No. 8, pp. 781-786, 1989.

15. Leishman, J.G. and Beddoes, T.S., **A Generalized Model for Airfoil Unsteady Aerodynamic Behaviour and Dynamic Stall using the Indicial Method.** Proceedings of the 42nd Annual Forum of the American Helicopter Society, Washington DC, 1986.

16. Leishman, J.G. and Beddoes, T.S., **A Semi-Empirical Model for Dynamic Stall.** Journal of the American Helicopter Society, Vol. 34, No. 3, pp. 3-16, Jul 1989.

17. Leishman, J.G., Tyler, J.C., **Analysis of Pitch and Plunge Effects on Unsteady Airfoil Behaviour.** Journal of the American Helicopter Society, pp. 69-83, Jul 1992.

18. Leishman, J.G., **Validation of Approximate Indicial Aerodynamic Functions for Two-Dimensional Flow.** AIAA Journal of Aircraft, Vol. 25, No. 10, pp. 914-922, 1988.

19. Lomax, H., Heaslet, M.A., Fuller F.B., and Sluder L., **Two Dimensional and Three Dimensional Unsteady Lift Problems in High Speed Flight.** NACA rep. 1077, 1952.

20. Lomax, H., **Indicial Aerodynamics.** AGARD Manual on Aeroelasticity, Part II, Chapter VI, 1968.

21. Mazelsky, B. and Drishler, J.A., **Numerical Determination of Indicial Lift and Moment Functions for a Two-Dimensional Sinking and Pitching Airfoil at Mach Numbers 0.5 and 0.6.** NACA TN-2739, 1952.

22. Mazelsky, B., **On the Non-Circulatory Flow About a Two-Dimensional Airfoil at Subsonic Speeds.** Journal of the Aeronautical Sciences , Vol.19, No. 12, 1952.

23. Moon, Francis C., **Chaotic Vibrations.** John Wiley & Sons, New York, 1987.

24. Nayfeh, Ali H., Balachandran, Balakumar, **Applied Nonlinear Dynamics.** John Wiley & Sons, New York, 1995.

25. Peterson, L.D., Crawley, E.F., **Improved Exponential Time Series Approximation of Unsteady Aerodynamic Operators.** AIAA Journal of Aircraft, Vol. 25, No.2, 1988.

26. Price, S.J., Alighanbari, H., Lee, B.H.K., **The Aeroelastic Response of a Two-Dimensional Airfoil with Bilinear and Cubic Structural Nonlinearities.** Journal of Fluids and Structures, Vol. 9, pp. 175-193, 1995.

27. Price, S.J., Keleris, J.P., **Non-Linear Dynamics of an Airfoil Forced to Oscillate in Dynamic Stall.** Journal of Sound and Vibration, 194(2), pp. 265-283, 1995.

28. Reissner, E., **On the Application of Mathieu Functions in the Theory of Subsonic Compressible Flow Past Oscillatory Airfoils.** NACA TN-2363, 1951.

29. Tang, D.M., Dowell, E.H., **Flutter and Stall Response of a Helicopter Blade with Structural Nonlinearity.** Journal of Aircraft, Vol. 29, No. 5, 1992.

30. Theodorsen, T., **General Theory of Aerodynamic Instability and the Mechanism of Flutter.** NACA TR-496, 1935.

31. Thompson, J.M.T., Stewart, H.B., **Nonlinear Dynamics and Chaos.** John Wiley & Sons, New York, 1986.

32. Thwaits, B., **Incompressible Aerodynamics.** Cambridge University Press, 1961.

33. Tran, C.T., Petot, D., **Semi-Empirical Model for the Dynamic Stall of Airfoils in View of the Application to the Calculation of Responses of a Helicopter Blade in Forward Flight.** Vertica, Vol.5, pp. 35-53, 1981.

Appendix 1-A: Determination of Time Constants

This appendix demonstrates, through an example, how the time constants are determined for the impulsive loading terms, for a complete explanation refer to (Leishman, 1987).

Lomax's exact solution (Lomax, 1968): $C_{n\alpha} = \frac{4}{M}[1 - \frac{1-M}{2M}s]$

Solution adopted by this thesis: $C_{n\alpha} = [\frac{4}{M}\phi_\alpha^I(s,M) + C_{l\alpha}(M)\phi_\alpha^C(s,M)]$

where $\phi_\alpha^c(s,M) = 1 - A1\exp(-b1\beta^2 s) - A2\exp(-b2\beta^2 s)$, $\phi_\alpha^I(s,M) = \exp(-\frac{s}{T_I})$ and

A1=0.3, A2=0.7, b1=0.14, b2=0.53, $\beta^2 = (1-M^2)$.

At s=0 the slope of Lomax's solution should be exactly equal to the slope of the Solution adopted by this thesis. The slope of Lomax's solution is therefore equal to the slope of the circulatory contribution added to the slope of the impulsive contribution. Since everything besides the impulsive time constant T_I is known, the following equation allows for the solution of T_I:

$$\frac{dC_{n\alpha}(s=0,M)}{ds} = \frac{dC_{n\alpha}{}^C(s=0,M)}{ds} + \frac{dC_{n\alpha}{}^I(s=0,M)}{ds}$$

Left Hand Side

Lomax : $$\frac{dC_{n\alpha}(s=0,M)}{ds} = -\frac{2(1-M)}{M^2}$$

Right Hand Side

Circulatory: $$\frac{dC_{n\alpha}{}^{C}(s=0,M)}{ds} = C_{l\alpha}(M)\beta^2(A1b1 + A2b2)$$

Impulsive: $$\frac{dC_{n\alpha}{}^{I}(s=0,M)}{ds} = -\frac{4}{M}T_I$$

If we combine equations and solve for T_I: $$T_I = \frac{4M}{2(1-M) + C_{l\alpha}(M)M^2\beta^2(A1b1 + A2b2)}$$

According to experiments, however, it was found that T_I approached 1.5 as M approached 0, therefore the time constant was altered to the following form (Leishman and Beddoes, 1989):

$$T_I = \frac{3M}{2(1-M) + C_{l\alpha}(M)M^2\beta^2(A1b1 + A2b2)}$$

It was found that all of the other impulsive time constants, including moment terms, were almost equal and therefore only one universal impulsive time constant was chosen .

Appendix 1-B: Linear Superposition

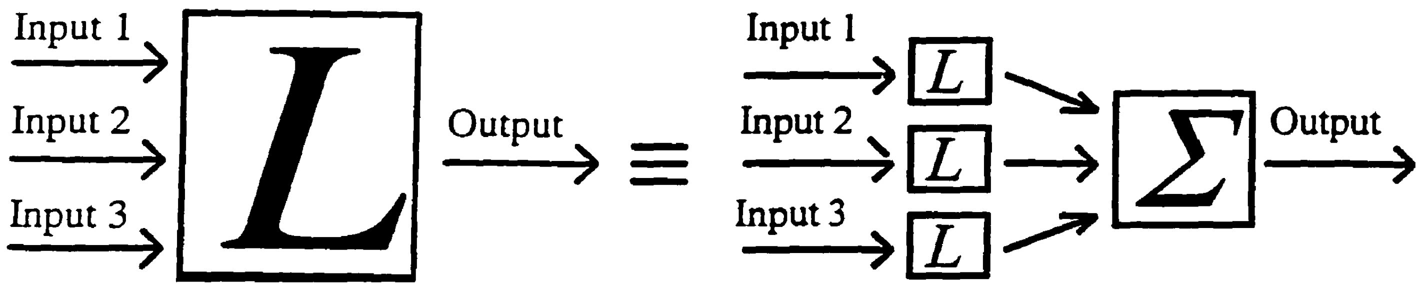

Where L is a linear operator and Σ is the superposition of outputs.

Arbitrary Input Approximated as The Sum of Step Inputs

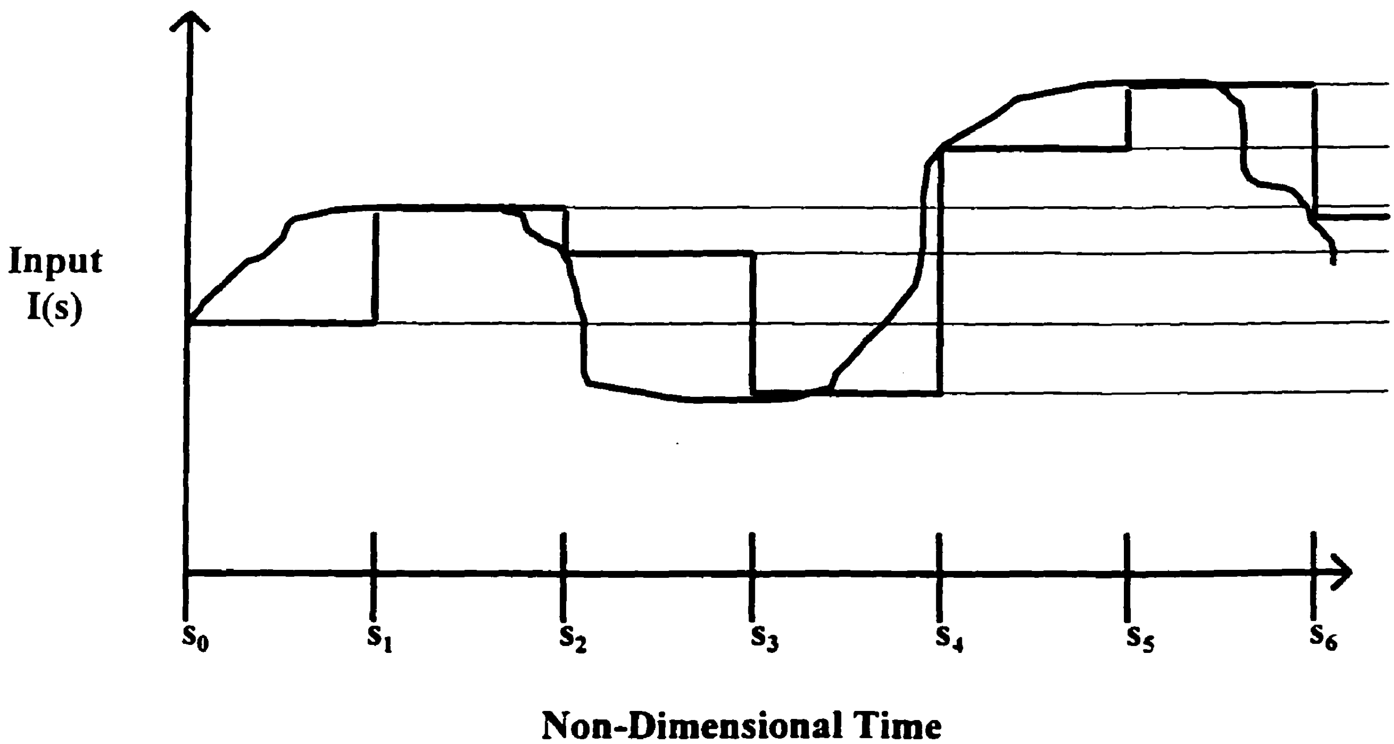

Approximated Total Input

Total Input=Input1+Input2+Input3+... or

$$I(s) \approx [I(s_o)]1(s_o) + [I(s_1) - I(s_o)]1(s_1 - s_o) + [I(s_2) - I(s_1)]1(s_2 - s_1) + [I(s_3) - I(s_2)]1(s_3 - s_2) + \ldots + [I(s) - I(s - \Delta s)]1(s - (s - \Delta s))$$

where $1(s)$ is a step input

Output to a Step Input

$$O(s) = [A\exp(\frac{-s}{T})]1(s)$$

Total Output Using Linear Superposition

Total Output=Output1+Output2+Output3...

Time(Non -Dim.)	Output1	Output2	Output3	Output4	Linear Superposition
0	$[A]I(s_o)$	0	0	0	$O(s_o)=[A]I(s_o)$
Δs	$[A\exp(\frac{-\Delta s}{T})]I(s_o$	$[A](I(s_1)-I(s_o))$	0	0	$O(s_1)=O(s_0)\exp(-\frac{\Delta s}{T})+[A](I(s_1)-I(s_o))$
$2\Delta s$	$[A\exp(\frac{-2\Delta s}{T})]I(s_o$	$[A\exp(\frac{-\Delta s}{T})](I(s_1)-I(s_0))$	$[A](I(s_2)-I(s_1))$	0	$O(s_2)=O(s_1)\exp(-\frac{\Delta s}{T})+[A](I(s_2)-I(s_1))$
$3\Delta s$	$[A\exp(\frac{-3\Delta s}{T})]I(s_o$	$[A\exp(\frac{-2\Delta s}{T})](I(s_1)-I(s_o))$	$[A\exp(\frac{-\Delta s}{T})](I(s_2)-I(s_1))$	$[A](I(s_3)-I(s_2))$	$O(s_3)=O(s_2)\exp(-\frac{\Delta s}{T})+[A](I(s_3)-I(s_2))$

Since Δs is a constant, the value of a variable at a specific time may be considered to be at the nth sample. This means that that the output to an arbitrary input which is sampled at equally spaced time intervals is

$$\text{Input: } I(n) \Rightarrow \text{ Output: } O(n) = O(n-1)\exp(-\frac{\Delta s}{T}) + A(I(n) - I(n-1))$$

Appendix 1-C: Explanation of Piston Theory

For the mathematical derivation refer to (Bisplinghoff, Ashley and Halfman, 1955). When the airfoil experiences a step change in motion (pitch, plunge or pitch rate) it causes a step change in the boundary condition defined by equation (2-12), which means a step change in normal velocity. At the first instant in time during the step change each element of the airfoil may be considered as an infinitesimally small piston moving impulsively in a gas at rest. This means that if the induced vertical velocity is in the positive z-direction, it will create a compression wave on the top surface while creating a rarefaction wave on the bottom. The mathematical problem is summarized as follows

Acoustic Equation: $$\frac{\partial^2 \Phi'}{\partial z^2} = 1/a_\infty^2 \frac{\partial^2 \Phi'}{\partial t^2}$$

Boundary Condition: $$\frac{\partial \Phi'}{\partial z} = w_a(x,t) = -[\dot{h}(t) - \dot{\alpha}(t)[x-(c*a)/2] - U_\infty \alpha(t)]1 \quad \text{for } -c/2 \le x \le c/2$$

Let us consider a single elemental piston as defined in the following figure:

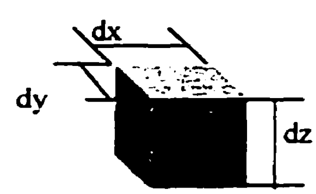

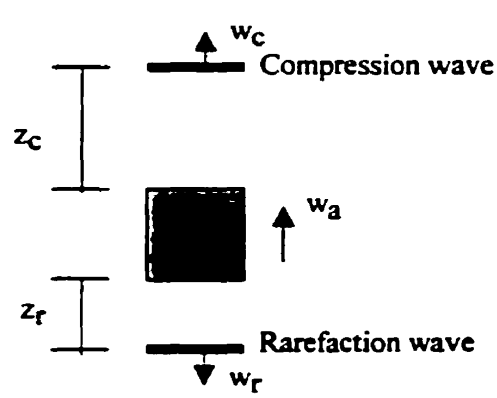

This figure shows the travel of the two waves after an infinitesimal time period dt starting at t=0. The following may be said of the above scenario:

Velocity of compression wave : $w_c = a_\infty + w_a$
Velocity of rarefaction wave : $w_r = w_a - a_\infty$
Distance travelled by compression wave : $z_c = (a_\infty + w_a)dt$
Distance travelled by rarefaction wave : $z_r = (w_a - a_\infty)dt$
Mass of compression wave : $m_c = \rho_\infty\{[(w_a + a_\infty)dt]dxdy\}$
Mass of rarefaction wave : $m_r = \rho_\infty\{[(w_a - a_\infty)dt]dxdy\}$
Acceleration of compression wave : $ac_c = (w_a)/dt$
Acceleration of rarefaction wave : $ac_c = (w_a)/dt$

Using the above, Newton's second law may be applied to determine the forces required to generate these waves and hence the pressures on the upper and lower surfaces.

$$p_{upper} - p_\infty = \frac{F_{upper}}{dxdy} = \frac{m_c ac_c}{dxdy} = \rho_\infty(w_a + a_\infty)w_a = \rho_\infty a_\infty w_a \text{ (ignoring higher order terms ie : } w_a{}^2\text{)}$$

$$p_{lower} - p_\infty = \frac{F_{lower}}{dxdy} = \frac{m_r ac_r}{dxdy} = \rho_\infty(w_a - a_\infty)w_a = -\rho_\infty a_\infty w_a \text{ (ignoring higher order terms ie : } w_a{}^2\text{)}$$

Coefficient of Change in Pressure: $$\Delta C_p = \frac{p_{lower} - p_{upper}}{\frac{1}{2}\rho U_\infty{}^2}$$

Combining everything: $$\Delta C_p(x, t=0) = -\frac{4}{M}\frac{w_a(x)}{U_\infty}$$

Once the coefficient of change in pressure has been found the lift and moment may be found by simple integration using the following formulas which may be found in any aerodynamic text book:

$$C_n(t=0) = \frac{1}{c}\int_0^c \Delta C_p(x, t=0)dx \qquad C_{m@1/4c}(t=0) = \frac{1}{c^2}\int_0^c \Delta C_p(x, t=0)(x - 1/4c)dx$$